Thesis

Measurement of neutrino oscillation parameters using neutrino and antineutrino data of the T2K experiment

HAEGEL, Leïla

Abstract

This thesis presents a measurement of the neutrino oscillation parameters with the T2K experiment. A simultaneous analysis of ND280 and Super-Kamiokande data is performed to measure sin^2 θ_23, ∆m^2_32, sin^2 θ_13 and δ_CP. The parameters estimations performed in this thesis rely on a Bayesian statistical method sampling the parameters posterior probability distributions with a Markov chain Monte-Carlo technique. The analysed data correspond to an exposure of 7.482·10^20 protons on target (POT) in ν-mode and 7.471·10^20 in antiν-mode, consisting of the T2K runs 1 to 7. The mixing angle θ_13 is precisely measured in reactor experiments; using this external input the neutrino mixing parameters are measured to be sin^2 θ_23=0.51+0.04−0.05, ∆m^2_32=2.54+0.12−0.12·10^3 eV^2·c^−4,sin^2 θ_13=0.0219±0.0011, and δ_CP=−1.79+0.91−0.66 rad. CP-conservation in the neutrino sector is excluded with a 90% credibility (or C.L.). An analysis separating νμ from antiνμ disappearance finds consistent results between neutrino and antineutrino oscillations.

Reference

HAEGEL, Leïla. *Measurement of neutrino oscillation parameters using neutrino and antineutrino data of the T2K experiment*. Thèse de doctorat : Univ. Genève, 2017, no. Sc. 5120

DOI : 10.13097/archive-ouverte/unige:103796
URN : urn:nbn:ch:unige-1037969

UNIVERSITÉ
DE GENÈVE

UNIVERSITÉ DE GENÈVE FACULTÉ DES SCIENCES
Département de Physique Nucléaire et Corpusculaire Professeur A. Blondel

Measurement Of Neutrino Oscillation Parameters Using Neutrino And Antineutrino Data Of The T2K Experiment

THÈSE

présentée à la Faculté des Sciences de l'Université de Genève
pour obtenir le grade de docteur ès Sciences, mention Physique

par

Leïla Haegel
de
France

Thèse n° 5120

GENÈVE
Atelier d'impression ReproMail
2017

UNIVERSITÉ
DE GENÈVE

FACULTÉ DES SCIENCES

DOCTORAT ÈS SCIENCES, MENTION PHYSIQUE

Thèse de Madame Leïla HAEGEL

intitulée :

«Measurement of Neutrino Oscillation Parameters Using Neutrino and Antineutrino Data of the T2K Experiment»

La Faculté des sciences, sur le préavis de Monsieur A. BLONDEL, professeur ordinaire et directeur de thèse (Département de physique nucléaire et corpusculaire), Monsieur P. MERMOD, professeur assistant (Département de physique nucléaire et corpusculaire), Monsieur A. DE ROECK, professeur (Centre européen de recherche nucléaire, Genève, Suisse), Monsieur A. KABOTH, docteur (Department of physics, Royal Holloway, University of London, United Kingdom), autorise l'impression de la présente thèse, sans exprimer d'opinion sur les propositions qui y sont énoncées.

Genève, le 8 novembre 2017

Thèse - 5120 -

Le Doyen

N.B. - La thèse doit porter la déclaration précédente et remplir les conditions énumérées dans les "Informations relatives aux thèses de doctorat à l'Université de Genève".

« Voici encore des arbres et je connais leur rugueux, de l'eau et j'éprouve sa saveur. Ces parfums d'herbe et d'étoiles, la nuit, certains soirs où le cœur se détend, comment nierais-je ce monde dont j'éprouve la puissance et les forces ? Pourtant toute la science de cette terre ne me donnera rien qui puisse m'assurer que ce monde est à moi. Vous me le décrivez et vous m'apprenez à le classer. Vous énumérez ses lois et dans ma soif de savoir je consens qu'elles soient vraies. Vous démontez son mécanisme et mon espoir s'accroît. Au terme dernier, vous m'apprenez que cet univers prestigieux et bariolé se réduit à l'atome et que l'atome lui-même se réduit à l'électron. Tout ceci est bon et j'attends que vous continuiez. Mais vous me parlez d'un invisible système planétaire où des électrons gravitent autour d'un noyau. Vous m'expliquez ce monde avec une image. Je reconnais alors que vous en êtes venus à la poésie : je ne connaîtrai jamais. Ai-je le temps de m'en indigner ? Vous avez déjà changé de théorie. Ainsi cette science qui devait tout m'apprendre finit dans l'hypothèse, cette lucidité sombre dans la métaphore, cette incertitude se résout en œuvre d'art. Qu'avais-je besoin de tant d'effort ? Les lignes douces de ces collines et la main du soir sur ce cœur agité m'en apprennent bien plus. Je suis revenu à mon commencement. Je comprends que, si je puis par la science saisir les phénomènes et les énumérer, je ne puis pour autant appréhender le monde. Quand j'aurais suivi du doigt son relief tout entier, je n'en saurais pas plus. Et vous me donnez à choisir entre une description qui est certaine, mais qui ne m'apprend rien, et des hypothèses qui prétendent m'enseigner, mais qui ne sont point certaines. Étranger à moi-même et à ce monde, armé pour tout secours d'une pensée qui se nie elle-même dès qu'elle s'affirme, quelle est cette condition où je ne puis avoir la paix qu'en refusant de savoir et de vivre, où l'appétit de conquête se heurte à des murs qui défient ses assauts ? Vouloir, c'est susciter les paradoxes. »

- Le Mythe de Sisyphe, A. Camus

Abstract

Neutrinos are the lightest fermions in the Standard Model of particle physics. While the origin of their mass is yet to be understood, their massive nature has been proven by the phenomenon of neutrino oscillations, where a neutrino created in a certain flavour can be detected in another flavour. Neutrino oscillations are parameterised by the PMNS matrix, and the oscillation probability depends on six parameters which remain to be measured with accuracy. An accurate knowledge on the oscillation parameters is primordial to constraint beyond-Standard-Model theories, as well as cosmological models such as leptogenesis. This thesis presents one of the world best measurement of four of the six oscillation parameters, namely $\sin^2\theta_{23}$, Δm^2_{32}, $\sin^2\theta_{13}$ and δ_{CP}, using the data of the T2K experiment.

The T2K experiment is a long baseline neutrino oscillation experiment located in Japan. A $\overset{(-)}{\nu}_{\mu}$ beam is created in J-PARC and travels 295 Km before reaching the Super-Kamiokande detector consisting of a 50 KTon cylindrical water tank. The detector is located 2.5° off-axis the beam center in order to intercept a narrow beam of peak energy 0.6 GeV, corresponding to the maximal expected $\overset{(-)}{\nu}_{e}$ appearance probability for this baseline. Neutrinos interact via charged-current with the oxygen of the water, creating charged leptons that cross the detector emitting Cherenkov photons. The fuziness of their Cherenkov ring enables the separation of electrons from muons, giving access to the measurement of $\overset{(-)}{\nu}_{\mu}$ disappearance and $\overset{(-)}{\nu}_{e}$ appearance. Two near detectors are placed 280 m from the target: the on-axis detector INGRID monitors the beam stability and the off-axis detector ND280 is used to constrain the neutrino interaction rate.

This thesis present a simultaneous analysis of ND280 and Super-Kamiokande data to measure $\sin^2\theta_{23}$, Δm^2_{32}, $\sin^2\theta_{13}$ and δ_{CP}. The parameters estimations performed in this thesis rely on a Bayesian statistical method sampling the parameters posterior probability distributions with a Markov chain Monte-Carlo technique. The analysed data correpond to an exposure of $7.482 \cdot 10^{20}$ protons on target (POT) in ν-mode and $7.471 \cdot 10^{20}$ in $\bar{\nu}$-mode, consisting of the T2K runs 1 to 7. The mixing angle θ_{13} is precisely measured in reactor experiments; using this external input the neutrino mixing parameters are measured to be $\sin^2\theta_{23}{=}0.51^{+0.04}_{-0.05}$, $\Delta m^2_{32}{=}\ 2.54^{+0.12}_{-0.12} \cdot 10^3\,\mathrm{eV}^2 \cdot \mathrm{c}^{-4}$, $\sin^2\theta_{13}{=}\ 0.0219 \pm 0.0011$, and $\delta_{\mathrm{CP}}{=}\ -1.79^{+0.91}_{-0.66}\,\mathrm{rad}$. CP-conservation in the neutrino sector is excluded with a 90% credibility (or C.L.). An analysis separating ν_μ from $\bar{\nu}_\mu$ disappearance finds consistent results between neutrino and antineutrino oscillations. The measurements provided in this thesis are the most stringent constraints on the neutrino oscillation parameters obtained with the T2K experiment as of today, and preliminary continuation of the analysis with the run 8 data shows an exclusion of CP-conservation at 2σ. The thesis demonstrates the power of Bayesian analyses applied to the inference of neutrino oscillation parameters, providing accurate measurements leading the path to understand this beyond Standard Model phenomenon.

Résumé

Les neutrinos sont les fermions les plus légers du modèle standard de la physique des particules. Bien que l'origine de leur masse ne soit pas encore comprise, leur masse non-nulle a été prouvée par le phénomène d'oscillation des neutrinos, où un neutrino d'une certaine saveur peut être détecté dans une autre saveur. Les oscillations de neutrinos sont paramétrisées par la matrice PMNS, et la probabilité d'oscillation dépend de six paramètres qui ne sont pas connus avec une grande précision. Une connaissance précise des paramètres est importante pour contraindre des théories au-delà du modèle standard, ainsi que des modèles cosmologiques tels la leptogenèse. Cette thèse présente la mesure de quatre des six paramètres d'oscillation, $\sin^2\theta_{23}$, Δm^2_{32}, $\sin^2\theta_{13}$ and δ_{CP}, avec les données de l'expérience T2K.
T2K est une expérience d'oscillation de neutrinos située au Japon. Un faisceau de $\overset{(-)}{\nu}_\mu$ est créé à J-PARC et parcourt 295 Km avant d'atteindre le détecteur Super-Kamiokande, qui consiste en un tank cylindrique de 50 KTon rempli d'eau. Le détecteur est situé est placé à 2.5° du centre du faisceau pour intercepter un flux dont le spectre d'énergie est réduit et le maximum se situe à une énergie de 0.6 GeV, ce qui correspond à la probabilité maximale d'apparition des $\overset{(-)}{\nu}_e$ à cette distance. Les neutrinos interagissent par des courants chargés avec l'oxygène de l'eau, créant des leptons chargés qui parcourt le détecteur en créant un effet Cherenkov. La granularité des anneaux Cherenkov permet la séparation des électrons et des muons pour mesurer la disparition des $\overset{(-)}{\nu}_\mu$ et l'apparition des $\overset{(-)}{\nu}_e$. Deux detectors proches se trouvent à 280 m de la cible: le détecteur sur axe INGRID qui mesure la direction et la stabilité du faisceau, et le détecteur hors axe ND280 qui

mesure les taux d'interaction des neutrinos et leurs caractéristiques.

Cette thèse présente une analyse simultanée des données de ND280 et Super-Kamiokande pour mesurer $\sin^2\theta_{23}$, Δm^2_{32}, $\sin^2\theta_{13}$ and δ_{CP}. L'estimation des paramètres effectuée dans cette thèse utilise la statistique Bayésienne pour échantillonner les distributions de probabilités postérieures des paramètres avec une technique Monte-Carlo de chaînes de Markov. Les données analysées correpondent à $7.482 \cdot 10^{20}$ protons sur cible (POT) en ν-mode et $7.471 \cdot 10^{20}$ POT en $\bar{\nu}$-mode, soit les runs 1 à 7 de T2K. En utilisant les résultats des expériences de neutrinos réacteurs pour le paramètre θ_{13}, les paramètres sont mesurés avec les valeurs $\sin^2\theta_{23}{=}0.51^{+0.04}_{-0.05}$, $\Delta m^2_{32}{=}\ 2.54^{+0.12}_{-0.12} \cdot 10^3\,\mathrm{eV}^2 \cdot \mathrm{c}^{-4}$, $\sin^2\theta_{13}{=}\ 0.0219 \pm 0.0011$, et $\delta_{\mathrm{CP}}{=}\ -1.79^{+0.91}_{-0.66}\,\mathrm{rad}$, et l'hypothèse de la conservation de la symétrie CP est exclue avec une crédibilité de 90% (ou C.L.). Une analyse utilisant les anneaux muoniques en $\nu-$ et $\bar{\nu}$-mode ne trouve pas de différence entre les paramètres d'oscillation des neutrinos et antineutrinos. Les mesures obtenues dans cette thèse sont les contraintes les plus strictes obtenues par T2K sur les paramètres d'oscillation, et les résultats préliminaires de la continuation de cette analyse avec le run 8 permettent d'exclure la conservation de la symmétrie CP à plus de deux écarts-types.

Cette thèse démontre la puissance de l'analyse Bayésienne appliquée à l'inférence des paramètres d'oscillation des neutrinos, qui fournit des mesures précises menant la voie vers la compréhension de ce phénomène au-delà du modèle standard.

List of Publications

The work presented in this thesis has been published in the following articles:

- T2K collaboration, Phys. Rev. D 96, 092006 (2017),
  DOI: 10.1103/PhysRevD.96.092006,
  "Measurement of neutrino and antineutrino oscillations by the T2K experiment with an additional sample of charged-current ν_e interactions at the far detector with one charged pion in the final state"
- T2K collaboration, Phys. Rev. Lett., 118, 151801 (2017),
  DOI: 10.1103/PhysRevLett.118.151801,
  "Combined analysis of neutrino and antineutrino oscillations at T2K"
- T2K collaboration, Phys. Rev. D 96, 011102 (2017),
  DOI: 10.1103/PhysRevD.96.011102,
  "Updated T2K measurements of muon neutrino and antineutrino disappearance using $1.5 \cdot 10^{21}$ protons on target"
- C. Wilkinson et al., Phys. Rev. D 93, 072010 (2016),
  DOI: 10.1103/PhysRevD.93.072010,
  "Testing CCQE and 2p2h models in the NEUT neutrino interaction generator with published datasets from the MiniBooNE and MINERνA experiments"

and following proceedings of conferences:

- L. Haegel for the T2K collaboration, proceeding of the EPS-HEP conference (2017), Proceedings of Science 314/112,
  "Latest oscillation results from T2K"
- L. Haegel for the T2K collaboration, Summary Proceeding of the PhyStat-nu conference (2016) in preparation, (poster available),
  "Estimation of neutrino oscillation parameters with Markov Chain Monte Carlo"
- L. Haegel for the T2K collaboration, proceeding of the nuFACT conference (2016), arXiv:1701.02559,
  "T2K near detector constraints for oscillation results"
- L. Haegel for the T2K collaboration, proceeding of the ICHEP conference (2014), Nucl. Part. Phys. Proc. 273-275 (2016) 2696-2698, DOI: 10.1016/j.nuclphysbps.2015.10.034,
  "The T2K off-axis near detector: recent physics results"

Acknowledgements

While this manuscript is written under my name, the four years of my thesis have not (only) been the experience of myself sharing time with pens, papers and computers, but benefited from the support of many.

The neutrino group of the University of Geneva has been an excellent host, and I would like to thank Professeur Alain Blondel for having accepted that I perform a Summer internship in the group while I still was in the middle of my Master studies. This few months spent at CERN made me confident about staying in the field of particle physics in general, and neutrino physics in particular, and I have been delighted when Alain proposed me to return for the PhD program. Four years gave more time to dive in the depths of science, and I would like to thank Alain for having letting me explore the physics potential in T2K, while still asking me relevant questions about the path of my research. Melody Ravonel deserves a special recognition for guiding my first steps in the T2K path: merci pour ton aide, ta patience, ta bonne humeur dans le bureau, et le rappel qu'il y a d'autres choses aussi importantes que la Physique. My work has benefited from discussions and advices given by the ones who have gone this road before me, and I would like to thank Davide Sgalaberna and Mark Rayner for all the support they provided. I am very grateful to have spend this time with other PhDs, and Enrico Scantamburlo has been very helpful in using the T2K framework and choosing karaoke songs, while our latest team recruit Lucie Maret brought her deep insight of quantum physics along a good mood in the office. Finally, I would like to thank Antoaneta Damyanova, Saba Parsa, Etam Noah, François Drielsma and Yordan Karadzhov for insightful physics conversations beyond the scope of T2K (and sometimes physics), and Alessandro Bravar for comments on this manuscript.

I am also grateful to Tobias Gölling, Philippe Mermod, and Teresa Montaruli for the teaching experience I have acquired with them. I somehow found some time to get to know people beyond my group and duties, and Magdeleine, Iaroslav, Stéphanie, Thierry, Stefania, Anatoly, Marta, Bogdana, Arnaud, Anthony, Andrii, David, Valentina, Stefan, Reni and Kelly have been the key to time happily spent *in* and *ex universitas*.

Beyond the University of Geneva, those four years have been full of exchange with the delightful T2K collaboration. I would like to thank Alexander Izmaylov, Anselmo Cervera, Anthony Hillairet, Federico Sanchéz and Kendall Mahn for the time they spent explaining me the mysteries of the experiment, and answering my many questions while I was starting my PhD. As I was taking interest in neutrino oscillations, Asher Kaboth deserves a big thanks for having welcomed me in the oscillation analysis group and spent time sharing with me his knowledge of Bayesian statistics. I would like to thank to whole MaCh3 group for the support and creativity we have shared in those analyses, and the conveners Mark Hartz and Claudio Giganti for all the organisation and comments we received. I have been happily surprised of the atmosphere of the collaboration and praise all the collaborators with whom I have shared nice moments, with special greetings to Paul, Simon, Pierre, Pierre, Callum, Clarence, Raquel, Jiae, Javi, Lukas, Zoya, Teppei and Erez for the quality time spent in Tokai and wandering in Japan.

Now that the four years are arriving to an end, I would like to thank Asher Kaboth, Albert de Roeck and Philippe Mermod to have accepted to be part of the jury in charge of evaluating my work. I also acknowledge the support of the Swiss National Fund that funded my research with a working quality I could not imagine of, and the Département de l'Instruction Publique that financed the education duties I was responsible of. The University of Geneva, through its financial and academical support, and the Conférence Universitaire de Suisse Romande, have also been strong assets in carrying my research and improving my education. Finally, I would like to thank Sascha Husa and Alicia Sintés for having invited me to join the University of Balearic Islands, motivating me to finish in time and giving me the excitement of pursuing the adventure of studying (few cool phenomena of) the Universe for some more years.

Alors que cette étape s'achève, il est temps de prendre une pause pour remercier ceux qui ont été là pour moi depuis le début. Merci à mes parents pour la vie qu'ils m'ont donné: il n'y a rien de plus vrai que dire que je ne serais pas là où je suis sans votre éducation, votre amour et votre respect. Merci à mes sœurs d'avoir été de si bonnes compagnes de vie pendant de nombreuses années, puis d'être restées toujours unies dans nos chemins divergents. Merci à Billie d'avoir accueilli mon arrivée avec des ronronnements, et Pauline et Adrien pour les retrouvailles drômoises. Merci au reste de ma famille que le travail ne me laisse pas visiter autant que je voudrais, mais avec qui le contact est toujours là. Une mention spéciale aux physiciens de ma famille: Habibi, pour avoir toujours eu une longueur d'avance sur mes études en m'instruisant pendant l'été, quitte à le faire sur le sable des plages marocaines, et Tatatou pour me donner l'exemple d'aller où les études le demandent. Danièle, aurais-je jamais fini dans un laboratoire si tu ne m'avais pas suggérée de postuler pour un stage à l'Institut Pluridisciplinaire Hubert Curien ? Je te remercie de m'avoir fait découvrir la recherche, ainsi que Marcos Dracos de m'avoir permis de découvrir la physique des neutrinos dans son groupe et Jacques Wurtz pour son soutien sans faille depuis ce stage.

Последнее слово - для Руслана. Спасибо, что держишься за штурвалом со мной, за твою страсть и терпение. И ничего я не желаю более, чем продолжить навигацию по океану жизни рядом с тобой.

Contents

List of Figures

List of Tables

CHAPTER 1

Introduction

1.1 A brief history of neutrino physics

Neutrino physics have gone a long path since the particle itself was postulated by Pauli in 1930 to explain the continuous energy spectrum of electrons emitted in β-decay [1]. In 1956, the same year the antineutrino was directly detected in the Cowan-Reines experiment [2], it was found to be the only fundamental particle with a single helicity [3]. The discovery of the muon neutrino in 1962 [4], in addition to Pauli's electron neutrino, has been followed by the observation of a third neutrino of tau flavour in collider experiments [5] whose interactions with matter were detected in 2001 [6]. Since 1968, and the first observation of neutrinos from the Sun, much effort was spent trying to solve the so-called "solar neutrino problem", i.e. the fact the experiments aiming at measuring the flux of neutrinos created by the Sun only recorded about a third of the expected event rates [7]. The explanation relies on the phenomenon of neutrino oscillation proposed by Pontecorvo in 1957 [8], i.e. the possibility of detecting neutrinos in a different flavour than the one in which they were created, as proved by the Sudbury Neutrino Observatory (SNO) experiment in 2002 [9].

Meanwhile the Super-Kamiokande (Super-K) experiment had established the existence of oscillations by observing neutrinos from the Sun and from interactions of cosmic rays with the Earth atmosphere [10]. An accurate knowledge of the neutrino oscillation mechanism required to control the neutrino flux, and the Tokai-to-Kamioka (T2K) experiment was designed to send a muon (anti)neutrino beam towards the Super-K detector with an oscillation baseline of 295 Km [11]. Neutrino oscillations are modelled with a rotation matrix parametrising the relation between the neutrino mass and flavour eigenstates. In the three-neutrino framework, the mixing of the neutrino states lead to a probability of oscillation depending on a *extrinsic* parameter, the distance over neutrino energy ratio $\frac{L}{E_\nu}$, as well as on six *intrinsic* parameters: the three angles θ_{12}, θ_{23} and θ_{13}, the two mass eigenstates differences Δm^2_{21} and Δm^2_{32} and the $\delta_{\rm CP}$ phase that has the possibility of encoding a different oscillation probability for neutrinos and antineutrinos (to which two or more phases must be added if neutrinos are Majorana particles). The T2K experiment has been designed to observe electron neutrino appearance, giving the first indications of the non-zero value of $\sin^2\theta_{13}$ [12], but can also provide an accurate measurement of $\sin^2\theta_{23}$ and Δm^2_{32} from muon neutrino disappearance [13]. When I joined the T2K collaboration in 2013, as I was starting the Doctor of Philosophy (PhD) program of the University of Geneva, the experiment had just discovered the electron neutrino appearance in the muon neutrino beam [14] while reactor neutrino experiments reported accurate measurements of $\sin^2 2\theta_{13} > 0$ [15]. It enabled long-baseline accelerator neutrino experiments to measure the $\delta_{\rm CP}$ phase, and the T2K collaboration decided to run alternatively with a muon neutrino and muon antineutrino beam in order to probe the difference between electron neutrino and electron antineutrino appearance probabilities. This thesis reports an analysis of the muon neutrino and antineutrino disappearance, as well as electron neutrino and antineutrino appearance, in order to constrain the neutrino oscillation parameters $\sin^2\theta_{23}$, $\sin^2\theta_{13}$, Δm^2_{32} and $\delta_{\rm CP}$.

1.2 Thesis outline

After the brief reminder of the history of neutrino physics given in this chapter, Chapter 2 reviews the current knowledge on these particles. It begins by presenting the Standard Model of particle physics and how neutrinos fit in this framework. The discussion follows on the mass of neutrinos that is still of unknown origin as of today, but may rely on the possibility of the neutrino to be a Majorana particle. The massive nature of neutrinos combined with their extremely small mass difference enables the oscillation phenomenon, that is further described with the up-to-date knowledge on the oscillation parameters. The last section connects particle physics to cosmology, by describing how neutrino oscillations may have contributed to baryogenesis during the evolution of the Universe and the possibility of dark matter to be composed of right-handed neutrinos.

This thesis presenting studies performed using T2K data, the experiment is described in Chapter 3. The first section outlines the production of the off-axis muon (anti)neutrino beam, followed by a description of the near detector complex used to constrain the flux and interaction models. Oscillated neutrino events are detected in the far detector Super-K that is depicted in the third section, the neutrino interactions being modelled with the custom generator NEUT described on the fourth section.

The analysis presented in this thesis uses a Markov chain Monte Carlo method to sample the posterior probability distributions of the neutrino oscillation parameters. Chapter 4 presents the analysis strategy and the statistical method, from the Metropolis-Hastings algorithm creating the semi-random walk of the Markov chain to the extraction of credible intervals and best fit points. Both near and far detector data are included in the analysis, and the second section provides a description of the samples selected in each detector. The systematic uncertainties due to the flux, interaction and detectors models are outlined in the third section with their impact on the number of predicted events.

Chapter 5 presents the first analysis performed in this thesis, using muon neutrino and antineutrino disappearance only. The oscillation parameters encoding the muon neutrino and antineutrino oscillation probabilities are estimated separately in order to probe the existence of physics beyond the Standard Model, such as symmetry violation or the presence of non-standard neutrino interactions. The near detector data are included in the fit to provide constraint on the nuisance parameters. The estimated parameters are in agreement, showing no evidence of unknown physics, but providing an additional sensitivity on this test compared to the measurements reported by previous experiments.

The second analysis presented in this thesis is described in Chapter 6. Both muon neutrino and antineutrino disappearance data, as well as electron neutrino and antineutrino appearance data, are analysed with the near detector data to extract the most accurate estimation of the neutrino oscillation parameters. The analysis reports the best constraints ever obtained by T2K, with a value of $\sin^2\theta_{23}$ compatible with maximal muon (anti)neutrino disappearance, and the exclusion of non-CP violation at 1σ when using T2K data alone, 90% when adding the reactor information on $\sin^2\theta_{13}$.

The results are summarised in Chapter 7, with a discussion on the proposed future projects aiming at improving the measurement of the neutrino oscillation parameters within T2K. Both the T2K-II program and the Hyper-Kamiokande (Hyper-K) experiment intend to decrease the statistical uncertainties by providing a higher number of events from a longer use of the T2K beam or a larger number of target nuclei. However, the discovery of δ_{CP} requires a reduction of the systematic uncertainties as well, that could be achieved by implementing state-of-the-art nuclear models in NEUT and upgrading the near detectors.

The analyses presented in Chapters 5 and 6 rely on a Markov chain Monte-Carlo technique described in Chapter 4. Markov chains are semi-random walks that differ from independent throw methods, and details on their properties are given on Appendix A. Convergence diagnostics, i.e. tests of the ability of the chain to sample the posterior probability distribution, are also described.

While Chapter 4 briefly outlines the systematic uncertainties on the near and far detector selections, the evaluation of two near detector uncertainties have been performed in the scope of this thesis. Appendix B describes the estimation of the uncertainties on the background originating outside the fiducial volume of the targets of the near detector, as well as on the matching of tracks necessary to select events.

CHAPTER 2

Neutrino physics overview

This chapter presents the current status of the knowledge on fundamental particles, the first section describing the Standard Model (SM) of particle physics. All predictions derived in the framework of the SM agree with experiments, however it lacks in explaining the origin of neutrino masses, to which the second section is dedicated. The massive nature of neutrinos leads to the phenomenon of neutrino oscillations, where a neutrino produced in a certain flavour is detected in another flavour. This process is at the core of this thesis and is detailed in the third section. Finally, although particle physics is the domain of the subatomic scale, it is strongly connected to the evolution of the Universe. The last section reviews how the current progress on neutrino physics impacts cosmological models.

2.1 3ν Standard Model of particle physics

The twentieth century saw the emergence of a description of matter as particles being excitations of quantum fields and organised in the SM of particle physics [16]. The SM is a gauge theory of group G_{SM} based on the internal symmetry:

$$G_{SM} = SU(3)_c \otimes SU(2)_T \otimes U(1)_Y \tag{2.1}$$

where $(S)U(n)$ are the (Special) Unitary groups of degree n and respective generators the colour c, the weak isospin $\vec{T}$ and the hypercharge Y. Each group corresponds to a fundamental force carried by $n^2 + 1$ gauge bosons of spin 1. $SU(3)$ is the gauge group corresponding the strong force carried by eight gluons between six fermionic particles (e.g. of spin $\frac{1}{2}$) named quarks. The $SU(2) \otimes U(1)$ group forms the electroweak group at energies greater than the weak scale. The generator of $SU(2)$ is the weak isospin and the corresponding weak force is carried by the bosons W^0, W^1, W^2, while the generator of $U(1)$ is the hypercharge corresponding to the electromagnetic force of a vector field B_μ. The spontaneous breaking of the electroweak symmetry at energies inferior to the weak scale mixes the two electroweak vector fields W^0 and B_μ with the Weinberg angle θ_W:

$$\begin{pmatrix} \gamma \\ Z^0 \end{pmatrix} = \begin{pmatrix} \cos\theta_W & sin\theta_W \\ -\sin\theta_W & cos\theta_W \end{pmatrix} \begin{pmatrix} B_\mu \\ W^0 \end{pmatrix} \tag{2.2}$$

creating two electroweak bosons: the photon γ and the boson Z^0. γ interacts with the charged fermions, therefore the quarks but also the charged leptons electron e^-, muon μ^- and τ^- ; and Z^0 interacts with all fermions including the electrically neutral leptons named neutrinos, of electron (ν_e), muon (ν_μ) and tau (ν_τ) flavours. W^1 and W^2 mix in a linear combination to the W^+ and W^1 bosons vehiculating the weak interaction between all fermions. Table 2.1 shows the SM particles with their masses and quantum numbers under the three symmetry generators, except Y that can be inferred from the electric charge Q and weak isospin third projection T_3 with the weak analogue of the Gell-Mann-Nishijima formula:

$$Q = T_3 + \frac{Y}{2} \tag{2.3}$$

The masses of SM fermions and bosons arise from an additional scalar (spin 0) field named the Higgs field and carried by the boson h. It holds four degrees of freedom, three being absorbed by the masses of the $W^{+/-}$ and Z^0 bosons after the spontaneous breaking of the electroweak symmetry. The remaining degree of freedom gives energy to the vacuum expectation value (vev) of the Higgs boson. The fermion fields ψ acquire mass by interacting with the Higgs fields ϕ with the so-called Yukawa interaction of Lagrangian:

$$\mathcal{L}_y = g_y \ \bar{\psi}(x)_L \ \phi(x) \ \psi(x)_R + h.c. \tag{2.4}$$

category	*particle*	m [eV/c^2]	$\vec{S}$	Q	$\vec{T}$	c
quark fermions	u	$2.2^{+0.6}_{-0.4}$ M	$\frac{\vec{1}}{2}$	$+\frac{2}{3}$	$L : \frac{\vec{1}}{2}$ $R : \vec{0}$	$(R/G/B)$
	d	$4.7^{+0.5}_{-0.4}$ M		$-\frac{1}{3}$		
	c	$1.28^{+0.03}_{-0.03}$ G		$+\frac{2}{3}$		
	s	96^{+8}_{-4} M		$-\frac{1}{3}$		
	t	$173.1^{+0.6}_{-0.6}$ G		$+\frac{2}{3}$		
	b	$4.18^{+0.04}_{-0.03}$ G		$-\frac{1}{3}$		
lepton fermions	e^-	$511 \pm 3 \cdot 10^{-9}$ K	$\frac{\vec{1}}{2}$	-1	$L : \frac{\vec{1}}{2}$ $R : \vec{0}$	0
	μ^-	$105.7 \pm 2 \cdot 10^{-6}$ M		-1		
	τ^-	$1.78 \pm 1 \cdot 10^{-4}$ G		-1		
	ν_e	$\sum_3 m_\nu < 0.23$		0		
	ν_μ			0		
	ν_τ			0		
gauge boson	$W^{+/-}$	80.39 ± 0.02 G	$\vec{1}$	$+/-1$	$+/-1$	0
	Z^0	$91.19 \pm 2 \cdot 10^{-3}$ G		0	0	0
	γ	$0(< 10^{-18})$ eV		0	0	0
	g	0		0	0	$(R/G/B)$
scalar boson	h	125.09 ± 0.24 G	$\vec{0}$	0	$\frac{\vec{1}}{2}$	0

Table 2.1: Known particles and their mass m, spin $\vec{S}$, electric charge Q, weak isospin $\vec{T}$ (according to the fermion chirality L or R), and colour charge c [17]. The hypercharge Y can be inferred from Q and the third weak isospin projection T_3 with Equation (2.3). In the mass column, "K" stands for 10^3, "M" for 10^6, "G" for 10^9.

where g_y is the coupling strength, L and R design the chirality, and *h.c.* stands for "hermitian conjugate".

Chirality is the Lorentz-invariant form of the helicity, and is equivalent to helicity for particles of null mass. Helicity is the projection of the particle spin on its momentum, with the two states of right-handed R (when the particle spin is aligned with its momentum) and left-handed L (when the particle spin is anti-align with its momentum). Spin-$\frac{1}{2}$ fermionic fields are plane-wave solutions to the Dirac equation:

$$(i\ \gamma^\mu \partial_\mu \ -\ m)\ \psi \ =\ 0 \tag{2.5}$$

and form a 4-dimensional spinor that can be decomposed into two so-called

Weyl spinors in the chiral representation:

$$\psi \;=\; P_R\psi \;+\; P_L\psi \;=\; \psi_L \;+\; \psi_R \tag{2.6}$$

where $P_{R,L} = \frac{1\pm\gamma^5}{2}$ is the chirality projector. All fermions have been found to exist in the two states, except the neutrinos that have only been detected in the left-handed state [3].

Particles can be represented according the their weak isospin third projection values T_3. All left-handed fermions have $T_3 = \pm\frac{1}{2}$ and can be organised in doublets:

$$\begin{array}{l} T_3 = +\frac{1}{2} \\ T_3 = -\frac{1}{2} \end{array} \quad \underbrace{\begin{pmatrix} u \\ d \end{pmatrix}_L \begin{pmatrix} c \\ s \end{pmatrix}_L \begin{pmatrix} t \\ b \end{pmatrix}_L}_{\text{quarks } q_L} \quad \underbrace{\begin{pmatrix} \nu_e \\ e^- \end{pmatrix}_L \begin{pmatrix} \nu_\mu \\ \mu^- \end{pmatrix}_L \begin{pmatrix} \nu_\tau \\ \tau^- \end{pmatrix}_L}_{\text{leptons } l_L} \tag{2.7}$$

while the right-handed fermions have $T_3 = 0$ and are organised in singlets:

$$\begin{array}{l} T_3 = 0 \\ T_3 = 0 \end{array} \quad \underbrace{\begin{array}{lll} (u)_R & (c)_R & (t)_R \\ (d)_R & (s)_R & (b)_R \end{array}}_{\text{quarks } q_R} \quad \underbrace{(e^-)_R \;\; (\mu^-)_R \;\; (\tau^-)_R}_{\text{leptons } l_R} \tag{2.8}$$

The charge of the weak force being the weak isospin, weak interaction only occurs with fermions of $T_3 \neq 0$, therefore only to left-handed fermions. Consequently, the weak force breaks the parity symmetry of the SM by only connecting to one chirality. The structure in Equation (2.7) and (2.8) makes explicit the $n_f = 3$ generations, i.e. the fact that the second and third (fourth to sixth) quark doublet (singlets) q_L (q_R) are the same particles than the first doublet, but with a higher mass; and similarly for the leptons.

Weak interactions can occur by Charged-Current (CC) or Neutral-Current (NC) depending if the exchanged boson is respectively $W^{+,-}$ or Z^0. Figure 2.1 shows the Feynman diagrams corresponding to the two currents for an elastic interaction between an electron neutrino and a nucleon.

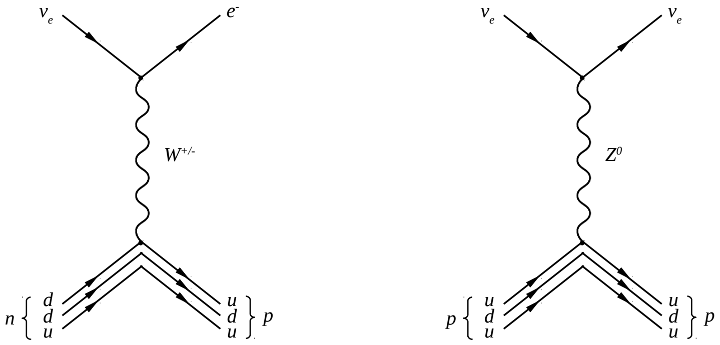

(a) CC elastic $\nu - n$ interaction **(b)** NC elastic $\nu - p$ interaction

Figure 2.1: Feynman diagram of CC (2.1a) and NC (2.1b) elastic interactions between an electron neutrino and a nucleon.

2.2 The origin of neutrino masses

2.2.1 Dirac and Majorana particles

The Lagrangian of a fermion interacting with the Higgs field is given in Equation (2.4), leading to the fermion acquiring the mass m appearing in the Dirac Equation (2.5) - therefore so called "Dirac" mass. However it can be seen that the coupling to the Higgs field transforms the chirality of the fermion from left to right-handed (and vice-versa). Because only left-handed neutrinos are known to exist in nature, it brings three possible conclusions: either neutrinos are massless, either right-handed neutrinos do exist but are unseen, or neutrinos become massive a different way.

Neutrinos have been thought to be massless for a long time, as they are notably produced in the radioactive β-decay of unstable elements with the reaction:

$$\begin{aligned} \beta^- : \quad & {}^{A}_{Z}X \rightarrow {}^{A+1}_{Z-1}Y + e^- + \bar{\nu_e} \\ \beta^+ : \quad & {}^{A}_{Z}X \rightarrow {}^{A-1}_{Z+1}Y + e^+ + \nu_e \end{aligned} \tag{2.9}$$

The study of the electron spectra showed an end point energy consistent with a null mass for the neutrino; however if the $\overset{(-)}{\nu_e}$ mass is very small it would distort the end spectra with an effect smaller than the uncertainty on the electron energy, as shown in Figure 2.2. While the non-zero masses of neutrinos has been proven from the oscillation process described in Section 2.3, accurate measurements of the energy spectra of beta-decay electrons are still ongoing in order to measure the absolute $\overset{(-)}{\nu}_e$ mass.

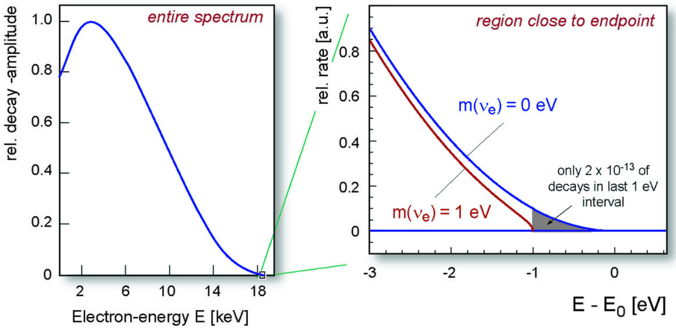

Figure 2.2: Electron energy spectrum in Tritium decay. The left figure shows the whole spectra where the spectra appears to be consistent with a null neutrino mass, while the right figure shows a zoom on the end point where the effect of a small neutrino mass can be seen in the spectrum distortion. Figure from KArlsruhe TRItium Neutrino (KATRIN) experiment [18].

The number of *active* left-handed neutrinos, i.e. interacting via weak interaction, has been determined to be three with great accuracy from the direct measurement of Z^0 decay [19], and in agreement with indirect measurement such as Cosmic Microwave Background (CMB) fits [20]. Right-handed neutrinos cannot be probed in weak boson decays as the bosons are blind to this chirality, and such *sterile* particles remain challenging to detect - although they could be probed in specific processes mentioned later in this chapter.

Applying the Charge-Parity-Time (CPT) symmetry to the particles of Table 2.1 transforms them into their antiparticles. Particles and antiparticles only differ by their scalar quantum numbers having an opposite sign, the vectorial numbers remaining unchanged. The Charge symmetry reversal leads to an opposite electric charge ($Q \rightarrow -Q$) while the Parity symmetry flips the chirality of the particle ($L \rightarrow R$), and the Time symmetry reverses the time of the actions ($t \rightarrow -t$).

While charged fermions have their antiparticle differing in term of chirality and electromagnetic charge, the zero electromagnetic charge Because neutrinos have zero electric charge, they have the possibility to be "Majorana" fermions - a type of particles that is possible in the context of the SM, but which realisation has yet to be found. Such particle would follow the Majorana equation:

$$i\,\gamma^{\mu}\partial_{\mu}\,\psi - \; m\,\psi_C \;=\; 0 \tag{2.10}$$

analogous to Dirac Equation (2.5) but involving ψ_C, the charge conjugate of ψ under the operator C that also apply to the chirality of the particle:

$$\psi_R^C = \gamma^0 C \bar{\psi}_R^T = \psi_L \tag{2.11}$$

The lepton number ℓ characterise all leptons with a value of $\ell = 1$ for particles and $\ell = -1$ for antiparticles. The conservation of ℓ in SM interactions is due to the $U(1)_Y$ symmetry, under which the Majorana Lagrangian is not invariant, leading to a violation of ℓ-conservation as shown in Equation (2.11) where a particle mix with its antiparticle. Majorana neutrinos enable other $\ell-$violating interactions such as neutrinoless double beta decay where the simultaneous decay of two neutrons creates two protons and two electrons, but no neutrinos:

$$2n \rightarrow 2p + 2e^- \tag{2.12}$$

This process being a signature of Majorana neutrinos, it is investigated by several experiments amongst which the ones shown in Figure 2.3 in order to determine if neutrinos behave like Majorana particles.

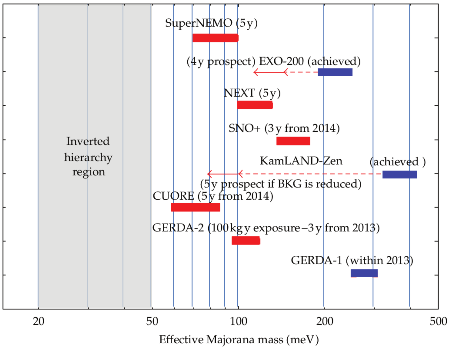

Figure 2.3: Running or finished in 2012 (blue) and predicted in 2012 (red) neutrinoless double beta decay experiments. The sensitivity to the effective neutrino Majorana mass, explained in greater details in Section 2.3.2, is given with the x-axis. Figure from [21].

2.2.2 The see-saw mechanism

Solutions to the Majorana Equation (2.10) are singlet neutral particles, that can hold for right-handed neutrinos N_R that are of numbers n. They can form a Weyl spinor with the right-handed charged leptons l_R to complete the leptonic spinor:

$$\psi_{lepton} = \begin{pmatrix} \psi_L \\ \psi_R \end{pmatrix} = \begin{pmatrix} \nu_L \\ l_L \\ N_R \\ l_R \end{pmatrix}$$

Additional mass terms appear in the Lagrangian, of form:

$$\mathcal{L}_M = -\frac{1}{2} \left(\bar{\nu}_L \ \bar{N}_R^C\right) \underbrace{\begin{pmatrix} m_M^L & m_D \\ m_D^T & m_M^R \end{pmatrix}}_{M_\nu} \begin{pmatrix} \nu_L^C \\ N_R \end{pmatrix} + h.c. \tag{2.13}$$

where m_M^L is the 3×3 left-handed Majorana mass matrix that is null due to electroweak gauge invariance [22], m_D and m_D^T are the $(n \times 3)(^T)$ Dirac masses matrices, m_M^R is the $n \times n$ right-handed Majorana mass matrix of unknown eigenvalue. When postulating $m_M^R >> m_D$, the see-saw mechanism approximates the eigenvalues of the matrix M_ν to the following mass terms:

$$m_1 = \frac{\|m_D^2\|}{\|m_M^R\|} \quad ; \quad m_2 = \|m_M^R\| \tag{2.14}$$

where $\|m\|$ denotes the norm of the matrix m.

Because the distortion of the β-decay electron spectrum is indistinguishable (as shown in Figure 2.2), neutrino mass must be very small. However, the neutrino density was very high in the early Universe and their mass impacts acoustic oscillation in the CMB and for baryons. Neutrinos are also ejected in great amount in supernova explosions, the dynamic of the star being influenced by the particle masses. Consequently, the current strongest constraint on the sum of the neutrino mass comes from cosmological measurements assuming three massive active neutrinos and the cold dark matter ΛCDM model. The combination of the CMB data of the Planck satellite, the super-novae light curves and baryon acoustic oscillations leads to the 95% Confidence Level (CL) [20]:

$$\sum_i^3 m_i \; = \; 0.23\,\mathrm{eV} \tag{2.15}$$

Model-independent results can be obtained from charged leptons β-decay experiments, though measuring the mass of the flavour state and with a higher upper bound than the cosmological fit. The Troitsk experiment reports an upper bound on the mass of the electron antineutrino of $m_{\bar{\nu}_e} < 2.05\,\mathrm{eV}^2$ [23] and the KATRIN experiment aims at decreasing the upper bound of one order or magnitude [24]. The time of flight of neutrinos emitted by supernova burst can also be used to estimated the $\bar{\nu}_e$ mass and put a lower constraint on neutrino masses [25, 26], however assuming a certain model of supernova dynamics. Comparing with the masses of the other particles, the neutrino masses are of the order $\mathcal{O}(10^{-7})$ the mass of the lightest fermion (e^-) and $\mathcal{O}(10^{-12})$ the mass of the heaviest known particle (t quark). The ordering of masses and the generations of the SM are of unknown origin, and are one of the most compelling appeal for a Grand Unified Theories (GUT) at a more fundamental level from which they could be derived. The see-saw mechanism is a candidate theory to explain the smallness of neutrino masses, as Equation (2.14) explicit two mass terms where m_1 is relatively small and m_2 is relatively heavy. The see-saw mechanism presented in this section is called "type I", as it was the first formulated and only requires the the introduction of a singlet right-handed Majorana neutrino per family. Other seesaw types have been postulated, the type II introducing a scalar triplet and the type III a fermionic triplet [27].

2.3 Neutrino oscillations

It has been noticed before the discovery of neutrino masses that if neutrinos are massive, there exist a possibility that the neutrino mass eigenstate and flavour eigenstate do not coincide [8]. Indeed, neutrinos are produced by weak interactions in a flavour eigenstate (ν_e, ν_μ, ν_τ) but propagate in their mass eigenstate (ν_1, ν_2, ν_3). During the propagation, the flavour eigenstates undergo a rotation that can result to a projection of the flavour state being different than the flavour in which the neutrinos have been produced. This effect is called *neutrino oscillations* and has lead to the discovery of the massive nature of neutrinos.

2.3.1 Neutrino oscillations formalism

The neutrino flavour eigenstates ν_α is linked to the neutrino mass eigenstate ν_i by the Pontecorvo-Maki-Nakagawa-Sakata (PMNS) matrix, which takes the form of a rotation matrix U_{PMNS}:

$$\underbrace{\begin{pmatrix} |\nu_e\rangle \\ |\nu_\mu\rangle \\ |\nu_\tau\rangle \end{pmatrix}}_{\nu_\alpha} = \underbrace{\begin{pmatrix} U_{e1} & U_{e2} & U_{e3} \\ U_{\mu 1} & U_{\mu 2} & U_{\mu 3} \\ U_{\tau 1} & U_{\tau 2} & U_{\tau 3} \end{pmatrix}}_{U_{\alpha i} \equiv U_{\text{PMNS}}} \underbrace{\begin{pmatrix} |\nu_1\rangle \\ |\nu_2\rangle \\ |\nu_3\rangle \end{pmatrix}}_{\nu_i} \tag{2.16}$$

Neutrinos can be created by CC interactions of Lagrangian:

$$\mathcal{L}_{CC} = -\frac{g}{\sqrt{2}}\, \bar{l}_\alpha\, \gamma^\mu\, P_L\, \nu_i\, U_{\alpha i}\, W_\mu^- - \frac{g}{\sqrt{2}}\, \bar{\nu}_i\, \gamma^\mu\, P_L\, l_\alpha\, U_{\alpha i}^*\, W_\mu^+ \tag{2.17}$$

in a flavour state that is a linear combination of mass states:

$$|\nu_\alpha(0)\rangle = \sum_i^3 U_{\alpha i}^* \,|\nu_i\rangle \tag{2.18}$$

The evolution in vacuum of the state $|\nu_\alpha\rangle$ during a time t where the neutrino crossed the distance x is given by the following Schrödinger equation:

$$i\,\hbar\,\frac{\partial}{\partial t}\;|\nu_\alpha(t)\rangle = H_v\;|\nu_\alpha(t)\rangle \tag{2.19}$$

where H_v is the Hamiltonian operator for the propagation in vacuum. Equation (2.19) has for solution the plane-wave equation:

$$|\nu_\alpha(t)\rangle = \sum_i^3 U_{\alpha i}^*\; e^{-i(E_i t - \vec{p}_i \vec{x}_i)}\;\; |\nu_i\rangle \tag{2.20}$$

If an interaction occurs, the incident particle will interact with the neutrino flavour eigenstate. The probability that the neutrino is detected in a flavour β is:

$$\begin{aligned} P(\nu_\alpha \to \nu_\beta) &= \langle \nu_\beta | \nu_\alpha(t) \rangle \\ &= \left| \sum_i^3\; U_{\alpha i}^*\; U_{\beta i}\; e^{-i(E_i t - \vec{p}_i \vec{x}_i)} \right|^2 \end{aligned} \tag{2.21}$$

It can be shown [28], with the assumption that neutrinos are highly relativistic and travel at $v \simeq c$ (motivated by their extremely low mass), that the relative phase of the propagation amplitude can be expressed:

$$-\,i(E_i t - \vec{p}_i \vec{x}_i) \cong \frac{m_i^2 L}{2E} \tag{2.22}$$

In which case, in the assumption that the matrix U is unitary, Equation (2.21) has the expression:

$$\begin{aligned} P(\nu_\alpha \to \nu_\beta) = \delta_{\alpha\beta} \; & - \; 4 \sum_{i>j} \Re(U^*_{\alpha i}\; U_{\beta i}\; U_{\alpha j}\; U^*_{\beta j}) \; \sin^2\left(\frac{\Delta m^2_{ij} L}{4E}\right) \\ & + \; 2 \sum_{i>j} \Im(U^*_{\alpha i}\; U_{\beta i}\; U_{\alpha j}\; U^*_{\beta j}) \; \sin\left(\frac{\Delta m^2_{ij} L}{4E}\right) \end{aligned} \tag{2.23}$$

where $\delta_{\alpha\beta}$ is the Kronecker delta, and $\Delta m^2_{ij} = m^2_j - m^2_i$. Similar derivation in the antineutrino case lead to a factor -2 instead of a factor $+2$ in the third term of Equation (2.23). It can be noted that neutrinos oscillate because they are in a coherent superposition of mass eigenstates as the uncertainty on their energy is large with respect to the difference between two mass eigenstates [29].

When neutrinos cross matter, like the solar medium or the Earth crust or mantle, interactions can occur with the surrounding electrons and nucleons. Because muons and taus are absent in stable matter, $\overset{(-)}{\nu}_\mu$ and $\overset{(-)}{\nu}_\tau$ will interact via neutral currents only, while $\overset{(-)}{\nu}_e$ will interact through neutral and charged currents. This dichotomy leads to a modification of the vacuum Hamiltonian of Equation (2.19) to take into account the potential V_e created by charged currents (the neutral current not participating to the potential as they are of similar amplitude for the three flavours):

$$H_m = U_{\text{PMNS}} \; \frac{1}{2E} \begin{pmatrix} m_1^2 & 0 & 0 \\ 0 & m_2^2 & 0 \\ 0 & 0 & m_3^2 \end{pmatrix} U^\dagger_{\text{PMNS}} + \begin{pmatrix} V_e & 0 & 0 \\ 0 & 0 & 0 \\ 0 & 0 & 0 \end{pmatrix} \tag{2.24}$$

with the potential:

$$V_e = \pm 2 \; E \; \sqrt{2} \; G_F N_e \tag{2.25}$$

where $(+)$ is for ν_e and $(-)$ for $\bar{\nu}_e$, G_F is the Fermi constant and N_e the number of electrons in the medium.

Disappearance and appearance of neutrinos of specific flavours due to neutrino oscillations have been detected by several experiments, but the confirmation was provided by the SNO experiment that aimed at observing the neutrino flux from the ^8B decay channel in the Sun [30]. The detector was made of heavy water D_2O in order to detect neutrino CC interactions with the Cherenkov effect and NC interactions from the dissociation of the deuteron. The charged-current ν_e flux and neutral current $\nu_e{+}\nu_\mu{+}\nu_\tau$ flux were measured to be consistent with an oscillation of ν_e neutrinos to ν_μ and ν_τ neutrinos [9]:

$$\begin{aligned} \phi^{CC}_{SNO}(\nu_e) \quad &= (1.76 \pm 0.06(stat) \pm 0.09(syst)) \times 10^6\,\text{cm}^-2 \cdot \text{s}^1 \\ \phi^{NC}_{SNO}(\nu_e + \nu_\mu + \nu_\tau) &= (5.09 \pm 0.44(stat) \pm 0.46(syst)) \times 10^6\,\text{cm}^-2 \cdot \text{s}^1 \end{aligned} \tag{2.26}$$

2.3.2 Status of $U_{\mathbf{PMNS}}$ knowledge

In the 3ν case, the neutrino oscillation matrix of Equation (2.16) can be written as a function of three rotation angle θ_{12}, θ_{13}, θ_{23} and three phases $\delta, \alpha_{21}, \alpha_{31}$ [31, 32]:

$$U_{\nu\ \text{osc}} = \underbrace{\begin{pmatrix} c_{12} & s_{12} & 0 \\ -s_{12} & c_{12} & 0 \\ 0 & 0 & 0 \end{pmatrix}}_{solar} \underbrace{\begin{pmatrix} c_{13} & 0 & s_{13}e^{-i\delta} \\ 0 & 0 & 0 \\ -s_{13}e^{i\delta} & 0 & c_{13} \end{pmatrix}}_{accelerator+reactor} \underbrace{\begin{pmatrix} 0 & 0 & 0 \\ 0 & c_{23} & s_{23} \\ 0 & -s_{23} & c_{23} \end{pmatrix}}_{atmospheric} \underbrace{\begin{pmatrix} 1 & 0 & 0 \\ 0 & e^{i\frac{\alpha_{21}}{2}} & 0 \\ 0 & 0 & e^{i\frac{\alpha_{31}}{2}} \end{pmatrix}}_{Majorana} \tag{2.27}$$

where $c_{ij} = \cos\theta_{ij}$ and $s_{ij} = \sin\theta_{ij}$. The notation *solar* means that the concerned angle θ_{ij} have a dominant effect on the oscillation probability of neutrinos coming from the Sun, *accelerator+reactor* from human controlled sources of neutrinos such as accelerator or nuclear reactor facilities, and *atmospheric* from neutrinos created by the collision of cosmic particles with the Earth atmosphere. Counting the degrees of freedom of a $n \times n$ matrix where $n = 3$, and distributing them to the neutrinos mass and weak eigenstates and rotation angles, leaves one remaining degree of freedom corresponding to the phase δ [33]. The $Majorana$ matrix holds the two phases arising if neutrinos are Majorana particles [34], it becomes a unity $I_{3\times3}$ matrix if $\alpha_{21} = \alpha_{31} = 0$. U_{PMNS} corresponds to the matrix $solar \times accelerator + reactor \times atmospheric$.

Looking at Equations (2.23) and (2.27), it can be seen that neutrino oscillations can be described by six parameters (plus the two Majorana phases α_{ij}): the rotation angles θ_{12}, θ_{13}, θ_{23}, the mass differences Δm^2_{32} and Δm^2_{21} (the third mass difference being a sum of both: $\Delta m^2_{31} = \Delta m^2_{32} + \Delta m^2_{21}$) and phase δ. Using the PMNS matrix as noted in Equation (2.27), the oscillation probability for a transition from $\overset{(-)}{\nu}_\mu$ to $\overset{(-)}{\nu}_e$ for neutrinos of energy $\mathcal{O}$(GeV) travelling $\mathcal{O}$(100 Km) takes the form [35]:

$$
\begin{aligned}
P(\overset{(-)}{\nu}_\mu \to \overset{(-)}{\nu}_e) = {} & s_{23}^2\ s_{13}^2 \left(\frac{\Delta_{13}}{A \pm \Delta_{13}}\right)^2 \sin^2 \frac{|A \pm \Delta_{13}| + L}{2} \\
& + c_{13}^2\ \sin^2 2\theta_{12} \left(\frac{\Delta_{12}}{A}\right)^2 \sin^2 \frac{AL}{2} \\
& + J\ \cos\delta \left(\frac{\Delta_{12}}{A}\right) \left(\frac{\Delta_{13}}{|A \pm \Delta_{13}|}\right) \cos \frac{\Delta_{13}L}{2} \sin \frac{AL}{2} \sin \frac{|A \pm \Delta_{13}| + L}{2} \\
& \mp J\ \sin\delta \left(\frac{\Delta_{12}}{A}\right) \left(\frac{\Delta_{13}}{|A \pm \Delta_{13}|}\right) \sin \frac{\Delta_{13}L}{2} \sin \frac{AL}{2} \sin \frac{|A \pm \Delta_{13}| + L}{2}
\end{aligned}
\tag{2.28}
$$

where:

$$
\begin{aligned}
& \pm \text{ and } \mp \text{ are for } \nu \text{ or } \bar{\nu} \\
& s_{ij}^2 \text{ and } c_{ij}^2 \text{ are for } \sin_{ij}^2 \text{ and } \cos_{ij}^2 \\
& \Delta_{ij} = \frac{\Delta m_{ij}^2}{2E} \\
& A = \sqrt{2} G_F N_e \\
& J = c_{13}^2\ \sin^2 2\theta_{12}\ \sin^2 2\theta_{13}\ \sin^2 2\theta_{23}
\end{aligned}
\tag{2.29}
$$

The first term of this equation is denominated the *leading* term, while the second is the *matter* term as A is part of the matter potential of Equation (2.25). The third term includes the δ phase in the Jarlskog invariant J [36], but is constant for ν_μ as $\bar{\nu}_\mu$ transition and is therefore referred to as the *Charge-Parity conserving (CPC)* term. Because the fourth term of Equation (2.28) changes of sign according if the probability applies to neutrinos or antineutrinos, Charge-Parity (CP) violation may occur if this term in non-zero, i.e. if $\sin\delta$ is non-zero. For this reason, the phase is often called the *CP-violating phase* and will be denoted since now on: $\delta_{CP} \equiv \delta$; the term is similarly named the *Charge-Parity violating (CPV)* term. It can be noticed that the α_1 and α_2 phases of Equation (2.27) do not affect neutrino oscillations [37, 38]. The four terms of Equation (2.28), as well as the total ν_μ to ν_e appearance probability, are shown in Figure 2.4 for a 295 Km flight distance.

The current knowledge on the values of the neutrino oscillation parameters is described in the following paragraphs and summarised in Table 2.2.

- **$\boldsymbol{\theta_{12}}$:** the rotation angle dominating the $P(\bar{\nu}_e \to \bar{\nu}_e)$ for a baseline $L_{Sun \to Earth}$ and a neutrino energy of $\mathcal{O}$(MeV). The Kamioka Liquid Scintillator Antineutrino Detector (KamLAND) experiment was a neutrino experiment detecting $\bar{\nu}_e$ from 53 nuclear reactors with a mean L/E com-

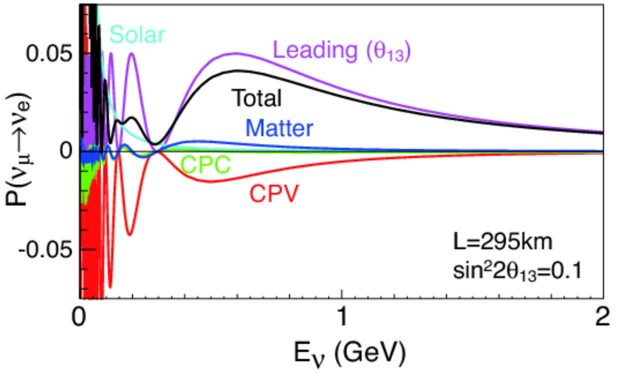

Figure 2.4: Total ν_μ to ν_e oscillation probability as a function of the ν_μ energy. A 295 Km flight distance, normal ordering of neutrino masses, $\sin^2 2\theta_{13} = 0.1$ and $\delta_{\mathrm{CP}} = -\frac{\pi}{2}$ are assumed. The contribution of the different terms of Equation (2.28) is also shown. From [39].

parable to the one of solar neutrinos [40]. The best constraint on $\sin^2\theta_{12}$ comes from a joint fit of solar neutrino data and KamLAND, giving a value of $\tan^2\theta_{12} = 0.436^{+0.029}_{-0.025}$ [41].

- **Δm^2_{21}:** the joint KamLAND + solar neutrino fit on [41] was performed in the $\tan^2\theta_{12} - \Delta m^2_{12}$ space as shown in Figure 2.5. The minimal χ^2 value was found for: $\Delta m^2_{21} = 7.53^{+0.18}_{-0.18} \cdot 10^{-5}\,\mathrm{eV}^2 \cdot \mathrm{c}^{-4}$, measuring the mass ordering $m_2 > m_1$.

- **Δm^2_{32}:** If the magnitude of Δm^2_{32} is determined from fits of atmospheric, accelerator-made and solar neutrinos, the sign $\pm\Delta m^2_{32}$ is still unknown. It is referred as the *Mass Ordering (MO)*, where the *Normal Ordering (NO)* holds for $\Delta m^2_{32} > 0$ and the *Inverted Ordering (IO)* for $\Delta m^2_{32} > 0$. In the convention used, the ν_e content decreases while the mass eigenstate index increases, leading to a decreasing ν_e content with increasing mass in the NO case, while it is larger for the lighter mass eigenstate in the IO case as shown in Figure 2.6. A global fit of accelerator and reactor measurements results in the absolute value of $|\Delta m^2_{32}| = 2.51 \pm 0.06 \cdot 10^{-3}\,\mathrm{eV}^2 \cdot \mathrm{c}^{-4}$ in the NO case, and $|\Delta m^2_{32}| = 2.44 \pm 0.06 \cdot 10^{-3}\,\mathrm{eV}^2 \cdot \mathrm{c}^{-4}$ in the IO case [32]. The sign of Δm^2_{32} can be measured with different approaches, one being the distortion of the the $\bar{\nu}_e$ disappearance probability for $E_\nu \sim \mathcal{O}(100\,\mathrm{KeV})$ at a distance of $L = 55\,\mathrm{Km}$. The Jiangmen Underground Neutrino Observatory (JUNO) experiment aims at measuring the $\bar{\nu}_e$ spectra with a high enough energy resolution to probe the subdominant oscillations visible in Figure 2.7a. Another method relies on the difference on the $\overset{(-)}{\nu}_e$ appearance probabilities

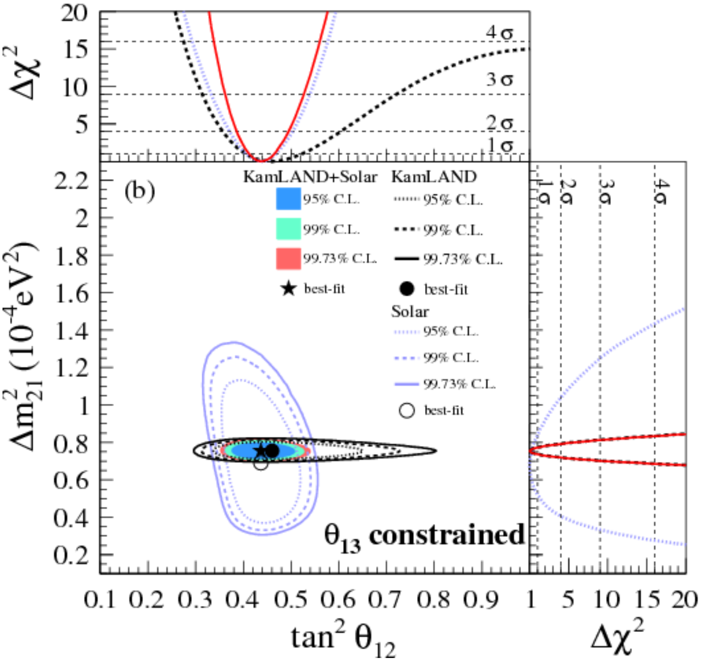

Figure 2.5: Global fit of solar neutrino experiments and KamLAND data in the $\tan^2\theta_{12} - \Delta m^2_{12}$ space. From [41].

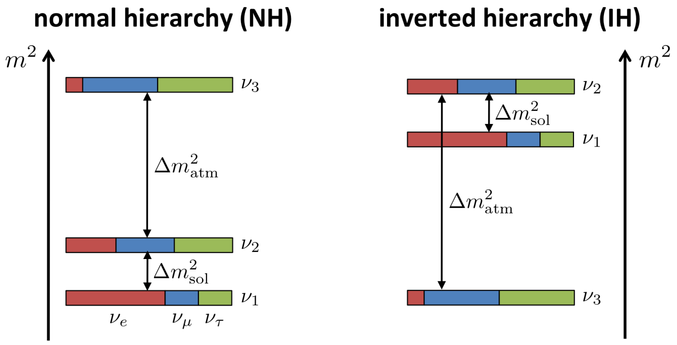

Figure 2.6: The two possible configuration of neutrinos mass eigenstates, or "mass orderings". Δm^2_{sol} refers to Δm^2_{21} and Δm^2_{atm} to Δm^2_{32}. Figure from [42]

in a $\overset{(-)}{\nu}_\mu$ beam according to the sign of Δm^2_{32}, the discrepancy being enhanced by the matter effect term. Long-baseline accelerator experiments like NuMI Off-Axis ν_e Appearance (NOνA) aim at observing this effect shown in Figure 2.7b. In the case of a supernova explosion in the vicinity of the Solar System, the passage of neutrinos through shock waves could produce a significant matter effect resonance enabling a large scale Cherenkov detector such as IceCube or the future Hyper-K, or a liquid argon detector such as Deep Underground Neutrino Experiment (DUNE) to be able to measure the mass ordering [43]. It can be noted that in order to have neutrino oscillations, at least two neutrino mass eigenstates must have $\nu_{i,j} \neq 0$. Therefore, a lower bound on the neutrino mass can be obtained from neutrino oscillation where, in the NO (IO) case, ν_1 (ν_3) can have a null mass and the lower bound on ν_2 is Δm^2_{21} (Δm^2_{32}) and the lower bound on ν_3 (ν_1) is $\Delta m^2_{21} + \Delta m^2_{32}$ ($\Delta m^2_{32} - \Delta m^2_{21}$). Furthermore, analyses of neutrino oscillation parameters leads to lower bounds where all mass eigenstate are non-zero [46].

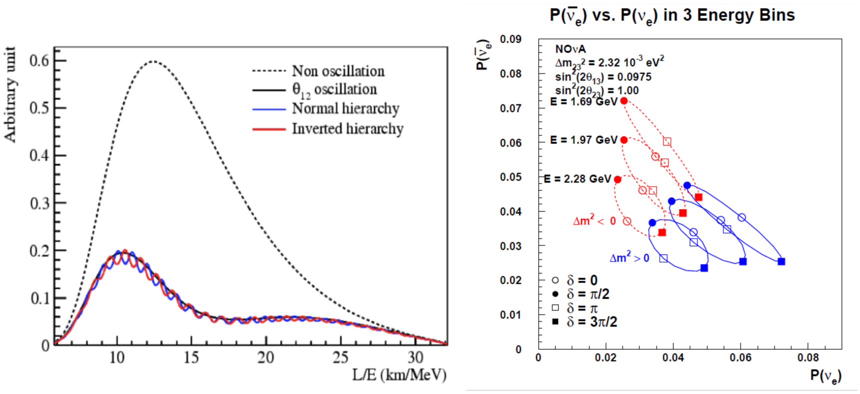

(a) JUNO

(b) NOνA

Figure 2.7: Determination of the neutrino mass ordering with reactor (left) and accelerator experiment (right). Figure 2.7a shows the predicted $\bar{\nu}_e$ energy spectra at the JUNO experiment, where the mass ordering modifies the oscillation spectrum with an opposite phase (from [44]). Figure 2.7b shows the bi-probability of ν_e and $\bar{\nu}_e$ as a function of the phase $\delta = \delta_{CP}$ and the mass ordering for three neutrino energies (from [45]).

- **θ_{23}:** the rotation angle dominating the $\overset{(-)}{\nu}_\mu$ disappearance probability. The amplitude is degenerate in Δm^2_{32} and θ_{23}, therefore a global fit of atmospheric, accelerator-based and solar experiments returns the two values: $\sin\theta_{23} = 0.437^{+0.020}_{-0.043}$ if $\Delta m^2_{32} > 0$ and $\sin\theta_{23} = 0.569$ (with the 1σ CL of $4.28 - 4.91 \oplus 5.18 - 5.97$) if $\Delta m^2_{32} < 0$ [47].

- $\boldsymbol{\theta_{13}}$**:** can be notably measured in accelerator and reactor experiments, the latter having a better sensitivity because of the higher number of events they detect by placing the detector closer to the source. The Particle Data Group (PDG) reports an average of the Daya Bay, Reactor Experiment for Neutrino Oscillation (RENO) and Double Chooz experiments results of $\sin\theta_{13} = 0.0219 \pm 0.0012$ [32].

- $\boldsymbol{\delta_{CP}}$**:** the CP violating term of Equation (2.28) change the ν_e and $\bar{\nu}_e$ appearance probability with opposite sign. However, it has a degenerate effect with the mass ordering as shown in Figure 2.7b. Preliminary constraints have been reported by the NOνA [48], Main Injector Neutrino Oscillation Search (MINOS) [49] and the T2K experiment. The latter reported the stronger constraints with a 90% CL of $\delta_{CP} \in [-3.13, -0.39]$ if NO and $\delta_{CP} \in [-2.09, -0.74]$ if IO [50]. This thesis present an update of the T2K analysis leading to a better constraint of δ_{CP}.

- $\boldsymbol{\alpha_{1,2}}$**:** the Majorana phases do not enter the ℓ-conserving oscillations, but can be probed in ℓ-violating experiments. The neutrinoless double beta decay experiments referred to in Section 2.2 can measure the effective Majorana mass of equation:

$$| < \Delta m > | = |m_1|U_{e1}^2|^2 + m_2|U_{e2}^2|^2 e^{i\alpha_{21}} + m_3|U_{e3}^2|^2 e^{i\alpha_{31}}| \tag{2.30}$$

giving information on the mass eigenstates and Majorana phases. However, the sensitivity of the experiments depends on the mass ordering as shown in Figure 2.8. The Majorana phase can also be probed in neutrinos to antineutrinos oscillations $P(\nu_\alpha \to \bar{\nu}_\beta)$ and vice-versa [52].

In the case where only three left-handed neutrinos exist in nature, the PMNS matrix must be unitary in order to ensure the consistency of the probability. The unitary of U_{PMNS} is expressed as:

$$U^\dagger_{\mathrm{PMNS}}\, U_{\mathrm{PMNS}} \;=\; U_{\mathrm{PMNS}}\, U^\dagger_{\mathrm{PMNS}} \;=\; 1 \tag{2.31}$$

and implies the following three rows $(U^\dagger U)_{\alpha\alpha}$ and three columns $(U^\dagger U)_{ii}$ normalisations, as well as the three row triangles $(U^\dagger U)_{\alpha\beta}$ and three column triangles $(U^\dagger U)_{ij}$ closures [53, 54]:

$$\begin{array}{rclllr}
(U^\dagger U)_{\alpha\alpha} & \Leftrightarrow & |U_{\alpha 1}|^2 & + |U_{\alpha 2}|^2 & + |U_{\alpha 3}|^2 & = 1 \\
(U^\dagger U)_{ii} & \Leftrightarrow & |U_{ei}|^2 & + |U_{\mu i}|^2 & + |U_{\tau i}|^2 & = 1 \\
(U^\dagger U)_{\alpha\beta} & \Leftrightarrow & |U_{\alpha 1}U^*_{\beta 1} & + U_{\alpha 2}U^*_{\beta 2} & + U_{\alpha 3}U^*_{\beta 3}| & = 1 \\
(U^\dagger U)_{ij} & \Leftrightarrow & |U_{ei}U^*_{ej} & + U_{\mu i}U^*_{\mu j} & + U_{\tau i}U^*_{\tau j}| & = 1
\end{array} \tag{2.32}$$

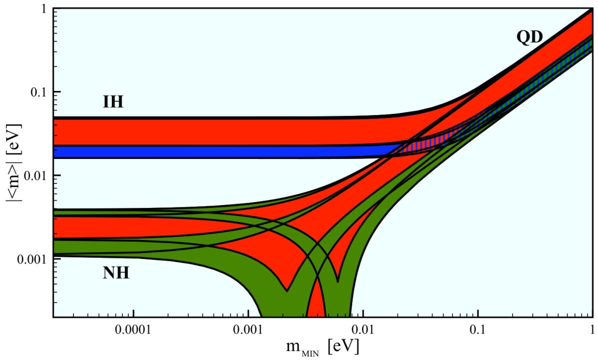

Figure 2.8: Effective Majorana neutrino mass $| < \Delta m > |$ as a function of the minimal mass eigenstate value m_i. The Majorana phases $\alpha_{1,2}$ are varied in $[0, 2\pi]$. NO and IO refers to the mass ordering and QD stands for Quasi Degenerate mass ordering. Figure adapted from [51] for PDG [32]

parameter		*best fit value*	*1σ CL*	*most accurate experiments*
$\mathbf{sin^2\theta_{12}}$		0.304	$[0.291; 0.317]$	SNO KamLAND
$\mathbf{sin^2\theta_{23}}$	NO	0.437	$[0.427; 0.480]$	T2K, NOνA
	IO	0.569	$[4.28; 4.91] \oplus [5.18; 5.97]$	
$\mathbf{sin^2 2\theta_{13}}$		0.085	$[0.080; 0.090]$	Daya Bay Double Chooz
$\mathbf{\Delta m^2_{21}}$		$7.53 \cdot 10^{-5}\,\text{eV}^2 \cdot \text{c}^{-4}$	$[7.35; 8.11 \cdot 10^{-5}]\text{eV}^2 \cdot \text{c}^{-4}$	SNO KamLAND
$\mathbf{\Delta m^2_{32}}$	NO	$-2.44 \cdot 10^{-3}\,\text{eV}^2 \cdot \text{c}^{-4}$	$[-2.50; -2.37 \cdot 10^{-3}]\text{eV}^2 \cdot \text{c}^{-4}$	T2K, NOνA, IceCube
	IO	$2.51 \cdot 10^{-3}\,\text{eV}^2 \cdot \text{c}^{-4}$	$[2.45; 2.57 \cdot 10^{-3}]\text{eV}^2 \cdot \text{c}^{-4}$	
$\mathbf{\delta_{CP}}$	NO	?	$[-\pi; -0.02] \oplus [2.8; \pi]$	T2K, NOνA
	IO	?	$[-2.8; 0]$	
$\mathbf{\alpha_{1,2}}$		?	?	0$\nu\beta\beta$ exp.

Table 2.2: Current best fit values and 1σ CL for the neutrino oscillation parameters. The latest column represent the experiments able to put the tightest bounds as for 2017 (0$\nu\beta\beta$ refers to neutrinoless double beta decay.)

A violation of the equalities of Equation (2.32) would imply a mixing to a fourth neutrino, opening new perspectives for particle physics. Global fits of neutrino experiments data have been performed both with and without a unitarity assumption [55, 56]. The lack of $\overset{(-)}{\nu}_\tau$ oscillation measurement leads to build the unitarity triangles by determining the interval where the third triangle vertex would be located if the matrix was unitary as shown in Figure 2.9. The unitarity postulate impacts the neutrino experiments global data fit by modifying the 3σ CL of the U_{PMNS} entries as shown in Figure 2.10. While the unitarity of the matrix is strongly constrained by the measurement of three neutrino flavours from Z^0 decay [19], more accurate measurements of neutrino oscillations would provide additional constraints on the unitarity of the PMNS matrix.

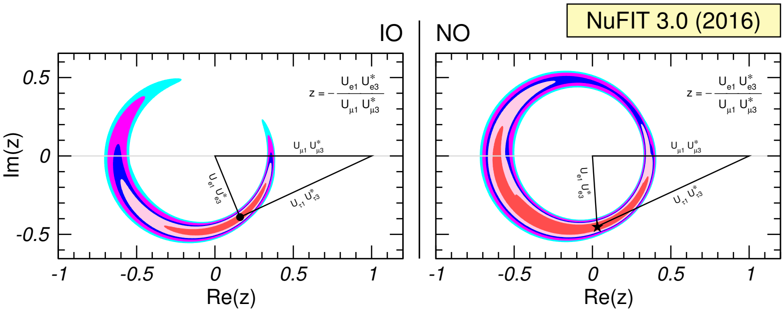

Figure 2.9: One of the three leptonic unitary column triangle. The coloured areas show by increasing surface the 1σ, 90%, 2σ, 99% and 3σ CL for the third triangle vertex when fitting the neutrino experiments data assuming unitarity of the U_{PMNS} matrix. The left figure shows IO of neutrino masses, the right figure NO. Figure from [55]

$$|U|^{\textbf{w/o Unitarity}}_{3\sigma\ \text{(with Unitarity)}} = \begin{pmatrix} U_{e1} & U_{e2} & U_{e3} \\ U_{\mu1} & U_{\mu2} & U_{\mu3} \\ U_{\tau1} & U_{\tau2} & U_{\tau3} \end{pmatrix} = \begin{pmatrix} \underset{(0.79\to0.85)}{0.76\to0.85} & \underset{(0.50\to0.59)}{0.50\to0.60} & \underset{(0.14\to0.16)}{0.13\to0.16} \\ \underset{(0.22\to0.52)}{0.21\to0.54} & \underset{(0.43\to0.70)}{0.42\to0.70} & \underset{(0.62\to0.79)}{0.61\to0.79} \\ \underset{(0.24\to0.54)}{0.18\to0.58} & \underset{(0.47\to0.72)}{0.38\to0.72} & \underset{(0.60\to0.77)}{0.40\to0.78} \end{pmatrix}$$

Figure 2.10: 3σ CL of the elements of the PMNS matrix from a global fit to neutrino experiments data with and without (w/o) assuming unitarity of the matrix. Figure adapted from [56]

The parameters of U_{PMNS} must be measured are they are free parameters of the present theory, but it has been postulated that they may be deduced from a discrete flavour gauge symmetry [57]. The breaking of this symmetry would distinguish charged leptons from neutrinos, and according to the group symmetry, would lead to different templates of U_{PMNS}. The different postulated symmetries are the bimaximal or tribimaximal forms, of golden ratio types or hexagonal forms [58]. They now agree within the uncertainties of the measured neutrino oscillation parameters, but a more stringent constraint on some parameters could lead to the refutation of some models.

2.4 Neutrinos and cosmology

While the nowadays laws of Physics describe separately the very small scale, with Quantum Field Theory (QFT), and the very large scale, with General Relativity (GR), the two are strongly entangled. From the earliest time we can infer in the history of our Universe, it appears to be in expansion from a very dense phase that was only populated of elementary particles of very low mean free path. The evolution from this homogeneous very energetic phase to the present Universe containing distinct objects forming structures is strongly governed by the properties of particle physics.

2.4.1 Baryon number asymmetry

Particles and antiparticles are symmetrically described by QFT. However, analyses of CMB and light elements abundance (hydrogen, deuterium and helium) produced at the so-called Big Bang Nucleosynthesis (BBN) era where the Universe temperature was $T_{Universe} \sim 1\,\mathrm{MeV}$ [59] lead to the baryon asymmetry [60]:

$$\eta_{\mathscr{b}} = \frac{n_{\mathscr{b}} - n_{\bar{\mathscr{b}}}}{n_\gamma} \;\in\; [5.8\;;\;6.6 \cdot 10^{-10}] \qquad (95\%\ CL) \tag{2.33}$$

where $n_{\mathscr{b}}$ is the density of baryons in the Universe, $n_{\bar{\mathscr{b}}}$ is the density of antibaryons, and n_γ is the density of photons. The baryon number $\mathscr{b}$ is the analogous of ℓ but for baryons, as it characterises the matter made of quarks and has for equation:

$$\mathscr{b} = \frac{1}{3}(n_q - n_{\bar{q}}) \tag{2.34}$$

where n_q is the number of quarks and $n_{\bar{q}}$ the numbers of antiquarks. The low value of $\eta_{\mathscr{b}}$ indicates that the Universe as we know it is dominated by matter over antimatter. Yet it does not imply that matter and antimatter were not present in equal densities in an earlier phase. If it was the case, then a mechanism must have driven the disappearance of antimatter ; this process is referred to as "baryogenesis". The Sakharov conditions derived by the eponymous physicist stipulate that according to our current knowledge of Physics, baryon asymmetry requires the three following conditions [61]:

(1) $\mathscr{b}$ conservation violation

(2) C and CP symmetry violation

(3) interactions out of thermal equilibrium

The condition (1) ensures naturally that the baryon number of the Universe evolves with time. The condition (2) sets that the evolution of $\mathscr{b}$ occurs at different rates for matter and antimatter. The condition (3) implies that matter and antimatter do not annihilate each other before processes (1) and (2) take place.

Section 2.3 describes how CP violation occurs in neutrino oscillation. Analogously to the U_{PMNS} matrix encoding the neutrino flavour mixing, quarks undergo flavour mixing in weak interactions encoded by the Cabibbo-Kobayashi-Maskawa (CKM) matrix U_{CKM} [62, 63]:

$$\underbrace{\begin{pmatrix} |d'\rangle \\ |s'\rangle \\ |b'\rangle \end{pmatrix}}_{q_\alpha} = \underbrace{\begin{pmatrix} U_{ud} & U_{us} & U_{ub} \\ U_{cd} & U_{cs} & U_{cb} \\ U_{td} & U_{ts} & U_{tb} \end{pmatrix}}_{U_{\mathrm{CKM}}} \underbrace{\begin{pmatrix} |d\rangle \\ |s\rangle \\ |b\rangle \end{pmatrix}}_{q_i} \tag{2.35}$$

where q_α are the flavour eigenstates and q_i the mass eigenstates. Analyses of kaon and B-mesons decay resulted in an accurate knowledge of U_{CKM} [64]:

$$U_{\mathrm{CKM}} = \begin{pmatrix} 0.97422 \to 0.97445 & 0.22456 \to 0.22556 & 0.00342 \to 0.00372 \\ 0.22442 \to 0.22542 & 0.97338 \to 0.97364 & 0.0398 \to 0.0424 \\ 0.00842 \to 0.00907 & 0.0390 \to 0.0416 & 0.99910 \to 0.99920 \end{pmatrix} \tag{2.36}$$

Compared to the PMNS matrix of Figure 2.10, the CKM matrix is closer to a diagonal unitary matrix. It implies that quarks undergo little flavour mixing, and CP violation in kaon decay has been measured with an amplitude of $\mathcal{O}(10^{-3})$, insufficient to explain the measured baryon asymmetry [65, 66].

A possible explanation consistent with the SM is that baryogenesis occurred through *leptogenesis*, i.e. a lepton number ℓ asymmetry. In the hypothesis where one or several Majorana singlet neutrinos N_i are added to the known particles of the SM as described in Section 2.2, they can

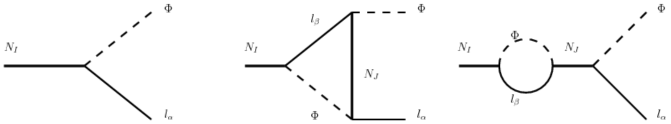

Figure 2.11: Decay of a Majorana neutrino N_I into a left-handed neutrino l_α and a Higgs boson ϕ. The three processes violate lepton number conservation with $\Delta\ell = 2$. From [67].

decay with process of $\Delta\ell = 2$ as shown in Figure 2.11. Interferences between the ℓ-violating processes involve the CP-violating phases δ_{CP}, α_{21} and α_{32}, leading to a different ℓ-violation for matter and antimatter [68] and satisfying the Sakharov condition (2). If the decay occur at $T_{Universe} > T_{electroweak}$, the ℓ violation can be turned into a $\mathscr{b}$ violation due to a non perturbative topological process to satisfy Sakharov condition (1). Such processes arise due to the spontaneous breaking of the electroweak symmetry leading to degenerate vacua of different energies [69], separated by energy walls which saddle point is named *sphalerons*. Because the lepton and baryon symmetries are not conserved at the quantum level, a topological quantum tunnelling between two vacua violate ℓ and $\mathscr{b}$ but conserve $\ell - \mathscr{b}$ [70], converting $\Delta\ell \neq 0$ into $\Delta\mathscr{b} \neq 0$ [67]. The non equilibrium Sakharov condition (3) holds if the decay width of N_i is smaller that the expansion rate of the Universe.

Many scenarii have been postulated in order to explain the baryon number asymmetry. The simple leptogenesis model presented in this section has the advantage of taking place in the SM as we know it if Majorana singlets exist. However, other leptogenesis process involving other see-saw types, electroweak phase transitions, or GUT have been postulated, with the lepton flavour mixing of different importance according to the process involved.

2.4.2 Neutrinos as dark matter component

The study of galaxy rotation curves [71], galaxy cluster motion [72], gravitational lensing [73] and CMB power spectrum [20] have shown that the matter as described in the SM was not enough to describe the gravitational motion and density of the observed matter with the law of GR applying to the Friedmann–Lemaître–Robertson–Walker (FLRW) metric used to describe the Universe. The anomaly is referred to as "Dark Matter (DM)" and the analysis of the Planck satellite data have lead to an estimation of its normalised density [20, 74]:

$$\Omega_{DM} = \frac{\rho_{DM}}{\rho_{crit}} = 0.258(11) \tag{2.37}$$

where ρ_{DM} is the density of DM and ρ_{crit} is the critical density (i.e. the energy density for a flat Universe in the FLRW metric) today. The DM density is ~ 5 times higher than the density of baryons:

$$\Omega_{\ell} = \frac{\rho_{\ell}}{\rho_{crit}} = 0.0484(10) \tag{2.38}$$

and its composition is unknown as today. It must be non-relativistic to avoid the washout of galaxy formation, stable with time as they have been observed as well in CMB that in our vicinity, and have little coupling with electromagnetic interaction as we cannot see it [75].

Several theories have been postulated to explain the DM anomaly, involving new particles from GUT or primordial black holes. Majorana neutrinos described in Section 2.2 are a simple candidate in the category of very weakling interacting massive particles, in the hypothesis where they decay rate is low enough to ensure a sufficient relic density. It has been shown that a model adding three Majorana singlets to the SM could account for both left-handed neutrino mass generation, leptogenesis and DM [76], and could be probed by the proposed Search for Hidden Particles (SHiP) experiment [77].

Conclusion:

Neutrinos have the unique features of being the only particles of the SM to exist only in the left-handed chirality state. Consequently, the origin of their mass cannot be explained from interaction with the Higgs boson without postulating the existence of right-handed neutrinos, that may be Majorana particles. However, the massive nature of neutrinos imply that they oscillate, i.e. can be detected in flavour different from the flavour of production, and a precise measurement of the neutrino oscillation parameters is essential to constraint predicted new flavour symmetries. It would also consist in an estimation of any mixing with a fourth neutrino state that would prevent the unitarity of the U_{PMNS} matrix and could shed light on non-weakly interacting neutrinos, the generations of the SM or the nature of DM. A precise measurement of the CP-violating phase is also of first importance to constraint the postulated process of leptogenesis that explains the measured baryon asymmetry of the Universe. This thesis presents an estimation of four of the six oscillation parameters of the U_{PMNS} matrix with the T2K experiment, which setup is described in the next chapter.

CHAPTER 3

The T2K experiment

This chapter presents the T2K experiment setup, both in term of hardware and simulation. The first section describes the neutrino beam production, the second section depicts the two on- and off-axis near detectors, and the third section presents the far detector Super-K. The latest section details the simulation of neutrino interactions with NEUT, the T2K custom Monte-Carlo (MC) event generator.

3.1 The T2K beam

3.1.1 The neutrino beamline

The neutrino beam is created in the Japan Proton Accelerator Research Complex (J-PARC) in Tokai, Ibaraki prefecture, Japan [78]. A proton beam is accelerated in a linear accelerator up to a kinetic energy of 400 MeV, then supplied to a rapid-cycling synchrotron of 25 Hz frequency accelerating the beam up to 3 GeV. A spill is constituted of eight bunches that are transmitted to the main ring synchroton to be accelerated up to 30 GeV, then extracted with five magnets towards the neutrino beamline. In order to create an intense beam, the main ring can perform with a power up to 750 KW (having now reached 470 KW) and deliver $3 \cdot 10^{14}$ protons per spill. The spill are $\sim 5\,\mu$s long and the whole experiment relies on a GPS synchronisation providing a ~ 50 ns resolution, enabling the triggers in the subsequent detectors to be synchronised with the spill to reject background (such as cosmic events). The stability of the beam is guaranteed using a series of detectors monitoring the beam intensity, position, profile and loss along the beamline [11].

The proton beam arrives at the target station shown in Figure 3.1 where it hits a graphite target circled by a titanium case and cooled by flowing helium gas. The target is a 94 cm long and 2.6 cm diameter rod, of density $1.8\,\mathrm{g \cdot cm^{-3}}$, giving a proton interaction length of 1.9 [79]. The interaction of protons with the target creates $\pi^{\pm}$ and $K^{\pm}$, focused and selected according to their polarity by three 2.1 T magnetic horns [80] to create a neutrino or antineutrino-enhanced beam, referred in this thesis as ν*-mode* and $\bar{\nu}$*-mode* beam. If the horn current is =+320 KA, positively charged particles are

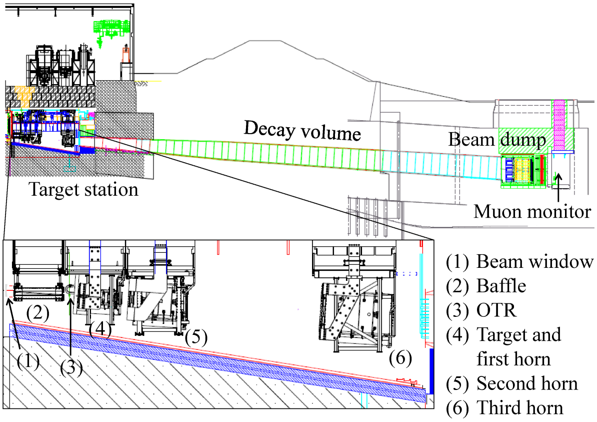

Figure 3.1: Schematic view of the beamline from the target station to the muon monitor. The beam window separates the target station from the proton beam vacuum. The baffle is a 1.7 m long graphite block, and OTR stands for Optical Transition Radiation Monitor. The proton beam hits the graphite rod target, creating $\pi^{\pm}$ and $K^{\pm}$ focused by the first horn while the two other horns select positive or negative particles. The $\pi^{\pm}$ and $K^{\pm}$ decay to $\mu^{\pm}$ and $\overset{(-)}{\nu}_{\mu}$ in the decay tunnel, the long-lived particles being stopped by the iron and graphite beam dump. The muon monitor measures the profile of the $\mu^{\pm}$ to monitor the beam intensity and direction. Figure from [11].

oriented towards the decay tunnel to create a ν_μ-enhanced beam ; while if the horn current is -320 KA, negatively charged particles decay into an $\bar{\nu}_\mu$-enhanced beam as shown with the main contributing particle decays in Equation (3.1).

$$\begin{aligned} I_{horn} &= +320\,\mathrm{KA} \quad \Longleftrightarrow \quad K^+ \;/\; \pi^+ \;\rightarrow\; \mu^+ + \nu_\mu \\ I_{horn} &= -320\,\mathrm{KA} \quad \Longleftrightarrow \quad K^- \;/\; \pi^- \;\rightarrow\; \mu^- + \bar{\nu}_\mu \end{aligned} \tag{3.1}$$

The decay occurs in a 96 m-long decay tunnel of increasing section, shielded by 6 m thick concrete volume and water cooled. The long-lived $\pi^\pm$ and $K^\pm$ are stopped by a beam dump made of graphite (3.174 m length) and iron (2.4 m length). The MUon MONitor (MUMON) measures the $\mu^\pm$ profile with arrays of ionisation chambers, Si-PIN diodes and emulsion films to monitor the beam direction [81], the $\mu^\pm$ being correlated with the $\overset{(-)}{\nu}_\mu$ kinematics as the majority of them originates from two-body decay.

3.1.2 The off-axis setup

Because $\overset{(-)}{\nu}_\mu$ are produced in a two-body decay, is is not possible to obtain a monochromatic neutrino beam. As the oscillation probability depends on the neutrino energy, detection of oscillation benefits from a maximum of $\overset{(-)}{\nu}_\mu$ having the energy corresponding to the maximal oscillation for a given distance. T2K achieves to reduce the energy width of the beam with an off-axis method [82]. The energy of a neutrino produced in pion decay as in Equation (3.1) is:

$$E_\nu = \frac{m_\pi^2 - m_\mu^2}{2(E_\pi - p_\pi \cos\theta_{\pi\nu})} \tag{3.2}$$

where $m_{\pi,\nu}$ are the $\pi^\pm$ and $\mu^\pm$ masses respectively (m_ν is neglected), $E_{\nu,\pi}$ are the $\overset{(-)}{\nu}_\mu$ and $\pi^\pm$ energy, p_π is the $\pi^\pm$ momentum, and $\theta_{\pi\nu}$ the angle between the $\pi^\pm$ and $\overset{(-)}{\nu}_\mu$ directions. Figure 3.2a shows E_ν as a function of E_π for several values of $\theta_{\pi\nu}$, where it can be seen that the E_ν distribution becomes flatter as $\theta_{\pi\nu}$ increases. Consequently, at large $\theta_{\pi\nu}$, the neutrino energy has a low dependence on the pion energy, and a beam with a restricted range of neutrino energy can be obtained from a wide pion energy distribution. This is illustrated in Figure 3.2b for the T2K flux in the off-axis detectors located at $\theta_{\pi\nu} = 2.5°$, making the distribution peaks at $E_\nu \simeq 600\,\mathrm{MeV}$, corresponding to the maximal ν_μ disappearance probability and ν_e appearance probability at a distance of 295 Km.

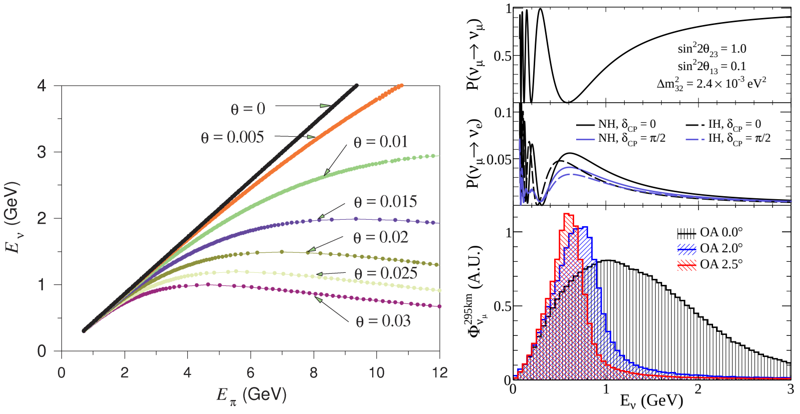

(a) **(b)**

Figure 3.2: The off-axis technique provide a narrow energy neutrino beam from a wide energy pion beam. Figure 3.2a (from [83]) shows E_ν as a function of E_π for several values of $\theta \equiv \theta_{\pi\nu}$ as given by Equation (3.2). At wider angle, the E_ν distribution has lower dependence in E_π. The resulting neutrino beam is more peaked in energy, as shown for the T2K flux in Figure 3.2b (from [14]). The T2K off-axis detectors are located at $\theta = 2.5°$ so the maximum energy $E_\nu^{max} = 600\,\text{MeV}$ coincides with the maximum ν_μ disappearance and ν_e appearance probabilities (assuming $\sin^2 2\theta_{13} = 0.1$, $\sin^2 2\theta_{23} = 1$, $|\Delta m^2_{32}| = 2.4 \cdot 10^{-3}\,\text{eV}^2$ and a distance of 295 Km).

3.1.3 The flux simulation

Protons interactions with the target are modelled with the FLUktuierende KAskade (FLUKA) 2008 software [84, 85], that was found to be the most accurate simulation of hadronic interactions [86]. However, the T2K flux simulation does not depend only on MC modelling and the FLUKA output is tuned to hadron production measurements. It particularly relies on the NA61 / SPS Heavy Ion and Neutrino Experiment (NA61/SHINE), that measured the $\pi^\pm$ and $K^\pm$ production rates from a target located in the Super Proton Synchrotron (SPS) of Centre Européen de Recherche Nucléaire (CERN) [87]. NA61/SHINE ran with the same proton beam energy as T2K and operated with a replica of the T2K target, from which the emitted particles are measured by several Time Projection Chamber (TPC) and Time-of-Flight (ToF) detectors. At the time of this thesis, the T2K flux simulation was tuned to the results of the 2007 and 2009 runs [88].

The components from the target station to the beam dump, as well as the following detectors described in the next sections, are modelled with the GEometry ANd Tracking (GEANT)-3 software [89]. The interactions of particles exiting the target with the surrounding materials are simulated with the GCALOR package. The final predicted flux in Near Detector at 280m (ND280) and Super-K is shown in Figure 3.3, where it can be seen that although the ν-mode is dominated by ν_μ and the $\bar{\nu}$-mode by $\bar{\nu}_\mu$, the ν_μ contamination is relatively high in $\bar{\nu}$-mode Because a proton beam arrives on the target irrespectively of the mode, more π^+ than π^- are produced in both cases. The horn selection being less efficient at high momentum (where the particle trajectory bends less), it leads to a higher ν contamination in $\bar{\nu}$-mode.

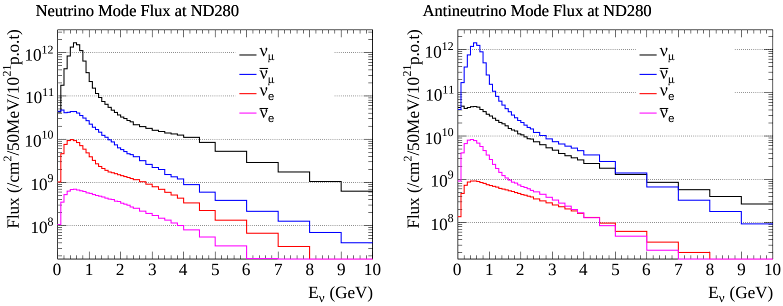

(a) ND280, ν-mode **(b)** ND280, $\bar{\nu}$-mode

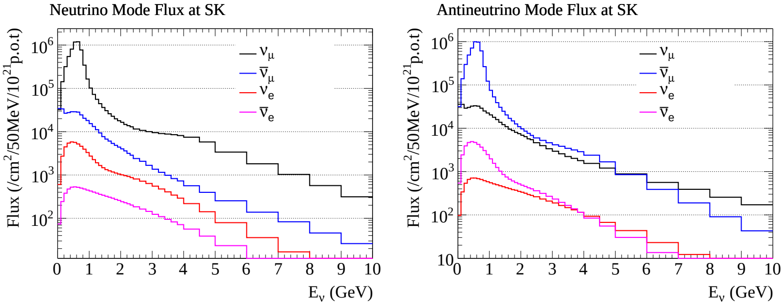

(c) Super-K, ν-mode **(d)** Super-K, $\bar{\nu}$-mode

Figure 3.3: Prediction of the T2K flux in the off-axis near (ND280) and far (Super-K) detectors in ν- and $\bar{\nu}$-mode. Figure from T2K [90].

3.2 The near detector complex

The T2K near detector complex is located in J-PARC, 280 m downstream the target. It holds the on-axis Interactive Neutrino GRID (INGRID) detector monitoring the beam intensity and direction and described in Section 3.2.1. The off-axis ND280 detector aims at constraining the neutrino flux and interaction models, it is placed above INGRID and described in Section 3.2.2.

3.2.1 INGRID

The INGRID detector is located on-axis the beam, which $\pm 1\sigma$ aperture has a width of ~ 5 m at a distance of 280 m from the target. The detector is shaped as a 10 m wide, 10 m high cross made of 16+1 modules [91] shown in Figure 3.4a. The targets of the 16 identical modules are nine iron plates, interlaid with eleven tracking plates made of scintillator as shown in the top Figure 3.4b. Scintillator bars are assembled into veto planes placed around the modules as shown in the bottom Figure 3.4b. The cross vertical and horizontal segments hold six modules each, two modules overlapping in the

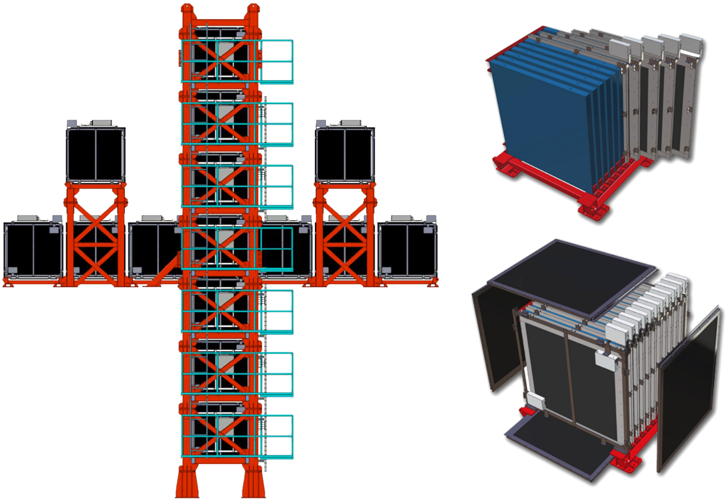

(a) Full INGRID detector **(b)** INGRID module

Figure 3.4: The on-axis near detector INGRID. Figure 3.4a shows the $x - y$ view of the full detector. Figure 3.4b shows one of the seventeen module, the top diagram describing the interlaid iron and scintillating layers, and the bottom the veto layers. From [91].

center of the cross and two additional modules located around the upper arm of the cross monitoring the symmetry of the beam. The last module is called the *proton module* as it is only made of scintillator planes, it is placed between the two arms in the center of the cross to measure the CC $\overset{(-)}{\nu}_\mu$ interaction rate. INGRID monitors the beam intensity and direction on a daily basis with an 0.4 mrad precision [11].

3.2.2 ND280

The ND280 detector is located 2.5° off-axis the beam center and is composed of several subdetectors shown in Figure 3.5. The center part contains the tracker, holding two Fine Grained Detector (FGD) and three TPCs. The π^0 Detector (P∅D) is located upstream the tracker, both being surrounded by several Electromagnetic Calorimeter (ECal). All those subdetectors are placed inside the UA1 magnet, that contains the Side Muon Ranger Detector (SMRD) interlaid with the coils. In total, ND280 measures 7.6 × 5.6 × 6.1 m and the subdetectors are described below.

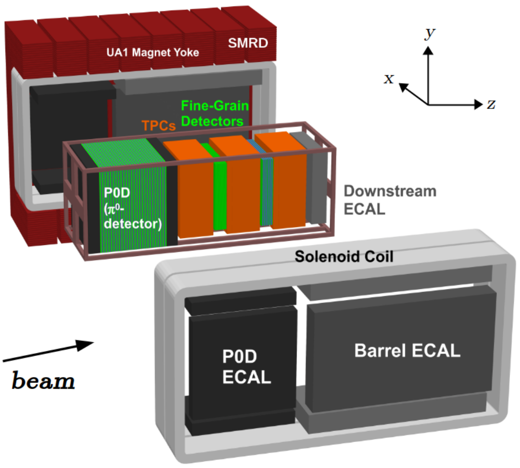

Figure 3.5: Exploded view of the off-axis near detector ND280 and its subdetectors: the two FGD, the three TPC, the P∅D, the several ECals, the SMRD and the UA1 magnet.

Magnet: The magnet is refurbished from the UA1 experiment [92]. It consists of two symmetrical parts containing eight yokes, themselves made of sixteen iron plates [79] to deliver a 0.2 T horizontal magnetic field with an uncertainty measured to be $2 \cdot 10^{-5}$ T in a field mapping survey [11]. The bending of charged particles in the magnetic field enables the determination of their momenta and electric charges.

SMRD: The SMRD holds 192 horizontal and 248 vertical modules placed in the air gap of the magnet. The modules comprise scintillator slabs embedding WaveLength Shifting (WLS) fibers in order to detect cosmic events or outer detector neutrino interactions, and to measure the momentum of high-angle $\mu^{\pm}$ from $\overset{(-)}{\nu}_{\mu}$ interactions in the internal subdetectors [93].

ECal: Thirteen ECals surround the inner detectors to ensure the proper detection of cosmic events and to contribute to the identification of photons from neutral pions [94]. Six modules are placed around the tracker (Barrel ECals), each one consisting of 31 layers of polystyrene doped scintillating bars, oriented alternatively in the $\vec{z}$ and $\vec{x}$ or $\vec{y}$ direction according to the ECal orientation, and crossed transversely by WLS fiber. 1.75 mm lead sheets are interposed between the layers, providing at total 9.7 interaction length to convert photons into e^-/e^+ showers [11]. Six other modules circle the P∅D (P∅DEcal) made of six layers of the same scintillating bars as in the Barrel ECal, all oriented along $\vec{z}$, interlaid with 4 mm lead sheets giving 3.6 radiation length. The final module placed downstream the tracker (DsEcal) exhibits the same structure, with 34 scintillating layers placed consecutively along $\vec{x}$ then $\vec{y}$, and 10.6 radiation length provided by 1.75 mm lead sheets.

P∅D: The P∅D aims at measuring the π^0 production rate from $\overset{(-)}{\nu}$. It contains 40 modules of two layers of triangular polystyrene scintillator bars, the first layer consisting of 134 vertical bars and the second layer 126 horizontal bars [95], all of them containing a WLS fiber in its center. The first seven and last seven modules form the *upstream* and *downstream ECal* shown in Figure 3.6a by alternating scintillator modules and 4 mm thick lead sheets. The remaining bars form the *upstream* and *central water target* by interlaying scintillator modules, 4 mm thick brass sheets and 28 mm thick water bags layers. The lead and brass sheet aim at creating e^-/e^+ showers from photons emitted in π^0 decay, and the water bags can be emptied between T2K runs in order to extract the cross-section on H_2O with a subtraction method.

Tracker: the two targets of the tracker are the two FGD. The first FGD (FGD1) consists of 15 modules, each modules containing two layers 192 extruded polystyrene scintillator bars placed consecutively along $\vec{x}$ then $\vec{y}$ to ensure the tracking of the charged particles. The second FGD (FGD2) contains eight modules identical to FGD1, between which 25 mm thick water

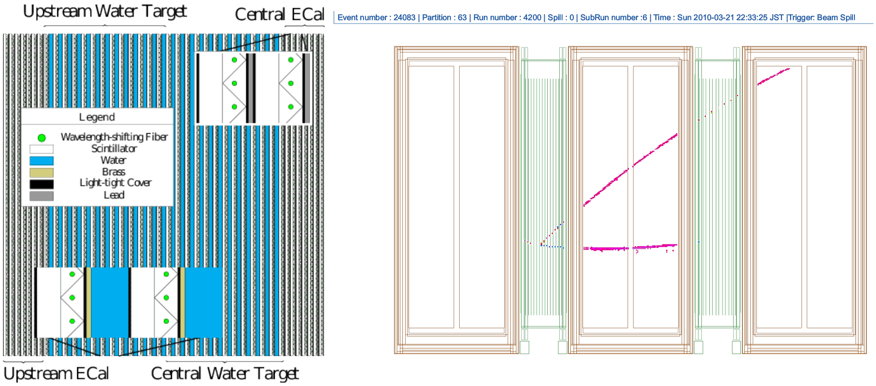

(a) P∅D **(b)** Tracker

Figure 3.6: The inner subdetectors of ND280, with the ν beam entering from the left. Figure 3.6a shows a schematic view of the P∅D and its four parts interlaying scintillator modules, water bag, lead and brass sheet (from [95]). Figure 3.6b shows an event display in the tracker of a ν interaction in the first FGD (green) creating charged tracks crossing the downstream TPC (brown) and the second FGD.

bag layers are interlaid [96]. Three TPCs are placed before, between and after the FGD as shown in Figure 3.6b. They are filled with a gas mixture mainly composed of argon (Ar : CF4 : iC4H10 with the ratio 95:3:2) and holds in their middle a central cathode creating a linear electric field of $280\,\mathrm{V}\cdot\mathrm{cm}^{-1}$ in the $\vec{x}$ direction [97]. The charged particles entering the TPC ionise the gas, creating electrons drifting towards the MicroMegas readout planes [98]. The energy loss measured from the charge of the readout plane, combined with the momentum measurement from the curvature of the particle track in the magnetic field, enables the identification of charged particles.

3.3 The far detector Super-Kamiokande

The far detector Super-K is located 295 Km downstream the target, in Kamioka, Gifu prefecture, and is placed 2.5° off-axis the beam center [99]. It is a 50 Kton Cherenkov detector of cylindrical shape with 39 m diameter and 41 m height as shown in Figure 3.7. The volume is filled with pure water and consists of two parts: the Outer Detector (OD) and the Inner Detector (ID). The ID is a 33.8 m wide and 36.2 m high cylinder of inner surface covered at 40% by 11,146 50 cm diameters Hamamatsu R3600 PhotoMultiplier Tube (PMT) [11]. It is surrounded by the 2 m thick OD, separated from the ID by

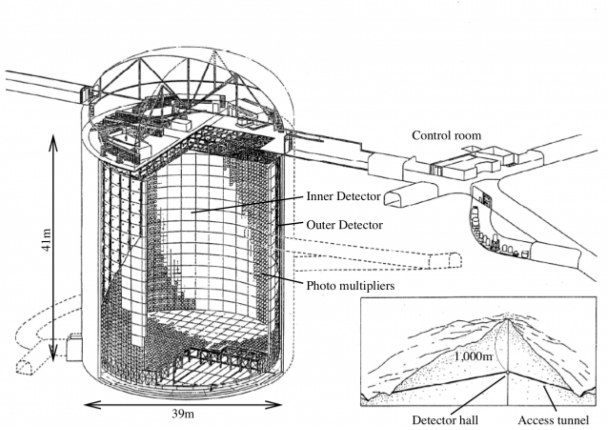

Figure 3.7: Schematic view of the far detector Super-K. The cylindrical 50 Kton Cherenkov detector in located 295 Km downstream the target in Kamioka mine and shielded from cosmic rays by 1 Km of rocks. Figure from [100].

a 55 cm stainless steel structure supporting the PMT and their electronic, the OD side containing 611 Hamamatsu R1408 PMTs and 1,274 R5912 PMT. The detector is shielded from cosmic rays by 1 Km of rocks that muons of energy $< 1.3\,\mathrm{TeV}$ cannot cross, minimising the muon background to $\mathcal{O}(1\,\mathrm{cm}^{-2} \cdot \mathrm{s}^{-1} \cdot \mathrm{sr}^{-1})$.

When $\overset{(-)}{\nu}$ interactions in water produce charged particles, the latter are detected using the Cherenkov effect [101]. Charged particles crossing a dielectric medium of refractive index n at a velocity $v_p = \beta_p c$ larger than the speed of light $v_\gamma = \frac{c}{n}$ induce a local polarisation of the medium. The perturbation propagates in water with a velocity $v_\gamma < v_p$ creating a shock wave front emitting photons along a cone of opening angle $\theta_c = \mathrm{arcos}\frac{1}{\beta_p n}$. If the event occurs inside Super-K and the charged particle stops before exiting the detector, the PMT on the walls will measure signals forming a ring which diameter is related to β_p and thickness to the momentum of the particle. The Particle IDentification (PID) can be achieved from the granularity of the signal as shown in Figure 3.8: charged particles such as $e^\pm$ undergo multiple scattering dispersing the Cherenkov photons, while heavier particles such as $\mu^\pm$ scatter less and the majority of photons are aligned in the ring. T2K events are selected inside the ID, which PMT have a quantum efficiency of 20% and acquisition channels a timing resolution $\lesssim 2\,\mathrm{ns}$ for a charge $\gtrsim 1$ photoelectron(p.e.) [102]. The OD is used to detect events occurring from cosmic rays or in the rocks around Super-K.

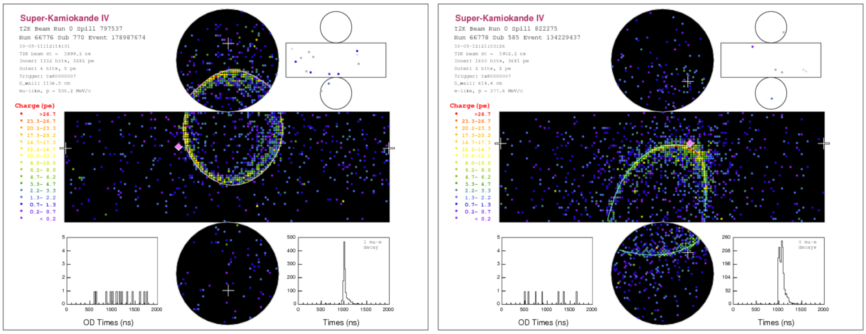

(a) $\mu^{\pm}$ ring

(b) $e^{\pm}$ ring

Figure 3.8: Reconstructed Cherenkov rings in Super-K for a muon (3.8a) and an electron (3.8b). The different amount of multiple scattering induced by the difference of mass enables the particle identification.

3.4 The neutrino interaction event generator NEUT

Neutrino interaction physics is an active field of research. The near and far detectors geometry are simulated with the GEANT-4 software [103], which also encodes the interaction of hadronic and electromagnetic particles. However, no "standard model" of neutrino interactions exists nowadays with sufficient level of confidence to be implemented as usable out of the box, and a specific neutrino interaction event generator has been developed for the Super-K and T2K experiments, named NEUT [104]. The analysis presented in this thesis used NEUT version 5.3.2, where the model has been selected using information from other neutrino experiments [105]. Several models of nucleon distributions and nuclear effects have been tested against the Mini Booster Neutrino Experiment (MiniBooNE) and Main Injector Experiment for $\nu - A$ (MINERνA) CCQuasi-Elastic (QE) cross-section measurements, and the NEUT implementation describing best the data has been chosen to generate neutrino interaction events in T2K. CCQE interactions refers to a $W^{+/-}$ exchange between a neutrino and a nucleon, producing a charged lepton and a nucleon, and is the dominant process at the peak energy of T2K flux as shown in Figure 3.9.

The scattering of neutrinos on free nucleons is described by the Lewellyn-Smith formalism [106] and the bounding of the nucleons in the nucleus is added by the Smith-Moniz global Relativistic Fermi Gas (RFG) model [107].

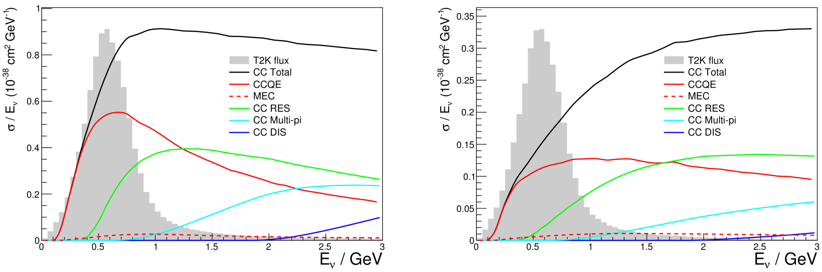

(a) ν_μ

(b) $\bar{\nu}_\mu$

Figure 3.9: CC cross-section as predicted by NEUT version 5.3.2 for ν_μ (3.9a) and $\bar{\nu}_\mu$ (3.9b). The different process are explained in the text, and the T2K flux spectra is shown with arbitrary units.

The RFG consists in nucleons described by plane-wave states filling a potential up to a common Fermi level, the adjective *global* referring to a common Fermi momentum and binding energy between the nucleons (in opposition with local RFG that is currently being implemented in NEUT [108]). The distribution of charges in the nucleus follows a Wood-Saxon potential which parameters are determined from electron scattering data [109]. CCQE interactions induced by a $\nu_\mu(\bar{\nu}_\mu)$ transform the target neutron(proton) into proton(neutron) which propagation in the nucleus is affected by long-range correlations The resulting medium polarisation, referred to as Random Phase Approximation (RPA), induces a screening effect on the neutrino-nucleus cross-section [110]. On the short range scale, nucleons can exchange mesons currents leading to the ejection of several nucleons; the case of a CC neutrino interaction producing a lepton and two protons have been introduced in NEUT using the model on [111], it is referred to as Meson Exchange Current (MEC) (or 2p-2h) .

Resonant CC and NC interactions refers to the creation of a Δ^{1232} resonance decaying into $\pi^{\pm}$. The production rate and particle kinematics are calculated using the resonant Rein-Sehgal model [112], choosing the parameters from a fit to bubble chamber pion production experiments [113]. Coherent CC and NC interactions are events occurring mainly for low energy neutrinos which de Broglie wavelength is of the order of the nucleus size. The neutrino interaction with the whole nucleus can emit a pion that are generated with the coherent Rein-Sehgal model [114, 115] but tuned afterwards to the Berger-Sehgal model [116] that has been found in better agreement with the MINERνA measurement [117]. The CC multipion production and Deep Inelastic Scattering (DIS) processes occur at higher neutrino energies, requiring a different modelling of the nucleus using GRV98 structure functions [118] including Bodek-Yang corrections [119].

Hadrons produced during neutrino interactions may interact in the nuclear medium, referred to as Final State Interactions (FSI). The implementation follows a cascade model, i.e. the particle is moved by a certain length and after each "step" the probability of interaction is calculated, until the particle interacts or exits the nucleus [104]. The propagation considers the case of pion elastic and inelastic scatterings, absorption or production, and exchange of charge in interactions.

Conclusion:

The T2K experiment is a long-baseline neutrino experiment using a beam mainly composed of ν_μ or $\bar{\nu}_\mu$ and directed off-axis the far detectors in order to reduce its energy width. The beam stability is monitored by the on-axis near detector INGRID located 280 m from the target and forming a cross composed of sandwiched layers of iron and scintillator. Above INGRID is located the off-axis near detector ND280 holding scintillator and water targets spaced by TPC and circled by ECals, all located inside a magnet producing a 0.2 T magnetic field. The far detector is located 295 Km from the target and consist of a 50 Kton cylindrical Cherenkov detector distinguishing electrons from muons thanks to the granularity of the Cherenkov ring. Neutrino interactions in the detectors are simulated with the NEUT generator, created and maintained by the T2K Collaboration. The next chapter presents the strategy of the oscillation analysis performed with events selected in the near and far off-axis detectors.

CHAPTER 4

Oscillation analysis methodology

The T2K experiment has been designed to measure the neutrino oscillation parameter $\sin^2\theta_{23}$ with great precision, as well as to constrain $|\Delta m^2_{32}|$ and estimate the probability of a non-zero $\sin^2\theta_{13}$. The confirmation of $\sin^2\theta_{13} > 0$ from the observation of reactor $\bar{\nu}_e$ disappearance [15] has enabled the measurement of δ_{CP} in long-baseline experiments. The first section of this chapter presents the Bayesian analysis, relying on Markov Chain Monte-Carlo (MCMC), used to compute the posterior probability on the four aforementioned oscillation parameters. The selection of the events used in the analysis is then described in the second section, while the last section gives details on the prior knowledge of systematic uncertainties.

4.1 Bayesian inference of neutrino oscillation parameters

4.1.1 Analysis principle

The purpose of the analysis presented in this thesis is the estimation of the U_{PMNS} parameters. The probability of 600 MeV $\overset{(-)}{\nu}_\mu$ to oscillate into $\overset{(-)}{\nu}_e$ being maximal for flight distance of 295 Km, as shown in Figure 4.1, the oscillation parameters can be estimated with events occurring in the far detector Super-K. Figure 4.2 shows the expected spectra of the R_e and R_μ samples in the unoscillated and oscillated cases (assuming the oscillation parameters obtained by most sensitive experiments as described in Section 4.2.2). The $\overset{(-)}{\nu}_\mu$ disappearance probability depends on the oscillation parameters $\sin^2\theta_{23}$ and $|\Delta m^2_{32}|$, the location of the oscillation dip present at $\sim$ 600 MeV in Figure 4.2a depending $\sin^2\theta_{23}$ and its depth on $|\Delta m^2_{32}|$. The oscillated ν_e spectrum shown in Figure 4.2b depends on the parameters $\sin^2\theta_{13}$, δ_{CP} and the sign of Δm^2_{32} (i.e. the neutrino mass ordering).

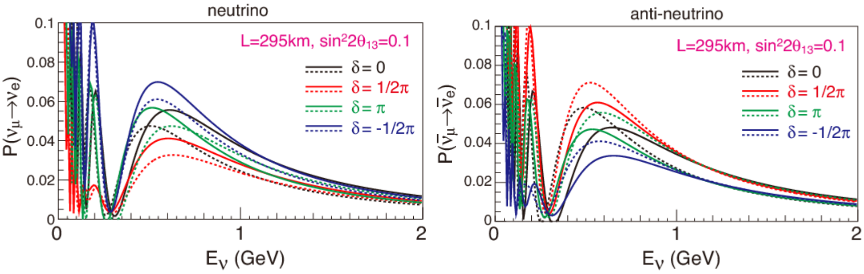

(a) $P(\nu_\mu \to \nu_e)$ **(b)** $P(\bar{\nu_\mu} \to \bar{\nu_e})$

Figure 4.1: The ν_μ to ν_e (right) and $\bar{\nu}_\mu$ to $\bar{\nu}_e$ (left) oscillation probabilities as a function of the neutrino energy and CP-violating phase. The solid(dashed) lines represent the NO(IO) of neutrino masses, and a 295 Km flight distance and $\sin^2 2\theta_{13} = 0.1$ is assumed. From [39].

A known difficulty when analysing the properties of neutrino is their very small cross-section ($\mathcal{O}$(fb)) leading to important statistical uncertainties. The issue is minimised in T2K by the use of an intense neutrino beam ($3.3 \cdot 10^{14}$ protons per pulse) and a large far detector (50 Kton) in order to detect enough interactions to measure the oscillation parameters with the desired accuracy. For the analysis, a maximum of events detected in Super-K

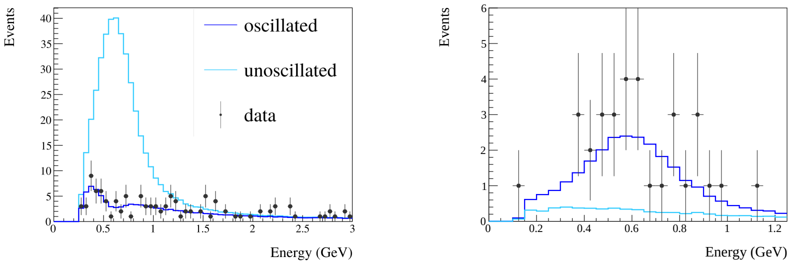

(a) ν_μ CCQE-like

(b) ν_e CCQE-like

Figure 4.2: Energy spectra of the Super-K samples of muon rings (4.2a) and electron rings (4.2b) in ν-mode. The spectra are predicted with the nominal Super-K and shown for the unoscillated (light blue) and oscillated (dark blue) cases, with the Super-K data overlaid as black points.

are included to the oscillation fit to fully benefit from the design of the experiment. Chapter 6 notably presents the inclusion of a new Super-K electron ring CC-1π sample not used in a T2K analysis so far.

However, the estimation of neutrino oscillation parameters is also subject to systematic uncertainties. The number of events detected at Super-K follows the equation:

$$N_{\nu_\alpha}(E_\nu) \; = \; \phi_{\nu_\mu}(E_\nu)\; P_{\nu_\mu \to \nu_\alpha}(E_\nu)\; \sigma_{\nu_\alpha}(E_\nu)\; \epsilon_{\nu_\alpha}(E_\nu) \tag{4.1}$$

Consequently, the effects of the flux ϕ_{ν_μ}, the cross-section σ_{ν_α}, or the detector efficiency ϵ_{ν_α} uncertainties on the event spectra are degenerate with the oscillation probability $P_{\nu_\mu \to \nu_\alpha}$. According to the models used for those nuisance parameters described in Section 4.3, the total systematic uncertainty on the number of events in the selected Super-K samples is between $\sim 12\%$ to $\sim 21\%$. In order to reduce the impact of those uncertainties, the nuisance parameters are constrained with events selected in ND280, located 280 m from the target to guarantee that no oscillation occurred. The inclusion of the ND280 samples in the analysis leads to threefold decrease the variation in the number of events in the CC-0π samples due to systematic uncertainties (twofold decrease for the CC-1π sample) the variation in the number of events due to systematic uncertainties as shown in Tables 4.15 and 4.16 of Section 4.3.5. In order to avoid any assumptions in the extrapolation of a ND280-only fit to a separate Super-K fit, this thesis presents a simultaneous analysis of the off-axis near and far detectors data.

4.1.2 Markov chain Monte Carlo with the Metropolis-Hastings algorithm

A difficulty arising for the execution of the simultaneous analysis is the high number of parameters: if there are only six oscillation parameters, there are 751 nuisance parameters (described in Section 4.3). Monte-Carlo methods provide a solution to the high dimensionality problem by sampling distributions with a random walk in a parameter space of any finite number of dimensions D. The simplest process consists in throwing points randomly in a flat bounded distribution in D dimensions, with the properties of the distribution $f(\vec{x})$ evaluated from the throws as shown in Figure 4.3. The integral is approximated with:

$$\frac{V}{N}\sum_{i}^{N} f(\vec{x_i}) \quad \xrightarrow{CLT} \quad \int_0^1 f(\vec{x})\ d\vec{x} \tag{4.2}$$

where V is the volume of the sampled space, N is the number of throws, and CLT stands for the Central Limit Theorem ensuring that the sampled integral gets closer to the continuous integral as N increases. The uncertainty on the integral given by Equation (4.2) is $V\frac{\sigma_N}{N}$ where $\sigma_N = var(f(\vec{i}))$, implying that a large number of throws is necessary to estimate the integral with a minimised sampling error. Even though the uncertainty on the integral is independent from the number of dimensions [121], generating the throws randomly could land a majority of points outside the integral. Several

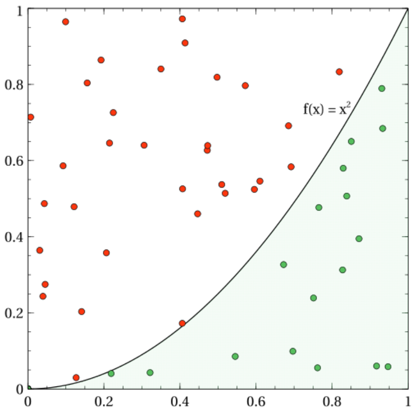

Figure 4.3: Estimation of the integral of $f(x) = x^2$ in $x \in [0, 1]$ from random throw Monte-Carlo. From [120].

techniques have been developed to minimise the computational waste, such as the semi-random walk MCMC method.

Any algorithm generating a new point x_i in the space of dimension D only based on the knowledge of x_{i-1} forms a Markov chain process. The lack of memory of the chain ensures its ability to converge to a stationary sampled distribution, at the condition of being *ergodic*, i.e. of being able to reach any point of the stationary distribution from any starting point (in multiple steps). Ergodicity can be attained by verifying the three following properties [122]:

- the chain is *irreducible*, i.e. it can eventually reach any step from any initial step;
- the chain is *aperiodic*, i.e. it does not returns periodically to the same step creating a loop passing only through a subsample of possible steps;
- the chain is *positively recurrent*, i.e. every step of the stationary distribution has a finite positive mean recurrence time at which it is visited by the chain, ensuring that the chain correctly samples the distribution once it reaches it.

The analysis performed in this thesis uses the Metropolis-Hastings algorithm [123] that fulfils the three ergodicity conditions to achieve the sampling of the target distribution $f(x)$. The algorithm walks in the parameter space of dimension D by obeying the following scheme:

0. Throw a first step randomly x_0 and compute $f(x_0)$.
1. Propose a new step with the jump function $J(x_{i+1}|x_i)$ [1] and compute $f(x_{i+1})$.
2. Compute the Metropolis ratio $r_{i+1} = \frac{f(x_{i+1})\ J(x_i|x_{i+1})}{f(x_i)\ J(x_{i+1}|x_i)}$.
3. Accept the step x_{i+1} according to the acceptance function: $A(x_{i+1}, x_i) = \min\{1, r_{i+1}\}$, which is equivalent to:
    (a) if $r_{i+1} > 1$, accept step x_{i+1};
    (b) if $r_{i+1} < 1$, throw a random number between 0 and 1 $U(0,1)$ and:
        - if $r_{i+1} \geq U(0,1)$, accept the step x_{i+1},
        - if $r_{i+1} < U(0,1)$, reject the step x_{i+1} and accept x_i again.
4. Start again from step 1.

---

[1] The jump function is also called proposal function in Bayesian literature.

The ability of the Metropolis-Hastings algorithm to sample the target distribution $f(x)$ emerges from the detailed balance condition. Defining the transition probability $T(x_{i+1}|x_i) = J(x_{i+1}|x_i) \times A(x_{i+1}, x_i)$ as the probability of arriving on the step x_{i+1}, and using the fact that the jump function is chosen to be symmetrical, the detailed balance equation can be derived:

$$f(x_i)\, T(x_{i+1}|x_i) \;=\; f(x_{i+1})\, T(x_i|x_{i+1}) \tag{4.3}$$

Equation (4.3) can be analysed in the following way: if the target function at the step x_{i+1} has a higher value than at the step x_i, i.e. $f(x_{i+1}) > f(x_i)$ then it will be automatically accepted and the transition probability is $T(x_{i+1}|x_i) = 1$. Therefore from the step x_{i+1}, the probability to go back to the step x_i is proportional to the ratio of target distribution values between the two steps: $T(x_i|x_{i+1}) = \frac{f(x_{i+1})}{f(x_i)}$. From the detailed balance equation it can be seen that the Metropolis-Hastings algorithm ensures that the chain will step with a frequency proportional to the target distribution, therefore correctly sampling it. The symmetrical jump function case forms the Metropolis algorithm, but the derivation has been extended to non-symmetrical jump functions by Hastings [123], forming the now known as Metropolis-Hastings algorithm. A striking feature lies in the algorithm always reaching the stationary sampled distribution regardless of the jump function chosen [124].

It can also be noted that MCMC has the advantage of being able to sample a distribution of any shape, contrarily to a minimisation likelihood method that could start risk being trapped in a local minimum. The non-zero probability to accept steps with lower posterior probability allows the Markov chain to escape local minima and give a correct coverage of the full target distribution.

4.1.3 Implementation for Bayesian inference

The paragraphs below explicit the implementation of the Metropolis-Hastings algorithm for the estimation of oscillation and nuisance parameters [125].

Target distribution: The target distribution to sample is the joint posterior probability of oscillation and nuisance parameters obtained with the Bayes theorem:

$$P(H(\vec{x})|D) = \frac{P(D|H(\vec{x}))\; P(H(\vec{x}))}{P(D)} \qquad \|M \tag{4.4}$$

where $P(H(\vec{x})|D)$ is the posterior probability of the hypothesis $H(\vec{x})$ given the data D, $P(D|H(\vec{x}))$ is the probability of obtaining the data D in the hypothesis $H(\vec{x})$, $P(H(\vec{x}))$ is the prior probability on the hypothesis $H(\vec{x})$ and $P(D)$ is the probability of the data D irrespectively of any hypothesis such as $P(D) = \int P(D|H(\vec{x}))P(H(\vec{x}))dH(\vec{x})$. The notation $\|M$ represents the prior information I included on the model M used, replacing the common writing $P(H(\vec{x})|D, I)$ for the convenience of the reader [126]. The hypothesis $H(\vec{x})$ is parametrised in the MC simulation used to predict the number of events at Super-K. The free parameters $\vec{x}$ of the MC model are the oscillation parameters $\vec{o}$, but also the nuisance parameters impacting the number of events, i.e. the flux parameters from the beam simulation described in Section 3.1.1 $\vec{b}$, the interaction parameters $\vec{i}$, and the detector uncertainty parameters $\vec{d}$.

The posterior probability needs to be evaluated by comparing the different shapes and normalisations of data and MC event distributions for the Super-K and ND280 samples described in Section 4.2. Consequently, events are stored in histograms and $P(D|H(\vec{x}))$ is a binned Poisson log-likelihood ratio of equation:

$$\begin{aligned} P(D|H(\vec{x})) = & \sum_{i}^{B\ bins} N_i^H - N_i^D + N_i^D \ ln\left(\frac{N_i^D}{N_i^H}\right) \\ & + \frac{1}{2} \sum_{j}^{\substack{o,b,i,d \\ pars}} \sum_{k}^{\substack{o,b,i,d \\ pars}} \Delta(o,b,i,d)_j \ (V^{-1}_{o,b,i,d})_{j,k} \ \Delta(o,b,i,d)_k \end{aligned} \tag{4.5}$$

where the first term is the binned Poisson log-likelihood ratio involving the number of data events N_i^D and the number of MC events N_i^D per bin i, and the second term a penalty term on the log-likelihood ratio with $V_{o,b,i,d}$ is the covariance matrix and $\Delta(o,b,i,d) = (o,b,i,d)_j - (o,b,i,d)_0$ is the difference between the value of the parameter at the throw $(o,b,i,d)_j$ and the prior value of the parameter $(o,b,i,d)_0$.

The prior probability of Equation (4.4) must carry as little information as possible on the oscillation parameters of interest: $\sin^2\theta_{23}$, Δm^2_{32}, $\sin^2\theta_{13}$ and $\delta_{\rm CP}$, it is therefore chosen to be uniform to not induce a preference for certain value(s). However the analysis is also performed assuming the reactor neutrino experiment value on $\sin^2\theta_{13}$ with a Gaussian prior. A study of the impact of the priors on the measurements is presented on Chapter 6. The prior probabilities of the nuisance parameters represent the prior knowledge as described Section 4.3, and are chosen to be a Gaussian with means and standard deviations the parameter prior values and uncertainties respectively.

Jump function: At every step i of the Markov chain, a new set of parameters $\vec{x_i}$ is proposed using the jump function. $J(x_{i+1}|x_i)$ is chosen to be a multivariate Gaussian of dimension $6 + 751$. The mean of the Gaussian is the value of the parameter at the step i, and its standard deviation is the prior uncertainty on the parameter multiplied by a scaling factor. The standard deviation of the jump function is called the step size, as it is the mean distance in the parameter space crossed by the chain when proposing x_{i+1}. The step size is a crucial parameter to estimate the convergence of the Markov chain towards the target distribution to sample in the available computational time. Appendix A presents in more details convergence studies and the impact of the step size on the analyses presented in the next chapters.

New step hypothesis: At every step proposed, the hypothesis corresponding the set of parameters proposed must be computed. However, the modification of the model cannot require to run a new full simulation at every step as it is too computationally expensive. Instead, it is obtained using a reweighting method: each MC event is multiplied by a factor mimicking the variation on the event distribution induced by a variation of the parameter. The oscillation weights are obtained using the Prob3++ software library [127]. The systematic weights have many origins, and their computation is outlined in Section 4.3.

Interval estimation: The Markov chain output contains the joint posterior probability $P(H(\vec{x})|D)$ in $6 + 751$ dimension. The posterior probability for a certain set of parameters, for example for the single parameter $x \in \vec{x}$ is obtained by projecting the values of $P(H(\vec{x})|D)$ as a function of x in a histogram. The resulting distribution integrates over the nuisance parameters, as the histogram content can be written [126]:

$$P(x|D) = \int P(x, (\vec{x'})|D)\ d\vec{x'} \qquad ||M \tag{4.6}$$

where $\vec{x'}$ is the vector of parameters $\vec{x}$ without the estimated parameter x. This process is called *marginalisation*, and has for effect to include the shape of the marginalised parameters distributions on the estimation of the marginalised posterior probability as shown on Figure 4.4a. The top figure shows the posterior probability distribution density in the $\sin^2\theta_{23}$-$\sin^2\theta_{13}$ space obtained after a fit of MC Super-K and data ND280 events as a blue

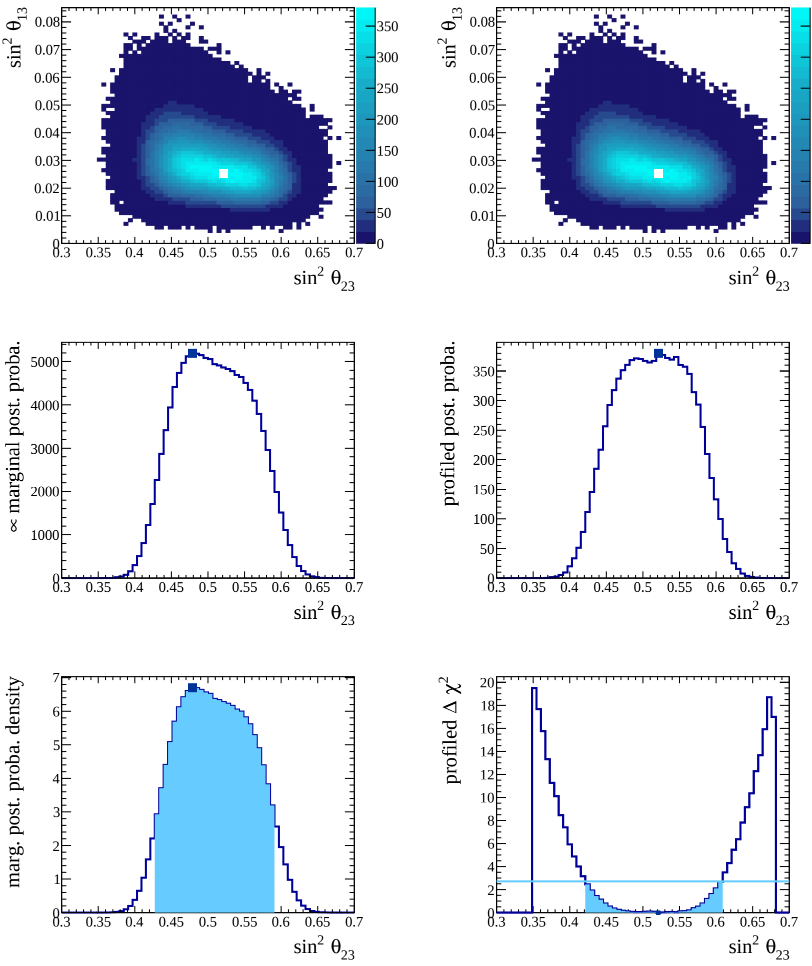

(a) Marginalisation.

(b) Profiling.

Figure 4.4: Example of marginal and profiled posterior probability from a non-Gaussian two-dimensional posterior probability density. The Markov chain includes real ND280 and simulated Super-K data. The top figures show the posterior probability distribution density in the $\sin^2\theta_{23}$-$\sin^2\theta_{13}$ space as a blue gradient, with the maximal posterior probability density displayed with a square marker. The middle figures show the projection (4.4a) or the profile (4.4b) of the two-dimensional posterior probability. The bottom figures show the 90% intervals as determined from counting the area of most probability (4.4a) or by comparing the $\Delta\chi^2$ distribution to the relevant χ^2 value, here shown as a blue line (4.4b).

gradient, with the maximal posterior probability density displayed with a square marker. The middle figure shows the projection of the 2-dimensional posterior probability along the $\sin^2\theta_{23}$ axis, which is proportional to the marginal posterior probability, and where it can see that the shape of the distribution includes the $\sin^2\theta_{13}$ uncertainty density. The bottom figure shows the histogram scaled to the marginal posterior probability density. The Credible Interval (CI), i.e. the interval in which there is a certain probability that the true value lie inside, is shown on the bottom figure as a blue area. It is directly computed by summing the most populated bins of the sampled posterior probability until reaching the level of credibility desired (e.g. 90% of entries for a 90% CI).

Marginalisation differs from the action of *profiling* shown on Figure 4.4b that consists in finding the highest probability for every value of $\sin^2\theta_{23}$ [128]. This method loses the information of the shape of the distribution of the non-plotted parameters, therefore it is not used in this thesis. However, it is often used in frequentist analysis, that convert the profiled likelihood into a $\Delta\chi^2$ distribution as shown on the bottom figure, and evaluate the interval from the intersection of the $\Delta\chi^2$ distribution with the χ^2 value corresponding to the desired probability coverage. The comparison is shown to illustrate the intervals provided by different analyses.

Parameter estimation: The best fit point is chosen to be the mode of the distribution, shown as a square in Figure 4.4. Marginalisation can lead to a displacement of the best fit point when reducing the number of dimensions by integrating the distribution of the parameters. On Figure 4.4a, the mode of the distribution is displaced towards lower $\sin^2\theta_{23}$ due to the integration of the $\sin^2\theta_{13}$ uncertainty density. On the contrary, when profiling the mode of the distribution is the same independently of the dimension used, and is found for the same $\sin^2\theta_{23}$ values on the top and middle figures of Figure 4.4b.

Hypothesis testing: Two hypothesis can be compared in the Bayesian framework from their posterior odds, i.e. their ratio of probabilities of equation:

$$\frac{P(H_1(\vec{x})|D)}{P(H_2(\vec{x})|D)} = \frac{P(D|H_1(\vec{x}))\;P(H_1(\vec{x}))}{P(D|H_2(\vec{x}))\;P(H_2(\vec{x}))} = B_{1/2}\frac{P(H_1(\vec{x}))}{P(H_2(\vec{x}))} \qquad \|M \quad (4.7)$$

where the ratio of likelihood $B_{1/2}$ is called the *Bayes factor*. If the prior are the same (e.g. comparing two areas of possible values for a parameter), the prior odds are reduced to the Bayes factor and it can be computed by directly taking the ratio of the number of steps in each area. A Bayes factor larger than 6 starts to indicate evidence, considered as strong for values higher than 10 [129].

4.2 Event selection

At the time the analyses presented in this thesis have been performed, seven runs of T2K took place. The amount of Protons On Target (POT) sent at each run is summarised in Table 4.1. The POT is not proportional to the run length, as the beam power has gradually increased during the run periods up to the maximal value of 425 kW as shown in Figure 4.5.

run period	***dates***	***ν-mode POT* ($\times 10^{20}$)**	***$\bar{\nu}$-mode POT* ($\times 10^{20}$)**
Run 1	Jan. 2010 - Jun. 2010	0.323	–
Run 2	Nov. 2010 - Mar. 2011	1.108	–
Run 3	Mar. 2012 - Jun. 2012	1.579	–
Run 4	Oct. 2012 - May 2013	3.560	–
Run 5	May 2014 - Jun. 2014	0.242	0.506
Run 6	Nov. 2014 - Jun. 2015	0.190	3.505
Run 7	Feb. 2016 - May 2016	0.480	3.460
Total	**Jan. 2010 - May 2016**	**7.482**	**7.471**

Table 4.1: Description of the seven T2K runs completed before 2017, with their duration, POT in ν-mode and $\bar{\nu}$-mode.

Section 4.2.1 described the selection of events in ND280, while Section 4.2.2 describes the selection in Super-K.

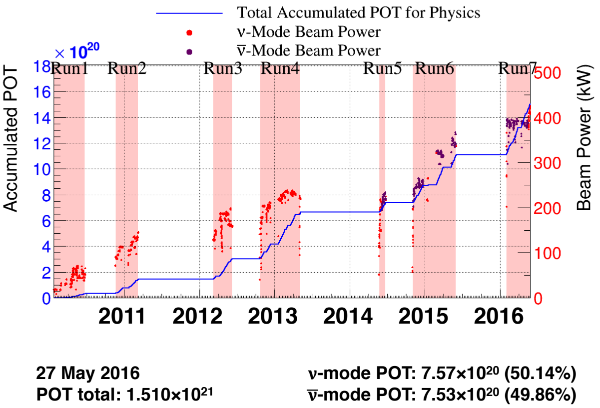

Figure 4.5: Accumulated POT and beam power in the different T2K runs.

4.2.1 ND280

The ND280 data are selected from $5.82 \cdot 10^{20}$ POT (runs 2, 3 and 4) in ν-mode and $2.84 \cdot 10^{20}$ (runs 5 and 6) in $\bar{\nu}$-mode. The selection strategy is optimised to select $\overset{(-)}{\nu}_\mu$ CC interactions in the two FGD with the list of cuts described in Table 4.2. The first section of the column refers to the selection of a *CC-inclusive* (*CC-inc*) sample from data obtained during normal operation of the detector (cut 1) and with a delay inferior to 60 ns from the bunch time (cut 2). As the TPCs provide PID and momentum estimation, it is required that at least one of the particles created in the interaction generates a track in the TPC with more than 18 hits to ensure a proper reconstruction (cut 4). The reconstruction algorithm fits cluster of hits in the TPC and progressively adds hits in the upstream FGD (starting from the downstream edge) to form TPC-FGD tracks. The first hit of the track is defined as the interaction point and must be located inside the FGD Fiducial Volume (FV) to be selected (cut 3). The TPC-FGD track is a candidate track if has the highest momentum amongst all tracks, and a curvature corresponding to a negative (ν_μ CC selection) or a positive particle ($\bar{\nu}_\mu$ CC selection) (cut 5). The FV geometry is defined with the goal of rejecting background events originating outside the FGD and consists of the FGD volume subtracting the (two) first layer(s) for FGD2(1) and 5.7 cm from each x and y edges. To ensure that tracks originate in the selected FGD, the event is rejected if a track is present in the upstream in TPC, or in the FGD1 when selecting in FGD2 (cut 6). Some tracks, notably at high angle, undergo failure during the matching reconstruction and appear as two tracks. In order to avoid to select the TPC-FGD track as the candidate track and ignore the FGD-only track, the TPC-FGD track must not start in the last two layers of the FGD when a FGD-only track is present (cut 7). The *CC-inclusive* sample is obtained after obtaining a TPC track dE/dx likelihood compatible with the $\mu^{\pm}$ hypothesis (cut 8).

modes	***sample***	**#**	***cut***
ν-mode & $\bar{\nu}$-mode	$CC-inc.$	1	data quality
		2	bunching
		3	FGD track multiplicity and FV
		4	TPC quality
		5	highest momentum negative/positive track
		6	backward going tracks
		7	broken FGD track
		8	muon PID
ν-mode	CC-0π	9a	rejects if $\pi^{\pm}$ or $e^{\pm}$ in TPC or decay e^{-} or $\pi^{\pm}$ FGD
	CC-$1\pi^{+}$	9b	rejects if π^{-} or $e^{\pm}$ in TPC selects if π^{+} in TPC and decay e^{-} or π^{+} in FGD
	$CC-oth.$	9c	selects if $e^{\pm}$ or π^{-} in TPC or > 1 π^{+} in TPC and decay e^{-}
$\bar{\nu}$-mode	$CC-1tr.$	9d	rejects if $\pi^{\pm}$ or $e^{\pm}$ in TPC or decay $e^{\pm}$ or $\pi^{\pm}$ FGD
	$CC-Ntr.$	9e	selects all events except those in $CC-1tr.$

Table 4.2: Description of the cuts used to select the ND280 samples used in the fit. The *CC-inclusive* (*CC-inc*) sample is broken down in subsambles with the cuts 9a to 9e.

The *CC-inclusive* samples are selected for the ν_{μ} CC events in ν-mode, $\bar{\nu}_{\mu}$ CC events in $\bar{\nu}$-mode, and ν_{μ} CC events in $\bar{\nu}$-mode. If only one ν_{μ} sample is necessary in ν-mode due to the little amount of $\bar{\nu}_{\mu}$ contamination (as seen in Figure 3.3), the ν_{μ} content in $\bar{\nu}$-mode is much higher and must be constrained in ND280 as the Cherenkov technique used in Super-K cannot determine the charge of particles. The three inclusive samples are broken down in subsamples according to their track topology in order to constrain specific parameters of the interaction model. The subsamples are described in the paragraphs below and their muon momentum distributions are shown in Figure 4.6 with their interaction compositions.

- **$\boldsymbol{\nu_\mu}$ in $\boldsymbol{\nu}$-mode $\boldsymbol{CC\text{-}0\pi}$:** The CC-0π sample is obtained by selecting events presenting only one TPC-FGD track compatible with a μ^- hypothesis (cut 9a). No sign of decay electron nor FGD contained $\pi^\pm$ must be seen. The sample is mainly composed of ν_μ CCQE interactions and holds the highest content of MEC (2p-2h) interactions.

- **$\boldsymbol{\nu_\mu}$ in $\boldsymbol{\nu}$-mode $\boldsymbol{CC\text{-}1\pi}$:** The CC-1π sample is obtained by selecting events with a TPC-FGD track compatible with a μ^-, plus a unique π^+ track in the TPC or FGD or a decay e^- (from μ^-) must be present (cut 9b). If a π^- or a $e^\pm$ not originating from $\mu^\pm$ decay is present in the TPC, the event is vetoed. This sample mainly contains CC-Resonant (Res) events producing π^+, as well as a certain amount of CC-Coherent (Coh) events.

- **$\boldsymbol{\nu_\mu}$ in $\boldsymbol{\nu}$-mode *CC-other*:** The *CC-other* sample is obtained by selecting all the tracks from the *CC-inclusive* samples that did not enter the CC-0π and CC-1π criteria (cut 9c). This includes track with a μ^- candidate in the TPC plus a a π^- or a $e^\pm$, or the presence of several π^+, or the presence of one π^+ and a decay e^-. This sample mainly contains CC-DIS and multipion interactions.

- **$\boldsymbol{\bar{\nu}_\mu}$ in $\boldsymbol{\bar{\nu}}$-mode $\boldsymbol{CC\text{-}1track}$:** The CC-$1track$ sample is analogous to the CC-0π sample but for the $\bar{\nu}$-mode. The TPC-FGD track must be compatible with a μ^+ hypothesis and no decay electron nor FGD contained $\pi^\pm$ must be seen (cut 9d). The sample is mainly composed of $\bar{\nu}_\mu$ CCQE interactions and some MEC (2p-2h) interactions.

- **$\boldsymbol{\bar{\nu}_\mu}$ in $\boldsymbol{\bar{\nu}}$-mode $\boldsymbol{CC\text{-}Ntrack}$:** The CC-$Ntrack$ samples contains the equivalent of both CC-1π and *CC-other* samples but for the $\bar{\nu}$-mode. In practice, all *CC-inclusive* events that do not enter the CC-$1track$ sample criteria fill this sample (cut 9e). The sample is mainly composed of $\bar{\nu}_\mu$ CC-Res and CC-DIS interactions.

- **$\boldsymbol{\nu_\mu}$ in $\boldsymbol{\bar{\nu}}$-mode $\boldsymbol{CC\text{-}1track}$:** The CC-$1track$ sample is analogous to the CC-0π sample but for the ν_μ contamination in $\bar{\nu}$-mode. The TPC-FGD track must be compatible with a μ^- hypothesis and no decay positron nor FGD contained $\pi^\pm$ must be seen (cut 9d). The sample is mainly composed of ν_μ CCQE interactions and some MEC (2p-2h) interactions.

- **$\boldsymbol{\nu_\mu}$ in $\boldsymbol{\bar{\nu}}$-mode $\boldsymbol{CC\text{-}Ntrack}$:** The CC-$Ntrack$ sample follows the same criteria than the $\bar{\nu}_\mu$ in $\bar{\nu}$-mode CC-$Ntrack$ sample (cut 9e), but for the ν_μ

contamination in $\bar{\nu}$-mode, i.e. all *CC-inclusive* events that do not enter the CC-1$track$ sample criteria fill this sample (cut 9e). The sample is mainly composed of ν_μ CC-Res and CC-DIS interactions.

The CC-1π and *CC-other* samples are merged into the CC-$Ntrack$ category for the $\bar{\nu}$-mode samples as there are not enough events in each category to satisfyingly separate the modes in the analysis. The lower number of events arise from the fact that not only the $\bar{\nu}$-mode POT analysed is about half the ν-mode POT, but also because the $\bar{\nu}_\mu$ CC cross-section is more than three times smaller than the ν_μ CC cross-section as shown in Figure 3.9, leading to an effective number of selected events much lower in $\bar{\nu}$-mode than ν-mode. The total number of expected and selected events for each sample is summarised in Table 4.3. The discrepancies between the predicted and observed numbers of events explicit the limitation of the flux, interaction and detector models, and voice for a better estimation that will be obtained from the analysis of these data.

mode	***sample***	***detector***	***predicted number of events***	***selected number of events***
ν-mode ν_μ	CC-0π	FGD1	16950.81	17354
		FGD2	17211.71	17650
	CC-1π	FGD1	4460.15	3984
		FGD2	3616.62	3383
	$CC - oth.$	FGD1	4009.78	4220
		FGD2	3626.56	4118
$\bar{\nu}$-mode ν_μ	$CC - 1tr.$	FGD1	2708.65	2663
		FGD2	2729.88	2762
	$CC - Ntr.$	FGD1	797.73	775
		FGD2	804.45	737
$\bar{\nu}$-mode $\bar{\nu}_\mu$	$CC - 1tr.$	FGD1	938.13	989
		FGD2	943.90	980
	$CC - Ntr.$	FGD1	995.33	1001
		FGD2	916.61	936

Table 4.3: Predicted (MC) and selected (data) number of events in the FGD1 and FGD2 for ND280 $\overset{(-)}{\nu}_\mu$ CC sample.

The ND280 samples are included in the Markov chains to provide a constraint on the flux and cross-section models parameters described in Section 4.3. The different interaction modes lead to different muon distributions in momentum and angle. Therefore, the likelihood is computed for $p_\mu - \cos\theta_\mu$ histograms, as shown in Figure 4.7 for the data events selected in FGD2. The following bin edges are used:

- **ν-mode *CC-0π*, *CC-other*** :

- p_μ: 0, 0.3, 0.4, 0.5, 0.6, 0.7, 0.8, 0.9, 1.0, 1.25, 1.5, 2.0, 3.0, 5.0, 30.0 $\mathrm{GeV}\cdot\mathrm{c}^{-1}$;
- $\cos\theta_\mu$: -1.0, 0.6, 0.7, 0.8, 0.85, 0.9, 0.92, 0.94, 0.96, 0.98, 0.99, 1.0.

- **ν-mode *CC-1π*** :

- p_μ: 0, 0.3, 0.4, 0.5, 0.6, 0.7, 0.8, 0.9, 1.0, 1.25, 1.5, 2.0, 5.0, 30.0 $\mathrm{GeV}\cdot\mathrm{c}^{-1}$;
- $\cos\theta_\mu$: -1.0, 0.6, 0.7, 0.8, 0.85, 0.9, 0.92, 0.94, 0.96, 0.98, 0.99, 1.0.

- **$\bar{\nu}$-mode *CC-1track*** :

- p_μ: 0, 0.5, 0.9, 1.2, 2.0, 10.0 $\mathrm{GeV}\cdot\mathrm{c}^{-1}$;
- $\cos\theta_\mu$: -1.0, 0.8, 0.92, 0.98, 1.0.

- **$\bar{\nu}$-mode *CC-Ntrack*** :

- p_μ: 0, 0.6, 1.0, 1.5, 2.2, 10.0 $\mathrm{GeV}\cdot\mathrm{c}^{-1}$;
- $\cos\theta_\mu$: -1.0, 0.8, 0.9, 0.97, 1.0.

ν-mode ***$\bar{\nu}$-mode***

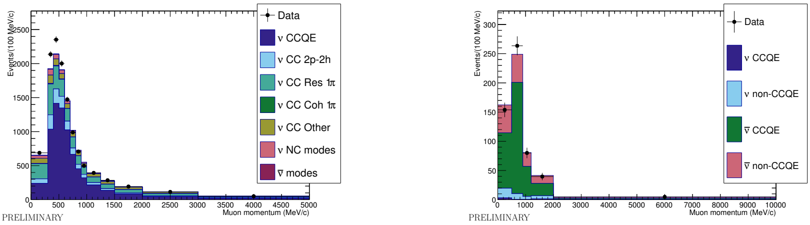

(a) ν_μ *CC-*0π **(d)** $\bar{\nu}_\mu$ *CC-1track*

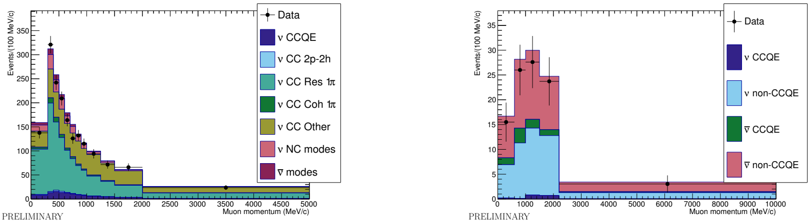

(b) ν_μ *CC-*1π **(e)** $\bar{\nu}_\mu$ *CC-Ntrack*

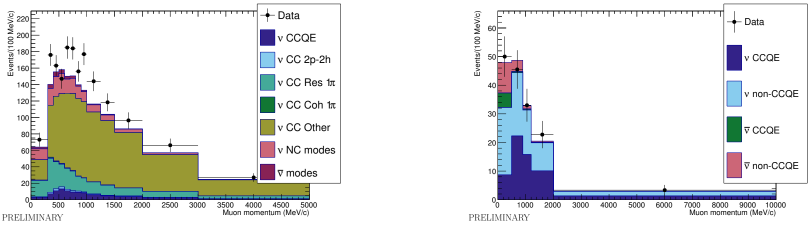

(c) ν_μ *CC-other* **(f)** ν_μ *CC-1track*

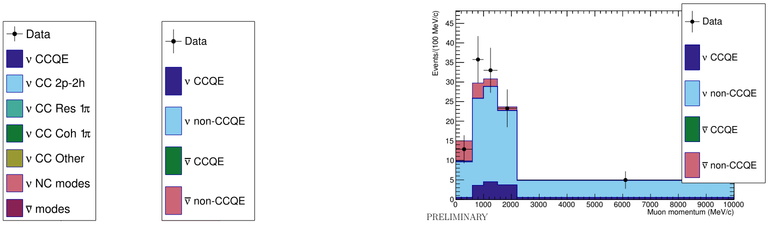

(g) ν_μ *CC-Ntrack*

Figure 4.6: Distribution of the events selected in the FGD2 of ND280 as a function of the $\mu^\pm$ momentum. The stacked histograms represent the simulated data with the different interaction modes separated, and the points are the real data. The x-axis shows the muon momentum p_μ (in $\mathrm{MeV} \cdot \mathrm{c}^{-1}$) and the y-axis shows the number of events per bin. The left column shows the ν-mode samples and the right column the $\bar{\nu}$-mode ones.

ν-mode ***$\bar{\nu}$-mode***

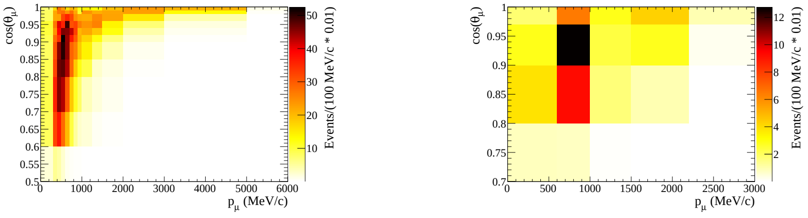

(a) ν_μ CC-0π **(d)** $\bar{\nu}_\mu$ CC-$1track$

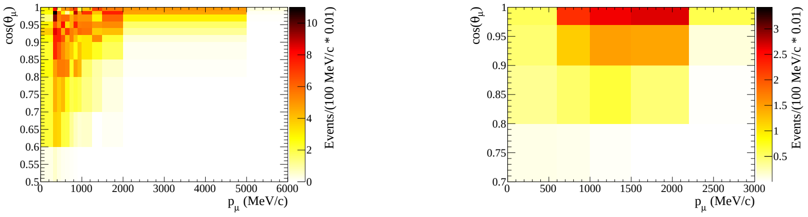

(b) ν_μ CC-1π **(e)** $\bar{\nu}_\mu$ CC-$Ntrack$

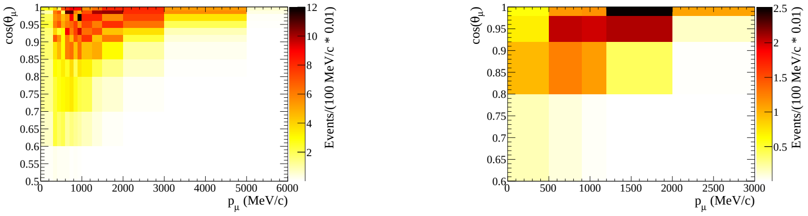

(c) ν_μ CC-$other$ **(f)** ν_μ CC-$1track$

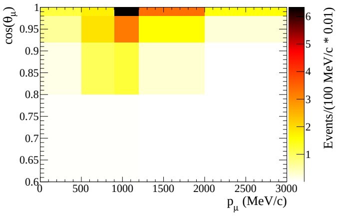

(g) ν_μ CC-$Ntrack$

Figure 4.7: Distribution of the events selected in the FGD2 of ND280 as a function of the $\mu^{\pm}$ momentum and cosine of the angle. The x-axis shows the muon momentum p_μ (in $\mathrm{MeV} \cdot \mathrm{c}^{-1}$) and the y-axis shows $\cos\theta_\mu$. The left column shows the ν-mode samples and the right column the $\bar{\nu}$-mode ones.

4.2.2 Super-Kamiokande

The Super-K data are selected from $7.482 \cdot 10^{20}$ POT (runs 1 to 7) in ν-mode and $7.471 \cdot 10^{20}$ (runs 5 to 7) in $\bar{\nu}$-mode. CCQE events produce only two outgoing particles: a nucleon under the Cherenkov threshold in a majority of events, and a charged lepton producing a Cherenkov ring in the detector. The neutrino energy E_ν^{rec} can be inferred from the kinematics information of the lepton ℓ as shown on Equation (4.8) for a neutrino interacting with a neutron n:

$$E_\nu^{rec}|_{CC\text{-}0\pi} = \frac{m_p - (m_n - E_B)^2 - m_\ell^2 + 2(m_n - E_B)E_\ell}{2(m_n - E_B - E_\ell + p_\ell \cos\theta_\ell)} \tag{4.8}$$

where m_p is the mass of the proton, m_n is the mass of the neutron assumed to be at rest (m_ν is neglected), E_B is the binding energy of the nucleus (here oxygen), m_ℓ, p_ℓ and θ_ℓ are respectively the mass, 3-momentum and angle of the outgoing lepton. As the neutrino oscillation probability depends on the neutrino energy, and p_ℓ can be determined from the thickness of the Cherenkov ring, the selection aims at creating samples of $\overset{(-)}{\nu}_\mu$ and $\overset{(-)}{\nu}_e$ CCQE events Fully Contained (FC) in the FV (FCFV) of Super-K. In order to increase the statistical power of the fit, a sample of FCFV ν_e CC-$1\pi^\pm$ production events is added, where the neutrino energy is computed assuming a resonant interaction:

$$E_\nu^{rec}|_{CC\text{-}1\pi} = \frac{2m_pE_\ell + m_\Delta^2 - m_p^2 - m_\ell^2}{2(m_p - E_\ell + p_\ell \cos\theta_\ell)} \tag{4.9}$$

where m_Δ is the mass of the Δ^{++} resonance.

The FCFV sample is obtained using the cuts on the upper part of Table 4.4. Events starting outside the ID, such as cosmic rays or interactions in the rocks, are considered background and rejected on the basis that they light at least 15 OD PMTs (cut 1). Events starting inside the ID must create at least 200 p.e. in ID PMTs in less than 0.3 µs, but if a single ID PMT sees more than half the total of p.e. the event is considered as noise and rejected (cut 2). Events are ensured to originate from beam neutrinos by requesting a time offset Δt to the bunch time of less than -2 µs and not bigger than $+10$ µs (cut 3). The event must start inside the Super-K FV, defined as the volume inside the ID when excluding 2 m starting from the walls (cut 4). The visible energy E_{vis}, computed as Cherenkov light emitted by an electromagnetic shower, must be greater than 30 MeV (cut 5) but only one Cherenkov ring must be seen (cut 6), including for the CC-$1\pi^{\pm}$ production sample. Consequently, the $\pi^{\pm}$ produced must be under the Cherenkov threshold, leading to a selection of CC-$\pi^{\pm}$ events with neutrino of relatively low energy, therefore close to the oscillation peak.

sample	#	***cut***
FCFV	1	< 15 OD PMT
	2	> 200 p.e. in ID PMT in $t < 0.3\,\mu\text{s}$ and 50% of p.e. in > 1 ID PMT
	3	$\Delta t \in [-2; +10\,\mu\text{s}]$
	4	event in Super-K FV
	5	$E_{vis} > 30\,\text{MeV}$
	6	$= 1$ Cherenkov ring
$R_{\overset{(-)}{\mu}}$ CC-0π	7a	$\mu^{\pm}$ PID and $p_{\mu}^{rec} > 200\,\text{MeV}$ and ≤ 1 $e^{\pm}$ decay
$R_{\overset{(-)}{e}}$ CC-0π	7b	$e^{\pm}$ PID and $E_{vis} > 100\,\text{MeV}$ and $E_{\nu}^{rec} < 1.25\,\text{GeV}$ no π^{0} and no $e^{\pm}$ decay
R_e CC-$1\pi^{\pm}$	7c	$e^{\pm}$ PID and $E_{vis} > 100\,\text{MeV}$ and $E_{\nu}^{rec} < 1.25\,\text{GeV}$ no π^{0} but 1 e^{-} decay

Table 4.4: Description of the cuts used to select the Super-K samples used in the fit. The FCFV sample is broken down in subsambles with the cuts 7a to 7c. The cuts are the same for ν-mode and $\bar{\nu}$-mode, $R_{\overset{(-)}{\mu}}$ and $R_{\overset{(-)}{e}}$ referring to muon and electron rings respectively in both modes.

The FCFV sample contains CC events, separated into CCQE interactions from $\overset{(-)}{\nu}_{\mu}$ that did not oscillate, and CCQE and CC$1\pi^{+}$ interactions from $\overset{(-)}{\nu}_{e}$ originating from $\overset{(-)}{\nu}_{\mu}$ oscillation. The five subsamples (three in ν-mode and two in $\bar{\nu}$-mode) are selected as defined below, the cuts being the same for ν-mode as for $\bar{\nu}$-mode as the Cherenkov technique does not bring information about the electric charge of the particle.

- ***CC*-0*π* R_{μ} in *ν*-mode and $R_{\bar{\mu}}$ in $\bar{\nu}$-mode:** The muon ring samples are selected by requesting a visible energy higher than 200 MeV, the minimum energy for $\mu^{\pm}$ to create a Cherenkov ring. The PID of the particle emitting the ring is determined from a fit taking into account the charge distribution and the opening angle of the Cherenkov cone [130] and must be compatible with a muon. The muon may decay into an electron, detected from a delayed peak in the hit distribution of the ID PMT [14], and the event is rejected if more than one decay electron is tagged to reject CC-$1\pi^{\pm}$ production events.

- **CC-0π R_e in ν-mode and $R_{\bar{e}}$ in $\bar{\nu}$-mode:** The electron ring samples are selected on the basis that PID is consistent with an electron, but rejecting events with visible energy lower than 100 MeV as they have been found to mainly originate from NC or particle decay. The reconstructed energy must be lower than 1.25 GeV as it has been found that above this energy, the selection only contained background. No decay electron must be seen, and the hypothesis that the ring has been created by a π^0 decay must be rejected.
- **CC-$1\pi^{\pm}$ R_e in ν-mode:** The CC-$1\pi^{\pm}$ electron rings sample is selected using the same cuts than the CC-0π electron rings sample, except that one decay electron must be detected. As it is a subsample of the FCFV selection requiring only one Cherenkov ring to be seen, the ring corresponds to the electron produced in the interaction and the pion remain under the Cherenkov threshold, being only tagged from the decay electron itself emitted by the decay of the muon emitted by the pion decay.

The predicted number of events in each sample has been computed in the case where no oscillation occurs, and for the oscillated case using the parameters values in Table 4.5 where the priors used to evaluate the posterior probability are also indicated. The prior values and uncertainties of $\sin^2\theta_{12}$ and Δm^2_{21} are the output of the solar neutrino data and KamLAND fit of [41] mentioned in Section 2.3.2. The $\sin^2\theta_{23}$, Δm^2_{32} and δ_{CP} values are the best fit values of the T2K ν-mode $R_\mu + R_e$ fit of [130] that notably found δ_{CP} close to the maximal CP violation value $\delta_{\mathrm{CP}}^{\mathrm{max\ CP}} = -\frac{\pi}{2}$. Finally, $\sin^2\theta_{13}$ prior value is the result of the PDG fit to reactor neutrino oscillation experiments, reporting $\sin^2 2\theta_{13} = 0.085 \pm 0.005$ [131].

osc. param.	***value***	***1σ prior uncertainty***
$\sin^2\theta_{12}$	0.304	0.05
Δm^2_{21}	$7.53\cdot10^{-5}\,\mathrm{eV}^2\cdot\mathrm{c}^{-4}$	$0.18\cdot10^{-5}\,\mathrm{eV}^2\cdot\mathrm{c}^{-4}$
$\sin^2\theta_{23}$	0.528	flat prior
Δm^2_{32}	$2.509\cdot10^{-5}\,\mathrm{eV}^2\cdot\mathrm{c}^{-4}$	flat prior
$\sin^2\theta_{13}$	0.0217	flat prior or 0.0013
δ_{CP}	-1.601 rad	flat prior

Table 4.5: Prior values of the oscillation parameters used to predict the expected number of events. The prior uncertainties used to compute the posterior probability with MCMC is also shown.

Table 4.6 shows the predicted number of events for each sample in the unoscillated and oscillated case, broken down by neutrino content: the beam ν_μ and $\bar{\nu}_\mu$ are signal events for the $R_{\overset{(-)}{\mu}}$ samples but background for the $R_{\overset{(-)}{e}}$ samples. The beam ν_e and $\bar{\nu}_e$ represent the intrinsic beam $\overset{(-)}{\nu}_e$ as shown in Figure 3.3 and must constrained with precision as they form a strong background to $\overset{(-)}{\nu}_e$ appearance due to oscillation in the $R_{\overset{(-)}{e}}$ samples. On the contrary, the oscillated ν_e and $\bar{\nu}_e$ are the $\overset{(-)}{\nu}_e$ originating from $\overset{(-)}{\nu}_\mu$ oscillation and are the signal content of the $R_{\overset{(-)}{e}}$ samples. A high contamination of ν_μ can be seen in the $R_{\bar{\mu}}$ sample: they represent $\sim 40\%$ of the events, the remaining $\sim 60\%$ being the $\bar{\nu}_\mu$ signal. This contamination is due to the high content of ν_μ present in the neutrino beam in $\bar{\nu}$-mode as shown in Figure 3.3d, which is enhanced by the ν_μ cross-section being ~ 3 times higher than the $\bar{\nu}_\mu$ one as shown in Figure 3.9. However, this contamination occurs at high energy and most $\bar{\nu}$-mode ν_μ do not oscillate into ν_e, as the oscillated ν_e contamination in the $R_{\bar{e}}$ sample is only $\sim 15\%$. Concerning the R_e CC-$1\pi^{\pm}$ sample, the unoscillated sample is mainly composed of ν_μ background from the beam. In the oscillated case, the expected amount of ν_e is not as high as the CC-0π sample as the resonant cross-section starts at higher energies as shown on Figure 3.9, and such interactions only constitute a small fraction of the expected oscillated events.

The ND280 data are of prime importance to evaluate the proportion of ν_μ and $\bar{\nu}_\mu$ in each mode, as the near detector is magnetised. In a first, a fit of the ND280 data has been performed to evaluate the constraints on the parameters of the flux and interaction models given by the near detector alone. The fit uses the five ND280 samples described in Section 4.2.1 to constrain the parameters in Section 4.3.1 and 4.3.2. The Super-K MC can be tuned afterwards to the results of the ND280 fit in order to estimate the expected number of events in the hypothesis where the nuisance parameters values are the post-ND280 fit ones. Table 4.7 shows the total expected number of events per sample when using the nominal Super-K MC (pre-ND280 fit MC) and when tuning it to the ND280-only fit results (post-ND280 fit MC). As shown on Table 4.3, more CCQE data events are detected in ND280 than predicted and the fit finds the CCQE parameters higher than the nominal values, while less CC-Res data events are detected than predicted and the corresponding post-ND280 fit parameters are lower than nominal. This translates in Table 4.7 by the post-ND280 fit prediction of CC-0π samples being higher than the pre-ND280 fit, while it is lower for the CC-$1\pi^{\pm}$ sample. However, it does not imply that the post-ND280 fit

sample		***beam***				***osc***		***Total***
		$\boldsymbol{\nu_\mu}$	$\boldsymbol{\nu_e}$	$\boldsymbol{\bar{\nu}_\mu}$	$\boldsymbol{\bar{\nu}_e}$	$\boldsymbol{\nu_e}$	$\boldsymbol{\bar{\nu}_e}$	
$\boldsymbol{R_\mu}$	unosc:	466.350	0.352	14.649	0.031	0.000	0.000	**481.381**
$\boldsymbol{CC\text{-}0\pi}$	osc:	120.819	0.348	8.291	0.031	0.346	0.002	**129.837**
$\boldsymbol{R_e}$	unosc:	2.243	3.388	0.085	0.163	0.000	0.000	**5.879**
$\boldsymbol{CC\text{-}0\pi}$	osc:	1.754	3.156	0.083	0.155	20.866	0.149	**26.163**
$\boldsymbol{R_e}$	unosc:	2.539	0.488	0.042	0.003	0.000	0.000	**3.072**
$\boldsymbol{CC\text{-}1\pi^\pm}$	osc:	0.409	0.455	0.017	0.003	2.696	0.001	**3.581**
$\boldsymbol{R_{\bar{\mu}}}$	unosc:	47.133	0.105	130.209	0.068	0.000	0.000	**177.516**
$\boldsymbol{CC\text{-}0\pi}$	osc:	25.973	0.105	36.279	0.068	0.019	0.035	**62.477**
$\boldsymbol{R_{\bar{e}}}$	unosc:	0.321	0.569	0.507	0.920	0.000	0.000	**2.317**
$\boldsymbol{CC\text{-}0\pi}$	osc:	0.295	0.533	0.470	0.867	0.949	2.700	**5.815**

Table 4.6: Predicted number of events for the five Super-K samples in the unoscillated and oscillated cases. The total is broken down for the different neutrino types: *beam* $\overset{(-)}{\nu}_\mu$ and $\overset{(-)}{\nu}_e$ are intrinsic content of the flux, while *osc.* $\overset{(-)}{\nu}_e$ are events originating from $\overset{(-)}{\nu}_\mu$ oscillation. The nominal Super-K MC and the oscillation parameters of Table 4.5 have been used.

prediction being more adequate with the number of data events observed: if the R_μ and $R_{\bar{\mu}}$ predictions are close to the expected number of events, more R_e events are seen than predicted while less $R_{\bar{e}}$ are detected than expected as shown on the lower part of the table.

Figure 4.8 shows the energy spectra of the five samples for the unoscillated case and when tuning the pre-ND280 fit Super-K MC to the oscillation parameters of Table 4.5. The Super-K data are also shown and are distributed around the oscillated spectra. The interaction content of the oscillated Super-K MC five samples is exhibited in Figure 4.9. The variation in the expected number of events according to the δ_{CP} value is shown in Table 4.8 with the Super-K MC tuned to the post-ND280 fit values. As δ_{CP} is only present in the $\overset{(-)}{\nu}_e$ appearance probability (and not in the $\overset{(-)}{\nu}_\mu$ disappearance probability), the variation in the number of events in the R_μ and $R_{\bar{\mu}}$ samples is small (the affected events being only the oscillated ν_e and $\bar{\nu}_e$ background content). The variation in the R_e and $R_{\bar{e}}$ samples is more consequent, as the number of events increases of $\sim 30\%$ of events for the ν-mode samples between $\delta_{\mathrm{CP}}= 0$ and $\delta_{\mathrm{CP}}= +\frac{\pi}{2}$, and a decreases of $\sim 30\%$

for the ν-mode sample between the two same δ_{CP} values.

	R_μ CC-0π	R_e CC-0π	R_e CC-$1\pi^\pm$	$R_{\bar{\mu}}$ CC-0π	$R_{\bar{e}}$ CC-0π
pre-ND280 fit MC	129.837	26.163	3.581	62.477	5.815
post-ND280 fit MC	136.214	28.748	3.217	64.404	6.011
data	135	32	5	66	4
data / MC (pre-ND280 fit)	1.22	1.40	1.04	1.06	0.69
data / MC (post-ND280 fit)	0.99	1.11	1.55	1.02	0.67

Table 4.7: Predicted total number of events for the five Super-K samples in the oscillated case (using the parameters of Table 4.5). Pre-ND280 fit MC refers to the nominal Super-K MC while post-fit MC refers to the Super-K MC tuned to the output of a ND280-only fit. The number of events detected is also shown as data, with the ratio to the expected number of events to evaluate the adequation of the measurement with the prediction.

sample	$\delta_{\text{CP}} = -\frac{\pi}{2}$	$\delta_{\text{CP}} = 0$	$\delta_{\text{CP}} = +\frac{\pi}{2}$	$\delta_{\text{CP}} = +\pi$
R_μ CC-0π	136.21	135.86	136.06	136.45
R_e CC-0π	28.68	24.17	19.61	24.13
R_e CC-$1\pi^{+/-}$	3.13	2.74	2.26	2.65
$R_{\bar{\mu}}$ CC-0π	64.40	64.26	64.42	64.57
$R_{\bar{e}}$ CC-0π	6.01	6.90	7.67	6.77

Table 4.8: Predicted total number of events for the five Super-K samples in the oscillated cases. The oscillation parameters used are from Table 4.5, except δ_{CP} that has been varied. The Super-K MC has been tuned to the post-ND280 fit results.

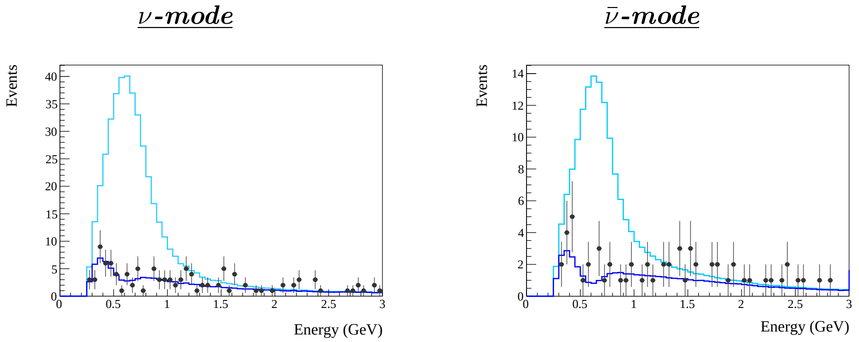

(a) R_μ CC-0π **(d)** $R_{\bar{\mu}}$ CC-0π

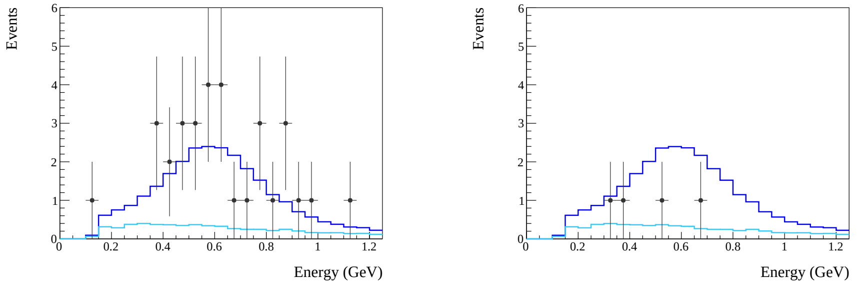

(b) R_e CC-0π **(e)** $R_{\bar{e}}$ CC-0π

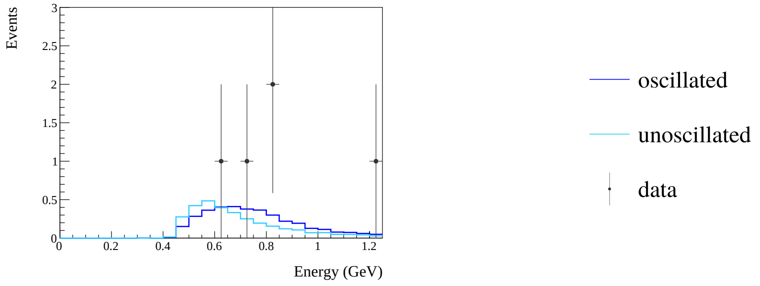

(c) R_e CC-$1\pi^\pm$

Figure 4.8: Energy spectra of the five Super-K samples in the unoscillated (light blue) and oscillated (dark blue) cases. The nominal MC and the oscillation parameters of Table 4.5 are used. The x-axis shows the neutrino reconstructed energy (in GeV) and the y-axis the number of events per bin. The left column shows the ν-mode samples and the right column the $\bar{\nu}$-mode ones, and the Super-K data are also shown.

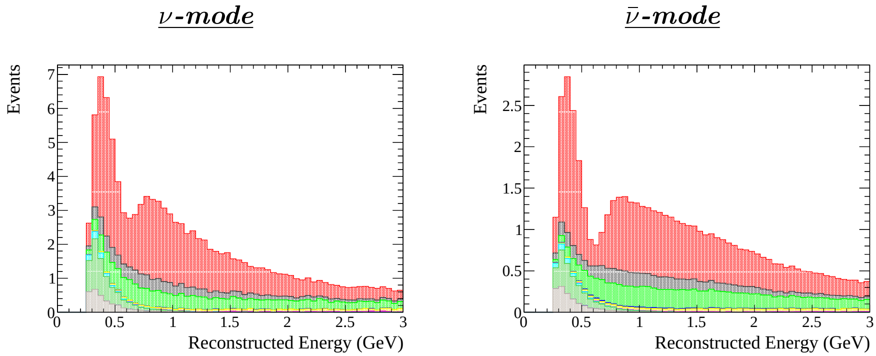

(a) R_{μ} CC-0π **(d)** $R_{\bar{\mu}}$ CC-0π

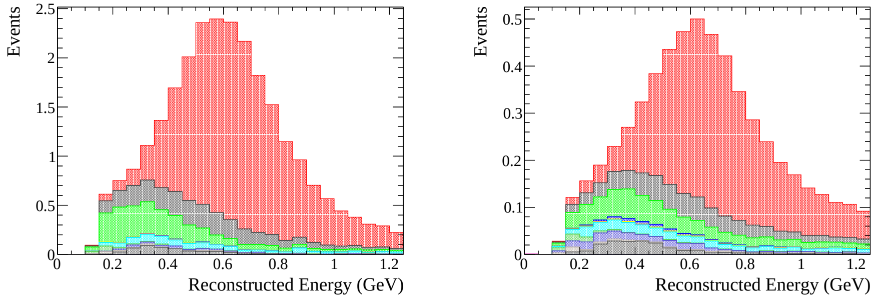

(b) R_{e} CC-0π **(e)** $R_{\bar{e}}$ CC-0π

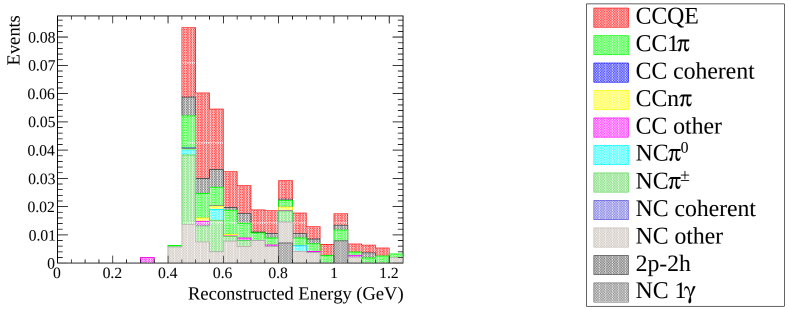

(c) R_{e} CC-$1\pi^{\pm}$

Figure 4.9: Predicted energy spectra of the five Super-K samples in the oscillated case with the interaction modes contents. The nominal MC and the oscillation parameters of Table 4.5 are used. The x-axis shows the neutrino reconstructed energy (in GeV) and the y-axis the number of events per bin. The left column shows the ν-mode samples and the right column the $\bar{\nu}$-mode ones.

The main goal of the Super-K samples is to provide constaints on the U_{PMNS} parameters. As the oscillation probability depends on the neutrino energy, all samples are fitted as a function of the reconstructed neutrino energy E_{ν}^{rec}. The Poisson likelihood is computed for E_{ν}^{rec} histograms only for muon rings samples, while information on the lepton angle θ_e is added for electron rings samples as shown on the $E_{\nu}^{rec} - \theta_{\ell}$ histograms of Figure 4.10. Adding the electron angle information enables better separation of NC interactions from CC interactions, as the former produces more forward electrons than the latter as shown on the left column of Figure 4.11. The $\bar{\nu}$ cross-section creates antileptons more forward-focused than the leptons produced in ν interactions, therefore adding the angle variable leads to better disentangle the ν_e content from the ν_e content in the $R_{\overset{(-)}{e}}$ sample as

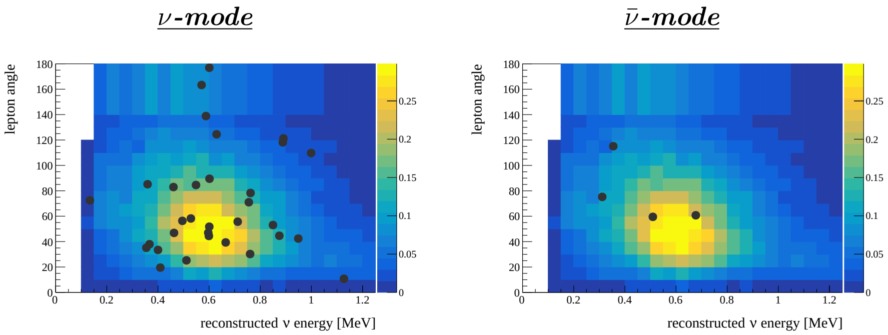

(a) R_e CC-0π **(c)** $R_{\bar{e}}$ CC-0π

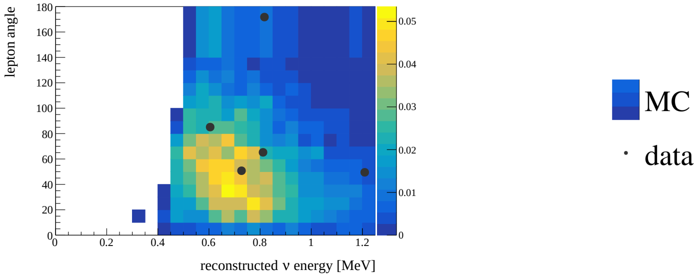

(b) R_e CC-$1\pi^{\pm}$

Figure 4.10: Distribution of the three electron rings sample as a function of the reconstructed energy (x-axis) and electron angle (y-axis). The left column shows the ν-mode samples and the right column the $\bar{\nu}$-mode ones. The coloured gradient represents the simulated data while the black dots represent the measured Super-K data.

shown on the right column of Figure 4.11. This is particularly important as the ν_e contamination is strong in $\bar{\nu}$-mode and the Super-K detector cannot distinguish the charge of single events. The oscillation fit has been performed with electron rings samples fitted in E_ν^{rec} only and in $E_\nu^{rec} - \theta_\ell$ in order to quantify the improvement given by the electron angle information.

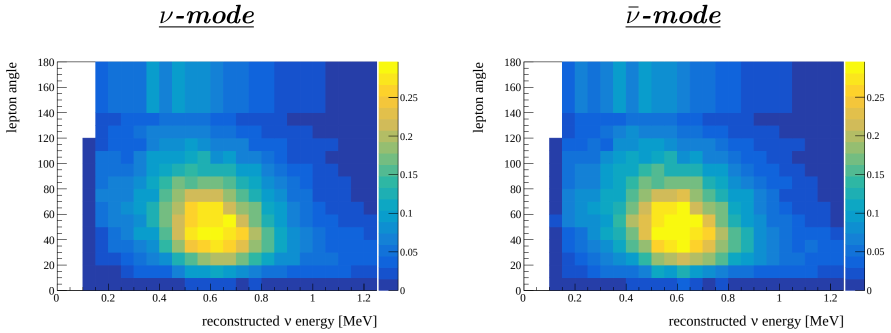

(a) R_e CC-0π: CC content

(c) $R_{\bar{e}}$ CC-0π: ν_e content

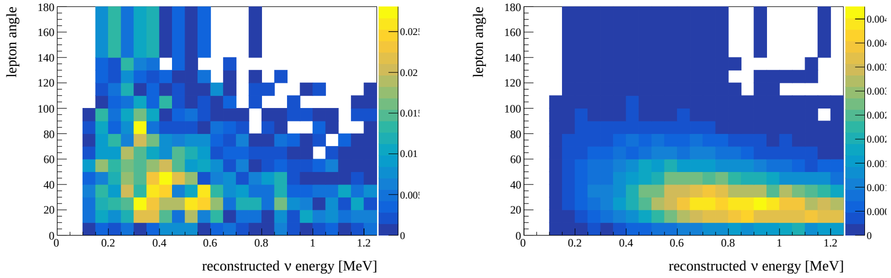

(b) R_e CC-0π: NC content

(d) $R_{\bar{e}}$ CC-0π: $\bar{\nu}_e$ content

Figure 4.11: Predicted distribution of the three electron rings sample as a function of the reconstructed energy (x-axis) and electron angle (y-axis). The left column shows the CC-0π R_e sample, Figure 4.11a being the CC content and Figure 4.11b the NC content. The right column shows the CC-0π $R_{\bar{e}}$ sample, Figure 4.11c being the beam and oscillated ν_e content and Figure 4.11d the beam and oscillated $\bar{\nu}_e$ content.

4.3 Source of systematic uncertainties

The systematic uncertainties are due to a lack of knowledge on the flux, interaction, ND280 or Super-K detector response. In order to be constrained, the models must incorporate free parameters taking into account the variation of the underlying processes. The four categories of uncertainties are described in the four first subsections below, while the last subsection reviews their impact on the number of events in the Super-K samples.

4.3.1 Flux model

The flux simulation described in Section 3.1.3 exhibits six sources of uncertainties:

(1) the alignment of the proton beam with the target;

(2) the number of protons sent on target;

(3) the interaction of protons with the target material and the interactions of produced hadrons in the target;

(4) the alignment of the target with the following horns;

(5) the current powering the horn and the resulting magnetic field;

(6) the modelling of material from the target to the decay volume.

As shown in Figure 4.12, the uncertainty on the hadroproduction uncertainty dominates, all other uncertainties being of the same order of magnitude. The total prior uncertainty is about 10% for the energies of the T2K flux.

The propagation of the uncertainties in the simulation leads to parameterise the variation of the flux in the detectors with 100 normalisation parameters of prior value 1 and prior uncertainty as given in Tables 4.9 and 4.10. 50 parameters affect the ND280 flux and 50 more the Super-K flux, and the weight is applied on the events according to the true neutrino energy with the binning given on the tables. The parameters are correlated as shown on the covariance matrix of Figure 4.13.

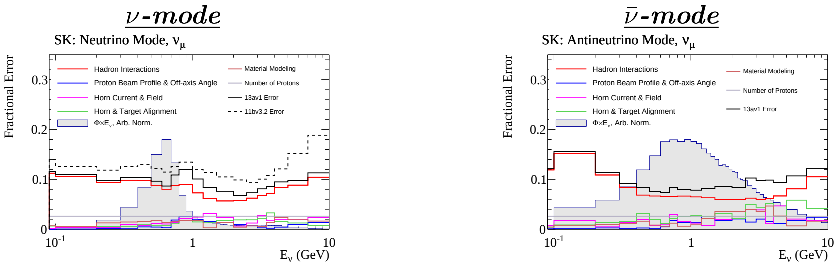

(a) ν_μ **(e)** ν_μ

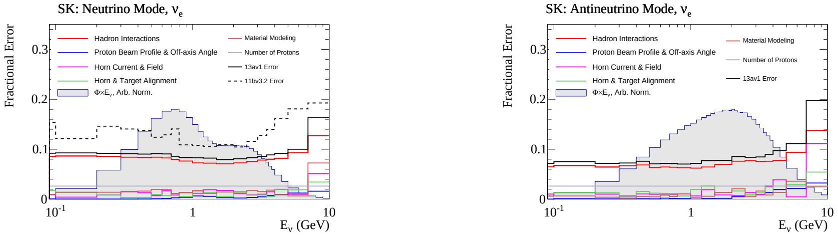

(b) ν_e **(f)** ν_e

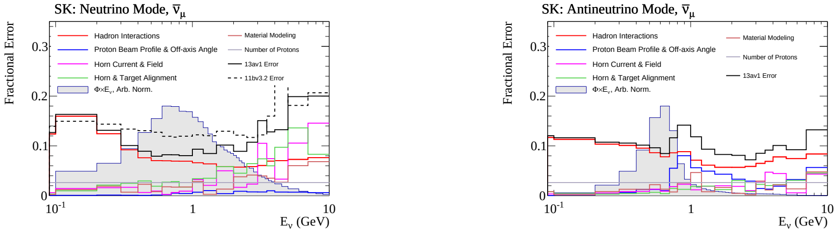

(c) $\bar{\nu}_\mu$ **(g)** $\bar{\nu}_\mu$

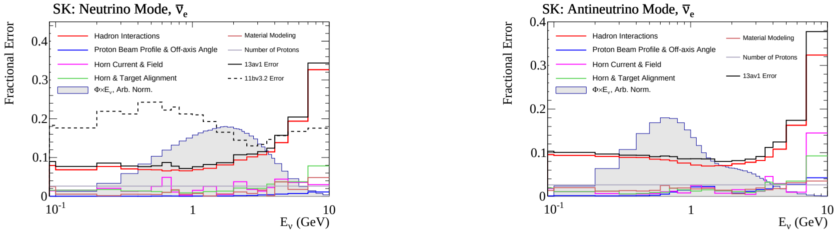

(d) $\bar{\nu}_e$ **(h)** $\bar{\nu}_e$

Figure 4.12: Uncertainties on the Super-K flux as a function of the neutrino energy for the ν_μ, ν_e, $\bar{\nu}_\mu$, $\bar{\nu}_e$ contents of the flux in ν-mode (left column) and $\bar{\nu}$-mode (right column). The red line is the uncertainty due to (3), the blue line due to (1), the pink line due (5), the green line due to (4), the brown line due to (6) and the grey line due to (2). The black solid line is the sum of all uncertainties, while the black dashed line represent the sum of all uncertainties in the previous flux tuning version. The grey area represents the flux as $\phi \times E_\nu$ with arbitrary normalisation.

ν-mode

beam content	*parameter E_ν bin [GeV]*	*ND280 value*	*ND280 uncertainty*	*Super-K value*	*Super-K uncertainty*
ν_μ	[0.0, 0.4[	1.0	0.097	1.0	0.092
	[0.4, 0.5[	1.0	0.101	1.0	0.080
	[0.5, 0.6[	1.0	0.093	1.0	0.083
	[0.6, 0.7[	1.0	0.087	1.0	0.083
	[0.7, 1.0[	1.0	0.107	1.0	0.082
	[1.0, 1.5[	1.0	0.105	1.0	0.103
	[1.5, 2.5[	1.0	0.074	1.0	0.098
	[2.5, 3.5[	1.0	0.069	1.0	0.090
	[3.5, 5.0[	1.0	0.082	1.0	0.087
	[5.0, 7.0[	1.0	0.098	1.0	0.119
	[7.0, 30.0[	1.0	0.114	1.0	0.114
$\bar{\nu}_\mu$	[0.0, 0.7[	1.0	0.101	1.0	0.085
	[0.7, 1.0[	1.0	0.081	1.0	0.075
	[1.0, 1.5[	1.0	0.078	1.0	0.097
	[1.5, 2.5[	1.0	0.082	1.0	0.091
	[2.5, 30.0[	1.0	0.086	1.0	0.139
ν_e	[0.0, 0.5[	1.0	0.090	1.0	0.068
	[0.5, 0.7[	1.0	0.092	1.0	0.089
	[0.7, 0.8[	1.0	0.090	1.0	0.095
	[0.8, 1.5[	1.0	0.087	1.0	0.086
	[1.5, 2.5[	1.0	0.088	1.0	0.092
	[2.5, 4.0[	1.0	0.082	1.0	0.090
	[4.0, 30.0[	1.0	0.096	1.0	0.090
$\bar{\nu}_e$	[0.0, 2.5[	1.0	0.074	1.0	0.092
	[2.5, 30.0[	1.0	0.140	1.0	0.158

Table 4.9: Prior values and uncertainties of the flux normalisation parameters in ν-mode. The parameter binning indicates the true E_ν energy range on which the parameter is applicable. There are 25 parameters modelling the ND280 flux, and 25 modelling the Super-K flux, they correspond to the row/column indices 0-24 and 25-49 of the covariance matrix of Figure 4.13 respectively.

$\bar{\nu}$-mode

beam content	*parameter E_ν bin [GeV]*	*ND280 value*	*ND280 uncertainty*	*Super-K value*	*Super-K uncertainty*
$\bar{\nu}_\mu$	[0.0, 0.4[	1.0	0.098	1.0	0.093
	[0.4, 0.5[	1.0	0.103	1.0	0.077
	[0.5, 0.6[	1.0	0.096	1.0	0.075
	[0.6, 0.7[	1.0	0.086	1.0	0.079
	[0.7, 1.0[	1.0	0.111	1.0	0.078
	[1.0, 1.5[	1.0	0.090	1.0	0.104
	[1.5, 2.5[	1.0	0.069	1.0	0.101
	[2.5, 3.5[	1.0	0.073	1.0	0.094
	[3.5, 5.0[	1.0	0.087	1.0	0.084
	[5.0, 7.0[	1.0	0.097	1.0	0.119
	[7.0, 30.0[	1.0	0.114	1.0	0.100
ν_μ	[0.0, 0.7[	1.0	0.102	1.0	0.077
	[0.7, 1.0[	1.0	0.078	1.0	0.073
	[1.0, 1.5[	1.0	0.083	1.0	0.093
	[1.5, 2.5[	1.0	0.084	1.0	0.091
	[2.5, 30.0[	1.0	0.085	1.0	0.126
$\bar{\nu}_e$	[0.0, 0.5[	1.0	0.089	1.0	0.068
	[0.5, 0.7[	1.0	0.089	1.0	0.084
	[0.7, 0.8[	1.0	0.085	1.0	0.094
	[0.8, 1.5[	1.0	0.080	1.0	0.090
	[1.5, 2.5[	1.0	0.078	1.0	0.090
	[2.5, 4.0[	1.0	0.083	1.0	0.082
	[4.0, 30.0[	1.0	0.093	1.0	0.078
ν_e	[0.0, 2.5[	1.0	0.074	1.0	0.088
	[2.5, 30.0[	1.0	0.128	1.0	0.154

Table 4.10: Prior values and uncertainties of the flux normalisation parameters in $\bar{\nu}$-mode. The parameter binning indicated the true E_ν energy range on which the parameter is applicable. There are 25 parameters modelling the ND280 flux, and 25 modelling the Super-K flux, they correspond to the row/column indices 50-74 and 75-99 of the covariance matrix of Figure 4.13 respectively.

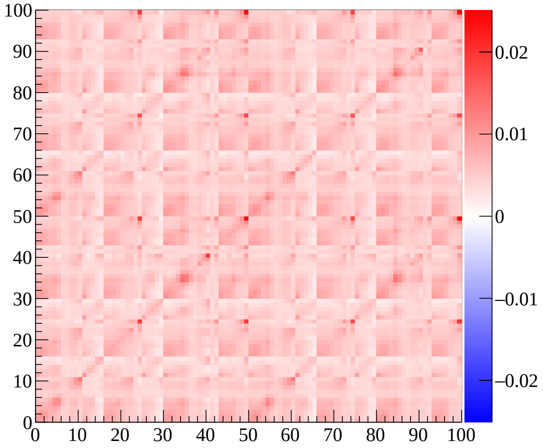

Figure 4.13: Prior covariance matrix of the 100 flux parameters. Parameters 0-24(25-49) affect the ν-mode($\bar{\nu}$-mode) flux in ND280. Parameters 50-74(75-99) affect the ν-mode($\bar{\nu}$-mode) flux in Super-K.

4.3.2 Cross-section model

The cross-section models implemented in the generator NEUT as described in Section 3.4 give rise to ten distinguishable interaction modes described in the following paragraphs with their relevant free parameters summarised in Table 4.11. The prior correlation between the interaction parameters are shown on the covariance matrix of Figure 4.14a. Some parameters scale the number of events uniformly, those *normalisation* parameters are parametrised as the same weight for all events concerned regardless of their kinematics. Other parameters do not only change the normalisation, but also the *shape* of the E_ν^{rec} or $E_\nu^{rec} - \theta_\ell$ distribution, therefore they cannot be modelled with a uniform parameter. In this case, the MC simulation is ran again for a set of parameters, i.e. for a parameter x the variation in the number of events if computed for $\{x \pm 5; x \pm 4; x \pm 3; x \pm 2; x \pm 1\sigma\}$. The variation is afterwards extrapolated between the point with a cubic spline function to obtain a continuous response function.

• **CCQE:** CCQE interactions occur through vector currents, known with great precision thanks to electron scattering experiments, and axial currents, where less external data are available to constrain the parameters [111]. The axial current is modelled with a dipole form of free parameter the axial mass, with prior value chosen to $M_A^{QE} = 1.2\,\mathrm{GeV} \cdot \mathrm{c}^{-2}$ from a fit of KEK-to-Kamioka (K2K) data [132]. The RFG model of the nucleus describes nucleons filling up a potential until a global Fermi momentum of values $p_F = 217\,\mathrm{MeV} \cdot \mathrm{c}^{-1}$ for carbon-12 and $p_F = 225\,\mathrm{MeV} \cdot \mathrm{c}^{-1}$ for oxygen-16. The nucleons are bounded in the nucleus with a binding energy of $E_B = 25 \pm 9\,\mathrm{MeV}$ for carbon and $E_B = 27 \pm 9\,\mathrm{MeV}$ for oxygen. The Fermi momentum and binding energy parameters values have been determined from electron scattering fits [133], although the uncertainties on E_B have been inflated to cover the different treatments of the binding energy between the models. The binding energy parameters are not allowed to vary outside the range $E_B \in [12; 42\,\mathrm{MeV}]$. A fit to MiniBooNE and MINERνA CCQE cross-section measurements has been performed in order to re-evaluate the CCQE parameters [105], but the lack of agreement between the datasets led to continue using the values mentioned above. The fit aimed at updating the prior uncertainties as well, and the inability to obtain a correct output resulted in using a flat prior on the axial mass and the Fermi momentum (within the range $p_F \in [200; 275\,\mathrm{MeV} \cdot \mathrm{c}^{-1}]$ allowed by the NEUT generator) as no reasonable uncertainty could be extracted. M_A^{QE} is anticorrelated with the Fermi momentum on carbon at 23%, but uncorrelated with the Fermi momentum on oxygen. The binding energy parameters are uncorrelated as well.

- **MEC:** MEC interactions are implemented in NEUT using the model on [111], that does not contain any free parameter. The uncertainty on the rate of MEC interactions is therefore modelled with a normalisation parameter set to MEC ^{12}C$=$ 100% of the predicted cross-section as prior value, and with a flat prior uncertainty. The parameter is correlated with M_A^{QE} at 50% and the Fermi momentum on carbon at 4.3%. The model scales the MEC cross-section with a linear dependence in the number of nucleons, which is in tension with fits to electron scattering data. Consequently, a normalisation of the ratio of MEC cross-section of oxygen over carbon is set to be MEC ^{16}O/^{12}C$=$ 100% with a flat prior uncertainty and a 82.5% correlation with MEC ^{12}C. The ratio parameter is also correlated with M_A^{QE} at 40.9% and the Fermi momentum on carbon at 3.6%. Other models of MEC have been derived, and it was noticed than the cross-section predicted with the model on [134] for $\bar{\nu}$ differs from the one predicted by the model implemented in NEUT. The uncertainty is covered by the implementation of a normalisation parameter scaling the antineutrino MEC cross-section with regard to the neutrino one: MEC $\bar{\nu}/\nu = 100\%$ with a flat prior uncertainty.

- **CC-Res:** The Rein-Sehgal model [112] used to implement CC-Res $\pi^{\pm}$ production in NEUT contains vector and axial form factors from [135]. Similarly to the CCQE model, the vector part is well-known while the axial part require neutrino scattering data sparsely available. The parameters of the axial form factors have been fitted to the reanalysed bubble chambers neutrino experiments data to extract their prior values and uncertainties [113]. The resonant axial mass have been found to be $M_A^{Res} = 0.95 \pm 0.15\,\mathrm{GeV}\cdot\mathrm{c}^{-2}$, and the normalisation of the axial form factor to be $C_A^5 = 1.01 \pm 0.12$. Resonant CC-$\pi^{\pm}$ production is a pure isospin $I = \frac{3}{2}$ process, therefore processes with $I = \frac{1}{2}$ form a background with prior 1.3 ± 0.2.

- **CC-Coh:** Measurement of the CC-Coh cross-section in MINERνA have shown a 30% deviation of the cross-section compared to the Berger-Sehgal model [117]. A normalisation parameter is set to $100 \pm 30\%$ and is 100% correlated between carbon and oxygen as the model is assumed to apply equally for both nucleus.

- **CC-Oth:** The CC-DIS, multipion production and CC-Res production of other particle than $\pi^{\pm}$ (such as γ, K or $\eta^{(')}$) cross-sections are merged into a single interaction mode as their topologies are similar, the CC-Other (Oth) category. A single parameter codes the variation of the normalisation and the shape of the cross-section with a cubic spline, which prior value is set to zero to not modify the NEUT nominal prediction, and the prior uncertainty is $\frac{40\%}{E_\nu}$ on the basis of MINOS cross-section measurements [136].

- **NC-π^0:** The NC π^0 production cross-section is simulated with the same Rein-Sehgal model than the CC-$\pi^\pm$ production and is modelled with the same parameters M_A^{Res}, C_A^5 and $I = \frac{1}{2}$ background.

- **NC-$\pi^\pm$:** The NC $\pi^\pm$ production cross-section is simulated with the same Rein-Sehgal model than the CC-$\pi^\pm$ production and is modelled with the same parameters M_A^{Res}, C_A^5 and $I = \frac{1}{2}$ background.

- **NC-Coh:** The NC coherent cross-section is parametrised by a single normalisation parameter set with a prior value of 100±30%. The 30% uncertainty originates from the different NC-Coh fractions measured by MiniBooNE [137] and the SciBar Booster Neutrino Experiment (SciBooNE) [138].

- **NC-1γ:** The NC 1γ production rate predicted by NEUT version 5.3.2 has been found to be half of the expected cross-section [139], therefore all events have a prior weight of 2 to fill the discrepancy. As no external data are available to constrain the cross-section, a 100% normalisation uncertainty on the total measurement is set.

- **NC-Oth:** The NC-Oth category includes γ, K, $\eta^{(')}$ and multipion production as DIS through Z^0 exchange. As no external data exist to constraint those cross-sections, a study varying NEUT parameters lead to assign a normalisation uncertainty of 30%. The NC-other content being different between the ND280 and Super-K samples, two parameters are set for the two different detectors with no correlation between them.

- $\overset{(-)}{\nu}_e$ ***CC-inclusive*:** $\overset{(-)}{\nu}_e$ CC interactions do not form an interaction category, but the uncertainties corresponding to the categories listed above have been determined for $\overset{(-)}{\nu}_\mu$ interactions. ν_e cross-section may differ from the different phase-space reachable by the lepton, radiative corrections at tree level, and effects of second class currents on the interaction form factors [140]. As those processes are not included in NEUT and their effects are predicted to be different for neutrinos and antineutrinos, two parameters vary the normalisation of the $\nu_e(\bar{\nu}_e)$ to $\nu_\mu(\bar{\nu}_\mu)$ cross-section with a 40% uncertainty determined from theoretical calculations. This uncertainty is applied on all CC interactions of $\overset{(-)}{\nu}_e$.

Once the interaction occurs, the outgoing particles may undergo secondary interactions that can lead to a modification of the reaction kinematics inducing a bias in the reconstructed neutrino energy. Such interactions are divided in three categories described in the following paragraphs.

matrix index	*parameter [unit]*	*uncertainty type*	*prior value*	*prior uncertainty*	*relevant modes*
0	M_A^{QE} [GeV · c^{-2}]	norm.+shape	1.20	flat prior	CCQE
1	p_F ^{12}C [MeV · c^{-1}]	norm.+shape	217	flat prior	
4	p_F ^{16}O [MeV · c^{-1}]	norm.+shape	225	flat prior	
3	E_B ^{12}C [MeV]	norm.+shape	25	9	
6	E_B ^{16}O [MeV]	norm.+shape	27	9	
2	MEC ^{12}C	norm.	100%	flat prior	CC-MEC
5	MEC ^{16}O/^{12}C	norm.	100%	flat prior	
7	MEC $\bar{\nu}/\nu$	norm.	100%	flat prior	
9	M_A^{Res} [GeV · c^{-2}]	norm.+shape	0.95	0.15	CC-Res NC-π^0 NC-$\pi^\pm$
8	C_5^A	norm.+shape	1.01	0.12	
10	$I - \frac{1}{2}$ background	norm.+shape	1.30	0.20	
14	CC-Coh ^{12}C	norm.	1.0	0.3	CC-Coh
15	CC-Coh ^{16}O	norm.	1.0	0.3	
13	CC-Oth	norm.+shape	0.0	0.4	CC-Oth
11	CC ν_e/ν_μ	norm.	1.0	0.4	all CC (only $\overset{(-)}{\nu}_e$)
12	CC $\bar{\nu}_e/\bar{\nu}_\mu$	norm.	1.0	0.4	
16	NC-Coh	norm.	1.0	0.3	NC-Coh
17	NC-1γ	norm.	2.0	1.0	NC-1γ
18	NC-Oth (ND280)	norm.	1.0	0.3	NC-Oth
19	NC-Oth (Super-K)	norm.	1.0	0.3	

Table 4.11: Interaction parameters with their prior values and uncertainties. The type "norm.+shape" indicates that the variation in events is computed with a cubic spline function, while the type "norm" means that the parameters vary the normalisation of the number of events. The relevant interaction modes for each parameter is also specified in the last column, while the first column give the row/column indices correspondence to the covariance matrix of Figure 4.14a.

- **FSI:** The FSI concerns the propagation of $\pi^{\pm/0}$ produced in neutrino interactions in the nuclear medium (the produced leptons are neglected as their cross-section is lower, as they are not subject to the strong force). The cascade model described in Section 3.4 holds six free parameters to vary the rate of inelastic scattering (inel.) at low and high energy (E), $\pi^\pm$ production (prod.) and absorption (abs.), and interactions transforming $\pi^\pm$ into π^0 (π ch.-exch.) at low and high energy. The uncertainties on those parameters have been determined from a fit to pion-nucleon scattering data and verified with pion photoproduction data [141]; they are shown in Table 4.12 for the treatment of FSI in ND280. The FSI uncertainties are propagated differently for the Super-K samples, as they are added to the detector covariance matrix with the two other interaction types described below, as shown on Figure 4.14b. The difference of treatment is meant to be temporary: in the first oscillation analysis of T2K, the FSI uncertainties were both added to the detector covariance matrix of ND280 and Super-K as their effect is degenerate with an imperfect resolution of the detector. Because external data can constrain the FSI model parameters, they have been migrated to cross-section parameters for ND280 and it is planned to unify the propagation between the two detectors in the future.

matrix index	*parameter [unit]*	*uncertainty type*	*prior value*	*prior uncertainty*	*relevant modes*
20	inel. low E	norm.+shape	0.0	0.41	CC-Res NC-π^0 NC-$\pi^\pm$
21	inel. high E	norm.+shape	0.0	0.34	
22	$\pi^\pm$ prod.	norm.+shape	0.0	0.50	
23	$\pi^\pm$ abs.	norm.+shape	0.0	0.41	
24	π ch.-exch. low E	norm.+shape	0.0	0.57	
25	π ch.-exch. high E	norm.+shape	0.0	0.28	

Table 4.12: FSI parameters used in ND280 with their prior values and uncertainties. The type "norm.+shape" indicates that the variation in events is computed with a cubic spline function (the mean prior value is arbitrarily set to 0). FSI only affect events creating a pion as specified in the last column, while the first column give the entry number for the covariance matrix of Figure 4.14a.

- **SI:** Pions that escaped the nucleus may undergo Secondary Interactions (SI) outside the nuclear medium, but inside the detector. SI are treated differently in the near and far detector, but are propagated with the detector uncertainties in both case. However in Super-K, the same cascade framework used for FSI simulates the effect in the detector simulation. The model is compared to pion scattering data to evaluate the SI uncertainties [141], and are contained in the covariance matrix of Figure 4.14b. In ND280, SI are propagated with the Bertini cascade model available in GEANT4 [142] and the uncertainties are obtained from the comparison with pion scattering data [143].

- **PN:** PhotoNuclear (PN) effects affect photons absorbed by a nucleus. This a particular concern if one the two photons created by π^0 decay is absorbed, and the remaining photon may convert into an $e^{\pm}$ in Super-K. Because almost no data exist, an uncertainty of 100% is set on the Super-K events and included on the covariance matrix of Figure 4.14b.

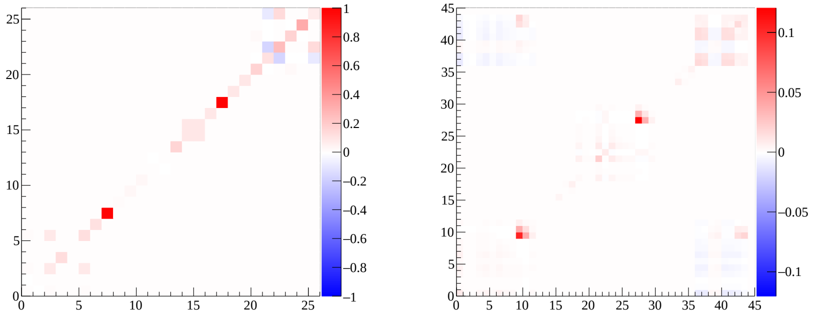

(a) Interactions + ND280 FSI

(b) Super-K FSI + SI + PN

Figure 4.14: Interaction parameters prior covariance matrix. 4.14a shows the matrix for the interaction parameters used for the ND280 and Super-K samples, as well as the FSI parameters for the ND280 samples. The row and column indices correspond to the parameters in Tables 4.11 and 4.12. 4.14b shows the matrix for the FSI, SI and PN parameters used for the Super-K samples. Their uncertainties are summed and they are included with the detector systematics as explained in Section 4.3.4.

4.3.3 ND280 detector model

The systematic uncertainties on the efficiency of the ND280 detector are determined from the comparison of simulated and real data distributions in control samples. Control samples contain events with a topology similar to the ones concerned by the uncertainty, but not included in the Markov chains to avoid a double counting of the uncertainty. The uncertainties are divided in 16 categories described in the paragraphs below and conservatively assumed to be uncorrelated at first. The propagation of the uncertainties to the variation in number of events differs according to the uncertainty type, and leads to the covariance matrix shown in Figure 4.15. The three types are:

- *observation (obs.)* systematics are uncertainties on reconstructed variables. The uncertainty is propagated by running the selection with different values of those variables.
- *efficiency (eff.)* systematics are uncertainties on variables affecting the rate of selection. The uncertainty is directly applied on the events to modify its weight after selection.
- *normalisation (norm.)* systematics affect the overall normalisation of concerned events and is applied directly.

The matrix entries affect the events as specified in Table 4.13.

matrix index	***sample***	***events affected***
0- 69	FGD1	CC-0π
70-139	ν_μ in	CC-1π^+
140-209	ν-mode	CC-$other$
210-229	FGD1 $\bar{\nu}_\mu$	CC-1$track$
230-249	in $\bar{\nu}$-mode	CC-$Ntrack$
250-269	FGD1 ν_μ	CC-1$track$
270-289	in $\bar{\nu}$-mode	CC-$Ntrack$
290-359	FGD2	CC-0π
360-429	ν_μ in	CC-1π^+
430-499	ν-mode	CC-$other$
500-519	FGD2 $\bar{\nu}_\mu$	CC-1$track$
520-539	in $\bar{\nu}$-mode	CC-$Ntrack$
540-559	FGD2 ν_μ	CC-1$track$
560-579	in $\bar{\nu}$-mode	CC-$Ntrack$

Table 4.13: Correspondence of the entries of the ND280 detector covariance matrix of Figure 4.15 with the relevant events.

• **TPC cluster efficiency** ***(eff.)*** **:** This uncertainty characterises the efficiency in finding a cluster of hits around points of the trajectory of charged particles in the TPC. It is evaluated by comparing the efficiency of simulated and real data in samples of beam and cosmic events; it was found to be 1.1% for vertical clusters and 7% for horizontal clusters.

- **TPC track reconstruction efficiency** ***(eff.)*** **:** This uncertainty characterises the ability of the reconstruction algorithm to merge hits into tracks in the TPC. Events with tracks in the detectors upstream and downstream the tested TPC are selected from a sample of through-going muons, and the presence of a TPC track in between signal an efficient reconstruction. The difference between the efficiencies obtained in simulated and real data gives an uncertainty of 0.3 to 0.5% for each TPC.

- **TPC track charge sign identification systematic** ***(eff.)*****:** This uncertainty characterises the uncertainty in finding the proper charge of a particle with a TPC track. The distribution of events in simulated and real data samples are fitted with a parametrised function, and the discrepancy between the parameters is taken as the uncertainty.

- **TPC PID** ***(obs.)*** **:** The PID of particles with a TPC track is determined from a pull computed between the measured and predicted energy loss $dE/dx^{meas,pred}$. The pull distribution is Gaussian, and the difference of means and ratio of standard deviations between the simulated and real data distributions are taken as uncertainties on the PID measurement.

- **TPC momentum resolution** ***(obs.)*** **:** The momentum resolution of simulated events with a TPC track is smeared until it reach the resolution of data events, and the smearing factor is taken as the uncertainty.

- **TPC momentum scale** ***(obs.)*** **:** As the momentum in the TPC is obtained from the curvatures of the tracks, the momentum scale uncertainty is inferred from the uncertainty on the magnetic field determined in a field mapping. It is set to 0.57%.

- **TPC field distortions** ***(obs.)*** **:** The magnetic field distortions in the TPC are measured with a system of lasers. They are afterwards applied to the simulated data and the reconstruction is re-ran to evaluate the difference between the no distortion and with distortion cases, that is taken to be the uncertainty.

- **FGD-contained tracking efficiency** ***(eff.)*** **:** FGD contained tracks are notably selected if they are compatible with the charged pions hypothesis. The selection efficiency can be computed by comparing the rate of FGD-only reconstructed tracks in a sample of FGD-TPC tracks. The difference of efficiencies between simulated and real data is taken as the uncertainty.

- **Muon decay electron systematics** ***(eff.)*** **:** Electrons originating from muon decay are tagged from delayed FGD hits. The uncertainty on the detection efficiency is set to be the difference of tagging rate between simulated and real cosmic events.

- **FGD PID** ***(obs.)*** **:** Similarly to the TPC PID uncertainties, the FGD ones are taken to be the the difference of means and ratio of standard deviations between the pull distributions of simulated and real data.

- **FGDs masses** ***(norm.)*** **:** The uncertainty on the FGDs masses impact the number of target nucleus in the detector. It is chosen to be the difference between the density set in the detector simulation compared to mass measurement of the FGD modules constituents.

- **Pion secondary interactions** ***(norm.)*** **:** SI are implemented as a detector effect but their uncertainties arise from the interaction model described in Section 4.3.2.

- **FGD-TPC matching efficiency** ***(eff.)*** **:** FGD-TPC tracks are selected in the samples analysed in ND280. The efficiency of matching a TPC tracks to hits in the FGD is evaluated by selecting tracks passing through two consecutive TPC and presenting a FGD-TPC track. The difference between the simulated and real data efficiencies is taken as the uncertainty. The estimation of this uncertainty has been a task of this PhD work and more details are given on Appendix B.2.

- **FGD1-FGD2 time of flight** ***(obs.)*** **:** The ToF information is used to select backward events originating in the FGD2 and reaching the FGD1. The difference between the ToF obtained simulated and real data is taken as the uncertainty.

- **Out-of-FV background** ***(norm.)*** **:** Background events which vertices are located outside the FV of the detector have different topologies. The evaluation of the uncertainty on each subcategory has been a task of this PhD work and is described on Appendix B.1.

- **Sand events background** ***(norm.)*** **:** Through-going events crossing the whole detector must have their vertex located outside the detector, where the material is sand. The rate obtained from a dedicated MC simulation is compared with the rate of events entering the upstream face of the P∅D to establish the uncertainty.

- **Event pile up** ***(norm.)*** **:** The number of events per bunch in the TPC is compared between simulated and real data, the difference between the two values is taken as the uncertainty.

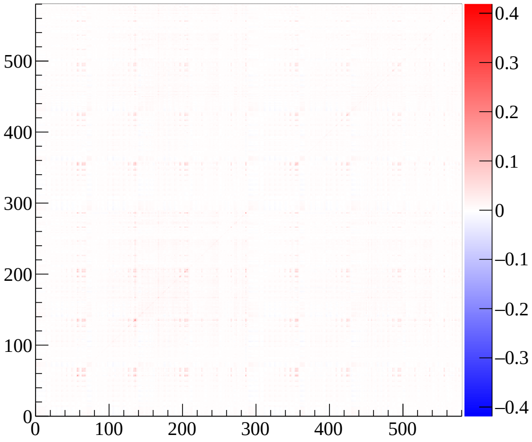

Figure 4.15: Prior covariance matrix of the ND280 detector uncertainties parameters. The uncertainties on the number of events selected in the FGDs is obtained by propagating the uncertainties of the 16 categories described in the text. The correspondence between the row/column indices and the relevant samples are specified in Table 4.13.

4.3.4 Super-Kamiokande detector model

The Super-K detector model uncertainties are assigned on the variables used to select events. They are estimated using control samples, which can be either atmospheric $\overset{(-)}{\nu}_\mu$ or $\overset{(-)}{\nu}_e$, cosmic muons stopping in the detector or *hybrid* π^0 events. The hybrid π^0 sample is created by selecting $e^\pm$ rings from cosmic muons stopping in Super-K. The ring is pretended to be a γ ring, and a second γ ring is simulated with kinematics consistent with π^0 decay. The hybrid π^0 sample is used to establish the uncertainties on the CC or NC events creating π^0, while the atmospheric and stopping muon samples are used to constrain CC events. No dedicated sample being available for $\pi^\pm$ produced by NC, the NC not producing π^0 are assigned a 100% uncertainty for the PID, ring counting and π^0 tagging uncertainties. The only exception is the NC-1γ events that has the same uncertainty as the $\overset{(-)}{\nu}_e$ CC events, shifted by 1%.

The uncertainties are afterwards propagated with a MCMC method to obtain the uncertainty on the number of events shown in the covariance matrix of Figure 4.16a. The uncertainties on FSI, SI and PN being uncorrelated to the detector, the covariance matrix in Figure 4.14b is added to obtain the covariance matrix of Figure 4.16b, used in the oscillation fit. The matrix elements affect the different samples as described in Table 4.14.

- **Flasher events:** Flasher events are caused by PMT dynode discharging while no events occur. The uncertainty on the rate of such events is evaluated from the rate difference between simulated and real data in a control sample of atmospheric neutrinos.

- **Vertex location:** The uncertainty on the vertex location affects the rate of selected FCFV events. It is estimated from the spatial reconstruction difference between simulated and real data in a control sample of atmospheric neutrinos.

- **Energy scale:** The energy scale is a constant shift in the energy reconstructed from the events compared to the true energy. The shift is evaluated to be 2.4% from several samples of cosmic rays with muons stopping in the detector and from NC from atmospheric neutrinos.

- **PID:** Misidentified PID is determined from the rate of electron rings tagged in a sample of stopping muons or hybrid π^0. The difference of MI's-PID rates between simulated and real data rate is taken to be the uncertainty on the PID.

- **Ring counting:** The uncertainty on the number of ring is taken to be the difference of single-ring event rates between simulated and real data in a control sample of atmospheric neutrinos or hybrid π^0.

- **$\boldsymbol{\pi^0}$ tagging:** The π^0 tagging is performed with a dedicated fitter, which difference of tagging rate between simulated and real data in a control sample of atmospheric neutrinos is taken as the uncertainty or hybrid π^0.

index	*sample*	*events affected*
1-3		oscillated CC $\overset{(-)}{\nu}_e$ with bin edges $[0; 0.35; 0.8; 1.25\,\mathrm{GeV}]$
4-6	R_e	beam CC $\overset{(-)}{\nu}_e$ with bin edges $[0; 0.35; 0.8; 1.25\,\mathrm{GeV}]$
7-9	CC-0π	beam CC $\overset{(-)}{\nu}_\mu$ with bin edges $[0; 0.35; 0.8; 1.25\,\mathrm{GeV}]$
10-12		NC with bin edges $[0; 0.35; 0.8; 1.25\,\mathrm{GeV}]$
13-15		CCQE $\overset{(-)}{\nu}_\mu$ with bin edges $[0; 0.4; 1.1; 30\,\mathrm{GeV}]$
16	R_μ	CC non-QE $\overset{(-)}{\nu}_\mu$
17	CC-0π	CC $\overset{(-)}{\nu}_e$
18		NC
19-21		oscillated CC $\overset{(-)}{\nu}_e$ with bin edges $[0; 0.35; 0.8; 1.25\,\mathrm{GeV}]$
22-24	$R_{\bar{e}}$	beam CC $\overset{(-)}{\nu}_e$ with bin edges $[0; 0.35; 0.8; 1.25\,\mathrm{GeV}]$
25-27	CC-0π	beam CC $\overset{(-)}{\nu}_\mu$ with bin edges $[0; 0.35; 0.8; 1.25\,\mathrm{GeV}]$
28-30		NC with bin edges $[0; 0.35; 0.8; 1.25\,\mathrm{GeV}]$
31-33		CCQE $\overset{(-)}{\nu}_\mu$ with bin edges $[0; 0.4; 1.1; 30\,\mathrm{GeV}]$
34	$R_{\bar{\mu}}$	CC non-QE $\overset{(-)}{\nu}_\mu$
35	CC-0π	CC $\overset{(-)}{\nu}_e$
36		NC
37-38		oscillated CC $\overset{(-)}{\nu}_e$ with bin edges $[0; 0.8; 1.25\,\mathrm{GeV}]$
39-40	R_e	beam CC $\overset{(-)}{\nu}_e$ with bin edges $[0; 0.8; 1.25\,\mathrm{GeV}]$
41-42	CC-$1\pi^\pm$	beam CC $\overset{(-)}{\nu}_\mu$ with bin edges $[0; 0.8; 1.25\,\mathrm{GeV}]$
43-44		NC with bin edges $[0; 0.8; 1.25\,\mathrm{GeV}]$
45	all	energy scale

Table 4.14: Correspondence of the entries of the Super-K detector covariance matrices of Figures 4.16 and 4.14b with the relevant events.

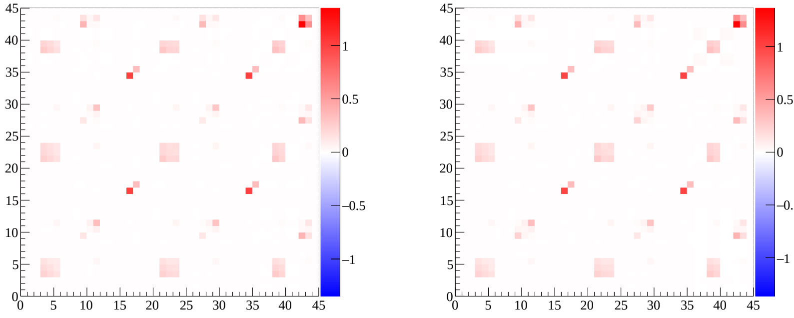

(a) Super-K detector

(b) Super-K detector + FSI + SI + PN

Figure 4.16: Super-Kamiokande detector parameters prior covariance matrix. 4.16a shows the matrix for the Super-K detector uncertainties only, obtained from the propagation of the uncertainties on the cuts explained on this subsection. 4.16b shows the matrix for the Super-K detector and FSI, SI and PN uncertainties, adding the values of the matrix in Figures 4.16a and 4.14b in quadrature. The correspondence between the row/column indices and the relevant events are specified in Table 4.14.

4.3.5 Impact on the number of events

The effect of the uncertainties on the number of events selected in Super-K is shown in Tables 4.15 and 4.16. The *prefit* uncertainties are obtained by throwing the values of the nuisance parameters according to their prior probabilities and computing the rate corresponding to those values. The *postfit* uncertainties are obtained by randomly selecting 5000 steps of the Markov chain and use the values of the parameters at each step to compute the new rates. Because most steps are located around the maximal posterior probability, this method enables to evaluate the postfit uncertainties including the correlations between the parameters. On both cases, the uncertainty is taken to be the standard deviation of the rate distribution divided by its mean.

Source of uncertainties	R_μ ***CC-0π***		R_e ***CC-0π***		R_e ***CC-1π***$^{\pm}$	
	prefit	***postfit***	***prefit***	***postfit***	***prefit***	***postfit***
Flux	7.7 %	2.7%	8.8 %	2.7%	8.8 %	2.6%
Cross-section	7.5 %	2.9%	7.0 %	3.8%	13.7 %	3.1%
Flux × cross-section (constrained by ND280)	10.7%	1.7%	10.8%	1.7%	16.2%	4.1%
Flux × cross-section (total)	10.8%	1.9%	11.2%	2.7%	16.3%	4.4%
Super-K detector	4.7 %	N/A	2.6 %	N/A	8.3 %	N/A
SI + FSI + PN	1.8 %	N/A	2.6 %	N/A	10.8%	N/A
Super-K detector + SI + FSI + PN	4.9 %	3.2%	3.6 %	2.9%	13.7 %	11.9%
Total	**11.8%**	**4.2%**	**11.7%**	**3.7%**	**21.1%**	**12.9%**

Table 4.15: Predicted variation of the total number of events in the ν-mode Super-K samples due to the systematic uncertainties.

Source of uncertainties	***$R_{\bar{\mu}}$ CC-0π*** *prefit*	*postfit*	***$R_{\bar{e}}$ CC-0π*** *prefit*	*postfit*
Flux	7.0 %	2.7%	7.9 %	2.9%
Cross-section	9.2 %	3.3%	9.8 %	4.2%
Flux × cross-section (constrained by ND280)	11.6 %	1.9%	12.4%	1.9%
Flux × cross-section (total)	11.6 %	1.9%	12.7%	2.9%
Super-K detector	3.9 %	N/A	3.3%	N/A
SI + FSI + PN	2.4 %	N/A	2.8%	N/A
Super-K detector + SI + FSI + PN	4.5 %	2.9%	4.2 %	3.6%
Total	**12.4 %**	**3.9%**	**13.4%**	**4.4%**

Table 4.16: Predicted variation of the total number of events in the $\bar{\nu}$-mode Super-K samples due to the systematic uncertainties.

Conclusion:

Five samples of $\overset{(-)}{\nu}_\mu$ and $\overset{(-)}{\nu}_e$ interactions in the Super-K detector are selected to constrain the oscillation parameters. They are subjected to systematic uncertainties due to a lack of knowledge on the flux, interaction and detectors responses. Seven samples of $\overset{(-)}{\nu}_\mu$ interactions are selected in ND280 to constrain the uncertainties on the flux and interaction models. A simultaneous analysis of the near and far detector events is performed with a MCMC method to obtain the posterior probability on oscillation parameters. The two next chapters will present the results of the oscillation analyses obtained with the framework described in this chapter.

CHAPTER 5

Muon (anti)neutrino disappearance analysis

5.1 Analysis description

The goal of the analysis presented in this chapter is to evaluate if oscillation parameters estimated with neutrino oscillations differ from the ones obtained with antineutrinos oscillations. Several beyond-SM theories postulate $P(\nu_\mu \to \nu_\mu) \neq P(\bar{\nu}_\mu \to \bar{\nu}_\mu)$, such as CPT violation or the presence of Non-Standard Interactions (NSI). NSI are neutrino interactions due to new physics that could be low-energy remnants of supersymmetric or additional Higgs models [144]. Their effect is usually implemented phenomenologically by adding extra terms to the neutrino evolution Hamiltonian, leading to new CC and NC interaction Lagrangians [145]. Consequently, the matter effect Hamiltonian of Equation (2.24) is modified and the impact on the resulting neutrino oscillation probability can be degenerate with the effect of the CP-violating phase [146].

As CP-violation does not occur in $\overset{(-)}{\nu}_\mu$ disappearance, only the $R_{\overset{(-)}{\mu}}$ rings are used to probe differences in the estimation of $\sin^2\theta_{23}$ and Δm^2_{32}. The seven ND280 samples described in Section 4.2.1 are included in the Markov chain to constraint the flux and cross-section parameters. The only oscillation parameters with a flat prior are $\sin^2\theta_{23}$ and Δm^2_{32}, that are evaluated separately from the R_μ and $R_{\overset{(-)}{\mu}}$ samples. The estimated parameters are decoupled by defining a total of four parameters with a flat prior: $\sin^2\theta_{23}$ and Δm^2_{32} that are used to apply the oscillation probability $P(\nu_\mu \rightarrow \nu_\mu)$ on the R_μ events, and $\sin^2\bar{\theta}_{23}$ and $\Delta\bar{m}^2_{32}$ that are used to apply the oscillation probability $P(\bar{\nu}_\mu \rightarrow \bar{\nu}_\mu)$ on the $R_{\overset{(-)}{\mu}}$ events. The Δm^2_{32} and $\Delta\bar{m}^2_{32}$ parameters have a 50% probability of changing of sign at every step to span both mass orderings. The other oscillation parameters are constrained: the solar parameters $\sin^2\theta_{12}$ and Δm^2_{21} have a Gaussian prior with mean and standard deviation with resulting values and uncertainties from the fit to solar neutrino experiments and KamLAND as described in Section 2.3.2. The $\sin^2\theta_{13}$ parameter prior is also a Gaussian function, with parameters from the best fit to reactor neutrino oscillation experiments [131], while the δ_{CP} value is fixed to zero to avoid inducing any CP-violation effect in the $\overset{(-)}{\nu}_\mu$ oscillation probabilities. The parameters and their priors are summarised in Table 5.1.

osc. param.	***value***	***1σ prior uncertainty***
$\sin^2\theta_{12}$	0.304	0.05
Δm^2_{21}	$7.53 \cdot 10^{-5}\,\text{eV}^2 \cdot \text{c}^{-4}$	$0.18 \cdot 10^{-5}\,\text{eV}^2 \cdot \text{c}^{-4}$
$\sin^2\theta_{23}$	0.528	flat prior
Δm^2_{32}	$2.509 \cdot 10^{-5}\,\text{eV}^2 \cdot \text{c}^{-4}$	flat prior
$\sin^2\bar{\theta}_{23}$	0.528	flat prior
$\Delta\bar{m}^2_{32}$	$2.509 \cdot 10^{-5}\,\text{eV}^2 \cdot \text{c}^{-4}$	flat prior
$\sin^2\theta_{13}$	0.0217	0.0013
δ_{CP}	0 rad	fixed

Table 5.1: Oscillation parameters used in the muon rings disappearance analysis. The values used to estimate the number of events, as well as the prior on the parameters, are also shown. This table differs from the one used in Table 4.5 from the decoupling of the parameters $\sin^2\theta_{23}/\Delta m^2_{32}$ and $\sin^2\bar{\theta}_{23}/\Delta\bar{m}^2_{32}$, as well as δ_{CP} being fixed to 0 rad.

5.2 Expected sensitivity

The analysis is initially performed using simulated Super-K data in order to estimate the T2K ability to measure the $\sin^2\theta_{23}$, Δm^2_{32}, $\sin^2\bar{\theta}_{23}$

and $\Delta\bar{m}^2_{32}$ parameters. The real ND280 data are included in order to take into account the actual constraint on the flux and cross-section parameters.

5.2.1 Number of events

The parameters used in this analysis only differ from the ones used to compute the number of events in Section 4.2.2 (summarised in Table 4.5) by the fact that $\delta_{\mathrm{CP}}= 0\,\mathrm{rad}$. The number of events expected at Super-K when $\delta_{\mathrm{CP}}= 0$ is given in Table 4.8, it is found to be 135.86 events for the R_μ sample and 64.26 events for the $R_{\bar{\mu}}$ sample. The numbers are very close to the ones estimated with the nominal oscillation parameters assuming $\delta_{\mathrm{CP}}= -1.601\,\mathrm{rad}$, which are 136.21 events for the R_μ sample and 64.40 events for the $R_{\bar{\mu}}$ sample. This is due to the fact that δ_{CP} only impacts the background content of oscillated $\overset{(-)}{\nu}_e$, which represents only $\sim 10^{-3}$ of the total number of events in the samples. As the difference is negligible, the description of the samples and uncertainties in Sections 4.2.2 and 4.3.5 is relevant for this chapter as well. A limitation of the analysis is due to the high ν_μ contamination in the $R_{\bar{\mu}}$ sample visible in Table 4.6: it is $\sim 30\%$, while the $\bar{\nu}_\mu$ contamination in the R_μ sample is less than 10%. Therefore, the $\sin^2\bar{\theta}_{23}$-$\Delta\bar{m}^2_{32}$ parameters measured with the $R_{\bar{\mu}}$ samples will also be sensitive ν_μ oscillation.

5.2.2 Posterior probabilities with simulated Super-Kamiokande data

In order to evaluate the sensitivity of the estimated the oscillation parameters, a Markov chain is initially run in with simulated Super-K data. This implies that the Super-K data are the MC prediction, that does not include any CPT violation nor NSI, and the estimate only represents the T2K sensitivity assuming that no beyond-SM physics occur. The real ND280 data are included in the Markov chain in order to incorporate the real constraint on the flux and cross-section parameters. The posterior probability density sampled by the Markov chain is shown in Figure 5.1, with the 90% and 68% CI. The posterior probability density is marginalised over the parameters not shown on the plot, and the marginalised 2D posterior mode is also shown. The mode is found to be very close to the value used to tune the MC in the $\sin^2\theta_{23}$-Δm^2_{32} parameter space shown in Figure 5.1a, while the $\sin^2\bar{\theta}_{23}$ posterior is found on the lower octant in Figure 5.1b. However, the posterior probability density is very flat at the posterior $\Delta\bar{m}^2_{32}$ point, implying that the posterior mode may be sensitive to small fluctuations in the sampling. As the input value is located inside the CI, the framework is qualified to behave properly.

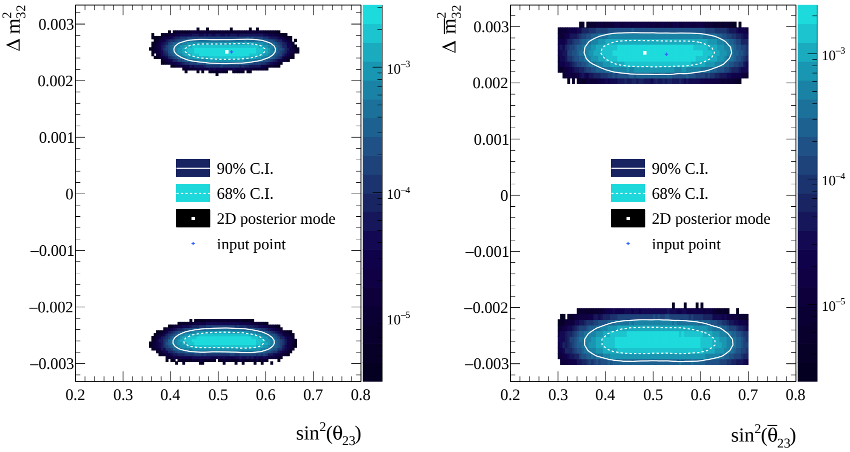

(a) $\sin^2\theta_{23}$-Δm^2_{32} **(b)** $\sin^2\bar{\theta}_{23}$-$\Delta\bar{m}^2_{32}$

Figure 5.1: Posterior probability density in the $\sin^2\theta_{23}$-Δm^2_{32} (left) or $\sin^2\bar{\theta}_{23}$-$\Delta\bar{m}^2_{32}$ (right) space using a Markov chain with real ND280 and simulated Super-K data. The white dashed(solid) line represents the 68%(90%) CI. The white square represents the 2D posterior mode and the blue cross the value of the parameters used to tune the MC. Both mass orderings are included.

The comparison of the CI from Figure 5.1 is shown in Figure 5.2. As the number of R_μ events is $\sim 50\%$ higher than the number of $R_{\bar{\mu}}$ events, the constraint obtained on the $\sin^2\theta_{23}$-Δm^2_{32} oscillation parameters is stronger than the one obtained on $\sin^2\bar{\theta}_{23}$-$\Delta\bar{m}^2_{32}$. Consequently, deviations on the estimated oscillation parameters would have to be large in order to be observed in this analysis.

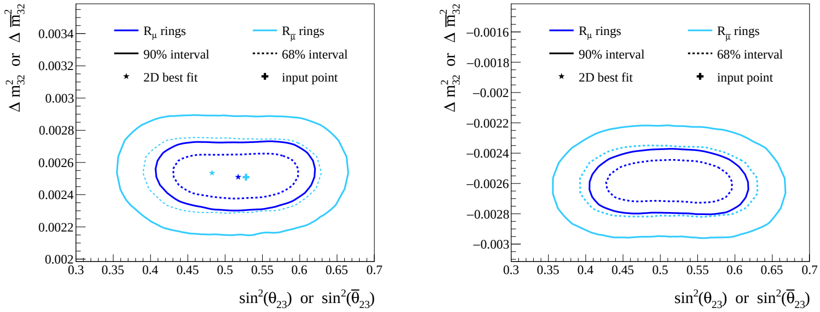

(a) Zoom on NO.

(b) Zoom on IO.

Figure 5.2: Comparison of the CI obtained on the $\sin^2\theta_{23}$-Δm^2_{32} parameters (from Figure 5.1a) and on the $\sin^2\bar{\theta}_{23}$-$\Delta\bar{m}^2_{32}$ parameters (from Figure 5.1b) using a Markov chain with real ND280 and simulated Super-K data. The stars represent the 2D posteriors and the cross the value of the parameters used to tune the MC. Both mass orderings are included, but the figures scale on the normal (left) and inverted (right) mass ordering case.

5.3 Results

The actual constraint on the oscillation parameters is obtained by running a Markov chain with real ND280 and Super-K data. The initial Super-K MC is tuned with the parameters of Table 5.1, and varied at every step to sample the posterior probability on $\sin^2\theta_{23}$, $\sin^2\bar{\theta}_{23}$, Δm^2_{32}, $\Delta\bar{m}^2_{32}$, as well as the systematic parameters.

5.3.1 Estimation of neutrino oscillation parameters

The posterior probability densities on the $\sin^2\theta_{23}$-Δm^2_{32} and $\sin^2\bar{\theta}_{23}$-$\Delta\bar{m}^2_{32}$ spaces are shown in Figure 5.3. The parameters not shown on the axes are marginalised, and both mass hierarchies are included. As expected from the sensitivity study of Section 5.2.2, the R_μ rings provide a tighter constraint on $\sin^2\theta_{23}$ and Δm^2_{32} than the $R_{\bar{\mu}}$ on $\sin^2\bar{\theta}_{23}$ and $\Delta\bar{m}^2_{32}$. This can be explained by the fact that about twice as many events are detected in ν-mode as compared to $\bar{\nu}$-mode: the samples contain 135 R_μ events, against only 66 $R_{\bar{\mu}}$ events. The mode of the distribution is found in the IO $\sin^2\theta_{23}$-Δm^2_{32} interval in Figure 5.3a, while it is found on the NO $\sin^2\bar{\theta}_{23}$-$\Delta\bar{m}^2_{32}$ interval in Figure 5.3b. However the posterior probability reaches similar values on both NO and IO area, and all 68% and 90% CI have a similar surface between NO and IO, therefore the difference of mode is not considered indicative.

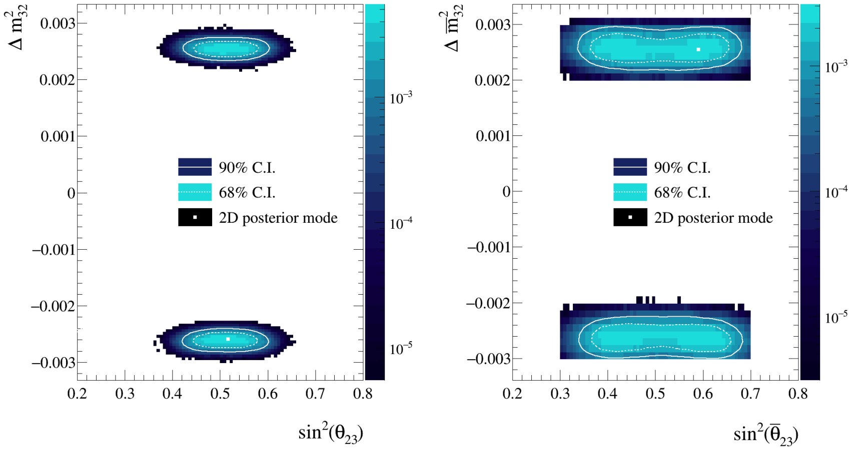

(a) $\sin^2\theta_{23}$-Δm^2_{32}

(b) $\sin^2\bar{\theta}_{23}$-$\Delta\bar{m}^2_{32}$

Figure 5.3: Posterior probability density in the $\sin^2\theta_{23}$-Δm^2_{32} (left) or $\sin^2\bar{\theta}_{23}$-$\Delta\bar{m}^2_{32}$ (right) space using a Markov chain with real ND280 and Super-K data. The white dashed(solid) line represents the 68%(90%) CI and the white square the 2D posterior mode. Both mass orderings are included.

Figure 5.4 shows the comparison of the 68% and 90% CI and modes shown in Figure 5.3. There is no disagreement between the $\sin^2\theta_{23}$-Δm^2_{32} and $\sin^2\bar{\theta}_{23}$-$\Delta\bar{m}^2_{32}$, showing no evidence for CPT violation nor NSI. Both modes find $\sin^2\theta_{23}$ or $\sin^2\bar{\theta}_{23}$ higher than the maximal disappearance value of 0.5, with the $\sin^2\bar{\theta}_{23}$ best fit being outside the 68% CI on $\sin^2\theta_{23}$ but inside the 90% CI. The $\sin^2\theta_{23}$-Δm^2_{32} CI are notably smaller than the ones obtained with simulated Super-K data, while the $\sin^2\bar{\theta}_{23}$-$\Delta\bar{m}^2_{32}$ CI are larger, explaining the difference of shape between the expected constraint of Figure 5.2 and the obtained constraint of Figure 5.4.

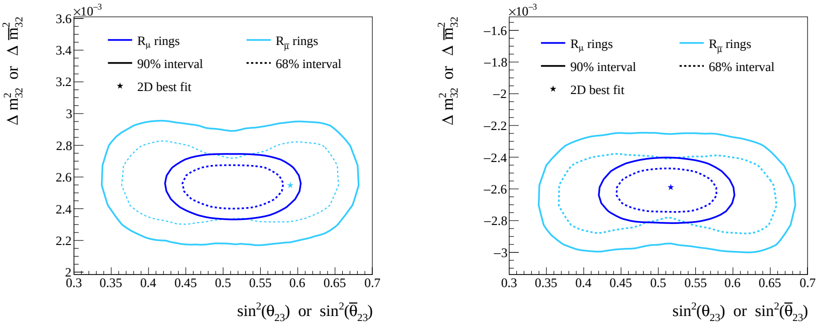

(a) Zoom on NO. **(b)** Zoom on IO.

Figure 5.4: Comparison of the CI obtained on the $\sin^2\theta_{23}$-Δm^2_{32} parameters (from Figure 5.1a) and on the $\sin^2\bar{\theta}_{23}$-$\Delta\bar{m}^2_{32}$ parameters (from Figure 5.1b) using a Markov chain with real ND280 and Super-K data. The stars represent the 2D posterior and both mass orderings are included, but the figures scale on the normal (left) and inverted (right) mass ordering case.

5.3.2 Posterior spectra

The expected spectra assuming the posterior value of the oscillation and nuisance parameters can be determined with a *posterior predictive* method. Similarly to the estimation of the uncertainties on the Super-K event rates shown in Tables 4.15 and 4.16, this method consists in sampling 2000 steps from the Markov Chain, and evaluating the spectrum for each Super-K sample according to the value of the parameters at each step. The distribution of the number of events in each bin is fitted with a Gaussian, whose mean is taken as the best fit number of events, and the standard deviation as the uncertainty on this number. The posterior spectra are shown in Figure 5.5, with a coarser binning than the one used in the fit to explicit the comparison between the spectra. Both R_μ and $R_{\bar{\mu}}$ posterior spectra have been obtained by sampling the value of the oscillation parameters relative to their sample (i.e. $\sin^2\theta_{23}$ and Δm^2_{32} for R_μ, $\sin^2\bar{\theta}_{23}$ and $\Delta\bar{m}^2_{32}$ for $R_{\bar{\mu}}$), and by sampling the values relative to the other sample. The dark blue spectrum is the one evaluated with the oscillation parameters of the sample, while the light blue spectrum is evaluated with the oscillation parameters of the other sample. The main difference is visible in the bin $[0.4; 0.7\,\text{GeV}[$ where the posterior predictive spectra obtained with the $\sin^2\bar{\theta}_{23}$-$\Delta\bar{m}^2_{32}$ parameters overestimate the number of events for the R_μ spectrum of Figure 5.5a.

This bin corresponds to the maximum disappearance peak, but Figure 5.5b shows that the posterior predictive spectra estimated with the $\sin^2\theta_{23}$-Δm^2_{32} parameters is inside the 1σ statistical uncertainty on the number of Super-K observed event in this bin, and thus acceptable.

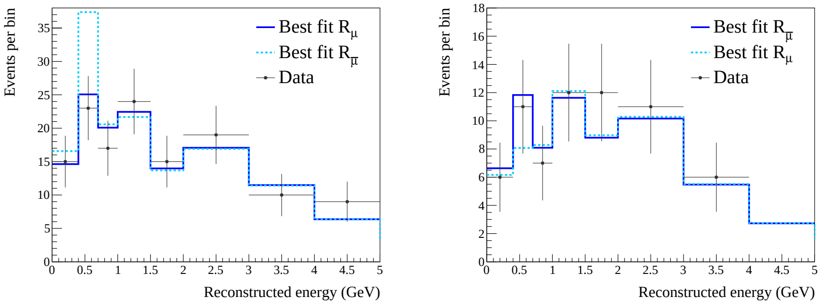

(a) R_μ sample **(b)** $R_{\bar{\mu}}$ sample

Figure 5.5: Comparison of the posterior spectra obtained by sampling 2000 steps from the Markov chain with real ND280 and Super-K data. The solid dark blue line shows the spectra evaluated with the oscillation parameters of the sample, and the dashed light blue line the spectra evaluated with the oscillation parameters of the other sample. The black points are the Super-K data.

5.3.3 Comparison with other experiments

The analysis presented in this chapter has notably already been performed by the MINOS experiment [147]. Similarly to T2K, MINOS finds consistent intervals from neutrino and antineutrino disappearance as shown in Figure 5.6. However T2K considerably improves the uncertainty on the parameter estimation, providing a more accurate test. Because MINOS performs the analysis assuming the NO of neutrino masses and reports CL, the comparison is done by selecting only the steps of the Markov chains with $\Delta m^2_{32} > 0$. They NO CI are afterwards converted to CL by following the procedure outlined in Section A.2.3. The results are in agreement between the two analyses, the T2K $\sin^2\theta_{23}$-Δm^2_{32} interval being placed inside the MINOS one, and similarly for the $\sin^2\bar{\theta}_{23}$-$\Delta\bar{m}^2_{32}$ intervals.

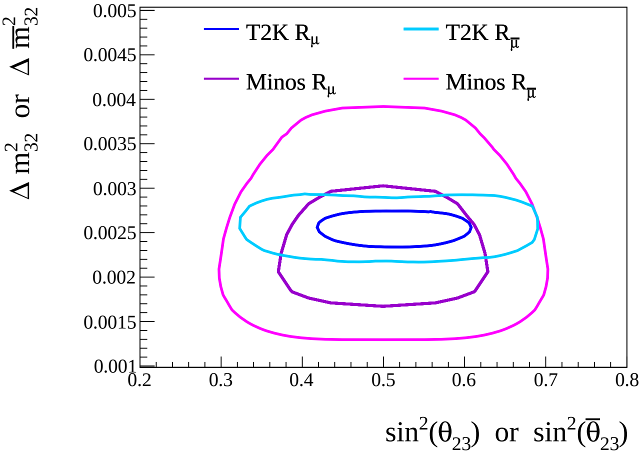

Figure 5.6: Comparison of the 90% CL obtained on the neutrino disappearance parameters by T2K and MINOS assuming the NO of neutrino masses. The dark(light) blue lines show the T2K CL on $\sin^2\theta_{23}$-Δm^2_{32}($\sin^2\bar{\theta}_{23}$-$\Delta\bar{m}^2_{32}$). The dark(light) magenta lines show the MINOS CL on $\sin^2\theta_{23}$-Δm^2_{32}($\sin^2\bar{\theta}_{23}$-$\Delta\bar{m}^2_{32}$), from [147].

Conclusion:

An analysis of the ν_μ and $\overset{(-)}{\nu}_\mu$ disappearance has been performed by disentangling the neutrino oscillation parameters. The sample of Super-K R_μ events has been used to constrain $\sin^2\theta_{23}$ and Δm^2_{32}, while the sample of $R_{\bar{\mu}}$ events constrained $\sin^2\bar{\theta}_{23}$ and $\Delta\bar{m}^2_{32}$. The CI have been found to be in agreement between the two sets of parameters, providing no evidence for beyond-SM physics such as CPT violation or the presence of NSI. While the analysis benefits from a higher sensitivity than the one reported by MINOS, it is limited by the high contamination of ν_μ in the $R_{\overset{(-)}{\mu}}$ samples. The next chapter will present a different analysis, using all the available Super-K samples in order to constrain the U_{PMNS} parameters assuming the same oscillation parameters for neutrino and antineutrinos.

CHAPTER 6

Joint muon (anti)neutrino disappearance and electron (anti)neutrino appearance analysis

6.1 Analysis description

The joint analysis of muon and electron rings includes information from $\overset{(-)}{\nu}_\mu$ disappearance and $\overset{(-)}{\nu}_e$ appearance to constrain the oscillation parameters $\sin^2\theta_{23}$, Δm^2_{32}, $\sin^2\theta_{13}$ and δ_{CP}. Contrarily to the analysis presented in Chapter 5, a single set of oscillation parameters is used, corresponding to the nominal parameters given in Table 4.5 and for which the expected event rates are derived in Section 4.2.2. The addition of the electron ring samples to the muon ring samples analysed in Chapter 5 enables the analysis to be sensitive to $\sin^2\theta_{13}$, δ_{CP} and the mass ordering, i.e. the sign of Δm^2_{32}. The inclusion of $\nu-$ and $\bar{\nu}$-mode events results in a stronger sensitivity to the CP violation phase compared to analysing ν or $\bar{\nu}$ only, the difference of oscillation probabilities between the two particles being directly incorporated. Initially, only four Super-K samples have been included: they are the four CC-0π samples described in Section 4.2.2, namely the muon ring and electron ring samples in ν-mode and $\bar{\nu}$-mode (R_μ, $R_{\bar{\mu}}$, R_e, $R_{\bar{e}}$). The results of the analysis with the four samples have been released by the T2K collaboration in [50]. Following this, a fifth sample of R_e CC-$1\pi^+$ events has been added in the Markov chains to decrease the statistical uncertainty on the oscillation parameters estimation. This inclusion led to the current best constraint on the oscillation parameters from T2K, and the sensitivity and results are described in Sections 6.2 and 6.3.

All analyses includes the seven ND280 samples described in Section 4.2.1 to constrain the systematic uncertainties. The systematic parameters prior probabilities are normal distributions with means and standard deviations as specified in Section 4.3. The priors set for the solar oscillation parameters $\sin^2\theta_{12}$ and Δm^2_{21} are Gaussian functions with mean and standard deviation as specified in Table 4.5. The priors set for the oscillation parameters to constrain are always uniform, at the exception of $\sin^2\theta_{13}$ which is either uniform, or Gaussian with mean and standard deviation as specified in Table 4.5. The Gaussian prior of $\sin^2\theta_{13}$ is referred to as *the reactor constraint*, with values originating from the PDG fit to reactor neutrino data [131]. Unless otherwise specified, the Markov chains include the R_e samples binned in $E_\nu^{rec} - \theta_\ell$, the R_μ samples binned in E_ν^{rec} and the ND280 samples in $p_\mu - \theta_\mu$ as described in Chapter 4.

6.2 Expected sensitivity

Initially, the expected constraints on the oscillation parameters according to our prior knowledge are evaluated. The simulated data used to compute the likelihood are the MC events, i.e. the data and the MC correspond exactly to each other in order to evaluate the sensitivity corresponding to the framework. Both are tuned to the nominal value of the systematic parameters, the oscillation parameters used being the ones specified in Table 4.5.

6.2.1 Likelihood scan

A likelihood scan does not use the MCMC method, but computes the value of the likelihood for a set of points forming a 2-dimensional grid. Figure 6.1 shows a histogram with axis $\sin^2\theta_{13}$ and δ_{CP}, and each bin is filled with the $\Delta\chi^2$ value corresponding to the bin center. The $\Delta\chi^2$ has been computed from the Poisson log-likelihood ratio as given by Equation (4.5), with no reactor constraint applied. As the prior uncertainties follow normal distributions, no marginalisation bias occurs and the minimal $\Delta\chi^2$ value is found in the bin corresponding to the input point as expected. This test guarantees a correct computation of the likelihood.

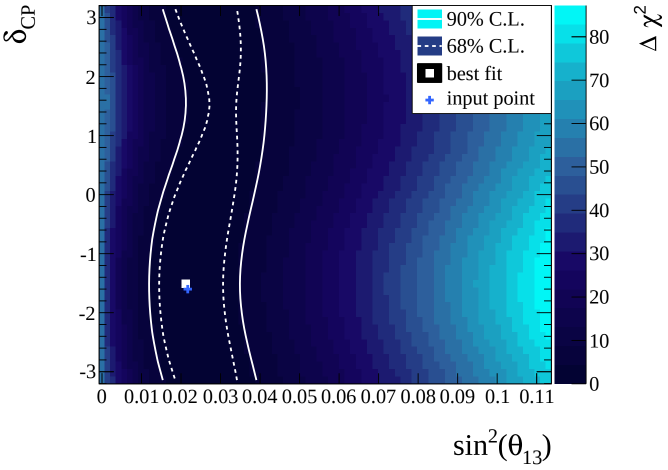

Figure 6.1: Likelihood scan in the $\sin^2\theta_{13}$-δ_{CP} space. The histogram bins are filled with the $\Delta\chi^2$ value corresponding to the bin center (the reactor constraint is not applied). The white dashed(solid) line shows the 68%(90%) constant-$\Delta\chi^2$ intervals, the blue cross is the parameters used to tune the MC and the white square the bin with minimal $\Delta\chi^2$.

6.2.2 Posterior probabilities with simulated Super-Kamiokande data

A more accurate estimation of the expected oscillation parameters posterior probabilities is obtained by using the MCMC with the MC as simulated data. The sections below show the results of the sampling with and without the reactor constraint, using the three Super-K R_e samples binned in $E_\nu^{rec} - \theta_\ell$ and the two Super-K R_μ samples binned in E_ν^{rec}. The Super-K data are the MC, while the ND280 data are the real data, in order to incorporate the real constraint on the flux and cross-section parameters in the Markov chain.

6.2.2.1 Point estimation

The best fit point is taken to be the mode of the posterior probability density. In order to avoid any bias induced by marginalising over oscillation parameters, the mode of the joint posterior probability in the 4-dimensional (4D) $\sin^2\theta_{23}$–Δm^2_{32}–$\sin^2\theta_{13}$–δ_{CP} space is chosen. However, a 4D histogram requires a very large number of steps to obtain a smooth distribution on which the mode would not be subject to statistical fluctuations. A continuous function is evaluated from the discrete content of the histogram with a Kernel Density Estimator (KDE), a smoothing method replacing the bin entries by a Gaussian with standard deviation depending on the density of points in the neighbouring bins [125]. The mode of the smoothed function is taken to be the best fit point, and is given in Table 6.1 for the simulated data Markov chains.

	$\sin^2\theta_{23}$	Δm^2_{32} ($\text{eV}^2\cdot c^{-4}$)	$\sin^2\theta_{13}$	δ_{CP} (rad)
input value for MC tuning	0.528	$2.509\cdot10^{-3}$	0.0217	-1.601
4D mode without reactor constraint	0.512	$2.516\cdot10^{-3}$	0.0228	-1.821
4D mode fit with reactor constraint	0.525	$2.516\cdot10^{-3}$	0.0218	-1.974

Table 6.1: Input values and 4D mode of the posterior probability distribution obtained when running the MCMC with simulated Super-K and real ND280 data. The 4D mode is obtained with a KDE method.

All 4D modes are found to be offset from the input value used to tune the MC, due to the marginalisation over the systematic parameters which distributions are non-symmetrical. Applying the reactor constraint prior led to the best fit value of $\sin^2\theta_{13}$ to be closer to the input value compared to using a flat prior. Because δ_{CP} is strongly correlated with $\sin^2\theta_{13}$ as shown in Figure 6.1, the δ_{CP} best fit is found to be lower when the $\sin^2\theta_{13}$ best fit is lower. $\sin^2\theta_{23}$ is correlated with $\sin^2\theta_{13}$, and its best fit is higher when $\sin^2\theta_{13}$ best fit is lower; while the constraint on $\sin^2\theta_{13}$ does not affect Δm^2_{32} best fit.

6.2.2.2 Credible intervals

Figure 6.2 shows the MCMC steps projected in the 2-dimensional $\sin^2\theta_{13}$–δ_{CP} or $\sin^2\theta_{23}$–Δm^2_{32} spaces, which is proportional to the posterior probability density. The 68% and 90% CI are also displayed, the interval area in $\sin^2\theta_{13}$–$\delta_{\rm CP}$ being smaller when using the reactor constraint as it excludes the values in $\delta_{\rm CP} \in [1; 2\,\text{rad}]$ while it is continuous when the prior on $\sin^2\theta_{13}$ is flat. The reactor constraint has a smaller impact on the $\sin^2\theta_{23}$–Δm^2_{32} intervals, yet the areas are smaller when using the Gaussian prior (notably for the inverted MO in the $\Delta m^2_{32} < 0$ section).

The input point used to tune the MC is shown as a blue cross, and the mode in the 2D space is shown as a white square. Contrarily to the likelihood scan, the MCMC output is a marginalised posterior probability where some systematic parameters distributions are non symmetrical, and the mode is not found exactly on the input point. If the $\sin^2\theta_{13}$ and Δm^2_{32} values are close to the input value, the $\delta_{\rm CP}$ value is found lower than the input point. However it can be noted that the marginalised $\delta_{\rm CP}$ distribution includes the posterior probability shape of $\sin^2\theta_{23}$ and Δm^2_{32}. The $\sin^2\theta_{23}$ mode is found lower than the maximal disappearance value of ${\sin^2\theta_{23}}^{\text{max disapp}} = 0.5$ when the reactor constraint is not applied, while it is found higher when it is applied. As the posterior distribution is stable across a wide range of $\sin^2\theta_{23}$ values, the 2D mode is subjected to statistical fluctuations in the number of steps. Because of the biases induced by marginalisation and fluctuations in the posterior probability density, the 2D posterior mode is not taken as the best fit point. Instead the 4D mode obtained as described in Section 6.2.2.1 is taken to be the best fit point.

Without reactor constraint

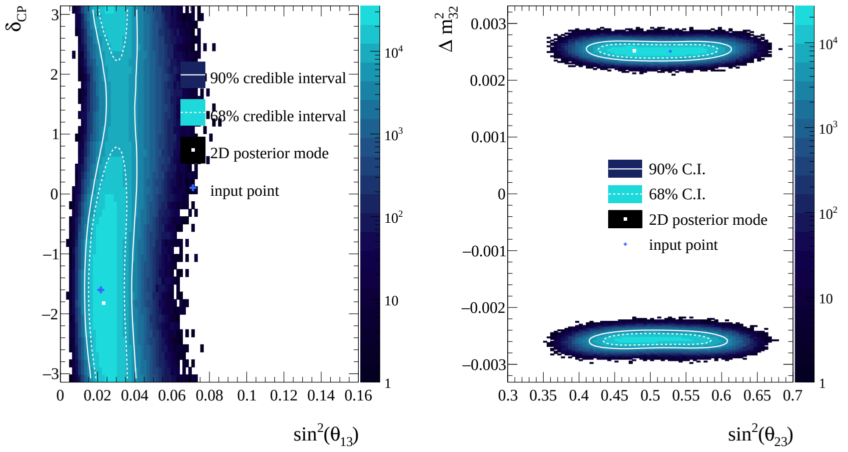

(a) $\sin^2\theta_{13}$–$\delta_{\rm CP}$ **(b)** $\sin^2\theta_{23}$–Δm^2_{32}

With reactor constraint

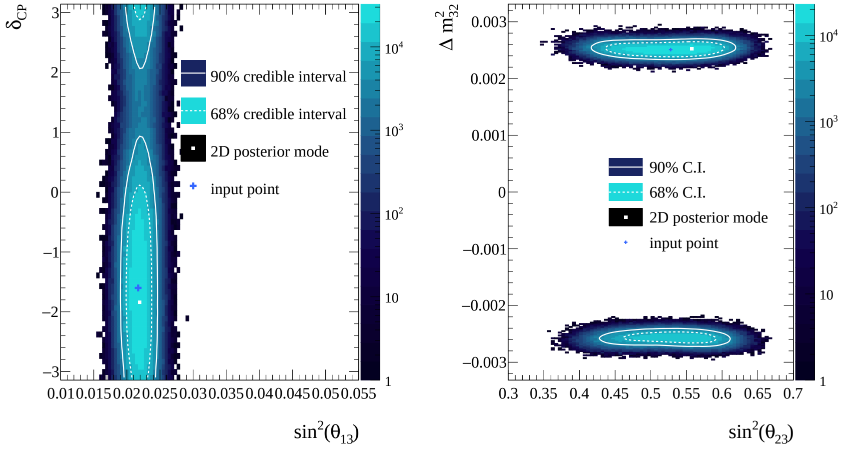

(c) $\sin^2\theta_{13}$–$\delta_{\rm CP}$ **(d)** $\sin^2\theta_{23}$–Δm^2_{32}

Figure 6.2: Oscillation parameters posterior probability densities obtained when running the MCMC with real ND280 and simulated Super-K data and with and without the reactor constraint. The blue gradient shows the posterior probability density in the $\sin^2\theta_{13}$–$\delta_{\rm CP}$ or $\sin^2\theta_{23}$–Δm^2_{32} spaces (the unit of the posterior probability density is the number of Markov steps in every bin). The dashed(solid) white lines show the 68%(90%) constant-$\Delta\chi^2$ intervals, the blue cross is the input point used to tune the MC and the white square is the mode of the 2D distribution.

6.2.2.3 Probability of mass ordering / octant

The θ_{23} value can be either $\theta_{23} < \frac{\pi}{4}$, referred to as the *lower octant*, or $\theta_{23} > \frac{\pi}{4}$, referred to as the *higher octant* ($\theta_{23} = \frac{\pi}{4}$ is the maximal disappearance case). As the Markov chain spans a space containing the two possibilities ($\sin^2\theta_{23}< 0.5$ or > 0.5), the relative number of steps in each subspace give the probability of the higher octant compared to the lower one. Similarly, the probability of each mass ordering can be obtained from the comparison of the posterior probability in the subspaces $\Delta m^2_{32} <$ or > 0. Table 6.2 shows the relative posterior probability for each octant and mass ordering case, from the chains with and without the reactor constraint. The hypotheses can be tested against each other with a Bayes factor as described in Section 4.1.3, resulting in:

$$\begin{aligned} B_{\text{high/low octant}} &= \frac{0.553\ (0.673)}{0.447\ (0.327)} &= 1.24\ (2.06) \\ B_{\text{NO/IO}} &= \frac{0.575\ (0.639)}{0.425\ (0.361)} &= 1.35\ (1.77) \end{aligned} \tag{6.1}$$

where $B_{\text{high/low octant}}$ is the Bayes factor of the high octant, BNO/IO is the Bayes factor of the mass ordering, and the numbers outside(inside) parentheses correspond to the fit without(with) the reactor constraint. All Bayes factors are too low to suggest any strong evidence on the hypotheses with the expected sensitivity, but the usage of the reactor constraint allow the analysis to distinguish better between the two hypotheses.

	$\sin^2\theta_{23} < 0.5$	$\sin^2\theta_{23} > 0.5$	**Sum**
$\Delta m^2_{32} < 0$ **(IO)**	0.192 (0.112)	0.233 (0.248)	**0.425 (0.361)**
$\Delta m^2_{32} > 0$ **(NO)**	0.255 (0.215)	0.320 (0.425)	**0.575 (0.639)**
Sum	**0.447 (0.327)**	**0.553 (0.673)**	**1**

Table 6.2: Relative posterior probabilities for the $\sin^2\theta_{23}$ octant and the mass ordering from the Markov chain with real ND280 data and simulated Super-K data. The values outside(inside) parentheses correspond to the fit without(with) the reactor constraint.

6.2.2.4 Effect of the reactor constraint

The CI in Figure 6.2 are smaller when the reactor constraint is applied, indicating a better resolution of the parameters. Similarly, the Bayes factors for the mass orderings and the $\sin^2\theta_{23}$ octants computed in Section 6.2.2.3 are both higher when the Markov chain is ran with the Gaussian prior on $\sin^2\theta_{13}$. Figure 6.3 shows a comparison of the posterior probability densities of $\sin^2\theta_{23}$, Δm^2_{32}, $\sin^2\theta_{13}$ and δ_{CP} when (not) applying the reactor constraint. All distributions are more peaked when using the Gaussian prior, Figure 6.3c shows that $\sin^2\theta_{13}$ distribution is more constrained by the prior than the T2K data. The better sensitivity on δ_{CP} visible in Figure 6.3d is consistent with the correlation between δ_{CP} and $\sin^2\theta_{13}$ shown in Figure 6.4: at low $\sin^2\theta_{13}$ value, the δ_{CP} 90% CI excludes values around $\delta_{\mathrm{CP}}=\frac{\pi}{2}$ rad.

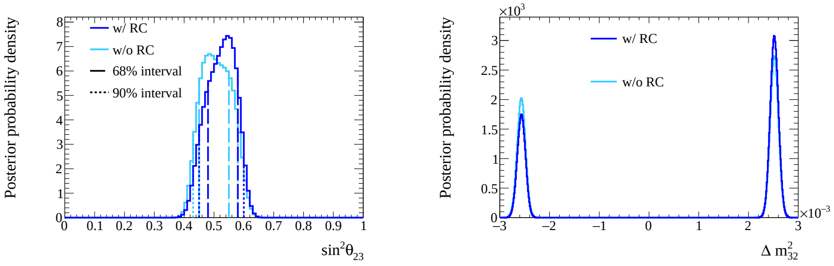

(a) $\sin^2\theta_{23}$

(b) Δm^2_{32}

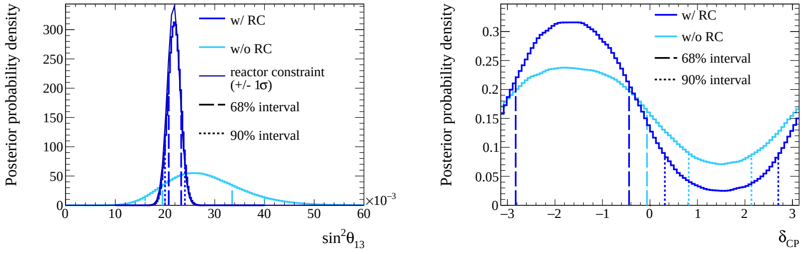

(c) $\sin^2\theta_{13}$

(d) δ_{CP}

Figure 6.3: Oscillation parameters posterior probability densities obtained from Markov chains with (w/) and without (w/o) the reactor constraint (RC) using real ND280 and simulated Super-K data. The 68% and 90% CI are also shown as dashed lines. Figure 6.3c also shows the Gaussian prior on $\sin^2\theta_{13}$ used when the reactor constraint is applied.

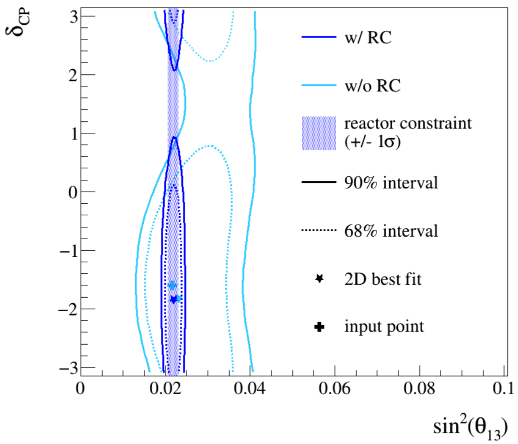

Figure 6.4: 68% and 90% CI from the posterior probability obtained from Markov chains with (w/) and without (w/o) the reactor constraint (RC) using real ND280 and simulated Super-K data. The blue band shows the $\pm 1\sigma$ prior on $\sin^2\theta_{13}$ when the reactor constraint is applied. The 2D modes are shown as stars, and the value used to tune the MC as a cross.

6.3 Results

This section presents the result of the analysis using real data from ND280 and Super-K. The Markov chains have been run with and without the reactor constraint, using the three Super-K R_e samples binned in $E_\nu^{rec} - \theta_\ell$ and the two Super-K R_μ samples binned in E_ν^{rec}.

6.3.1 Posterior probabilities with real Super-Kamiokande data

6.3.1.1 Point estimation

The best fit point is taken to be the mode of the 4-dimensional $\sin^2\theta_{23}$–Δm^2_{32}–$\sin^2\theta_{13}$–δ_{CP} marginal posterior probability, smoothed with the KDE as explained in Section 6.2.2.1. Table 6.3 shows the 4D mode obtained with and without the reactor constraint. $\sin^2\theta_{23}$ is found in the higher octant, and the value of Δm^2_{32} is stable regardless of the prior of $\sin^2\theta_{13}$. $\sin^2\theta_{13}$ is found larger than the PDG fit to reactor data when not using the reactor constraint, but the best fit value of δ_{CP} varies little with $\sin^2\theta_{13}$.

	$\sin^2\theta_{23}$	Δm^2_{32} $(\mathrm{eV}^2 \cdot c^{-4})$	$\sin^2\theta_{13}$	δ_{CP} (rad)
4D mode without reactor constraint	0.513	$2.543 \cdot 10^{-3}$	0.0254	-1.82
4D mode fit with reactor constraint	0.534	$2.539 \cdot 10^{-3}$	0.0219	-1.79

Table 6.3: 4-dimensional mode of the posterior probability distribution obtained when running the MCMC with real ND280 and Super-K data. The mode is extracted after smoothing the sampled $\sin^2\theta_{23}$–Δm^2_{32}–$\sin^2\theta_{13}$–δ_{CP} posterior probability with a KDE.

6.3.1.2 Credible intervals

Figure 6.5 shows the marginal posterior probability density of the oscillation parameters $\sin^2\theta_{23}$, Δm^2_{32}, $\sin^2\theta_{13}$ and δ_{CP} when using the reactor constraint on $\sin^2\theta_{13}$ prior. The posterior probability is notably much higher for $\Delta m^2_{32} > 0$ in Figure 6.5b, indicating a preference for normal mass ordering. The 68%, 90% and 95% CI are shown as blue areas and are summarised in Table 6.4. The CP-conserving values $\delta_{\mathrm{CP}} = \{-\pi; 0; \pi\,\mathrm{rad}\}$ are excluded at 68% and 90%, but only $\delta_{\mathrm{CP}} = 0$ is excluded at 95% in Figure 6.5d. The $\sin^2\theta_{23}$ 68% CI mainly includes values in the higher octant as shown in Figure 6.5a.

CI range	$\sin^2\theta_{23}$	Δm^2_{32} $(\mathrm{eV}^2 cdotc^{-4})$	$\sin^2\theta_{13}$	δ_{CP} (rad)
68%	0.49 – 0.58	2.42 – 2.66 $\cdot 10^{-3}$	0.0208 – 0.0230	-2.45 – -0.88
90%	0.46 – 0.59	-2.68 – -2.50 $\cdot 10^{-3}$ 2.39 – 2.70 $\cdot 10^{-3}$	0.0200 – 0.0240	-3.02 – -0.38
95%	0.44 – 0.60	-2.70 – -2.46 $\cdot 10^{-3}$ 2.36 – 2.72 $\cdot 10^{-3}$	0.0195 – 0.0242	-π – -0.06 3.02 – π

Table 6.4: 68%, 90% and 95% CI obtained from the Markov chain with real ND280 and Super-K data and with the reactor constraint. The CI are computed from the marginal 1-dimensional posterior distributions shown in Figure 6.5.

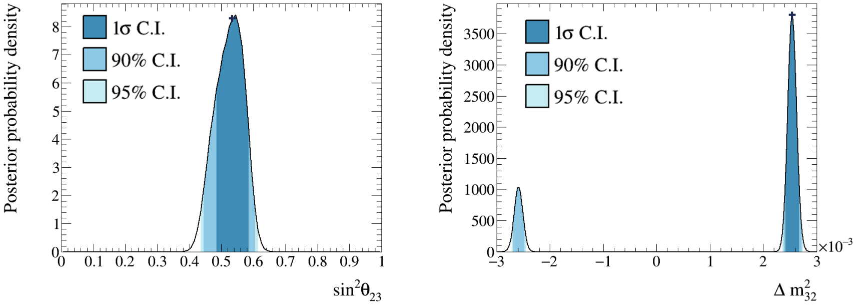

(a) $\sin^2\theta_{23}$ **(b)** Δm^2_{32}

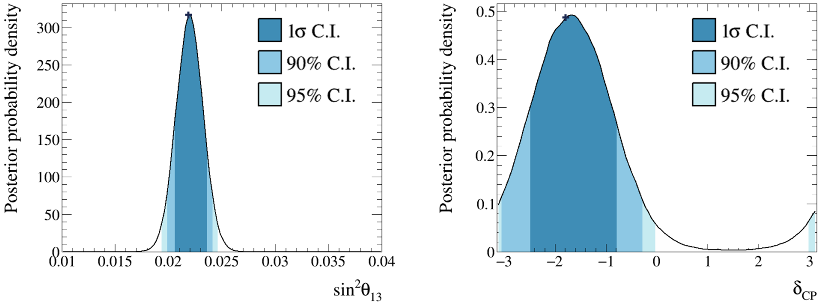

(c) $\sin^2\theta_{13}$ **(d)** δ_{CP}

Figure 6.5: The posterior probability density obtained when running the MCMC with real ND280 and Super-K data and with the reactor constrain. The dark(medium, light) blue area represent the 68%(90%, 95%) CI. The black cross indicate the location of the 4D mode given in Table 6.3.

Figure 6.6 shows the the marginal posterior probability density of the oscillation parameters $\sin^2\theta_{23}$, Δm^2_{32}, $\sin^2\theta_{13}$ and δ_{CP} obtained without the reactor constraint. Both mass orderings are included, but the parameter space is cropped to show values with $\Delta m^2_{32} > 0$ for better readability. In comparison with Figure 6.5c, the $\sin^2\theta_{13}$ CI are larger as they are not constrained by the Gaussian prior. Consequently, the δ_{CP} CI are also larger, the CP-conserving values being only excluded at 68%. The 2-dimensional histograms show the posterior probability density for two parameters, revealing the correlations between them and the relevant 68% and 90% CI. The CI extracted from the 1-dimensional posterior probability density are summarised in Table 6.5.

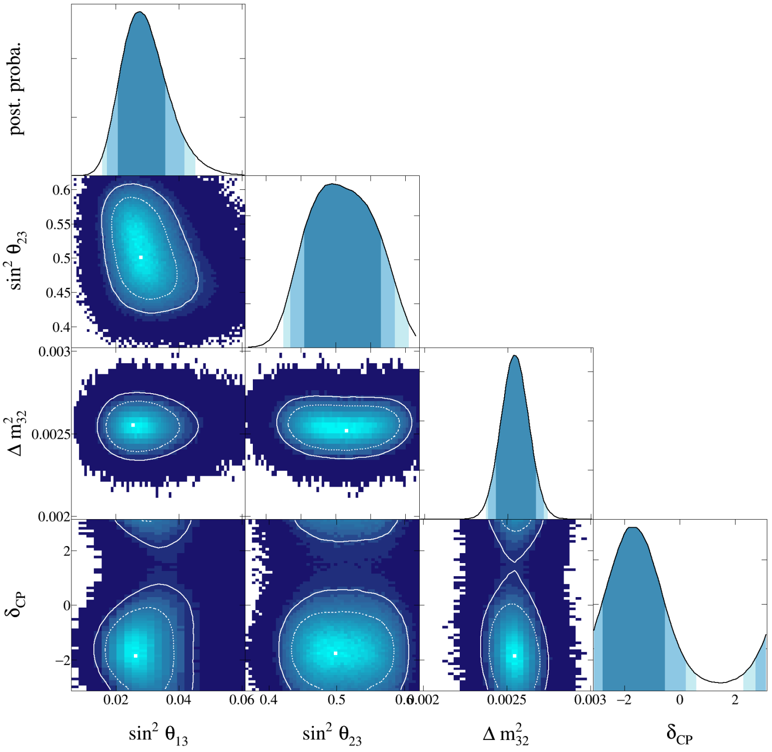

Figure 6.6: Oscillation parameters posterior probability densities obtained when running the MCMC with real ND280 and Super-K data and without the reactor constrain. The 2D histograms show the posterior probability as a blue gradient, the 68%(90%) CI as a dashed(solid) white line and the 2D posterior mode as a white square. The 1D histograms show the posterior probability as a black curve and the 68%(90%, 95%) CI as a dark(medium, light) blue area.

The posterior probability of parameters assuming a certain MO can be obtained by selecting steps with $\Delta m^2_{32} > 0$ (NO) or $\Delta m^2_{32} < 0$ (IO). Figure 6.7 shows the posterior probability densities and CI when selecting one or the other MO. The posterior probability on δ_{CP} has a different mode according to the mass ordering, and Figure 6.7a shows that the CI is smaller in the IO case when using the reactor constraint in the Markov chain. When the reactor constraint is not applied, the favoured $\sin^2\theta_{13}$ value also depends on the MO as shown in Figure 6.7b.

CI range	$\sin^2\theta_{23}$	Δm^2_{32} ($\mathrm{eV}^2 \cdot c^{-4}$)	$\sin^2\theta_{13}$	δ_{CP} (rad)
68%	0.46 – 0.55	-2.63 – -2.54 $\cdot 10^{-3}$ 2.44 – 2.65 $\cdot 10^{-3}$	0.0210 – 0.0350	-2.76 – -0.63
90%	0.44 – 0.58	-2.70 – -2.48 $\cdot 10^{-3}$ 2.39 – 2.70 $\cdot 10^{-3}$	0.0175 – 0.0410	$-\pi$ – 0.19 2.76 – π
95%	0.43 – 0.59	-2.72 – -2.45 $\cdot 10^{-3}$ 2.38 – 2.72 $\cdot 10^{-3}$	0.0160 – 0.0445	$-\pi$ – 0.57 2.32 – π

Table 6.5: 68% , 90% and 95% CI obtained from the Markov chain with real ND280 and Super-K data and without the reactor constraint. The CI are computed from the marginal 1-dimensional posterior distributions shown in Figure 6.6.

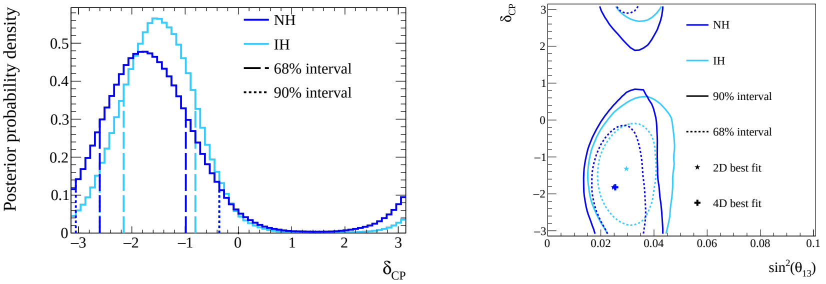

(a) With reactor constraint.

(b) Without reactor constraint.

Figure 6.7: Comparison of the posterior probability densities obtained when selecting normal or inverted neutrino MO. The left figure shows the δ_{CP} posterior probability density obtained from a Markov chain with reactor constraint when selecting NO (dark blue) or IO (light blue), with the 68% and 90% CI are as dashed lines. The right figures shows the 68% (dashed lines) and 90% (solid lines) CI obtained from a Markov chain without reactor constraint when selecting NO (dark blue) or IO (light blue). The 2D(4D) mode is shown as a star(cross).

6.3.1.3 Probability of mass ordering / octant

Using the probabilies of each $\sin^2\theta_{23}$ octant and MO in Table 6.6, the Bayes factor for the higher $\sin^2\theta_{23}$ octant is found to be:

$$B_{\text{high/low octant}} = 1.32\ (2.41) \tag{6.2}$$

where the value outside(inside) parentheses corresponds to the fit without(with) the reactor constraint. Similarly, the Bayes factor for the NO case is:

$$B_{\text{NH/IH}} = 2.28\ (3.72) \tag{6.3}$$

All Bayes factor are larger than the expected sensitivity given in Section 6.2.2.3, notably for the NO case. However, they are all below 6, considered as the minimal value for evidence, so the uncertainties on the parameters must be further reduced to be able to rule out the hypotheses.

	$\boldsymbol{\sin^2\theta_{23} < 0.5}$	$\boldsymbol{\sin^2\theta_{23} > 0.5}$	**Sum**
$\boldsymbol{\Delta m^2_{32} < 0}$ **(IO)**	0.137 (0.060)	0.168 (0.152)	**0.305 (0.212)**
$\boldsymbol{\Delta m^2_{32} > 0}$ **(NO)**	0.294 (0.233)	0.401 (0.555)	**0.695 (0.788)**
Sum	**0.431 (0.293)**	**0.569 (0.707)**	**1**

Table 6.6: Relative posterior probabilities for the $\sin^2\theta_{23}$ octant and the mass ordering from the Markov chain running with real ND280 and Super-K data. The values outside(inside) parentheses correspond to the fit without(with) the reactor constraint.

The δ_{CP} and sign of Δm^2_{32} parameters have a degenerate effect on the $\overset{(-)}{\nu}_e$ appearance probability given in Equation (2.28). Therefore, the NO probability varies with δ_{CP} as shown in Figure 6.8. The Bayes factor is found to be relatively low at ${\delta_{\text{CP}}}^{\text{best fit}} = -1.82\,\text{rad}$, while it is maximal at the 95% excluded value of ${\delta_{\text{CP}}}^{\text{max BF}} = 2\,\text{rad}$. Consequently, it appears that the most probable value of δ_{CP} is also the one that is the least sensitive to the Δm^2_{32} sign.

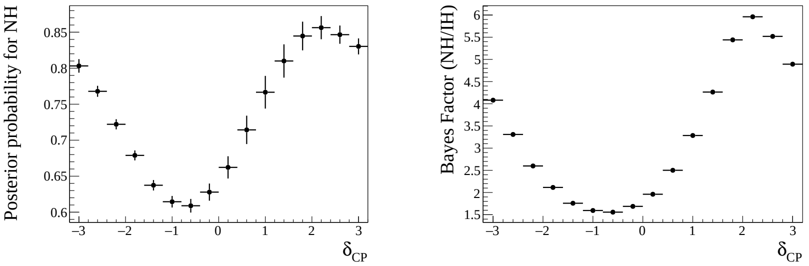

(a) Posterior probability **(b)** Bayes factor

Figure 6.8: Variation of the NO probability with δ_{CP} using the Markov chain with real ND280 and Super-K data and without reactor constraint. The left figure shows the posterior probability of the NO case as a function of δ_{CP}. The error bars represent the statistical uncertainty, computed from the effective number of independent steps as explained in Section A.1.3. The right figure shows Bayes factor of the NO hypothesis as a function of δ_{CP}.

6.3.2 Comparisons

6.3.2.1 Effect of the prior probability

The fact that the posterior probability relies on prior knowledge is often seen as an undesirable feature of Bayesian statistics. The choice of a correct prior is a delicate one, and one could ask if the "uninformative flat prior on δ_{CP}" chosen in Section 4.1.3 would not be more suitable for $\sin\delta_{\mathrm{CP}}$, as it is the quantity implying CP violation. Similarly the flat prior on $\sin^2\theta_{13}$ and $\sin^2\theta_{23}$ could be assigned on θ_{13} or θ_{23}. The dependence of the posterior probability can be quantified to understand if the prior probability strongly impacts the results. The power of the prior has not been estimated by re-running the Markov chain with an alternative prior, but by assigning a weight to every step thus mimicking the effects of a substitute prior. The transformation is applied the following way:

$$P(H(x)) \longrightarrow P'(H(x')) = P(H(x))\,\frac{dH(x)}{dH(x')} \tag{6.4}$$

where $P(H(x))$ is the initial prior as a function of the variable x, $P'(H(x'))$ is the substitute prior as a function of the variable x', and $\frac{dH(x)}{dH(x')}$ is the weight assigned to the steps of the chain. Despite the inability of this method to create the steps that an alternative prior could span, it is a computationally feasible estimation of a possible variation of the posterior probability. The following alternative priors have been tested:

(1) flat prior on $\sin\delta_{\mathrm{CP}}$ (instead of δ_{CP});

(2) flat prior on θ_{13} (instead of $\sin^2\theta_{13}$);

(3) flat prior on $\sin^2 2\theta_{13}$ (instead of $\sin^2\theta_{13}$);

(4) flat prior on θ_{23} (instead of $\sin^2\theta_{23}$).

Amongst those tests, only (1) and (2) had an effect on the CI estimated, shown in Figure 6.9. Figure 6.9a shows the same δ_{CP} posterior probability as in Figure 6.5d, but with the CI estimated with a flat prior on $\sin\delta_{\mathrm{CP}}$ overlaid. Because δ_{CP} is the parameter on which T2K is the least sensitive, the CI vary visibly and the 90% CI include the CP-conserving values $\delta_{\mathrm{CP}}=\{-\pi; 0\,\mathrm{rad}\}$ when a flat prior on $\sin\delta_{\mathrm{CP}}$ is assumed. A modification of the posterior probability with the prior indicates a weak constraint on the parameters, as demonstrated by the constraint on $\sin^2\theta_{23}$ not varying if the prior is flat in $\sin^2\theta_{23}$ or θ_{23}. Similarly, the constraint on $\sin^2\theta_{13}$ is not modified when the prior is changed from $\sin^2\theta_{13}$ to $\sin^2 2\theta_{13}$, but the CI undergo a transformation when it is changed to θ_{13} as shown in Figure 6.9b. However

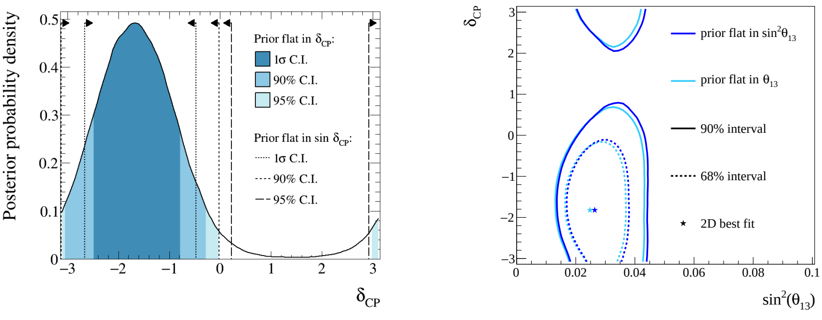

(a) δ_{CP}, with reactor constraint

(b) $\sin^2\theta_{13}$–δ_{CP}, without reactor constraint

Figure 6.9: Comparison of the CI obtained with alternative prior probabilities. The left figure shows the posterior probability density and 68%, 90% and 95% CI as blue areas obtained with the Markov chain with a flat prior in δ_{CP} with the reactor constraint applied. The dashes arrows represent the CI obtained when mimicking a flat prior on $\sin\delta_{\mathrm{CP}}$. The right figure shows the CI obtained with the Markov chain with a flat prior in $\sin^2\theta_{13}$ (dark blue) with no reactor constraint applied compared with mimicking a flat prior on θ_{13} (light blue). The dashed(solid) line represents the 68%(90%) CI.

the modification of the intervals is much weaker than the one seen by δ_{CP}, and the use of the reactor constraint (as a real alternative prior as the Markov chain is re-run with the Gaussian prior on $\sin^2\theta_{13}$) led to a control of this parameter as shown in Section 6.2.2.4.

6.3.2.2 Results compared to other experiments

Several neutrino oscillation experiments measured the $\sin^2\theta_{23}$–Δm^2_{32} parameters. The comparison of the T2K constraint with the Super-K, NOνA, MINOS+ and IceCube results is shown in Figure 6.10. Other experiments assuming the NO of neutrino masses, and using frequentist methods to measure a 90% CL, the T2K CI in the NO case has been converted into a constant $\Delta\chi^2$ interval on the figure. Super-K and IceCube agree with all experiments, but find larger intervals due to their lower sensitivity. NOνA excludes the maximal disappearance case of $\sin^2\theta_{23}$= 0.5, but also includes Δm^2_{32} values larger than the one found by T2K. On the contrary, the Δm^2_{32} interval found by MINOS+ includes lower values than found by T2K. Both NOνA and T2K are currently acquiring more data, the evolution of the constraint will be followed in the next years.

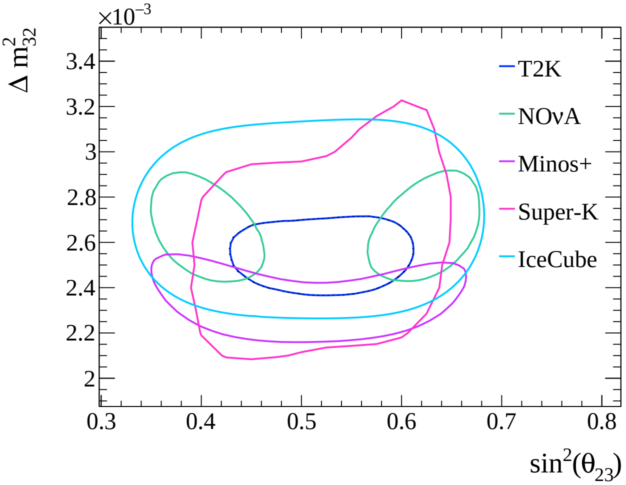

Figure 6.10: 90% CL in the $\sin^2\theta_{23}$–Δm^2_{32} space for several neutrino oscillation measurements assuming NO. The T2K constant $\Delta\chi^2$ interval has been obtained from the Markov chain with real ND280 and Super-K data and with reactor constraint.

6.3.2.3 Results compared to sensitivity

Section 4.2.2 describes the selection of events in the far detector, and Table 4.7 gives the expected and measured number of events in Super-K. If the numbers or $R_{\overset{(-)}{\mu}}$ events agree between the estimation and the actual measurement, more R_e are detected than expected. On the contrary, less $R_{\bar{e}}$ are detected than predicted, and this statistical fluctuation between the electron neutrinos and antineutrinos appearance leads to a stronger constraint on δ_{CP} than expected, as shown in Figure 6.11a. The $\sin^2\theta_{13}$ value preferred by the T2K data is also higher than the PDG fit to reactor experiments.

The $\overset{(-)}{\nu_e}$ appearance resolving $\pm\Delta m^2_{32}$, the CI shown in Figure 6.11b are smaller for the Markov chain with real Super-K data than with simulated Super-K data. The difference is stronger for $\Delta m^2_{32}< 0$, explaining the higher Bayes factor for the NO hypothesis computed in Section 6.3.2.2.

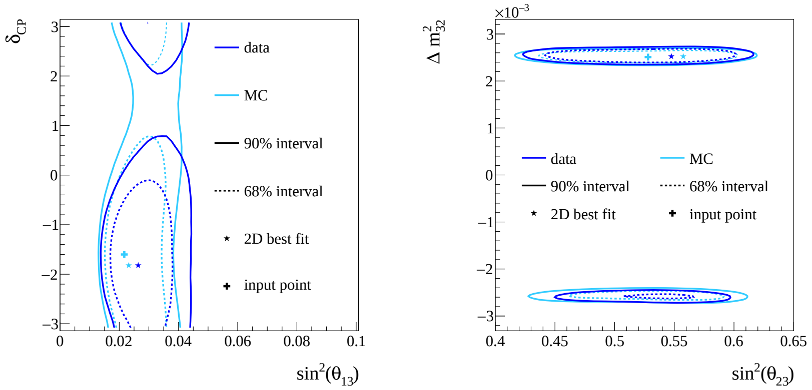

(a) $\sin^2\theta_{13}$–δ_{CP}, without reactor constraint

(b) $\sin^2\theta_{23}$–Δm^2_{32}, with reactor constraint

Figure 6.11: Comparison of the 68% and 90% CI between the Markov chain with simulated Super-K data (MC) and the Markov chain with real Super-K data (data) with both chains using real ND280 data. The 2D mode is shown as a star, and the value used to tune the MC as a cross.

6.3.2.4 Effect of the R_e CC-$1\pi^{\pm}$ sample

As mentioned in the introduction of this chapter, the Markov chain has been run initially with only four Super-K samples: the $R_{\overset{(-)}{\mu}}$ and $R_{\overset{(-)}{e}}$ CC-0π events. The R_e CC-$1\pi^{\pm}$ sample has subsequently been added, and this thesis presents the results including this fifth sample. Figure 6.12 shows the posterior probability density for both chains, with the reactor constraint applied on $\sin^2\theta_{13}$. The addition of the R_e CC-$1\pi^{\pm}$ sample leads to a better constraint of the CP violating phase, as both 68% and 90% CI are reduced when it is included.

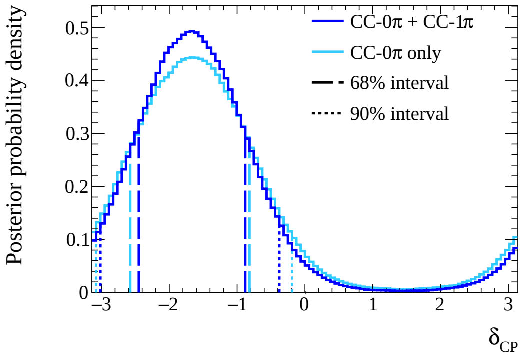

Figure 6.12: Comparison of the δ_{CP} posterior probability densities when using only the four Super-K $R_{\overset{(-)}{\mu}}$ and $R_{\overset{(-)}{e}}$ CC-0π samples (light blue) and when adding the R_e CC-$1\pi^{\pm}$ sample (dark blue). The Markov chain includes real ND280 and Super-K data and the reactor constraint is applied. The 68% and 90% CI are also shown as dashed lines.

6.3.2.5 Effect of the lepton angle information

The results presented above were all using the Super-K $R_{\overset{(-)}{e}}$ samples binned in $E_{\nu}^{rec} - \theta_{\ell}$, and the Super-K $R_{\overset{(-)}{\mu}}$ samples binned in E_{ν}^{rec}. The Markov chains have been run with the Super-K $R_{\overset{(-)}{e}}$ samples binned in E_{ν}^{rec} as well, and Figure 6.13 shows the comparison of CI between the two binning. The information brought by the lepton angle to distinguish ν_e from $\bar{\nu}_e$, and NC from CC, led to a better δ_{CP} constraint when using the sample binned in $E_{\nu}^{rec} - \theta_{\ell}$.

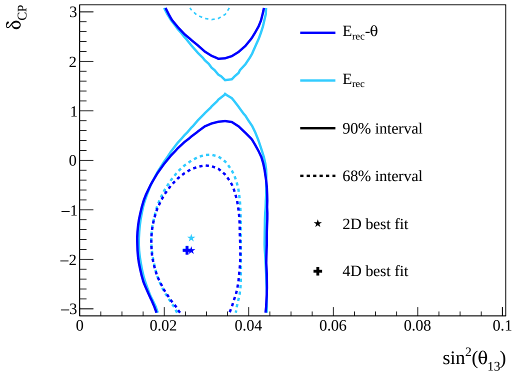

Figure 6.13: Comparison of CI when binning the Super-K $R_{\overset{(-)}{e}}$ samples in $E_{\nu}^{rec} - \theta_{\ell}$ (dark blue) or E_{ν}^{rec} (light blue). The dashed(solid) line represents the 68%(90%) CI, and the 2D(4D) modes are shown as a star(cross). The Markov chain includes real ND280 and Super-K data and the reactor constraint is not applied.

6.3.2.6 Constraint on the systematic parameters

As the Markov chain output is the joint posterior probability of all parameters, the posterior probability of the systematic parameters can be extracted as well. Figures 6.16 to 6.15 show the comparison of the posterior values and uncertainties on the flux, cross-section and detector parameters to the prior used in the Markov chains. The posterior uncertainties are determined by fitting the marginal 1D posterior probability densities with a Gaussian function, and taking the fitted mean and standard deviation as posterior value and uncertainties respectively. The values shown have been obtained from the Markov chain with real ND280 and Super-K data without the reactor constraint, since it has been observed that the $\sin^2\theta_{13}$ prior has a negligible effect on the systematic parameters.

Overall, the flux parameters are pulled towards higher values to compensate the deficit of predicted events seen in some ND280 samples, including the most populated ν-mode ν_μ CC-0π samples as summarised in Table 4.3. Similarly, the cross-section parameters of the Fermi momentum (pF) and MEC impacting the CCQE and MEC reactions dominating the CC-0π samples are pulled up; however the binding energy (Eb) and axial mass (MaQE) parameters are pulled down compared to the nominal value of 1. Because the number of predicted CC-$1\pi^+$ events is in excess compared to the data, the CC-Res parameters are pulled down (CA5 RES, MaRES), except the $I = \frac{3}{2}$

background (BgRES). In general, the posterior uncertainties on the other cross-section parameters do not differ drastically from their prior values, and are little constrained due to the small number of events in each relevant interaction mode. The ND280 detector posterior values are consistent with their prior, though most parameters have their uncertainty reduced. The posterior uncertainties on the Super-K detector parameters are in general similar to the prior.

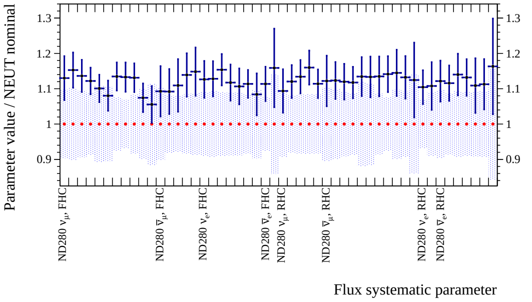

(a) Flux (ND280)

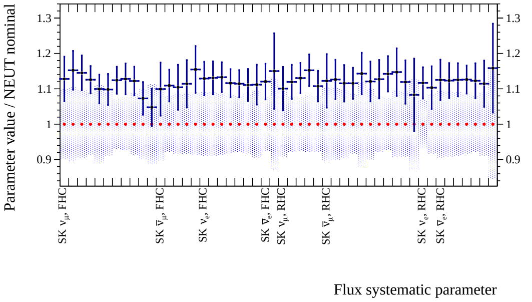

(b) Flux (Super-K)

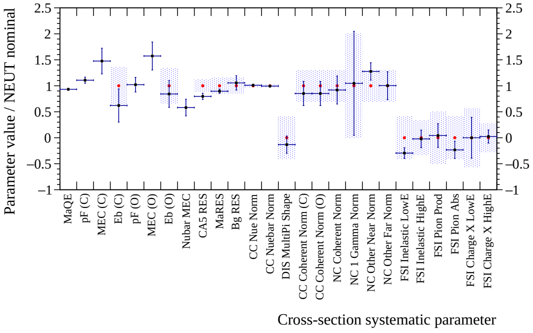

(c) Cross-section

Figure 6.14: Comparison of the prior (blue band) and posterior (black bar) probabilities on the systematic parameters for the flux and cross-section parameters. The y-axis represents the weight applied to the event to account for the modification of the parameter. The posterior probabilities have been determined with the Markov chain with real ND280 and Super-K data, and without the reactor constraint applied.

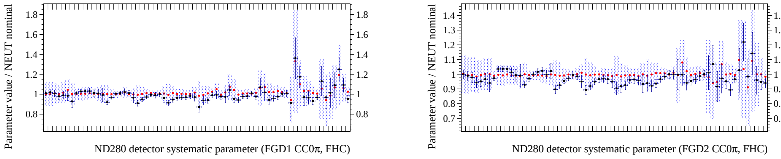

(a) ND280 detector, FGD1 CC-0π **(b)** ND280 detector, FGD2 CC-0π

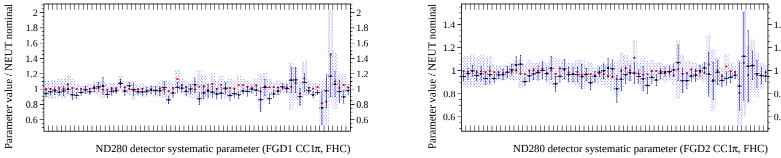

(c) ND280 detector, FGD1 CC-$1\pi^+$ **(d)** ND280 detector, FGD2 CC-$1\pi^+$

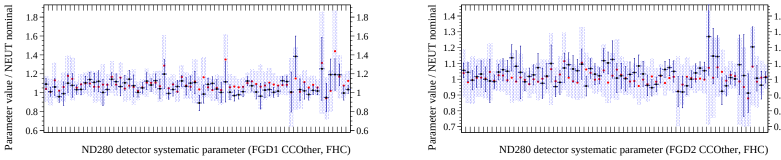

(e) ND280 detector, FGD1 CC-*other* **(f)** ND280 detector, FGD2 CC-*other*

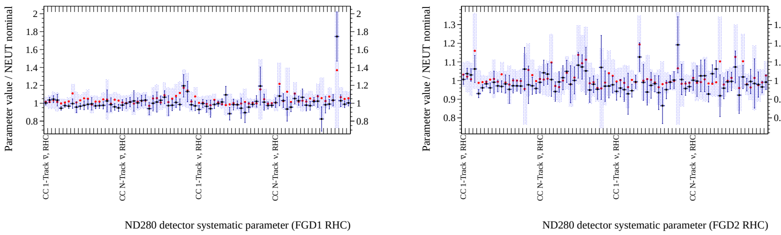

(g) ND280 detector, FGD1 $\bar{\nu}$-mode **(h)** ND280 detector, FGD2 $\bar{\nu}$-mode

Figure 6.15: Comparison of the prior (blue band) and posterior (black bar) probabilities on the systematic parameters for the ND280 detector. The y-axis represents the weight applied to the event to account for the modification of the parameter. The posterior probabilities have been determined with the Markov chain with real ND280 and Super-K data, and without the reactor constraint applied.

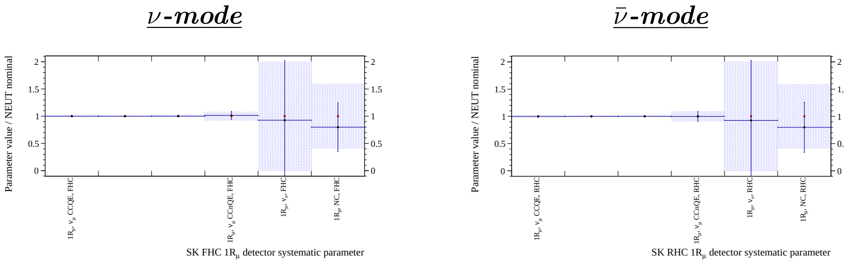

(a) Super-K detector R_μ CC-0π (d) Super-K detector $R_{\bar{\mu}}$ CC-0π

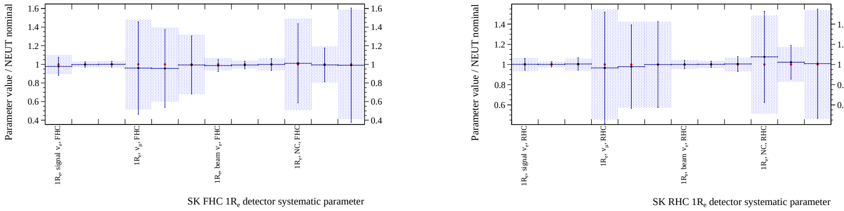

(b) Super-K detector R_e CC-0π (e) Super-K detector $R_{\bar{e}}$ CC-0π

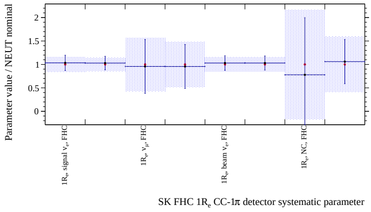

(c) Super-K detector R_e CC-$1\pi^{\pm}$

Figure 6.16: Comparison of the prior (blue band) and posterior (black bar) probabilities on the systematic parameters for the Super-K detector parameters. The y-axis represents the weight applied to the event to account for the modification of the parameter. The posterior probabilities have been determined with the Markov chain with real ND280 and Super-K data, and without the reactor constraint applied.

6.3.3 Postfit spectra and goodness-of-fit

6.3.3.1 Posterior predictive spectra

The posterior spectra are obtained with the same method described in Section 5.3.2, and Figure 6.17 shows the distribution of the $N = 2000$ spectra computed from N random selections of Markov chain steps. The distribution of events per bin is fitted with a Gaussian function, whose mean is taken as the best postfit spectrum. When selecting steps from the Markov Chain, it is possible to only reweight the spectrum for the values of the nuisance parameters at every step and assign a null value to the oscillation parameters. This way, the postfit unoscillated spectra can be obtained and compared to the oscillated ones as shown in Figure 6.18.

The spectra on the latter figure differ from the ones shown in Figure 4.8 since they represent the prediction according to the postfit parameters of the model, while the ones on Figure 4.8 represent the prediction according to the prefit parameters. The comparison between the prefit and postfit spectra is shown in Figure 6.18.

T2K finds a best fit $\sin^2\theta_{23}$ value of 0.534 (using the reactor constraint), while NOνA finds two degenerate values of $\sin^2\theta_{23}$= 0.404 or 0.624 [148]. The postfit spectra can be generated with the posterior predictive method while fixing the $\sin^2\theta_{23}$ value to one of the best NOνA fit value. The comparison of the NOνA-tuned T2K postfit spectrum of the Super-K R_μ sample with the one of Figure 6.17a is shown in Figure 6.20. As expected, the T2K best fit spectrum agrees better with the T2K data than the NOνA spectra that overestimates the number of events at low energy. When computing a χ^2 between the predicted spectrum and the data with a Poisson log-likelihood ratio, the T2K best fit spectrum has the lowest value of $\chi^2_{T2K}/NDoF = 0.58$, while the NOνA best fit spectrum generated with $\sin^2\theta_{23}$ in the (higher)lower octant have a higher value of $\chi^2_{NO\nu A}/NDoF = 0.88(0.85)$ (with $NDoF$ the number of degrees of freedom, i.e. the number of bins in the histogram subtracted of one).

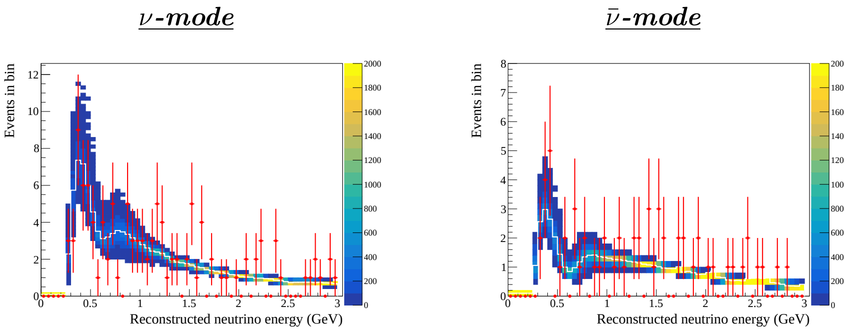

(a) R_μ CC-0π **(d)** R_μ CC-0π

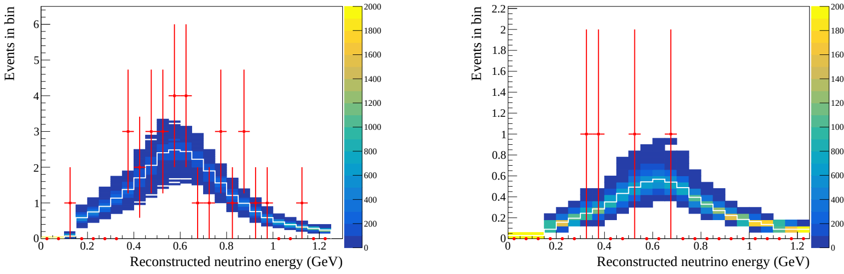

(b) R_e CC-0π **(e)** R_e CC-0π

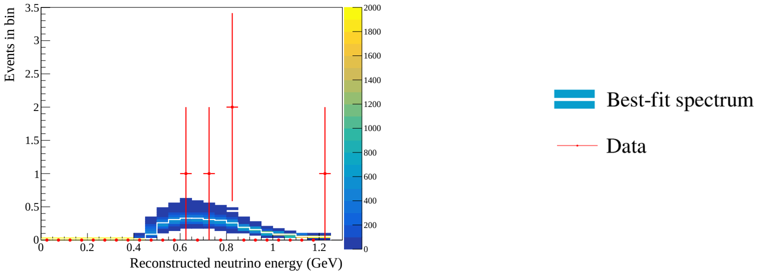

(c) R_e CC-$1\pi^{\pm}$

Figure 6.17: Postfit energy spectra of the five Super-K samples, with the x-axis as the neutrino reconstructed energy E_ν^{rec} and the y-axis the number of events per bin. The blue gradient shows the distribution of events per bin obtained when sampling steps from the Markov Chain (with reactor constraint) and recalculating the number of events according to the parameters at every step. The white line shows the best postfit spectra obtained from a Gaussian fit to the distribution of event rates in every bin. The left column shows the ν-mode samples and the right column the $\bar{\nu}$-mode ones, and the Super-K data are also shown as red dots.

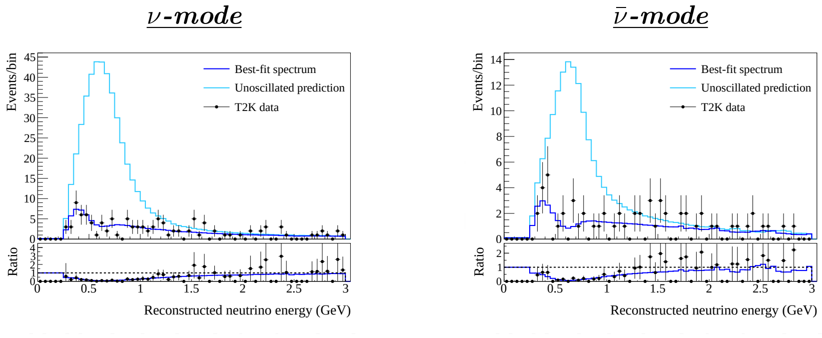

(a) R_μ CC-0π

(d) R_μ CC-0π

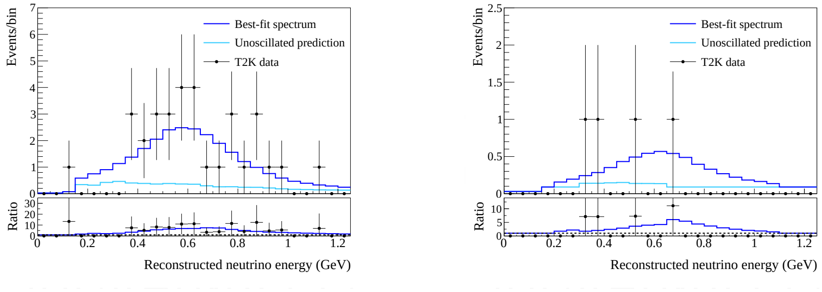

(b) R_e CC-0π

(e) R_e CC-0π

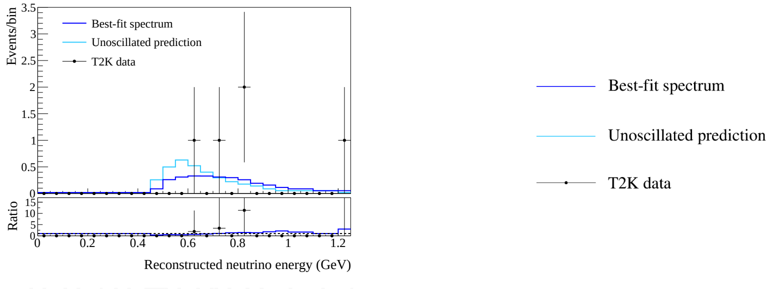

(c) R_e CC-$1\pi^{\pm}$

Figure 6.18: Postfit energy spectra of the five Super-K samples; the x-axis showing the neutrino reconstructed energy and the y-axis the number of events per bin. In the top histograms, the dark blue line shows the best postfit spectrum including the postfit oscillation values as shown in Figure 6.17. The light blue line shows the best postfit spectrum assuming null oscillation parameters. In the bottom histograms, the dark blue line shows the ratio of oscillated to unoscillated best postfit spectrum. The left column shows the ν-mode samples and the right column the $\bar{\nu}$-mode ones, and the Super-K data are also shown as black dots.

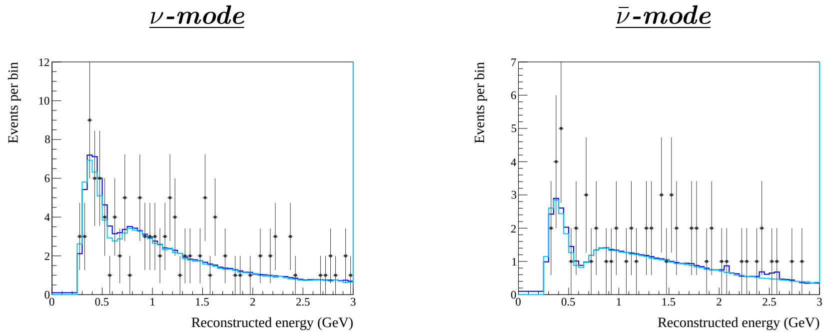

(a) R_μ CC-0π

(d) R_μ CC-0π

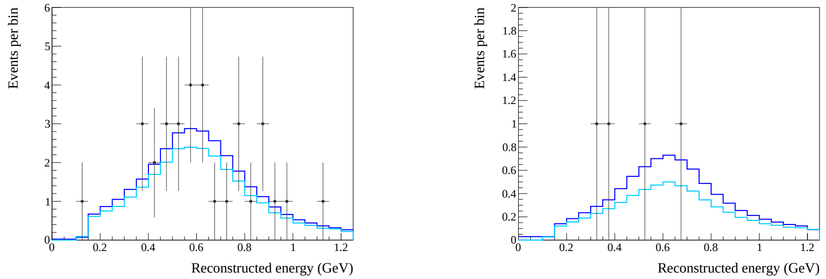

(b) R_e CC-0π

(e) R_e CC-0π

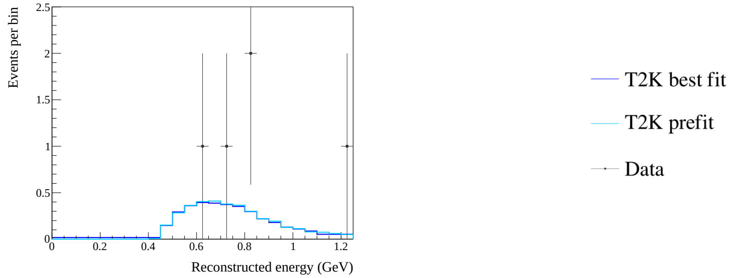

(c) R_e CC-$1\pi^\pm$

Figure 6.19: Comparison of the prefit and postfit spectra of the five Super-K samples. The prefit spectra (light blue) are from Figure 4.8 and generated with the prefit value of the oscillation and systematic parameters. The postfit spectra are from Figure 6.17 and are generated with the posterior predictive method. The left column shows the ν-mode samples and the right column the $\bar{\nu}$-mode ones, and the Super-K data are also shown as black dots.

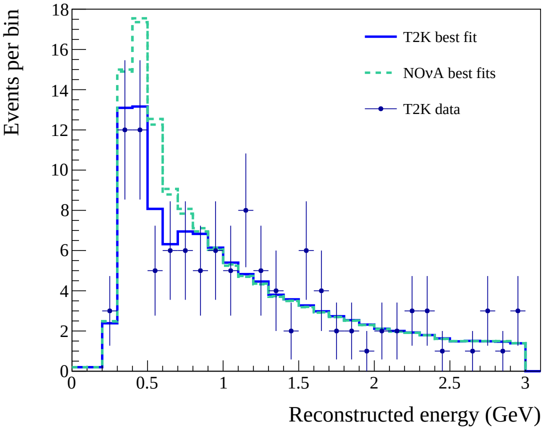

Figure 6.20: Comparison of the postfit predicted spectrum of the Super-K R_μ sample obtained with the posterior predictive method between constraining $\sin^2\theta_{23}$ with the T2K or the NOνA $\sin^2\theta_{23}$ best fit. The blue spectrum is the T2K best fit shown in Figure 6.17a. The teal spectra are the T2K postfit spectra obtained when $\sin^2\theta_{23}$ is fixed to one of the two NOνA best fit value. The T2K data are also shown as blue points.

6.3.3.2 Posterior predictive p-value

In order to evaluate the goodness of the fit, a p-value is computed from the posterior predictive spectra shown in Figure 6.17 following the procedure in [149]. At every step thrown to obtain the posterior spectra, a fake dataset is simulated by randomly throwing a new spectrum from the one predicted with the parameters of the step. The Super-K events only are thrown, in order to have a p-value that estimate the goodness of the oscillation parameters fit, and not of the nuisance parameters fit as it would result from including the ND280 samples. Two χ^2 are computed with a Poisson log-likelihood ratio, one between the fake data and the MC rates, the other between the real data and the MC rates. The distribution of χ^2 values is shown in Figure 6.21, from which the p-value is computed. The p-value represents the probability, according to the model obtained a posteriori, to observe the measured data or data agreeing less than the measured ones. It is equivalent to a hypothesis testing where the alternate hypothesis includes the whole subset of variations in the observed data. The fake dataset represents the statistical variations in the observed data, and the p-value is computed

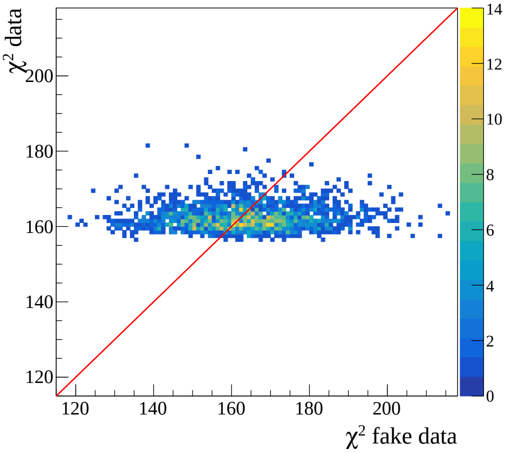

Figure 6.21: Distribution of χ^2 obtained when comparing the postfit to real data (χ^2 data) and to fake data (χ^2 fake data). The fake data are obtained from a throw of the predicted rate during the posterior predictive sampling of the Markov chain (without reactor constraint). The red line represents the line where χ^2 (data) $= \chi^2$ (fake data). A p-value can be computed as being the proportion of entries under the red line.

to be the proportion of steps for which the real data χ^2 is lower than the fake data χ^2, indicating a better agreement between the postfit model and the real data than with fake data. The p-value obtained for the fit without the reactor constraint is 0.51, for the fit with the reactor constraint is 0.49. As expected, the goodness-of-fit is better without the reactor constrain as the $\sin^2\theta_{13}$ value found by T2K is slightly different from the one found by the reactor experiments (used as a reactor constraint). However, both p-values are very similar and above 0.05, that has been chosen beforehand as the threshold under which the goodness-of-fit is considered too low for the fit to be exploited.

Conclusion:

A simultaneous analysis of the ND280 and Super-K samples, including the $R_{\overset{(-)}{\mu}}$ and $R_{\overset{(-)}{e}}$ samples, has been performed. $\sin^2\theta_{23}$ is found to be consistent with maximal mixing, and the NO of neutrino masses is favoured. The $\sin^2\theta_{13}$ best fit point constrained by T2K data only has a higher value than the one obtained by the PDG fit to reactor experiments, but the reactor best fit is inside the 68% CI. When constrained with T2K data only, the CP conserving values of $\delta_{\mathrm{CP}} = \{-\pi; 0; \pi\,\mathrm{rad}\}$ are excluded at 68%. However, the δ_{CP} parameter is degenerate with $\sin^2\theta_{13}$ and using the reactor experiment results in a Gaussian prior leads to exclude the CP conserving values at 90% CI. A stronger constraint on δ_{CP} requires an increase of the statistical power of the fit as well as a decrease of the systematic uncertainties, and the next chapter will review proposed solutions for the future of the T2K experiment.

CHAPTER 7

Conclusion and outlooks

7.1 Summary of the results

The results presented in this thesis provide the strongest constraints on the neutrino oscillation parameters measured in T2K. The simultaneous analysis of five $R_{\overset{(-)}{\mu}}$ and $R_{\overline{e}}$ Super-K samples, with the systematic parameters estimated with seven ν_μ and $\overset{(-)}{\nu}_\mu$ CC-interactions samples in ND280, led to the measurement of four of the six U_{PMNS} parameters as described in Chapter 6 and summarised on Tables 6.4 and 6.5.

When using T2K data only, $\sin^2\theta_{13}$ is found to be $0.025^{+0.01}_{-0.04}$, a value higher than the one found by the global fit of reactor experiments [131] but including it in the 1σ CI. Because T2K has less power in constraining $\sin^2\theta_{13}$ than the reactor experiments, the estimation of the other parameters has been done with T2K data only initially, then using the reactor results to constrain $\sin^2\theta_{13}$ (the reactor constraint).

T2K is a leading experiment in measuring $\sin^2\theta_{23}$, that is found to be $0.51^{+0.04}_{-0.05}$ with T2K data only and $0.53^{+0.05}_{-0.04}$ when using the reactor constraint, that has little effect on the measurement of this parameter. Both

$\sin^2\theta_{23}$ values are consistent with maximal $\overset{(-)}{\nu}_\mu$ disappearance, that is ruled out at 90% by the NOνA experiment [148]: future results will indicate if the two experiments are in tension or if they will converge to similar interval estimates.

The value of the Δm^2_{32} is constrained to be $2.54{\cdot}10^3\,\mathrm{eV}^2\cdot\mathrm{c}^{-4}$ when using T2K data only, with a 1σ CI including values in both NO ($[-2.63; -2.54\cdot 10^3\,\mathrm{eV}^2\cdot\mathrm{c}^{-4}]$) or IO ($[-2.44; -2.65{\cdot}10^3\,\mathrm{eV}^2\cdot\mathrm{c}^{-4}]$) of neutrino masses. Adding the reactor constraint does not result in a different best fit value, but leads to a better constraint on the parameter as the 1σ CI is restricted to the NO: $\Delta m^2_{32}= 2.54^{+0.12}_{-0.12}\cdot 10^3\,\mathrm{eV}^2\cdot\mathrm{c}^{-4}$

The ability of long-baseline accelerator neutrino experiments to measure the CP-violating phase originates from the non-zero value of $\sin^2\theta_{13}$, as it can be seen in Equation (2.28). T2K is currently the experiment providing the better constraint on δ_{CP}, as it is measured to be $-1.82^{+1.19}_{-0.94}$ rad with T2K data only. As the δ_{CP} value is strongly degenerate with the $\sin^2\theta_{13}$ value, applying the reactor constraints enables to reduce the uncertainty on the parameter, found to be $\delta_{\mathrm{CP}}= -1.79^{+0.91}_{-0.66}$ rad. Both intervals include the maximal CP-violation value of $\delta_{\mathrm{CP}}=-\frac{\pi}{2}$, that could enable the observed baryogenesis if leptogenesis would occur when the Universe thermal energy is of the order of the mass of the lightest right-handed neutrino [150].

By performing the analysis with a MCMC method, the results aforementioned include both neutrino mass orderings while most measurements provided by other experiments assume NO or IO. Due to the relatively short baseline of T2K (295 Km), the matter effect potential have little effect on the total oscillation probability and the mass ordering cannot be determined with strong accuracy. The Bayes factor for the NO is 2.28 when using T2K data only, and 3.72 when adding the reactor constraint.

In addition to measure the U_{PMNS} parameters, tests of the 3ν SM consistency can be performed by decoupling the parameters estimated with neutrino and antineutrino oscillations. The analysis presented in Chapter 5 estimates $\sin^2\theta_{23}$ and Δm^2_{32} from R_μ disappearance, and $\sin^2\bar{\theta}_{23}$ and $\Delta\bar{m}^2_{32}$ from $R_{\bar{\mu}}$ disappearance, in order to probe the presence of CPT violation or NSI. The agreement of the estimated parameters does not indicate any beyond-SM physics in this channel, but the study could benefit to be performed when more data will be available as the effect would be expected to be small.

7.2 Future of neutrino oscillation

As outlined in Chapter 2, the estimation of neutrino oscillation is motivated by further aims than the measurement of the free parameters of the SM. An accurate knowledge of the U_{PMNS} elements would enable to estimate the unitarity of the matrix, which would indicate mixing to unknown neutrinos if it is not achieved. Extensions of the SM postulating flavour symmetry breaking predict different template of U_{PMNS} matrix, that requires a precise measurement of neutrino oscillation parameters to be distinguished: notably an estimation of $\cos\delta_{\text{CP}}$ with an uncertainty of $\sim 10\%$ is required by some models [58]. Furthermore, one could note that such symmetry breakings give rise to scalar particles, usually denominated as *flavons*, that have not been observed as of today but could provide an additional research channel in order to probe those models. Additionally to probing physics beyond-SM, the value of the δ_{CP} phase is a key ingredient of the postulated phenomenon of leptogenesis that models the transfer of CP-violation in the neutrino sector to the observed baryogenesis. While the results shown in this thesis are the best constraint on the oscillation parameters provided by the T2K experiment at the time of composition, probing the unitarity of the U_{PMNS} matrix, its compatibility with flavour symmetries or the possibility of leptogenesis requires an even better knowledge of the neutrino oscillation parameters. The sections below review proposals aiming at decreasing the statistical or systematic uncertainties on their estimation. However, one can note from Figure 2.10 that the unitarity of the U_{PMNS} matrix requires measurements of $\overset{(-)}{\nu}_\tau$ appearance that are not accessible with the T2K beam energies. Furthermore, the leptogenesis model postulates the existence of right-handed neutrinos, yet to be found. Consequently, progress on neutrino oscillation physics must be achieved with a consistent roadmap of the next theoretical and experimental developments in order to access the unknown sectors of Physics.

7.2.1 Decreasing the statistical uncertainties

The main challenge in neutrino physics is their cross-section, of the order of the femtobarn ($10^{-39}\,\text{cm}^{-2}$), that limits the number of events occurring in the detectors. This section reviews propositions to increase the statistical power of the analysis.

7.2.1.1 Extension of Super-Kamiokande fiducial volume

The current Super-K FV is defined as the volume of the inner detector excluding the volume at less than 2 m from the wall, as shown in Figure 7.1. The resulting volume has a net mass of 22.5 Ktons, while the total mass of the ID is 32 Ktons. While the current FV has been determined in order to minimise the background, notably of interactions in the wall separating the ID from the OD, ongoing studies suggest that a hard cut on the vertex location can be avoided. This analysis benefits from a new reconstruction algorithm developed for Super-K, that is currently used to distinguish multiple $e^{\pm}$ rings in the Super-K selection described in Section 4.2.2. The current reconstruction algorithm is based on a *backward fitting* method, estimating the vertex location, number of rings and PID from the pattern of hits recorded by the PMTs. On the contrary, the new algorithm uses a *forward fitting* method predicting an hypothetical event, and comparing the likelihood of its topology with the one recorded by the detector. The second method has shown to be very powerful in rejecting the background, and offers the possibility to select events in the now-rejected volume around the wall with a projected increase of signal events of $\sim 15\%$.

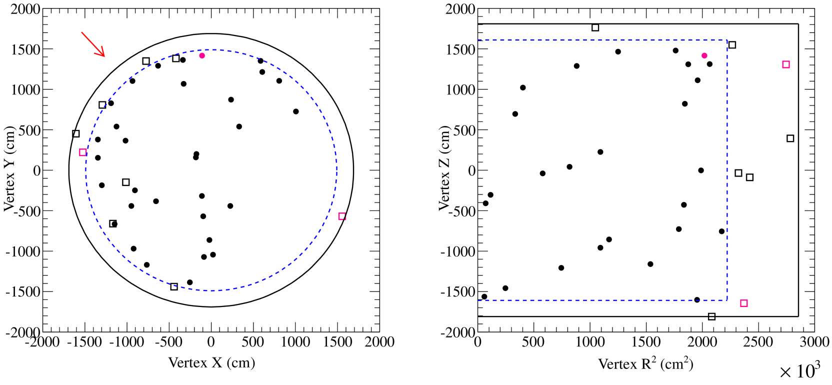

(a) R_e, $x-y$ vertex

(b) R_e, R^2 vertex

Figure 7.1: Vertex distribution of the R_e events selected in Super-K during runs 1-7 (events in pink correspond to run 7). The dashed blue line represents the FV defined to exclude the volume 2 m from the walls. The left figure shows the $x-y$ position of the vertex, while the right one shows the R^2 position. Plain dots show events selected as inside the FV, while open squares show events outside the FV.

7.2.1.2 T2K-II

T2K current goal is the accumulation of $7.8 \cdot 10^{21}$ POT, after which it plans to enter the T2K-II phase extending the POT up to $20 \cdot 10^{21}$ POT [151]. With the current expectation of the T2K beam power to increase up to 1.3 MW (from now 0.74 MW), this goal should be achieved by 2025. If the new reconstruction algorithm and expansion of the FV mentioned in Section 7.2.1.1 are applied, and new Super-K samples such as the R_e CC-$1\pi^{+/-}$ sample described in Section 4.2.2 are added, the efficiency in selecting events is assumed to increase of $\sim$ 50%. If the systematic uncertainties on the number of selected events decrease to 4%, sin $\delta_{\mathrm{CP}}= 0$ rad corresponding to no CP violation can be excluded at 3σ if $\delta_{\mathrm{CP}}= -\frac{\pi}{2}$ rad and the neutrino mass ordering is normal as shown in Figure 7.2a. If another experiment measures the mass ordering to be normal, the 3σ exclusion can be obtained for a wider range of δ_{CP} values including $\delta_{\mathrm{CP}}= -\frac{\pi}{2}$ rad.

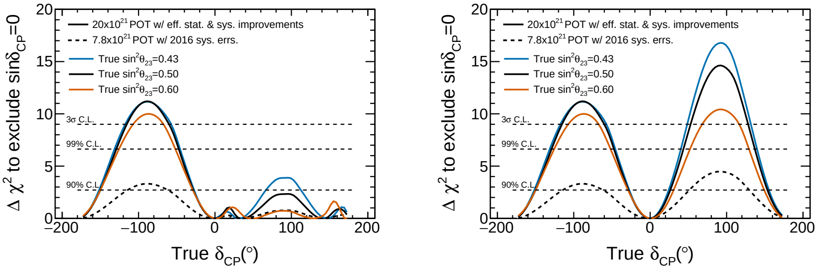

(a) Unknown mass ordering

(b) Known mass ordering

Figure 7.2: Expected sensitivity of T2K-II to exclude sin δ_{CP} as a function of δ_{CP}, the POT and the $\sin^2\theta_{23}$ true value. The dashed line shows the sensitivity for the full T2K statistics and assuming the same systematic uncertainties as in this thesis. The solid lines shows the sensitivity for the full T2K-II statistics, assuming a 50% increase in statistical efficiency and a 4% systematic uncertainties on the variation in the number of events at Super-K. Amongst the solid lines, the blue one assumes $\sin^2\theta_{23}= 0.43$, the black one assumes $\sin^2\theta_{23}= 0.5$ and the orange one assumes $\sin^2\theta_{23}= 0.6$. Both figures assume NO of neutrino mass, 7.2a assume that is is unknown and 7.2b that it has been determined by another experiment. From [151].

7.2.1.3 Hyper-Kamiokande

A radical reduction of the statistical uncertainty on the estimation of neutrino oscillation parameters require a bigger far detector. The proposed Hyper-K experiment would hold two Cherenkov detectors totalling a total net mass of 1 Mtons, 20 times the current net mass of Super-K [39]. In addition of increasing the number of events in the oscillated samples, the high number of target nuclei would lead to the detector uncertainties, determined from atmospheric neutrinos as outlined in Section 4.3.4, to decrease of about one order of magnitude. This is of particular importance as the systematic uncertainties on the number of Super-K events due to the detector are on the same order of magnitude as the flux and cross-section uncertainties after the constraint brought by the ND280 samples, as shown in Tables 4.15 and 4.16. Conservatively assuming that the the flux and cross-section uncertainties constrained by T2K will not vary when Hyper-K will be built, and with the T2K beam power planned to increase up to 1.3 MW, Hyper-K would be able to measure δ_{CP} with an accuracy of better than 0.33 rad (19°) as shown in Figure 7.3a if the neutrino mass ordering is normal (although assumed unknown). The 3σ sensitivity corresponding to evidence of CP violation is reached for 76% of the δ_{CP} value, and the 5σ sensitivity corresponding to discovery for 58%. Other parameters will also benefit from the decrease of statistical uncertainties, as shown by the $\sin^2\theta_{23}$-Δm^2_{32} constraint in Figure 7.3b.

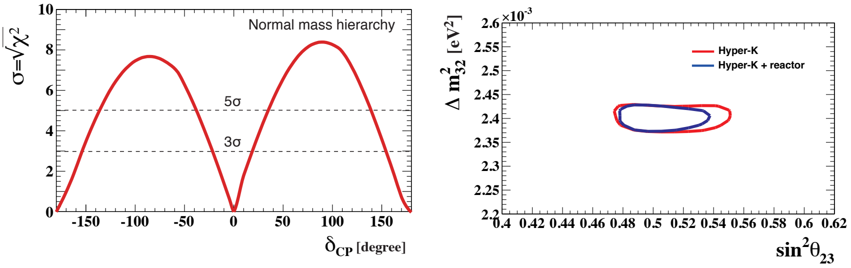

(a) δ_{CP}

(b) $\sin^2\theta_{23}$-Δm^2_{32}

Figure 7.3: Expected sensitivity of Hyper-K to measure the neutrino oscillation parameters. The left figure shows the δ_{CP} $\Delta\chi^2$, assuming NO but without knowing the mass ordering. The right figures shows the 80% CL in the $\sin^2\theta_{23}$-Δm^2_{32} space, assuming NO but without knowing the mass ordering, with (blue) and without (red) information on $\sin^2\theta_{13}$ from the reactor experiments. From [39].

7.2.2 Decreasing the systematic uncertainties

While the current uncertainties on the oscillation parameter estimation obtained with T2K are dominated by the statistical uncertainties, the proposals described in Section 7.2.1 plan to increase the number of events, leading for systematic uncertainties from the flux, interaction models and detector efficiencies to become a limitation on the future measurements. This section reviews suggestions aiming at decreasing the systematic uncertainties on the oscillation parameter estimation.

7.2.2.1 Interaction model

Latest years have shown that neutrino cross-sections are little known at low energy, notably the MiniBooNE differential CCQE measurements obtained with a $\overset{(-)}{\nu}_\mu$ beam of mean energy $< E_\nu >= 0.665\,\mathrm{GeV}$ show an excess compared to predictions [152, 153], that is not seen by the MINERνA measurements that uses $< E_\nu >= 3.5\,\mathrm{GeV}$ [154, 155]. The discrepancy has led to the effort of the community of theoretical physicists to develop nuclear models taking into account the latest measurements, such as the 2-protons 2-holes (2p2h) model [111] and the RPA model [110] including short and long-range correlations in the nucleus. The T2K collaboration is leading an ongoing effort in comparing the latest predictions to the available datasets [105] in order to incorporate the most up-to-date models in the NEUT generators. The uncertainties relative to the shape of the 2p2h cross-section and RPA are currently being implemented to be used in the next oscillation analysis.

7.2.2.2 Near detector upgrade

The expected T2K-II sensitivity shown in Figure 7.2 assume a reduction of the systematic uncertainties on the number of Super-K down to 4%. In addition to the improvement of the models implemented in the neutrino interaction generator, the near detector can be modified in order to deliver a better constraint on the flux and interaction parameters.

A new on-axis detector named WAGASCI, that will be placed beside INGRID, is under construction [156]. Its design alternates two layers of hydrocarbon and two layers of water as targets, surrounded by muon ranger detectors aiming at measuring the $\mu^\pm$ momentum as shown in Figure 7.4a.

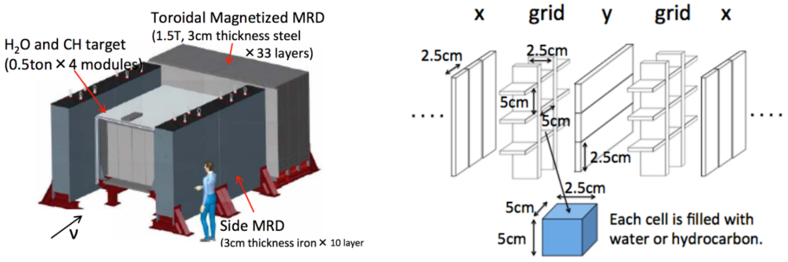

(a) Full detector. **(b)** Layer structure.

Figure 7.4: The WAGASCI detector, currently under construction. The central part of 7.4a holds two water layers and hydrocarbon layers as target, surrounded by Muon Ranger Detectors (MRD) aiming at measuring the $\mu^{\pm}$ momentum. The layer grid is detailed on 7.4b. From [157].

The layers have grid structure segmented into $5 \times 5 \times 2.5\,\mathrm{cm}^3$ cases from which the water can be emptied in order to measure the neutrino cross-section on water compared to carbon with a subtraction method, with a projected accuracy of few percents.

Upgrades have also been considered for the off-axis near detector ND280, which current limitations are the poor efficiency in selecting high-angle tracks, as well as a coarse granularity. A new design, including a rotation of the target detector and the addition of four TPCs as shown in Figure 7.5, is under investigation [158]. It would notably enable a high acceptance of tracks at ±180° in the $y - z$ plane, while it is now restricted to ±53°.

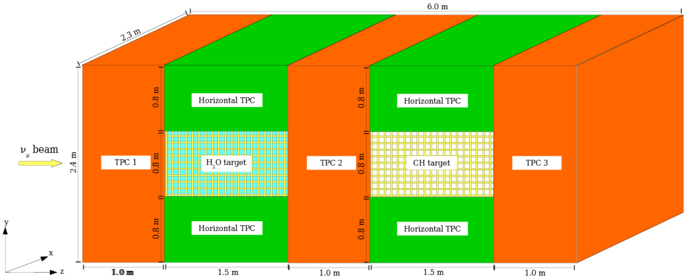

Figure 7.5: Proposed configuration for an upgrade of ND280. The three orange vertical TPCs are left unchanged. The H_2O and CH target are rotated, and might replaced by a finer grained design. The four green horizontal TPCs are added. From [159].

7.2.2.3 Intermediate detector

It has been postulated that a Cherenkov near detector would be a powerful addition to a composite detector to constraint the far detector event rate, as it relies on the same technology. The Tokai Intermediate Tank for the Unoscillated Spectrum (TITUS) detector is a proposed 2.1 Kton water detector proposed to be located off-axis at a distance of $\sim$ 2 Km from the target, where the flux is found to be the most similar to the far detector [160]. The cylindrical detector shown in Figure 7.6a would have the water doped with gadolinium (Gd) in order to tag neutrons produced in $\bar{\nu}_\mu$ and $\bar{\nu}_e$ CCQE reactions, enabling to distinguish ν_μ and ν_e from $\bar{\nu}_\mu$ and $\bar{\nu}_e$ without magnetic field.

An alternative method is proposed by neutrino Precision Reaction Independent Spectrum Measurement (nuPRISM), that also holds a Cherenkov detector shown on the middle in Figure 7.6b. The cylindrical water target can move vertically in order to measure the flux between 1 and 4° off-axis, the far detector flux being reproduced by a linear combination of the different flux templates for several off-axis angles [161]. Both detectors predict improvements in reducing the systematic uncertainties on the estimation of neutrino oscillation parameters.

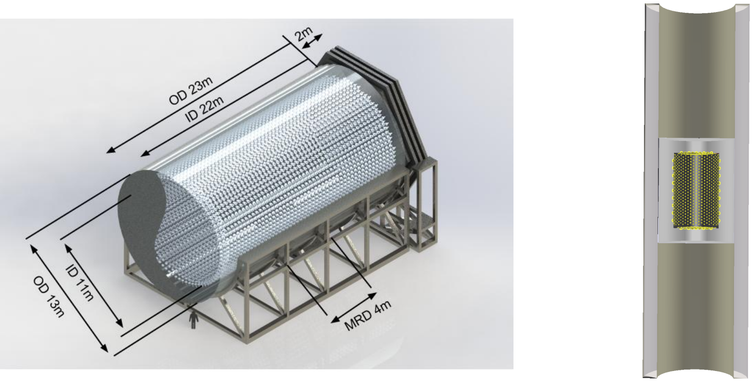

(a) TITUS

(b) nuPRISM

Figure 7.6: Two proposal for an intermediate Cherenkov detector.
7.6a: TITUS is a fixed water detector, *Gd* doped detector that would be located off-axis at a distance of $\sim$ 2 Km from the target. From [160]. 7.6b: nuPRISM (right) is a detector which water target can move vertically to measure the flux between 1 and 4° off-axis. From [161].

7.2.3 T2K run 1-8 analysis

In 2016-2017, T2K has acquired an additional POT of $7.252 \cdot 10^{20}$ in neutrino-mode during the run 8, leading to a total POT of $14.734 \cdot 10^{20}$ in neutrino mode (no antineutrino mode have ran). A continuation of the oscillation analysis presented in this thesis has been performed with those data, using the same statistical framework as described on Section 4. The main updates concern the usage of a new Super-K reconstruction algorithm that enabled to remove the hard-cut on the Super-K fiducial volume as described on Section 7.2.1.1, and the implementation of new interaction parameters controlling the uncertainties on short and long range correlations as explained on Section 7.2.2.1.

With those improvements, the expected and observed number of events selected in Super-K is given on Table 7.1. The observed number of R_μ rings match the simulation similarly to the run 1-7 analysis, furthermore the numbers of R_e CC-0π events show less discrepancy as well. The larger statistic obtained by the new neutrino-mode data, but also from the increase of events that were cut to be outside the fiducial volume for the $R_{\bar{e}}$ sample, enabled a disappearance of the probable statistical fluctuation previously observed. Only the observed number of R_e CC-$1\pi^\pm$ interactions is twice larger than expected.

	R_μ CC-0π	R_e CC-0π	R_e CC-$1\pi^\pm$	$R_{\bar{\mu}}$ CC-0π	$R_{\bar{e}}$ CC-0π
post-ND280 fit MC	267.8	73.5	6.92	63.1	7.93
data	240	74	15	68	7

Table 7.1: Predicted total number of events for the five Super-K samples in the oscillated case (using the parameters of Table 4.5), with the Super-K MC tuned to the output of a ND280-only fit. The number of events detected is also shown as data, and data from runs 1 to 8 have been used.

Preliminary analyses present smaller credible intervals when using T2K data only, but without changing the conclusion on the δ_{CP} allowed range as shown on Figure 7.7a. However, including the reactor constraint leads to exclude CP-conservation at 2σ (95.4%), as shown on Figure 7.7b. The $\sin^2\theta_{23}$ value is still consistent with maximal $\overset{(-)}{\nu}_\mu$ disappearance, while the preference for the normal mass hierarchy becomes even more explicit when

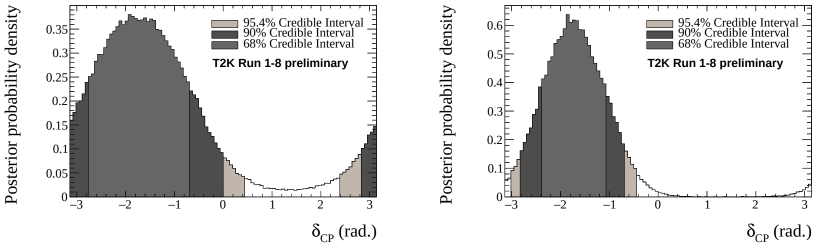

(a) Without reactor constraint **(b)** With reactor constraint

Figure 7.7: Posterior probability density of δ_{CP} from the run 1-8 analysis using T2K data only (7.7b) and using the reactor constraint on $\sin^2\theta_{13}$ (7.7a). The credible intervals are also shown, and both neutrino mass orderings are included.

adding run 8 data as shown on Figure 7.8.

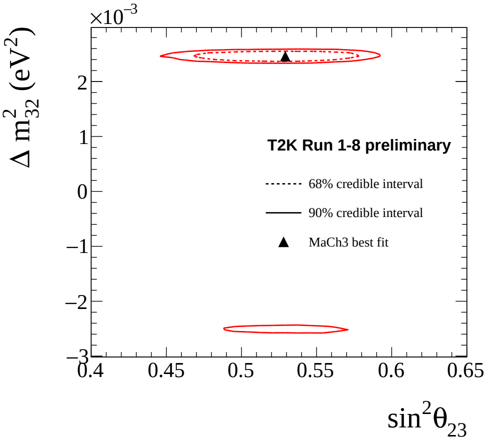

Figure 7.8: 90% and 68% credible intervals in the $\sin^2\theta_{23}$-Δm^2_{32} space from the run 1-8 analysis reactor constraint on $\sin^2\theta_{13}$.

7.2.4 Joint T2K and NOνA analysis

NOνA is a long baseline neutrino oscillation experiment located in the United States (US), which results have already been discussed in Section 6.3.3.1 of this thesis. Similarly to T2K, it holds off-axis near and far detectors measuring $\overset{(-)}{\nu}_\mu$ disappearance and $\overset{(-)}{\nu}_e$ appearance from a muon neutrino beam that can run in ν- or $\bar{\nu}$-mode. The beam energy peaks at

$\sim 2\,\mathrm{GeV}$ in the far detector, located 810 Km from the target. The longer baseline of the NOνA experiment leads to a higher sensitivity to the neutrino mass ordering, and both T2K and NOνA are sensitive to the δ_{CP} phase. Sensitivity studies suggest that a combination of T2K and NOνA data could lead to the measurement of the neutrino mass ordering and provide accurate constraints on δ_{CP} as shown in Figure 7.9 [162].

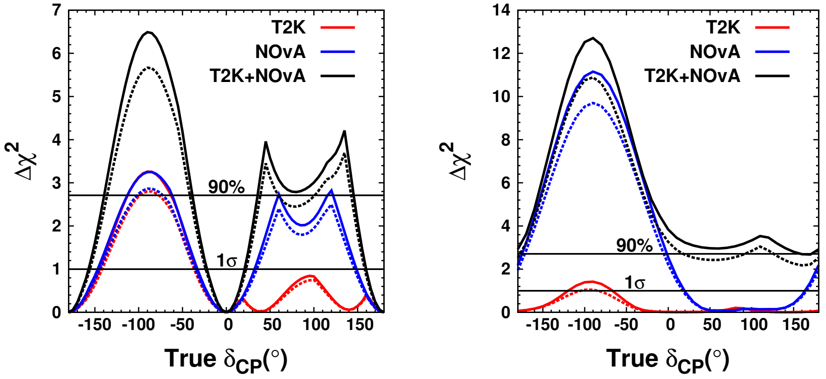

(a) Exclusion of sinδ_{CP}= 0 **(b)** Exclusion of IO

Figure 7.9: Sensitivity of excluding CP-conservation and incorrect neutrino mass ordering for T2K (red), NOνA (blue) and T2K+NOνA (black). The left figure shows the predicted $\Delta\chi^2$ for rejecting the sinδ_{CP}= 0 hypothesis as a function of δ_{CP}. The right figure shows the predicted $\Delta\chi^2$ for rejecting the sinδ_{CP}= 0 hypothesis as a function of δ_{CP}. $\sin^2\theta_{13}$= 0.1, $\sin^2\theta_{23}$= 0.5 and NO are assumed. From [162].

Conclusion:

This thesis presents the most accurate estimation on the neutrino oscillation parameters ever obtained by the T2K experiment. The CP-conserving δ_{CP} values are notably excluded at 1σ with T2K data only (90% when adding information of reactor experiments on $\sin^2\theta_{13}$). The analysis reports a $\sin^2\theta_{23}$ value compatible with maximal $\overset{(-)}{\nu}_{\mu}$ disappearance, as well as a non-significant indication of the NO of neutrinos masses. However, while T2K already provides stringent constraint on the U_{PMNS} parameters $\sin^2\theta_{23}$, Δm^2_{32}, and to a lesser extent $\sin^2\theta_{13}$ and δ_{CP}, constraints on (beyond) SM physics require higher accuracy. Several proposals aims at improving the determination of the neutrino oscillation parameters, amongst which the extension of the target POT to $20 \cdot 10^{21}$ in the T2K-II phase, the 20 times bigger Cherenkov detector of Hyper-K, and the upgrades of both on- and off-axis near detectors. Those developments are crucial to achieve better measurements of the oscillation parameters, and constrain postulated beyond SM theories or cosmological scenarii.

APPENDIX A

Markov Chain properties

Markov chains are semi-random walks where the step $i+1$ only depends on the previous step i. They are used in this thesis to sample the joint posterior probability distribution of oscillation and systematic parameters, as explained in Section 4.1.2. The posterior distribution represent the *target distribution* for the Metropolis-Hastings algorithm, and is effectively sampled thanks to the detailed balance condition of Equation (4.3). This appendix presents how the Markov chain was tuned to perform an adequate sampling, and the quality of the sampling was assessed.

A.1 Properties of Markov chain Monte-Carlo

A.1.1 Burn-in

The lengths of the Markov chains analysed in Chapters 5 and 6 are given in Table A.1. However, the total length do not result from a single chain, but from the concatenation of several chains of $400 \cdot 10^3$ steps for the chains of Chapter 5 and $120 \cdot 10^3$ steps for the chains of Chapter 6. For every step, the initial value of the systematic parameters are thrown randomly to

samples analysed	*simulated data*	*real data*
$R^{(-)}_{\mu}$	$11.05 \cdot 10^6$	$6.47 \cdot 10^6$
$R^{(-)}_{\mu} + R^{(-)}_{e}$ without reactor constraint	$11.58 \cdot 10^6$	$7.97 \cdot 10^6$
$R^{(-)}_{\mu} + R^{(-)}_{e}$ with reactor constraint	$6.14 \cdot 10^6$	$6.12 \cdot 10^6$

Table A.1: Lengths, in number of steps, of the Markov chains used for the analyses on Chapters 5 ($R^{(-)}_{\mu}$) and 6 ($R^{(-)}_{\mu} + R^{(-)}_{e}$).

obtain the first step (the initial value of the oscillation parameters is taken to be one used to tune the Super-K MC). Figure A.1 shows the evolution of the negative log-likelihood ratio with the steps, also called the *trace* of the log- ratio, for several chains including the real $R^{(-)}_{\mu}$ and $R^{(-)}_{e}$ Super-K samples without the reactor constraint analysed in Section 6.3. At first, the parameters used to tune the MC are thrown close to their prior value and the negative log-likelihood ratio is relatively high as the simulated data are quite different from the real data. As the parameters are more likely to be accepted if the log-likelihood decreases, indicating a better agreement between the

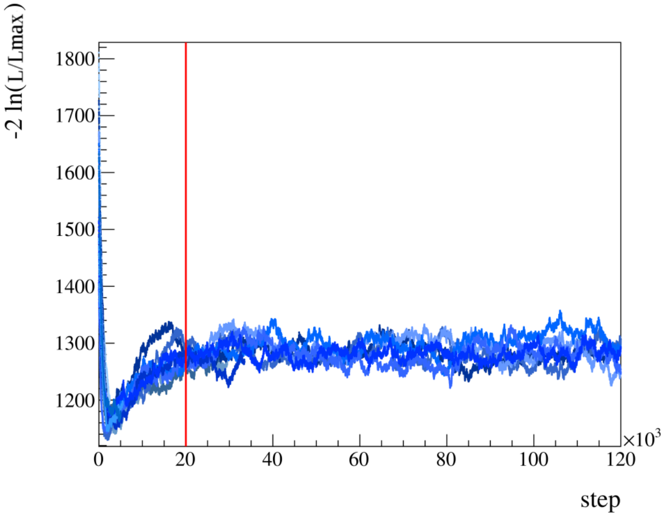

Figure A.1: Trace of the negative log-likelihood ratio as a function of the step for the $R^{(-)}_{\mu} + R^{(-)}_{e}$ fit of real T2K data with the reactor constraint analysed in Section 6.3. The blue lines are the traces for several Markov chains of $120 \cdot 10^3$ steps length, while the red line shows the burn-in. The steps after the burn-in are concatenated in the final Markov chain.

newly tuned MC and the data, the negative log-likelihood ratio starts by a decreasing phase until finding the parameters agreeing best with the data. Once the correct parameters are found, the chain samples the joint posterior probability to build the distribution: it is said to have *converged* in sampling the target distribution. The steps before the Markov chain converged cannot be analysed as they don't belong to the posterior distribution, therefore they are discarded: this process is called *burn-in* [163] and has been chosen to concern $50 \cdot 10^3$ steps for the chains of Chapter 5 and $20 \cdot 10^3$ steps for the chains of Chapter 6. The burn-in is shown as a red line in Figure A.1, and the steps after are concatenated into the final Markov chain from which the credible intervals and best-fit point can be evaluated.

A.1.2 Step size

When proposing a new step $i+1$, the parameters are thrown according to a Gaussian function centered on their value at the step i. The standard-deviation of this *proposal function* is called the step size, as it parameterises the distance between the values of the parameters between two consecutive steps. The step size has a strong influence on the convergence of the Markov chain: if all chains will eventually converge to sampling the target distribution as long as the detailed balance condition is fulfilled, the necessary time for convergence to occur can vary consequently. In the implementation of the Metropolis-Hastings algorithm used in this thesis, the proposal function is taken to be the prior uncertainty on the parameters. However, this prior step size σ_{prior} is scaled by an optimisation factor f_{opt} to ensure that the effective step scale σ_{step} leads to a computationally feasible convergence of the Markov chain:

$$\sigma_{step} = f_{opt}\ \sigma_{prior} \tag{A.1}$$

Extensive literature exists about choosing the right optimisation factor, and it has been derived to be [164]:

$$f_{opt} = \frac{2.38}{\sqrt{D}} \tag{A.2}$$

where D is the number of dimensions in which the Markov chain walks. This number has been shown to correspond to a step acceptance rate of $\sim 25\%$ [165] for which the Markov chain walk is the most efficient. The step acceptance rate is related to the step scale as if f_{opt} is too large, the parameters of the proposed step will be far from the highest posterior probability and likely to be rejected. On the opposite, if f_{opt} is too small, the parameters of the proposed steps will be very close to the prior ones and the Markov chain may take very long to converge to the stationary distribution, or to sample the whole posterior distribution.

In practice, it has been found that it was more efficient to set different step scales for five group of parameters, i.e. the flux, cross-sections, ND280 detector, Super-K detector, and oscillation parameters. The step scale is tuned by running a Markov chain with simulated data and try to obtain an acceptance of $\sim 25\%$, although it was noticed than values close to 25% could present non-convergence and values far from 25% could present convergence. Because the requirement on step acceptance is lose, tests described in Section A.2 have been used to assess the convergence status of the Markov chains used. Figure A.2 shows the trace of the $\sin^2\theta_{23}$ and $\Delta\bar{m}^2_{32}$ parameters from a simulated data fit of the analysis presented in Chapter 5. On the top figures, the step size is correct and $\sin^2\theta_{23}$ varies by small jump in Figure A.2a, while $\Delta\bar{m}^2_{32}$ changes of sign frequently in Figure A.2b. On the bottom figures, the step size is too large: $\sin^2\theta_{23}$ undergoes large variations, between which the chain stays with the same step values for many iterations because the new steps are always rejected. Similarly, the rate of sign switch of $\Delta\bar{m}^2_{32}$ is much lower as most proposed steps are rejected. The two sets of oscillation scales used for Markov chains analysed in Chapters 5 and 6 are given in Table A.2. The values are smaller than predicted by Equation (A.2), but have been found to produce convergence is a quicker time than when using larger values. The difference with the theoretical value may be due to the high number of dimensions used in our model, or to the correlations between the steps.

parameter category	$R_{\mu}^{(-)}$	$R_{\mu}^{(-)} + R_{e}^{(-)}$
flux	0.04	
cross-section	0.03	
ND280 detector	0.02	
Super-K detector	0.07	
oscillation	0.03	0.07

Table A.2: Optimisation factor f_{opt} used to tune the step sizes for the Markov chains used for the analyses on Chapters 5 ($R_{\mu}^{(-)}$) and 6 ($R_{\mu}^{(-)} + R_{e}^{(-)}$).

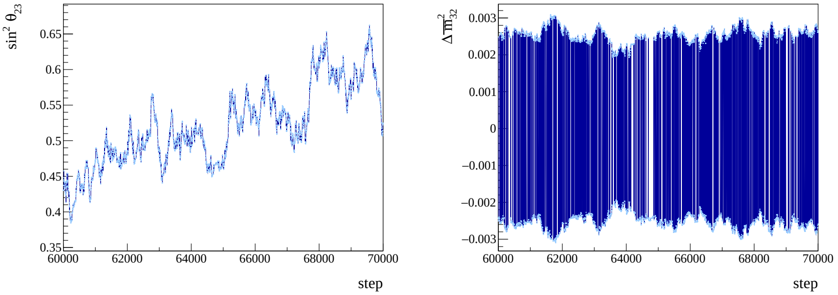

(a) $\sin^2\theta_{23}$, correct step scale

(b) Δm^2_{32}, correct step scale

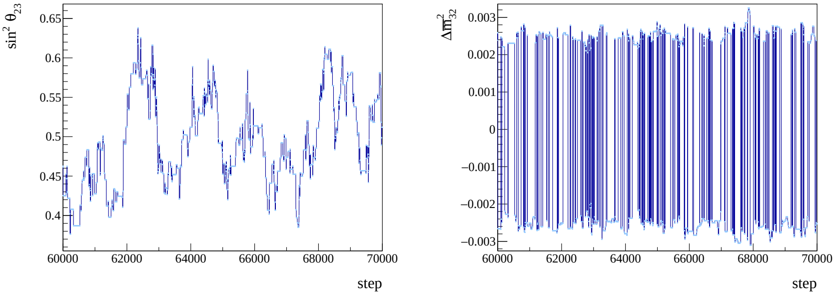

(c) $\sin^2\theta_{23}$, large step scale

(d) Δm^2_{32}, large step scale

Figure A.2: Traces of the parameters $\sin^2\theta_{23}$ (left figures) and $\Delta\bar{m}^2_{32}$ (right figures) from a simulated data fit of the analysis presented in Chapter 5. The top figures show traces with a correct step size, while the bottom figures show traces with a too large step size. A dark blue line link the consecutive value of the parameters between two steps, and the x-axis is truncated to only show steps $60-70\cdot10^3$.

A.1.3 Autocorrelation

The parameters values at each step of the Markov chain depend on their values at the previous step: therefore they are correlated. The autocorrelation function builds an estimate of the number of steps needed for one parameter x to be considered thrown independently of the previous parameters [163]. The autocorrelation formula is:

$$\rho(k) = \frac{\varrho(k)}{\varrho(0)} \tag{A.3}$$

where k is the lag, i.e. the distance between steps, for which the autocorrelation is computed and $\varrho(k)$ is the autocovariance at lag k given by the equation:

$$\begin{aligned}\varrho(k) &= \mathbb{E}(x_i - \bar{x})\ \mathbb{E}(x_{i+k} - \bar{x}) \\ &= \frac{1}{N-k}\sum_{i}^{N-k}(x_i - \bar{x})(x_{i+k} - \bar{x})\end{aligned} \tag{A.4}$$

where N is the total number of the step in the Markov chain (burn-in excluded) and $\mathbb{E}$ is the expectation value operator.

Figure A.3 shows the autocorrelation value as a function of the lag for the oscillation parameters constrained with $R_{\overset{(-)}{\mu}} + R_{\overset{(-)}{e}}$ fit with real Super-K data analysed in Section 6.3. By definition of $\rho(k)$, the autocorrelation

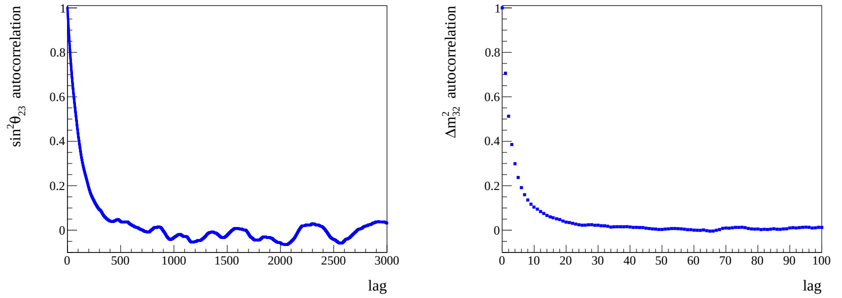

(a) $\sin^2\theta_{23}$ **(b)** Δm^2_{32}

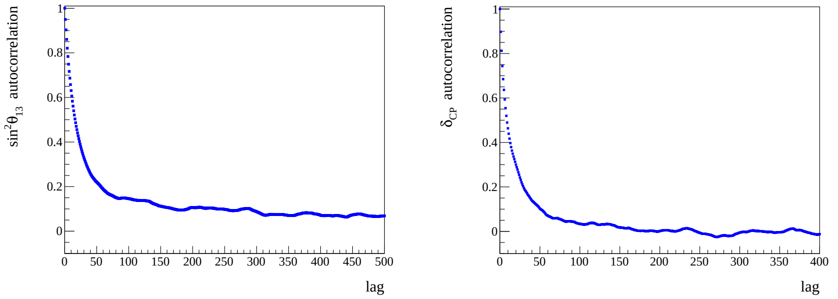

(c) $\sin^2\theta_{13}$ **(d)** δ_{CP}

Figure A.3: Autocorrelation at different lag for the four oscillation parameters of interest. The Markov chain for the $R_{\overset{(-)}{\mu}} + R_{\overset{(-)}{e}}$ fit with real Super-K data and without the reactor constraint (analysed in Section 6.3) has been used. The autocorrelation has been computed for $k \in [0; N]$ where N is the number of steps in the Markov chain when the burn-in is excluded, but the x-axes have been cropped to show the decrease from $k = 0$.

function is bounded in $[-1;1]$ and always starts at 1 for the lag $k = 0$. The autocorrelation value decreases at the lag between the step increases, demonstrating that the value x_i of a oscillation parameters at a step i depend less and less of the value x_{i-k} it had k steps away when k is large. For δ_{CP}, the necessary lag to consider steps as thrown independently can be inferred to be $k_{indep} = 200$ from Figure A.3d. Consequently, when computing the uncertainty on the posterior probability of the NO of neutrino masses as a function of δ_{CP} as shown in Figure A.4, the binomial uncertainty must be weighted to take into account the correlations between the steps. The uncertainty ϵ_j^{NO} on the fraction of NO steps f^{NO} in every δ_{CP} bin j is given by:

$$\epsilon_j^{NO} = \sqrt{\frac{f_j^{NO}(1 - f_j^{NO})}{N_{indep}}} \tag{A.5}$$

where $N_{indep} = \frac{N_{total}}{k_{indep}}$ is the effective number of independent steps. This method is approximate as the steps between N_{total} and N_{indep} are not 100% correlated, but ensures a conservative estimate of the statistical uncertainty.

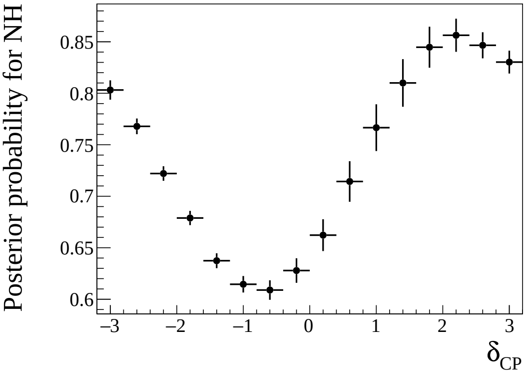

Figure A.4: Posterior probability of the NO case as a function of δ_{CP} from the Markov chain with real ND280 and Super-K data and without reactor constraint (duplicated from Figure 6.8a). The error bars represent the statistical uncertainties, computed from the effective number of independent steps.

A.2 Convergence diagnostics

While the Metropolis-Hastings algorithm ensures that any Markov chain will converge in sampling the target distribution, the required number of steps may vary according to the sampled distribution and the chosen parameters of the algorithm. This section presents tests aiming at assessing if Markov chains have converged.

A.2.1 Ergodicity

The parallelisation of the sampling described in Section A.1.1 enables to test the ergodicity of the Markov chain, i.e. its ability to reach any state of the target distribution from any starting state. By throwing the initial value of the systematic parameters randomly, chains starting in different states can be compared to infer their ability to sample the target distribution with the number of steps chosen. Figure A.5 shows the log-likelihood trace for a $R_{\overset{(-)}{\mu}} + R_{\overset{(-)}{e}}$ fit with real ND280 and simulated Super-K data and with the reactor constraint. Contrarily to Figure A.1, the different chains do not all

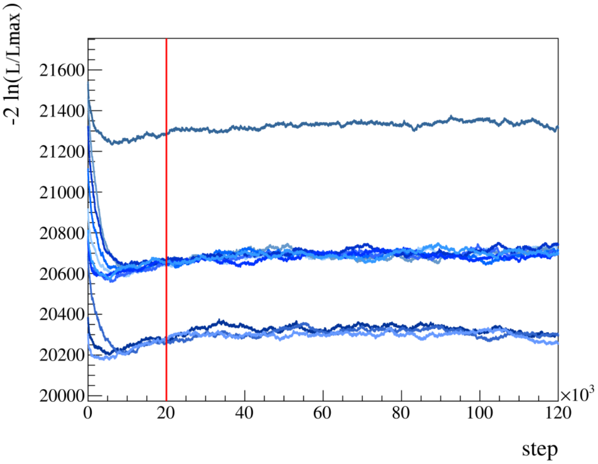

Figure A.5: Trace of the negative log-likelihood as a function of the step for the $R_{\overset{(-)}{\mu}} + R_{\overset{(-)}{e}}$ fit with simulated T2K data and with the reactor constraint (as analysed in Section 6.2). The blue lines are the traces for several Markov chains of $120 \cdot 10^3$ steps length, while the red line shows a tentative burn-in. The chosen step size is too small, leading to many chains not reaching the target distribution and remaining in a metastable state.

reach the log-likelihood value corresponding to the sampling of the target distribution, because some remain in a metastable state characterised by a higher log-likelihood. The issue has been solved by increasing the step size, allowing the chains to sample states further away and escape local minima so they all converge to sampling the posterior distribution.

A.2.2 Geweke diagnostic

The Geweke diagnostic aims at determining the most adequate burn-in by comparing the beginning and the end of a Markov chain [166]. Two subsamples of the chains are used to carry out the test: the first is the *initial subsample* and consists of 5% of the total length of the chain, it is chosen to be the first consecutive steps of the chain. The second sample is the *final subsample*, it is taken to be the 50% of the chain, from its middle to its end, for which it is assumed that the Markov chain has converged. The mean of a parameter x between the beginning and the end of the chain is compared with the Geweke factor G:

$$G = \frac{\bar{x}_{ini} - \bar{x}_{fin}}{\sqrt{\sigma(x)^2_{ini} + \sigma(x)^2_{fin}}} \tag{A.6}$$

where $\bar{x}_{ini}$ and $\bar{x}_{fin}$ are the mean value of the parameter x for the initial and final subsamples respectively, and $\sigma(x)^2_{ini}$ and $\sigma(x)^2_{fin}$ are the variance of the parameter x for the initial and final subsamples respectively. The starting value of the 5% of the chain selected to be the initial subsample is progressively increased to compare the Geweke factors obtained for different regimes.

Figure A.6 shows the Geweke factor computed with the negative log-likelihood ratio of several individual chains of the the $R_\mu + R^{(-)}_{e}$ fit with real Super-K data and without the reactor constraint (as in Figure A.1). The x-axis shows the step progress from which the initial subsample is extracted: it starts at 0% as the first subsample includes the steps from 0% to 5%, then at 5% as the second sample includes from 5% to 10%, repeated until the 45% to 50% segment. The y-axis shows the Geweke factor for every initial subsample: it is always found to be negative at the beginning, as the shape of the log-likelihood ratio decreases rapidly and the mean value of the log-likelihood ratio in the first part of the chain is smaller than in the final part. The red line shows the location of the burn-in chosen with Figure A.1, and the Geweke factor starts to increase on the chain shown in Figure A.6c, indicating a better agreement between the log-likelihood ratio of the initial and final subsamples. However, other chains have little variation of the Geweke factor while having converged before 50%. The Geweke factor theoretically follows a normal distribution, and values found inside the $-2, +2\sigma$ interval are considered as evidence for convergence. All Geweke factors being found in this interval, the diagnostic is considered as giving little power in estimating the adequate burn-in. Therefore the burn-in has been chosen to be determined from the trace of the negative log-likelihood ratio for all the analyses.

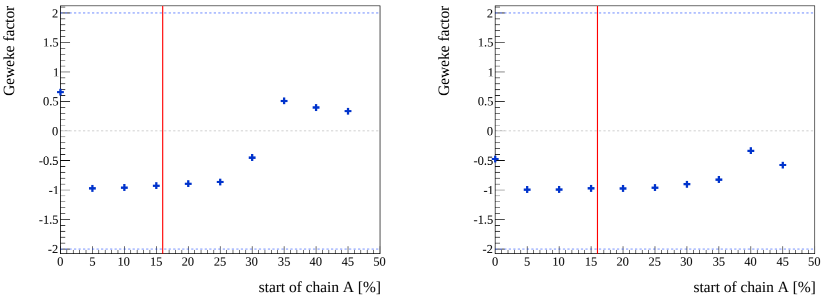

(a) Chain 1 **(b)** Chain 2

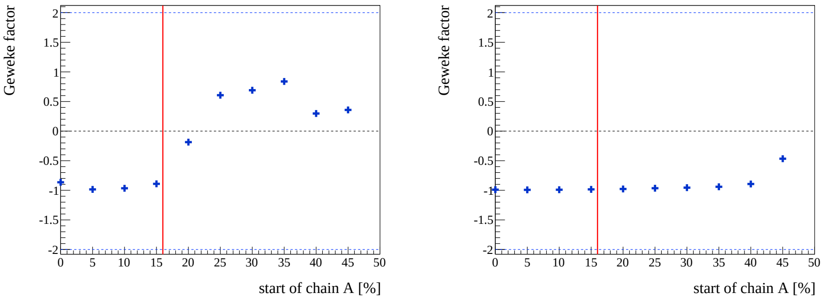

(c) Chain 3 **(d)** Chain 4

Figure A.6: Geweke factors for several Markov chains for the $R_\mu + R_e^{(-)}$ fit with real Super-K data and without the reactor constraint (analysed in Section 6.3). The x-axis represent the beginning of the 5% extraction of the initial subsample of the chain that is compared to the final 50%.

A.2.3 Comparison with semi-frequentist fits

The analyses reported in Chapters 5 and 6 have been performed using different statistical tools. Beside the MCMC technique presented in this thesis, a semi-frequentist method has notably been developed by the T2K collaboration. This method evaluates the marginal log-likelihood ratio for points of a grid spanning the space of the estimated parameters (e.g. $\sin^2\theta_{13}$-δ_{CP}, $\sin^2\theta_{23}$-Δm^2_{32} or δ_{CP} only). The $\Delta\chi^2$ is computed by subtracting the minimal log-likelihood ratio value corresponding to the best fit point, and constant-$\Delta\chi^2$ intervals are extracted from the $\Delta\chi^2$ mapping of the parameter space. Contrarily to MCMC, the minimising χ^2 procedure is not suitable for a high dimensional space, and cannot perform a joint ND280 and Super-K fit. Therefore, a first fit of the ND280 data is performed to compute the profiled likelihood of the flux and interaction parameters. They are used as prior uncertainty for the fit to Super-K data that provides the marginal likelihood on the oscillation parameters. By performing the fit in two steps, the semi-frequentist method approximate the extrapolation of the uncertainties from the near to the far detector to follow normal distributions, as the profiled uncertainties only match the marginal uncertainties in the Gaussian case. The MCMC analyses allow to verify the validity of this approximation, requiring to compare the intervals. Constant $\Delta\chi^2$ intervals are built from the credible interval by computing the $\Delta\chi^2$ equivalent to the posterior probability in every bin:

$$\Delta\chi^2_j = -2\ ln\left(\frac{P(H(\vec{x_j})|D)}{P(H(\vec{x_{max}})|D)}\right) \tag{A.7}$$

where $P(H(\vec{x_j})|D)$ is the posterior probability in the bin j and $P(H(\vec{x_{max}})|D)$ is the maximal posterior probability. The constant-$\Delta\chi^2$ intervals obtained from the $R_{\overset{(-)}{\mu}} + R_{\overset{(-)}{e}}$ fit with simulated T2K data and with the reactor constraint are shown in Figure A.7, with a comparison to the intervals obtained with the semi-frequentist method. They agree in Figures A.7a and A.7b, while the MCMC method finds smaller intervals in Figures A.7c and A.7d. After comparing the systematic parameters distributions, and evaluating the convergence of the Markov chain, it was found that the discrepancy was due to a lack of convergence, that was solved by increasing the step size. Consequently, the comparison of constant-$\Delta\chi^2$ intervals estimated with MCMC and frequentist methods can be used as a check of convergence, at the condition that the difference brought by the different frameworks are not responsible for the discrepancies seen.

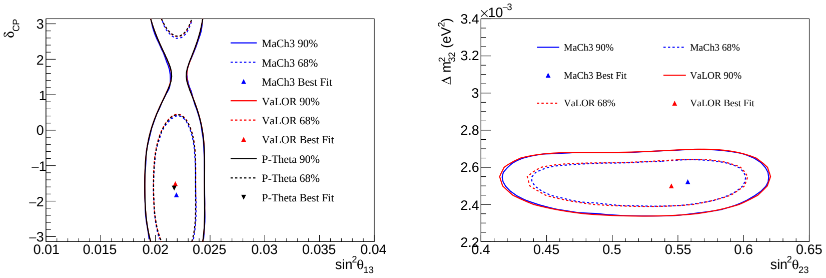

(a) $\sin^2\theta_{13}$-δ_{CP}, convergence **(b)** $\sin^2\theta_{23}$-Δm^2_{32}, convergence

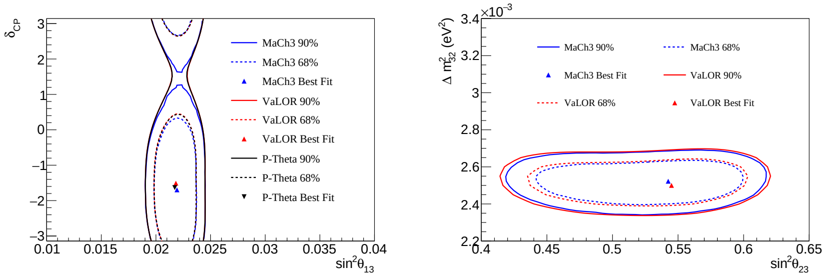

(c) $\sin^2\theta_{13}$-δ_{CP}, no convergence **(d)** $\sin^2\theta_{23}$-Δm^2_{32}, no convergence

Figure A.7: Comparison of the constant-$\Delta\chi^2$ intervals obtained with MCMC (blue) and semi-frequentist minimising $\Delta\chi^2$ independent fits (red, black). The intervals are obtained from the $R_\mu^{(-)} + R_e^{(-)}$ fit with simulated T2K data and with the reactor constraint (as analysed in Section 6.2). The dashed(solid) lines are the 68%(90%) constant-$\Delta\chi^2$ intervals, and the triangles show the best-fit points determined from the minimal $\Delta\chi^2$. Figures A.7a and A.7b present similar intervals for the two method, indicating convergence of the chain. Figures A.7c and A.7d exhibit smaller intervals for the MCMC method compared to the semi-frequentist ones, indicating a lack of convergence that can be solved by increasing the number of step or the step size.

Conclusion:

MCMC is a powerful statistical tool that requires an adequate choice of the free parameters of the Metropolis-Hastings algorithm in order to be computationally efficient. The step size tuning has a strong influence on the convergence of the Markov chain, which can be estimated from the trace of the likelihood. The autocorrelation of the parameters gives information on the memory of the chain and the available information compared to an independent throw method.

APPENDIX B

ND280 detector uncertainties

Section 4.3.3 describes the 16 categories of systematic uncertainties on the performance of the ND280 detector. The estimation of the uncertainties for two of those categories enters the scope of this thesis, and is presented in this appendix. The first sections outlines the uncertainties on the background of events selected outside the FGDs FVs, while the second section reports the estimation of the uncertainties on the matching of TPC tracks to upstream FGD tracks.

B.1 Background originating outside the FGDs fiducial volumes

The selection of events in ND280 described in Section 4.2.1 aims at creating samples of interactions in the two FGDs. However, a fraction of the selected events have their true vertex located outside the FGDs FVs although the reconstructed vertex is in the FV. Figure B.1 shows the CC-inclusive selections, including the background. The predicted rates of out-of-FV are summarised in Table B.1 for the CC-inclusive selections. However the rates

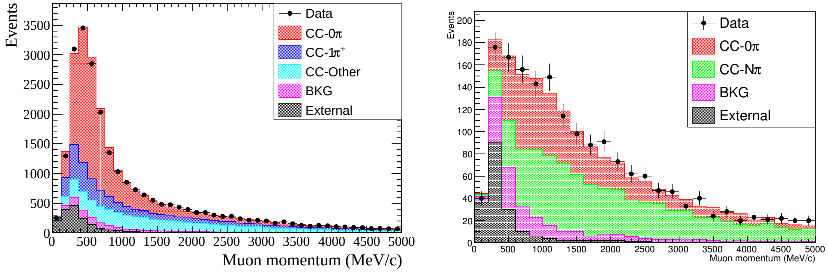

(a) ν-mode ν_μ **(b)** $\bar{\nu}$-mode ν_μ

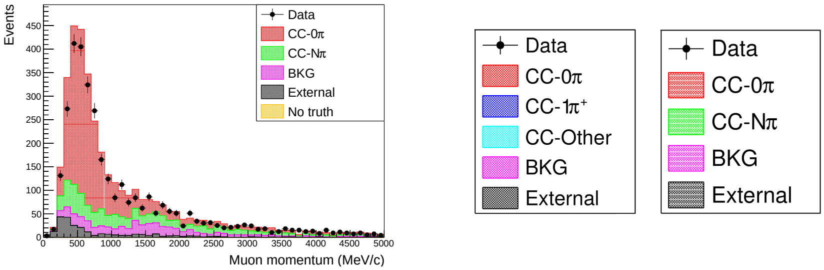

(c) $\bar{\nu}$-mode $\bar{\nu}_\mu$ **(d)**

Figure B.1: Distribution of the selected CC-inclusive samples in the FGD2 as a function of the $\mu^\pm$ momentum. The stacked histogram shows the MC prediction, the black point show the data. The MC prediction is broken down in topology modes, the black content representing the out-of-FV background on the three figures. The left legend of B.1d corresponds to B.1a, while the right legend corresponds to B.1b and B.1c.

are subject to uncertainties due to the lack of knowledge on interaction rates occurring outside the FGDs FVs, or mis-simulation of the tracks reconstructions leading to failures.

sample	*FGD1*	*FGD2*
ν-mode ν_μ	5.4%	7.0%
$\bar{\nu}$-mode ν_μ	9.3%	10.1%
$\bar{\nu}$-mode ν_μ	5.9%	6.0%

Table B.1: Predicted fraction of out-of-FV events in the CC-inclusive samples selected in both FGDs in ν- and $\bar{\nu}$-mode.

In order to evaluate the uncertainties on the out-of-FV events, the source of the miscategorisation has been evaluated with a visual scanning of background events. Nine exclusive categories of failures have been found and summarised below, the percentage in parenthesis indicating the fraction of out-of-FV events concerned for the ν_μ CC-0π sample in FGD1:

(1) *Events inside the FGD*: events which true vertex is in the FGD, but outside its FV (11.1%);

(2) *Events upstream the FGD*: events which true vertex is located in the tracker before the relevant FGD, mainly on dead material such as a TPC wall (3.3%);

(3) *Events downstream the FGD*: events which true vertex is located in the tracker after the relevant FGD, mainly on dead material such as a TPC wall (10.3%);

(4) *Events from NC*: secondary interactions in the FGD FV originating from a neutral particle created in a neutrino NC interaction (22.5%);

(5) *Events with backward tracks*: events creating a backward track stopping in the FGD, incorrectly reconstructed as a forward track starting in the FGD (17.1%);

(6) *Events with high angle tracks*: events where the FGD track is almost perpendicular with respect to the beam direction, and not properly matched to the TPC track (10.1%);

(7) *Events with "double skipped layers failure"*: events where no hits are found in two layers in a row, automatically creating a failure in the reconstruction breaking the track (5.8%);

(8) *Events with "last module failure"*: events occurring a hardware failure where no events are recorded in all x-oriented modules, making the track reconstruction fails when reaching the last module (5.5%);

(9) *Other out-of-FV events*: events not entering the categories above, mainly hard scattering of $\mu^\pm$ (14.2%).

B.1.1 Rate uncertainty

The uncertainty on the production rates of events of the ND280 samples are modelled by the variation of flux and cross-section parameters. However, interactions outside the FGDs FVs may occur with a nucleus which cross-section is not modelled by the parameters described in Section 4.3.2, such as lead, brass or iron. Therefore an additional uncertainty must cover the difference of cross-section between the nucleus implemented in NEUT (hydrogen, carbon, oxygen) and the missing ones.

Out-of-FGD FV events of categories (1) to (3) occur inside the tracker, which subdetectors are made of carbon (FGD1), water (FGD2), argon (TPCs) or aluminium (dead material). The scaling of light nuclei cross-sections as a function of the number of nucleons is considered well-known, and no additional uncertainties are set on those events to cover the difference of interaction rate between argon and aluminium with respect to carbon and oxygen. However, background events from categories (4) to (9) may occur outside the tracker, where heavier elements are present. Table B.2 shows the predicted proportion of background events outside the tracker in the different subdetectors. Because ECals surround the tracker, a majority of out-of-FV events originate from it, with the SMRD arriving in second position as it is located around the ECal. Events occurring in the P∅D are a strong content of the FGD1 selection as the detector is located one TPC away, compared to the FGD2 selection where the detector is placed more downstream. The uncertainties on those events are computed from the normalised differences between the $\overset{(-)}{\nu}_\mu$ predicted and measured number of events in each subdetector:

$$\delta_{det}^{rate} = \sqrt{\left(\frac{N_{det}^{MC} - N_{det}^{data}}{N_{det}^{MC}}\right)^2 + \left(\epsilon_{stat}^{MC}\right)^2 + \left(\epsilon_{stat}^{data}\right)^2} \tag{B.1}$$

where δ_{det}^{rate} is the normalised difference for events with true vertex located in

sample		***P∅D***	***ECal***	***SMRD***	***other detectors***
ν-mode ν_μ	FGD1	29.7%	45.0%	14.5%	10.8%
	FGD2	9.4%	62.2%	17.1%	11.3%
$\bar{\nu}$-mode ν_μ	FGD1	23.4%	49.4%	15.4%	10.8%
	FGD2	6.7%	69.5%	14.1%	9.7%
$\bar{\nu}$-mode ν_μ	FGD1	34.1%	42.7%	12.8%	10.4%
	FGD2	11.2%	64.8%	14.4%	9.6%

Table B.2: Predicted fraction of out-of-FGD-FV events occurring in each subdetectors, for the CC-inclusive samples selected in both FGDs in ν- and $\bar{\nu}$-mode. The *other detectors* category includes the dead material and the magnet.

the detector det, N^{MC}_{det} and N^{data}_{det} are the predicted and measured numbers of events respectively, and ϵ^{MC}_{stat} and ϵ^{data}_{stat} are the predicted and measured statistical uncertainties on the numbers of events respectively. The final uncertainties are taken to be $\epsilon^{rate}_{det} = 1 - \delta^{rate}_{det}$.

B.1.1.1 P∅D

The out-of-FGD FV events originating in the P∅D mainly occur from interactions downstream in the detector, where the central P∅D ECal is placed as shown on Figure B.2a. A selection of $\overset{(-)}{\nu}_\mu$ events with vertex reconstructed in the P∅D water target and central ECal has been performed to obtain three samples: ν_μ in ν-mode, ν_μ in $\bar{\nu}$-mode and $\bar{\nu}_\mu$ in $\bar{\nu}$-mode ans is shown on Figure B.2b. The selection used the cuts 1 to 4 of Table 4.2 (but using the P∅D instead of the FGD) to include any interaction with a TPC track appearing to originate in the P∅D, as the background is composed of CC- and NC-mediated events. The uncertainties computed with Equation (B.1) are summarised in Table B.3.

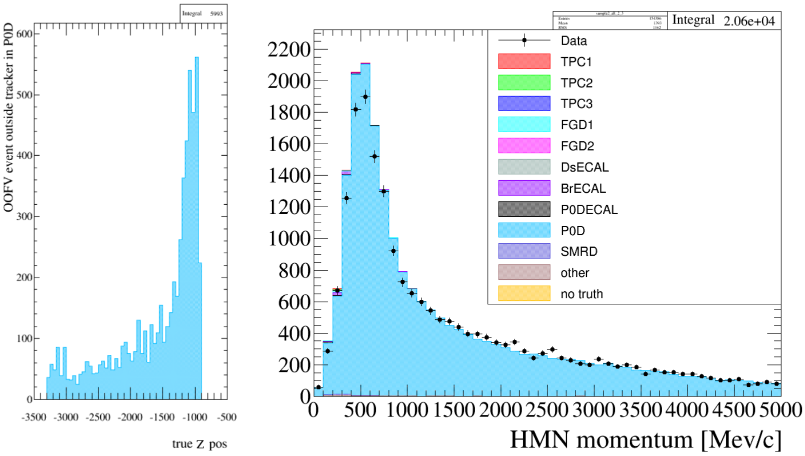

(a) Out-of-FGD FV **(b)** ν_μ CC events in P∅D

Figure B.2: The left figure shows the distribution of the out-of-FGD1-FV ν-mode ν_μ events originating in the P∅D along $\vec{z}$. The right figure shows the P∅D ν-mode ν_μ selection as a function of the Highest Momentum Negative (HMN) tracks momentum. The stacked histogram shows the MC prediction, the black point show the data, the difference being used to establish the uncertainty on the rate of events shown in the left figure.

B.1.1.2 ECals

The systematic uncertainties on out-of-FGD-FV events occurring in the P∅D, Barrel and downstream ECals are established from a selection of events in the Barrel ECals. The Barrel ECals surrounding the tracker, they are the only ECals in contact with the TPCs (with the downstream ECal, that however suffers from the fact that more interactions produce forward-going particles that do not traverse any subdetector). The TPCs being filled with gas, little scattering occur and they are the dedicated detectors to reconstruct tracks and matching them to adjacent detectors. As all ECals are composed of the same material (carbon and lead), the selection in the Barrel ECals is sufficient to establish an uncertainty on the cross-section on the nucleus for all other ECals. The samples are shown on Figure B.3, they are obtained after using cuts 1 to 4 of Table 4.2, with the FGD FV replaced by the Barrel ECals FV. The Barrel ECals FV are set to be the detectors

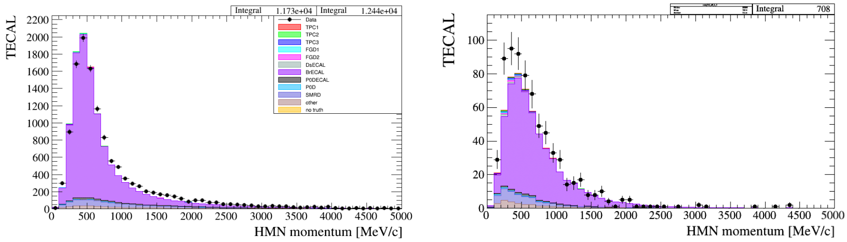

(a) ν-mode ν_μ **(b)** $\bar{\nu}$-mode ν_μ

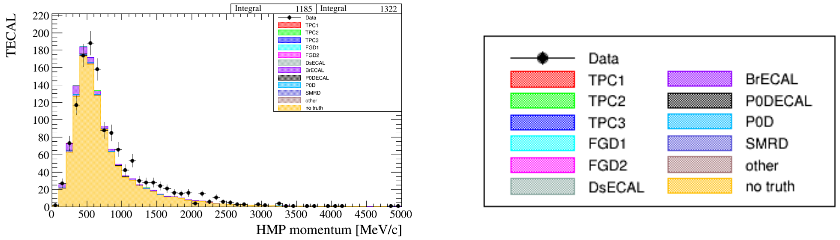

(c) $\bar{\nu}$-mode $\bar{\nu}_\mu$ **(d)**

Figure B.3: Distribution of the samples selected in the Barrel ECals as a function of the Highest Momentum Negative/Positive (HMN/HMP) track momentum. The stacked histograms show the MC prediction, the black point show the data. The MC prediction is given according to the detector in which the vertex is located (the information was not implemented for $\bar{\nu}_\mu$ interactions at the time the study was done, hence the "no truth" content in B.3c).

volumes from which 4 cm is removed from the x-y surfaces, 1.5 cm(0.5 cm) is removed from the outer(inner) x-z surfaces, and 20 cm(8 cm) is removed from the upstream(downstream) y-z surfaces (the wide cut on the upstream subsection leading to a better rejection of events occurring in the material outside ND280). The resulting uncertainties computed with Equation (B.1) are summarised in Table B.3.

B.1.1.3 SMRD

The SMRD being located between the magnet plates, it is not in direct contact with any TPC. Therefore the selection, shown in Figure B.4, is optimised to select tracks in the TPCs crossing the ECals and appearing to originate in the SMRD. The procedure still applies cuts 1 to 4 of Table 4.2, with the SMRD FV defined to be the detector volume from which 1 cm is removed from both x-y surfaces and the outer x-z surface, and 1 cm is

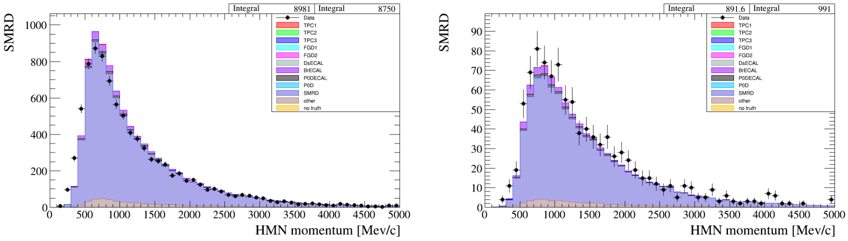

(a) ν-mode ν_μ **(b)** $\bar{\nu}$-mode ν_μ

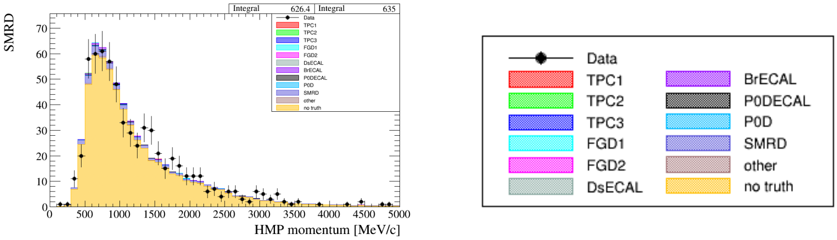

(c) $\bar{\nu}$-mode $\bar{\nu}_\mu$ **(d)**

Figure B.4: Distribution of the samples selected in the SMRDs as a function of the Highest Momentum Negative/Positive (HMN/HMP) track momentum. The stacked histogram shows the MC prediction, the black point show the data. The MC prediction is given according to the detector in which the vertex is located (the information was not implemented for $\bar{\nu}_\mu$ interactions at the time the study was done, hence the "no truth" content in B.4c).

removed from both y-z surfaces. The resulting uncertainties computed with Equation (B.1) are summarised in Table B.3.

B.1.1.4 Other detectors

No selection of events can be done in the magnet or dead material as they don't include any sensitive channel, therefore the uncertainties on those categories of events rely on the MC prediction. Still using Equation (B.1), the N_{det}^{data} number is replaced by the predicted number of events by the GENIE MC neutrino interaction generator [167] with the assumption that the difference between the models in NEUT and GENIE cover the discrepancy between the predicted and true rates. The uncertainties obtained with this method are summarised in Table B.3.

sample	*Tracker*	*P∅D*	*ECal*	*SMRD*	*Other detectors*
ν-mode ν_μ	0%	5.1%	11.6%	4.9%	13.6%
$\bar{\nu}$-mode ν_μ	0%	8.4%	8.8%	6.7%	13.5%
$\bar{\nu}$-mode ν_μ	0%	5.4%	6.7%	4.8%	24.0%

Table B.3: Systematic uncertainties applied on the rate out-of-FGD-FV events, computed with Equation (B.1). The *other detectors* category includes the dead material and the magnet.

B.1.2 Reconstruction uncertainty

Uncertainties on the reconstruction of tracks affect differently each category of out-of-FV events, and are consequently evaluated differently for each one. Only the background events originating from NC and backward events do not have a reconstructed uncertainty, the former because the rate purely relies on the interaction model, the latter because the reconstruction cannot distinguish forward from backward tracks (but the timing uncertainty described in Section 4.3.3 affect those events). The subsections below describe how the reconstruction uncertainties are evaluated for the other categories; they are summarised in Table B.4.

B.1.2.1 Events inside the FGD

Events occurring in the FGD, but outside the FV, are due to inefficiencies in recording hits. The threshold at which an FGD bar detects a signal is 5 p.e., about $\frac{1}{6}$ of a minimum ionising particle crossing a bar (~ 30 p.e.). Because there are 28 bars in the FGD1 FV, the expected rate of non detected event in the subdetector is $\sim \frac{1}{6\times28} = 0.6\%$. The total rate of out-of-FV in FGD1 being 5.4%, amongst which 11.1% are inside the FGD, $11.1\% \times 5.4\% = 0.6\%$ of the total selected events are not detected in the proper bar. As the expected background rates match the ones predicted from the hit inefficiency, and no further data/MC discrepancy has been observed in the reconstruction using the GEANT4 simulation, the uncertainty is considered to be negligible for this category.

B.1.2.2 Events downstream the FGD

Events occurring downstream the FGD are mainly due to interactions in the following TPC wall producing backward-going particles entering the FGD FV and forward-going particles in the TPC gas chamber. The reconstruction uncertainty is evaluated by modifying the χ^2 of matching TPC to FGD tracks in the reconstruction software, and evaluating the difference of out-of-FGD-FV events downstream the FGD expected rate. It was found to be 5%.

B.1.2.3 Events upstream the FGD

Events occurring upstream the FGD are mainly due to interactions in the preceding TPC wall passing in the dead material in between the FGD bars. Their uncertainty is measured with the same procedure as Section B.1.2.2, and was found to be negligible.

B.1.2.4 Events with high angle tracks

When an event produces a track orthogonal to the beam direction, the reconstruction may fails in matching the hits and create two tracks from a single broken track, one of them appearing to originate in the FGD. The uncertainty on those events is estimated with a control sample of cosmic events entering the FGD, selecting the tracks entering from the edges of the

FGD and including one TPC track. Amongst this sample of FGD1-TPC2 or FGD2-TPC3 events, the rate of TPC tracks which first hit is located inside the FGD FV is taken as the inefficiency rate, as it implies that the track is broken. Only events with a $\mu^{\pm}$ momentum $p_{\mu} < 0.7(1.0)\,\text{GeV.c}^{-1}$ are selected, to match the phase-space relevant for the background events in FGD1(FGD2) shown in Figure B.5. The normalised difference of inefficiency rates are estimated with the same equation as Equation (B.1), and found to be 33% in FGD1 and 28% in FGD2.

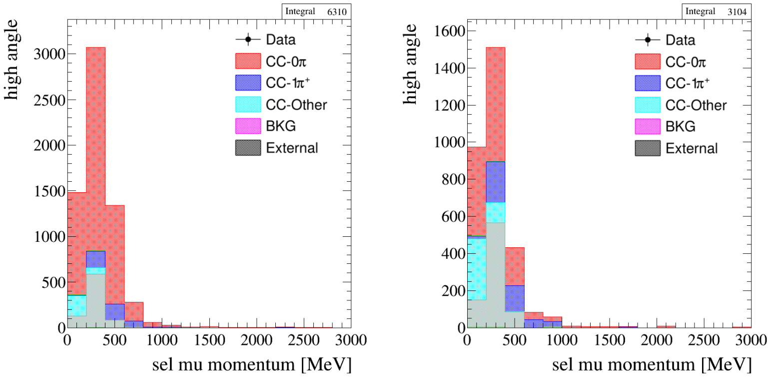

(a) FGD1 **(b)** FGD2

Figure B.5: Distribution of the out-of-FV events in the high angle category as a function of the μ^{-} (sel mu) momentum. The events have been selected in the ν-mode ν_{μ} CC-inclusive sample.

B.1.2.5 Events with "double skipped layers failure"

The "double skipped layers" failure occurs when the TPC drift velocity or time offset is perturbed and the x-coordinate is not reconstructed properly, making the track reconstruction fails when it reaches the last module. The uncertainty on this category of events is determined from a control samples of events going through the whole ND280 detector, selecting events with one track in two consecutive TPCs. In the obtained TPC1-TPC2(TPC2-TPC3) sample, events which TPC2(TPC3) track origin is located inside the FGD1(FGD2) FV consists in the inefficiency rate and is shown on Figure B.6. The difference of rate of events improperly reconstructed in the last module of the FGD between data and MC as given by Equation (B.1) is 55% for

FGD1 and 82% for FGD2 (respectively selecting events with $p_\mu < 0.5$ and $p_\mu < 1.0\,\mathrm{GeV.c^{-1}}$).

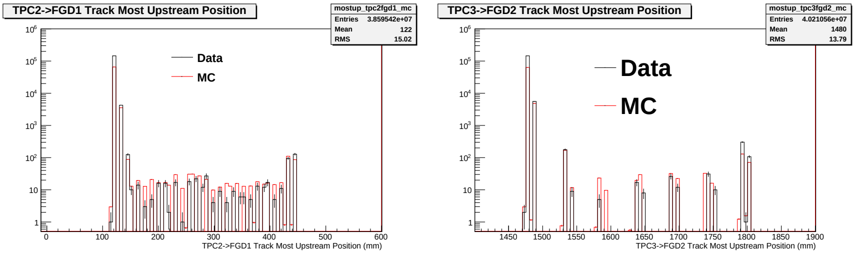

(a) FGD1 **(b)** FGD2

Figure B.6: Distribution of the z-position of the reconstructed vertex of events in a TPC1-TPC2(TPC2-TPC3) sample with the TPC2(TPC3) track improperly reconstructed as starting in FGD1(FGD2) on left(right) figure.

B.1.2.6 Events with "last module failure"

If no hit is present in two consecutive layers, the reconstruction breaks the track and a continuous track that would pass in the dead material between the bars in a whole module would appear as two events. The uncertainty on the reconstruction of those events is evaluated with the same control sample and procedure as in Section B.1.2.5, except that instead of using the inefficiency rate of events in the last module, events in all scintillator modules of Figure B.6 but the last ones are used. Selecting events with $p_\mu < 5.0(1.0)\,\mathrm{GeV.c^{-1}}$, the uncertainty is found to be 35%(17%) in FGD1(FGD2).

B.1.2.7 Other out-of-FV events

Out-of-FV events not entering the categories described above mainly have a broken track in the FGD. Consequently, the uncertainty is computed the same way as in Section B.1.2.6, but selecting events with $p_\mu < 1.0(1.5)\,\mathrm{GeV.c^{-1}}$ to match the phase-space of background events in FGD1(FGD2). The uncertainty is found to be 32% in FGD1 and 21% in FGD2.

#	*Category*	*FGD1*	*FGD2*
1	Events inside the FGD	0%	0%
2	Events upstream the FGD	0%	0%
3	Events downstream the FGD	5%	5%
4	Events from NC	0%	0%
5	Events with backward tracks	0%	0%
6	Events with high angle tracks	33%	28%
7	Events with "double skipped layer"	55%	82%
8	Events with "last module failure"	35%	17%
9	Other out-of-FV events	32%	21%

Table B.4: Uncertainties on the reconstruction of events for each category of out-of-FGD-FV background events according to the detector in which the vertex is reconstructed.

B.1.3 Future treatment of uncertainties

The uncertainties applied on the out-of-FV events do not have vocation to be the total uncertainties on those events, but to palliate the uncertainties not covered by the ones given in Section 4.3. By using an inefficiency rate to establish the reconstruction uncertainties on categories 6 to 9, the dependency of the number of events on the flux, cross-section and other detector systematic uncertainties is avoided. Indeed, they cancel in the equation of the inefficiency rate $\eta^{reco}_{\text{ineff}}$:

$$\eta^{reco}_{\text{ineff}} = \frac{N^{reco}_{\text{ineff}}}{N^{reco}_{all}} = \frac{\phi_{\nu_\mu}\ \sigma_{\nu_\mu}\ \epsilon^{\text{ineff}}_{\nu_\mu}\ \epsilon'_{\nu_\mu}}{\phi_{\nu_\mu}\ \sigma_{\nu_\mu}\ \epsilon'_{\nu_\mu}} \tag{B.2}$$

where N^{reco}_{ineff} and N^{reco}_{ineff} are the number of events inefficiently reconstructed and total number of events respectively, ϕ_{ν_μ} is the flux, σ_{ν_μ} is the cross-section, $\epsilon^{\text{ineff}}_{\nu_\mu}$ is the detector uncertainty estimated and ϵ'_{ν_μ} is the rest of the detector uncertainties. On the contrary, the rate uncertainties directly compare the event rates $N^{MC/data}$, and the flux, interaction and detector systematics are included when computing δ^{rate}_{det}. As those uncertainties are already accounted for by the parameters described in Section 4.3, the rate uncertainty is inflated by including them. A preliminary implementation of heavy nuclei (Fe, Cu, Pb) is ongoing in NEUT, and could be used in the future so background events occurring on different target could be accounted for by the interaction parameters without adding a specific detector systematics. If adding more parameters to the Markov chain ends being computationally unfeasible, the uncertainty on the $\overset{(-)}{\nu}_\mu$ cross-section on heavy nuclei can be propagated beforehand to obtain the expected variation in the number of events that would substitute the rate uncertainties derived in this chapter.

B.2 TPC-FGD matching efficiency

The selection of events in the tracker requires a track in a TPC from which hits in the upstream FGD are added in order to create a TPC-FGD track, that will be included in the analysis samples if the cuts described in Section 4.2.1 are fulfilled. If the reconstruction fails in matching FGD hits to TPC tracks, the efficiency of selecting interactions in the FGDs decreases.

The uncertainty has been estimated from hit efficiency in the FGDs, as a missed hit can break the matching of the TPC track to the FGD track. The hit efficiency is computed from a sample of events with TPC track and the presence of hits in the second most downstream layer, by taking the proportion of events presenting hits in the most downstream FGD layer. The hit efficiencies for both FGDs is summarised in Table B.5, the difference between the MC and data efficiencies being taken as the uncertainties on the matching of TPC to FGD tracks.

hit efficiency	***FGD1***	***FGD2***
MC	$96.9 \pm 0.8\%$	$96.5 \pm 0.85\%$
data	$97.6 \pm 0.45\%$	$97.1 \pm 0.50\%$

Table B.5: Hit efficiencies in the most downstream layer of FGD1 and FGD2.

Conclusion:

The systematic uncertainties on the background events originating from outside the FV of the FGD, and the matching of TPC to FGD tracks, have been computed. They have been assessed from the observation of discrepancies between predicted and measured quantities in control samples. The systematic uncertainties on the number of events in the predicted inclusive CC samples selected in FGD1 and FGD2 after propagation of the uncertainties described below are summarised in Table B.6. The total is dominated by the uncertainties on pion SI explained in Section 4.3.2.

uncertainty	$\bar{\nu}$***-mode*** ν_μ		$\bar{\nu}$***-mode*** ν_μ		$\bar{\nu}$***-mode*** $\bar{\nu}_\mu$	
	FGD1	***FGD2***	***FGD1***	***FGD2***	***FGD1***	***FGD2***
Out-of-FGD-FV	0.40%	0.47%	0.81%	0.75%	0.38%	0.33%
TPC-FGD matching	0.23%	0.29%	0.22%	0.31%	0.17%	0.31%
Total of 16 uncertainties	2.29%	2.27%	3.43%	2.71%	6.27%	4.07%

Table B.6: Variation of the predicted number of events selected in FGD1 and FGD2 for the inclusive CC samples due to the ND280 systematic uncertainties. The variation due to the uncertainties on out-of-FGD-FV background events, TPC-FGD track matching and the total of the 16 categories of uncertainties are shown.

Bibliography

[1] W. Pauli, Open letter to the radioactive group at the Gauverein meeting in Tübingen, 1930.

[2] C. L. Cowan et al., “Detection of the free neutrino: a confirmation”, Science **124**, 103–104 (1956).

[3] C. S. Wu et al., “Experimental Test of Parity Conservation in Beta Decay”, Phys. Rev. Lett. **105**, 1413 (1957).

[4] G. Danby et al., “Observation of high-energy neutrino reactions and the existence of two kinds of neutrinos”, Physical Review Letters **9**, 36 (1962).

[5] M. L. Perl et al., “Evidence for anomalous lepton production in e+- e- annihilation”, Physical Review Letters **35**, 1489 (1975).

[6] DONUT collaboration, “Observation of tau neutrino interactions”, Physics Letters B **504**, 218–224 (2001).

[7] B. T. Cleveland et al., “Measurement of the solar electron neutrino flux with the Homestake chlorine detector”, Astrophys. J. **496**, 505–526 (1998).

[8] B. Pontecorvo, “Neutrino Experiments and the Problem of Conservation of Leptonic Charge”, Sov. Phys. JETP **26**, [Zh. Eksp. Teor. Fiz.53,1717(1967)], 984–988 (1968).

[9] SNO Collaboration, "Direct evidence for neutrino flavor transformation from neutral-current interactions in the Sudbury Neutrino Observatory", Physical review letters **89**, 011301 (2002).

[10] Super-Kamiokande Collaboration, "Evidence for oscillation of atmospheric neutrinos", Physical Review Letters **81**, 1562 (1998).

[11] T2K Collaboration, "The T2K Experiment", Nuclear Instruments and Methods in Physics Research A **659**, 106–135 (2011).

[12] T2K Collaboration, "Indication of electron neutrino appearance from an accelerator-produced off-axis muon neutrino beam", Physical Review Letters **107**, 041801 (2011).

[13] T2K Collaboration, "First Muon-Neutrino Disappearance Study with an Off-Axis Beam", Phys. Rev. **D85**, 031103 (2012).

[14] T2K Collaboration, "Evidence of Electron Neutrino Appearance in a Muon Neutrino Beam", Phys. Rev. **D88**, 032002 (2013).

[15] Daya Bay Collaboration, "Observation of electron-antineutrino disappearance at Daya Bay", Physical Review Letters **108**, 171803 (2012).

[16] J.-P. Derendinger, "The Standard Model of Elementary Particle Physics", Notes from lectures at the University of Bern.

[17] C. Patrignani et al., "Particle Summary Tables", in *Review of particle physics*, Vol. C40 (Chinese physics C, 2016).

[18] *KATRIN webpage*, `https://www.katrin.kit.edu/79.php`, Accessed: 2017-03-27.

[19] L3 Collaboration, "Measurement of Z^0 decays to hadrons, and a precise determination of the number of neutrino species", Phys. Lett. B **237**, 136–146 (1990).

[20] Planck Collaboration, "Planck 2015 results. XIII. Cosmological parameters", A&A **594**, A13 (2016).

[21] A. Giuliani and A. Poves, "Neutrinoless Double-Beta Decay", Advances in High Energy Physics, 857016 (2012).

[22] V. A. Kostelecký and M. Mewes, "Lorentz and CPT violation in neutrinos", Phys. Rev. D **69**, 016005 (2004).

[23] V. Aseev et al., "An upper limit on electron antineutrino mass from the Troitsk experiment", Phys. Rev. D **84**, 112003 (2011).

[24] KATRIN Collaboration, "KATRIN design report 2004", FZKA report **7090** (2004).

[25] B. I. Goryachev, “Statistical analysis of neutrino events from SN1987A neutrino burst: estimation of the electron antineutrino mass”, arXiv preprint arXiv:0709.4627 (2007).

[26] G. Lambiase et al., “Lower Neutrino Mass Bound from SN1987A Data and Quantum Geometry”, Class.Quant.Grav. **23**, 1347–1358 (2006).

[27] P. F. Pérez, “Type III seesaw and left-right symmetry”, Journal of High Energy Physics **2009**, 142 (2009).

[28] B. Kayser, “Neutrino oscillation phenomenology”, in *Neutrinos in particle physics, astrophysics and cosmology*, edited by F. P. Soler, C. D. Froggatt, and F. Muheim (CRC Press, 2008).

[29] S. M. Bilenky, “Neutrino oscillations and time-energy uncertainty relation”, arXiv preprint hep-ph/0512215 (2005).

[30] N. Jelley, A. B. McDonald, and R. H. Robertson, “The Sudbury Neutrino Observatory”, Annual Review of Nuclear and Particle Science **59**, 431–465 (2009).

[31] M. Kobayashi and T. Maskawa, “CP-violation in the renormalizable theory of weak interaction”, Progress of Theoretical Physics **49**, 652–657 (1973).

[32] K. Nakamura and S. Petcov, “Neutrino mass, mixing, and oscillations”, in *Review of particle physics*, Vol. C40, edited by K. A. Olive et al. (Chinese physics C, 2016).

[33] S. M. Bilenky, J. Hošek, and S. Petcov, “On the oscillations of neutrinos with Dirac and Majorana masses”, Physics Letters B **94**, 495–498 (1980).

[34] S. T. Petcov, “The Nature of Massive Neutrinos”, Adv. High Energy Phys. **2013**, 852987 (2013).

[35] D. A. Harris, “Accelerator-based neutrino oscillation experiments”, in *Neutrinos in particle physics, astrophysics and cosmology*, edited by F. P. Soler, C. D. Froggatt, and F. Muheim (CRC Press, 2008).

[36] C. Jarlskog, “Commutator of the quark mass matrices in the standard electroweak model and a measure of maximal CP nonconservation”, Physical Review Letters **55**, 1039 (1985).

[37] S. M. Bilenky et al., “Constraints from neutrino oscillation experiments on the effective Majorana mass in neutrinoless double β-decay”, Physics Letters B **465**, 193–202 (1999).

[38] C. Giunti, “No Effect of Majorana Phases in Neutrino Oscillations”, Phys. Lett. **B686**, 41–43 (2010).

[39] Hyper-Kamiokande Collaboration, “A Long Baseline Neutrino Oscillation Experiment Using J-PARC Neutrino Beam and Hyper-Kamiokande”, in (2014).

[40] KamLAND Collaboration, “First results from KamLAND: evidence for reactor antineutrino disappearance”, Physical Review Letters **90**, 021802 (2003).

[41] KamLAND Collaboration, “Reactor on-off antineutrino measurement with KamLAND”, Physical Review D **88**, 033001 (2013).

[42] *JUNO page on University of Mainz website*, `http://www.staff.uni-mainz.de/wurmm/juno.html`, Accessed: 2017-04-04.

[43] V. Barger, P. Huber, and D. Marfatia, “Supernova neutrinos can tell us the neutrino mass hierarchy independently of flux models”, Physics Letters B **617**, 167–173 (2005).

[44] JUNO collaboration, “Neutrino Physics with JUNO”, J. Phys. **G43**, 030401 (2016).

[45] *NOνA webpage*, `http://www-nova.fnal.gov/plots_and_figures/plots_and_figures.html`, Accessed: 2017-03-27.

[46] R. Verma, “Lower bound on neutrino mass and possible CP violation in neutrino oscillations”, Physical Review D **88**, 111301 (2013).

[47] F. Capozzi et al., “Neutrino masses and mixings: Status of known and unknown 3ν parameters”, Nuclear Physics B **908**, 218–234 (2016).

[48] NOνA Collaboration, “First measurement of electron neutrino appearance in NOνA”, Phys. Rev. Lett. **116**, 151806 (2016).

[49] MINOS Collaboration, “Combined analysis of ν_μ disappearance and $\nu_\mu \to \nu_e$ appearance in MINOS using accelerator and atmospheric neutrinos”, Physical review letters **112**, 191801 (2014).

[50] T2K Collaboration, “First combined analysis of neutrino and antineutrino oscillations at T2K”, Phys. Rev. Lett. **118**, 151801 (2017).

[51] S. Pascoli and S. T. Petcov, “Majorana neutrinos, neutrino mass spectrum, and the $|< m >| \sim 10^{-3}$ eV frontier in neutrinoless double beta decay”, Physical Review D **77**, 113003 (2008).

[52] Z.-z. Xing and Y.-L. Zhou, “Majorana CP-violating phases in neutrino-antineutrino oscillations and other lepton-number-violating processes”, Physical Review D **88**, 033002 (2013).

[53] S. Parke and M. Ross-Lonergan, “Unitarity and the three flavor neutrino mixing matrix”, Physical Review D **93**, 113009 (2016).

[54] M. Ross-Lonergan, “Non-Unitarity in the 3×3 PMNS Matrix”, in NuFact Conference (2016).

[55] I. Esteban et al., “Updated fit to three neutrino mixing: exploring the accelerator-reactor complementarity”, arXiv preprint arXiv:1611.01514 (2016).

[56] S. Parke and M. Ross-Lonergan, “Unitarity and the three flavor neutrino mixing matrix”, Physical Review D **93**, 113009 (2016).

[57] I. Girardi et al., “Leptonic Dirac CP violation predictions from residual discrete symmetries”, Nuclear Physics B **902**, 1–57 (2016).

[58] I. Girardi, S. Petcov, and A. Titov, “Predicting the Leptonic Dirac CP Violation Phase from Sum Rules”, in Proceedings of the European Physical Society Conference on High Energy Physics (Vienna, Austria) (2015).

[59] S. Sarkar, “Measuring the baryon content of the universe: BBN vs CMB”, arXiv preprint astro-ph/0205116 (2002).

[60] B. Field, P. Molaro, and S. Sarkar, “Big Bang Nucleosynthesis”, in *Review of particle physics*, Vol. C40, edited by K. A. Olive et al. (Chinese physics C, 2016).

[61] D. V. Perepelitsa, “Sakharov conditions for baryogenesis”, Lecture at the University of Columbia **3** (2008).

[62] N. Cabibbo, “Unitary symmetry and leptonic decays”, Physical Review Letters **10**, 531 (1963).

[63] M. Kobayashi and T. Maskawa, “CP-violation in the renormalizable theory of weak interaction”, Progress of Theoretical Physics **49**, 652–657 (1973).

[64] A. Ceccucci, Z. Ligeti, and Y. Sakai, “The CKM quark-mixing matrix”, in *Review of particle physics*, Vol. C40, edited by K. A. Olive et al. (Chinese physics C, 2016).

[65] T. Gershon and Y. Nir, “CP violation in the quark section”, in *Review of particle physics*, Vol. C40, edited by K. A. Olive et al. (Chinese physics C, 2016).

[66] A. Riotto, “Theories of baryogenesis”, Summer School in High-energy Physics and Cosmology, Trieste, Italy **arXiv preprint hep-ph/9807454** (1998).

[67] M. Drewes, "The phenomenology of right handed neutrinos", International Journal of Modern Physics E **22**, 1330019 (2013).

[68] S. T. Petcov, "Leptonic CP violation and leptogenesis", International Journal of Modern Physics A **29**, 1430028 (2014).

[69] V. A. Rubakov and M. E. Shaposhnikov, "Electroweak baryon number non-conservation in the early universe and in high-energy collisions", Physics-Uspekhi **39**, 461–502 (1996).

[70] A. Riotto and M. Trodden, "Recent progress in baryogenesis", Annual Review of Nuclear and Particle Science **49**, 35–75 (1999).

[71] A. Kamada et al., "How the Self-Interacting Dark Matter Model Explains the Diverse Galactic Rotation Curves", arXiv preprint arXiv:1611.02716 (2016).

[72] J. Arabadjis, M. Bautz, and G. Arabadjis, "Extracting the dark matter profile of a relaxed galaxy cluster", The Astrophysical Journal **617**, 303 (2004).

[73] D. Clowe, A. Gonzalez, and M. Markevitch, "Weak-lensing mass reconstruction of the interacting cluster 1E 0657–558: Direct evidence for the existence of dark matter", The Astrophysical Journal **604**, 596 (2004).

[74] D. Groom, "Astrophysical Constants and Parameters", in *Review of particle physics*, Vol. C40, edited by K. A. Olive et al. (Chinese physics C, 2016).

[75] M. Drees and G. Gerbier, "Dark Matter", in *Review of particle physics*, Vol. C40, edited by K. A. Olive et al. (Chinese physics C, 2016).

[76] T. Asaka and M. Shaposhnikov, "The νMSM, dark matter and baryon asymmetry of the universe", Physics Letters B **620**, 17–26 (2005).

[77] S. Alekhin et al., "A facility to Search for Hidden Particles at the CERN SPS: the SHiP physics case", Reports on Progress in Physics **79**, 124201 (2016).

[78] Y. Yamazaki et al., "Accelerator technical design report for J-PARC", KEK-REPORT-2002-13, JAERI-TECH-2003-044, J-PARC-03-01 (2003).

[79] T. Nakadaira et al., "T2K target", in Aip conference proceedings, Vol. 981, 1 (AIP, 2008), pp. 290–292.

[80] A. Ichikawa, “Design concept of the magnetic horn system for the T2K neutrino beam”, Nuclear Instruments and Methods in Physics Research A **690**, 27–33 (2012).

[81] K. Matsuoka et al., “Design and performance of the muon monitor for the T2K neutrino oscillation experiment”, Nuclear Instruments and Methods in Physics Research A **624**, 591–600 (2010).

[82] K. McDonalds, “Neutrino Beam Design and Construction”, in *Long Baseline Neutrino Oscillation Experiment at the AGS*, Vol. Brookhaven National Laboratory Physics Design Report BNL, edited by K. A. Olive et al. (E889 Collaboration et al., 1995).

[83] K. T. McDonald, “An Off-axis neutrino beam”, Physics Examples (2001).

[84] G. Battistoni et al., “The FLUKA code: Description and benchmarking”, in AIP Conference proceedings, Vol. 896, 1 (AIP, 2007), pp. 31–49.

[85] A. Ferrari et al., “FLUKA: A multi-particle transport code”, CERN Technical Report **CERN-2005-010** (2005).

[86] T2K Collaboration, “T2K neutrino flux prediction”, Physical Review D **87**, 012001 (2013).

[87] NA61/SHINE Collaboration, “NA61/SHINE facility at the CERN SPS: beams and detector system”, JINST **9**, P06005 (2014).

[88] NA61/SHINE Collaboration, “Measurements of $\pi^{\pm}$, $K^{\pm}$, K^0_S, Λ and proton production in proton–carbon interactions at 31 GeV/c with the NA61/SHINE spectrometer at the CERN SPS”, The European Physical Journal C **76**, 1–49 (2016).

[89] R. Brun et al., *Geant3 user’s guide*, tech. rep. (CERN DD/EE/84-1, 1987).

[90] T2K Collaboration, “Measurement of neutrino and antineutrino oscillations by the T2K experiment with an additional sample of charged-current ν_e interactions at the far detector with one charged pion in the final state”, manuscript in preparation.

[91] T2K Collaboration, “Measurements of the T2K neutrino beam properties using the INGRID on-axis near detector”, Nuclear Instruments and Methods in Physics Research A **694**, 211–223 (2012).

[92] M. Calvetti, P. Cennini, and S. Centro, “UA1 central detector”, CERN-EP/82-44 (1982).

[93] S. Aoki et al., "The T2K side muon range detector (SMRD)", Nuclear Instruments and Methods in Physics Research A **698**, 135–146 (2013).

[94] D. Allan et al., "The electromagnetic calorimeter for the T2K near detector ND280", Journal of Instrumentation **8**, P10019 (2013).

[95] S. Assylbekov et al., "The T2K ND280 Off-Axis Pi-Zero Detector", Nucl. Instrum. Meth. **A686**, 48–63 (2012).

[96] P.-A. Amaudruz et al., "The T2K fine-grained detectors", Nuclear Instruments and Methods in Physics Research A **696**, 1–31 (2012).

[97] G. Vasseur, "Operation of the T2K time projection chambers", Journal of Instrumentation **7**, C02040 (2012).

[98] I. Giomataris et al., "Micromegas in a bulk", Nuclear Instruments and Methods in Physics Research A **560**, 405–408 (2006).

[99] Super-Kamiokande Collaboration, "The Super-Kamiokande detector", Nuclear Instruments and Methods in Physics Research A **501**, 418–462 (2003).

[100] Y. Itow et al., "The JHF-Kamioka neutrino project", arXiv preprint hep-ex/0106019 (2001).

[101] A. A. Watson, "The discovery of Cherenkov radiation and its use in the detection of extensive air showers", Nuclear Physics B-Proceedings Supplements **212**, 13–19 (2011).

[102] K. Abe et al., "Calibration of the Super-Kamiokande detector", Nuclear Instruments and Methods in Physics Research A **737**, 253–272 (2014).

[103] S. Agostinelli et al., "Geant4 - a simulation toolkit", Nuclear instruments and methods in physics research section A: Accelerators, Spectrometers, Detectors and Associated Equipment **506**, 250–303 (2003).

[104] Y. Hayato, "A neutrino interaction simulation program library NEUT", Acta Physica Polonica B **40**, 2477 (2009).

[105] C. Wilkinson et al., "Testing charged current quasi-elastic and multinucleon interaction models in the NEUT neutrino interaction generator with published datasets from the MiniBooNE and MINERνA experiments", Physical Review D **93**, 072010 (2016).

[106] C. L. Smith, "Neutrino reactions at accelerator energies", Physics Reports **3**, 261–379 (1972).

[107] R. Smith and E. J. Moniz, “Neutrino reactions on nuclear targets”, Nuclear Physics B **43**, 605–622 (1972).

[108] L. Alvarez-Ruso, Y. Hayato, and J. Nieves, “Progress and open questions in the physics of neutrino cross sections at intermediate energies”, New Journal of Physics **16**, 075015 (2014).

[109] C. De Jager, H. De Vries, and C. De Vries, “Nuclear charge-and magnetization-density-distribution parameters from elastic electron scattering”, Atomic data and nuclear data tables **14**, 479–508 (1974).

[110] J. Nieves, J. E. Amaro, and M. Valverde, “Inclusive quasielastic charged-current neutrino-nucleus reactions”, Physical Review C **70**, 055503 (2004).

[111] J. Nieves, I. R. Simo, and M. V. Vacas, “Inclusive charged-current neutrino-nucleus reactions”, Physical Review C **83**, 045501 (2011).

[112] D. Rein and L. M. Sehgal, “Neutrino-excitation of baryon resonances and single pion production”, Annals of Physics **133**, 79–153 (1981).

[113] C. Wilkinson et al., “Reanalysis of bubble chamber measurements of muon-neutrino induced single pion production”, Physical Review D **90**, 112017 (2014).

[114] D. Rein and L. Sehgal, “PCAC and the Deficit of Forward Muons in $\pi+$ Production by Neutrinos”, Physics Letters B **657**, 207–209 (2007).

[115] D. Rein and L. M. Sehgal, “Coherent π^0 production in neutrino reactions”, Nuclear Physics B **223**, 29–44 (1983).

[116] C. Berger and L. Sehgal, “Partially conserved axial vector current and coherent pion production by low energy neutrinos”, Physical Review D **79**, 053003 (2009).

[117] MINERνA Collaboration, “Measurement of Coherent Production of $\pi^{\pm}$ in Neutrino and Antineutrino Beams on Carbon from E_ν of 1.5 to 20 GeV”, Physical review letters **113**, 261802 (2014).

[118] M. Glück, E. Reya, and A. Vogt, “Dynamical parton distributions revisited”, The European Physical Journal C-Particles and Fields **5**, 461–470 (1998).

[119] A. Bodek et al., “Modeling neutrino and electron scattering cross sections in the few gev region with effective lo pdfs”, in Aip conference proceedings, Vol. 670, 1 (AIP, 2003), pp. 110–117.

[120] *WikiBooks: Molecular Simulation/Monte Carlo Methods*, `https://en.wikibooks.org/wiki/Molecular_Simulation/Monte_Carlo_Methods`, Accessed: 2017-04-04.

[121] C. B. Lang, "Monte Carlo methods", Lecture at the University of Graz **Chapter 1**.

[122] K. B. Athreya, H. Doss, J. Sethuraman, et al., "On the convergence of the Markov chain simulation method", The Annals of Statistics **24**, 69–100 (1996).

[123] W. K. Hastings, "Monte Carlo sampling methods using Markov chains and their applications", Biometrika **57**, 97–109 (1970).

[124] W. R. Gilks, S. Richardson, and D. J. Spiegelhalter, "Introducing Markov chain Monte Carlo", Markov chain Monte Carlo in practice **1**, 19 (1996).

[125] R. Calland, "A 3 Flavour Joint Near and Far Detector Neutrino Oscillation Analysis at T2K", Thesis defended at the University of Liverpool (2015).

[126] T. J. Loredo, "Bayesian astrostatistics: a backward look to the future", in *Astrostatistical challenges for the new astronomy* (Springer, 2013), pp. 15–40.

[127] *Prob*$3++$ *webpage*, `http://www.phy.duke.edu/~raw22/public/Prob3++`, Accessed: 2017-03-27.

[128] R. Trotta, "Bayesian inference: Principles and applications", in Lecture given at the XII School of Cosmology, Cargese, France (2014).

[129] R. E. Kass and A. E. Raftery, "Bayes factors", Journal of the american statistical association **90**, 773–795 (1995).

[130] T2K Collaboration, "Measurements of neutrino oscillation in appearance and disappearance channels by the T2K experiment with 6.6×10^{20} protons on target", Physical Review D **91**, 072010 (2015).

[131] "Neutrino Mixing (listing)", in *Review of particle physics*, Vol. C38, edited by K. A. Olive et al. (Chinese physics C, 2015).

[132] K2K Collaboration, "Measurement of the quasi-elastic axial vector mass in neutrino-oxygen interactions", Phys. Rev. **D74**, 052002 (2006).

[133] E. J. Moniz et al., "Nuclear fermi momenta from quasielastic electron scattering", Physical Review Letters **26**, 445 (1971).

[134] M. Martini et al., “Unified approach for nucleon knock-out and coherent and incoherent pion production in neutrino interactions with nuclei”, Physical Review C **80**, 065501 (2009).

[135] K. M. Graczyk and J. T. Sobczyk, “Form factors in the quark resonance model”, Physical Review D **77**, 053001 (2008).

[136] MINOS Collaboration, “Neutrino and antineutrino inclusive charged-current cross section measurements with the MINOS near detector”, Physical Review D **81**, 072002 (2010).

[137] MiniBooNE Collaboration, “First observation of coherent π^0 production in neutrino–nucleus interactions with $E_\nu < 2$ GeV”, Physics Letters B **664**, 41–46 (2008).

[138] SciBooNE Collaboration, “Improved measurement of neutral current coherent π^0 production on carbon in a few-GeV neutrino beam”, Phys. Rev. **D81**, 111102 (2010).

[139] E. Wang et al., “Photon emission in neutral current interactions at the T2K experiment”, Physical Review D **92**, 053005 (2015).

[140] M. Day and K. S. McFarland, “Differences in quasielastic cross sections of muon and electron neutrinos”, Physical Review D **86**, 053003 (2012).

[141] P. de Perio, “Joint Three-Flavour Oscillation Analysis of ν_μ Disappearance and ν_e Appearance in the T2K Neutrino Beam”, Thesis defended at the University of Toronto (2014).

[142] A. Heikkinen, N. Stepanov, and J. P. Wellisch, “Bertini intranuclear cascade implementation in GEANT4”, eConf **C0303241**, MOMT008 (2003).

[143] D. Ashery et al., “True absorption and scattering of pions on nuclei”, Physical Review C **23**, 2173 (1981).

[144] S. K. Agarwalla et al., “Probing Non-Standard Interactions at Daya Bay”, JHEP **07**, 060 (2015).

[145] T. Ohlsson, “Status of non-standard neutrino interactions”, Reports on Progress in Physics **76**, 044201 (2013).

[146] D. V. Forero and P. Huber, “Hints for leptonic CP violation or New Physics?”, Phys. Rev. Lett. **117**, 031801 (2016).

[147] MINOS Collaboration, “First direct observation of muon antineutrino disappearance”, Phys. Rev. Lett. **107**, 021801 (2011).

[148] NOνA collaboration, "Measurement of the Neutrino Mixing Angle θ_{23} in NOνA", Physical Review Letters **118**, 151802 (2017).

[149] X. L. M. A. Gelman and H. Stern, "Posterior Predictive Assessment of Model Fitness via Realized Discrepancies", Statistica Sinica **6**, 733–759 (1996).

[150] S. Pascoli, S. T. Petcov, and A. Riotto, "Connecting low energy leptonic CP-violation to leptogenesis", Phys. Rev. **D75**, 083511 (2007).

[151] T2K Collaboration, "Proposal for an Extended Run of T2K to 20×10^{21} POT", (2016).

[152] A. A. Aguilar-Arevalo et al., "First Measurement of the Muon Neutrino Charged Current Quasielastic Double Differential Cross Section", Phys. Rev. **D81**, 092005 (2010).

[153] A. A. Aguilar-Arevalo et al., "First measurement of the muon antineutrino double-differential charged-current quasielastic cross section", Phys. Rev. **D88**, 032001 (2013).

[154] L. Fields et al., "Measurement of Muon Antineutrino Quasielastic Scattering on a Hydrocarbon Target at Eν3.5GeV", Phys. Rev. Lett. **111**, 022501 (2013).

[155] G. A. Fiorentini et al., "Measurement of Muon Neutrino Quasielastic Scattering on a Hydrocarbon Target at Eν3.5GeV", Phys. Rev. Lett. **111**, 022502 (2013).

[156] T. Koga et al., "Water/CH Neutrino Cross Section Measurement at J-PARC (WAGASCI Experiment)", JPS Conf. Proc. **8**, 023003 (2015).

[157] A. Minamino, "WAGASCI and ND280 Upgrades", JPS Conf. Proc. **12**, 010038 (2016).

[158] A. Blondel, M. Zito, et al., "Near Detectors based on gas TPCs for neutrino long baseline experiments", (2017).

[159] B. Quilain and A. Minamino, "The WAGASCI detector as an off-axis near detector of the T2K and Hyper-Kamiokande experiments", in 27th International Conference on Neutrino Physics and Astrophysics (Neutrino 2016) London, United Kingdom, July 4-9, 2016 (2016).

[160] TITUS Collaboration, "TITUS: the Tokai Intermediate Tank for the Unoscillated Spectrum", (2016).

[161] nuPRISM Collaboration, "Letter of Intent to Construct a nuPRISM Detector in the J-PARC Neutrino Beamline", (2014).

[162] T2K Collaboration, “Neutrino oscillation physics potential of the T2K experiment”, PTEP **2015**, 043C01 (2015).

[163] C. Geyer, “Introduction to Markov Chain Monte Carlo”, in *Handbook of Markov Chain Monte Carlo*, edited by S. Brooks et al. (Chapman & Hall/CRC, 2011).

[164] G. O. Roberts, A. Gelman, W. R. Gilks, et al., “Weak convergence and optimal scaling of random walk Metropolis algorithms”, The annals of applied probability **7**, 110–120 (1997).

[165] J. Dunkley et al., “Fast and reliable Markov chain Monte Carlo technique for cosmological parameter estimation”, Monthly Notices of the Royal Astronomical Society **356**, 925–936 (2005).

[166] J. Geweke et al., *Evaluating the accuracy of sampling-based approaches to the calculation of posterior moments*, Vol. 196 (Federal Reserve Bank of Minneapolis, Research Department Minneapolis, MN, USA, 1991).

[167] C. Andreopoulos et al., “The GENIE Neutrino Monte Carlo Generator”, Nucl. Instrum. Meth. **A614**, 87–104 (2010).